UNIVERSITÀ
DEGLI STUDI
DI PADOVA

Administrative unit: **University of Padova**

Department: **Land, Environment, Agriculture and Forestry (TESAF)**

PhD Program: **Land, Environment, Resources and Health (LERH)**

Batch: XXXIV

Analysis of sediment connectivity in mountain catchments affected by natural disturbances

PhD Program Coordinator: Prof. Marco Borga

Supervisor: Dr. Lorenzo Picco

Co-Supervisor: Dr. Marco Cavalli

PhD student: Lorenzo Martini

Sede Amministrativa: **Università degli Studi di Padova**

Dipartimento: **Territorio e Sistemi Agro-Forestali (TESAF)**

Corso di dottorato di ricerca in: **Land, Environment, Resources and Health (LERH)**

Ciclo: XXXIV

Analisi della connettività dei sedimenti in bacini montani colpiti da disturbi naturali

Coordinatore: Prof. Marco Borga

Supervisore: Dott. Lorenzo Picco

Co-Supervisore: Dott. Marco Cavalli

Dottorando: Lorenzo Martini

Table of Contents

Summary

Sediment connectivity has become a fundamental concept to identify and analyse the linkages facilitating or inhibiting the sediment fluxes of any geomorphic system. Therefore, understanding how sediment connectivity operates and changes after natural disturbances, which can alter the properties of an entire geomorphic system, is fundamental to increase knowledge about functioning of mountain catchments. However, analysing the impact of such phenomena on sediment connectivity is still a major challenge. Hence, the main objective of the present PhD thesis is to investigate the effects of natural disturbances on sediment connectivity in different mountain catchments.

In the first chapter, two case studies are presented from Chile, where large natural disturbances are a major source of disruption for river basins. The first study investigated the impact of a volcanic eruption by developing a multi-temporal analysis of a gemorphometric indicator (i.e. the Index of Connectivity - IC), used to measure the degree of linkage between hillslopes and channel. The results showed a large increase in IC values after the eruption, due to the land cover changes and the widening of the active channel triggered by the disturbance. The second study case addressed the effects of wildfires in a catchment in central Chile. The methodology developed from a refined version of the approach proposed in the first study to enhance the assessment of sediment connectivity in fire-affected areas. The outcomes indicated that fire severity and IC variations followed similar spatial patterns and that IC increased less after the second wildfire due to residual effects of the first event.

The second chapter presents an analysis of the hydrological, geomorphic and sedimentological response of an alpine catchment to a storm. In 2018, the Vaia storm caused massive forest windthrows and large floods throughout the mountain sector of North-East of Italy. In this context, the comprehensive analysis carried out in the Rio Cordon catchment was necessary to inform about a wide range of effects that such event produced in a typical alpine stream. Sediment connectivity analysis, developed with IC and DEM of Difference (DoD), shed light on the role of the new sediment sources in providing the sediment from hillslopes to the stream. Therefore, the IC was used as a supportive tool to validate and link the outcomes of the other analyses, thus highlighting the whole sediment cascade.

In the third chapter and last study case, a deep focus on the IC is presented. The study tried to respond to recent challenges and doubts concerning the reliability of the IC and the need for its validation. Specifically, the capability of IC in depicting structural connectivity and predicting functional connectivity was statistically evaluated in the Rio Cordon. First, for each sediment source of the catchment the connectivity status in respect to channel network was assessed. Then, different

IC maps were computed and their capability in predicting the connectivity status was tested with logistic regression analysis. The results demonstrated that IC shows high accuracy when validating the static linkages and lower accuracy when predicting event-based linkages. Nevertheless, a threshold between high and low IC was derived, improving the reliability of IC maps as tools for watershed management.

Overall, in this PhD thesis, insights about how to investigate sediment connectivity in different contexts were provided. In multiple catchments, affected by natural disturbances it was possible to derive a common and useful methodology to represent sediment connectivity and its evolution. Moreover, I pointed out that a more quantitative approach, based on IC and geomorphic change detection, could support a more holistic study. Finally, I assessed the true meaning of IC, emphasizing its advantages and disadvantages in an alpine catchment and opening new challenges in the field of sediment connectivity.

Riassunto

La connettività dei sedimenti è diventata un paradigma fondamentale per identificare e analizzare i collegamenti che facilitano o inibiscono i flussi di sedimenti di qualsiasi sistema geomorfologico. Quindi capire come la connettività dei sedimenti opera e cambia dopo disturbi naturali, capaci di alterare le caratteristiche di un intero sistema geomofologico, è essenziale per aumentare la conoscenza riguardo il funzionamento dei bacini montani. Tuttavia, analizzare l'impatto di tali fenomeni naturali sulla connettività è ancora una grande sfida. Perciò, l'obiettivo principale della presente tesi di dottorato è quello di indagare gli effetti dei disturbi naturali sulla connettività dei sedimenti in diversi bacini idrografici montani.

Nel primo capitolo della tesi, sono presentati due casi di studio condotti in Cile. Il primo studio ha indagato l'impatto di un'eruzione vulcanica sviluppando un'analisi multi-temporale di un'indicatore geomorfometrico (Indice di Connettività -IC), che misura il grado di collegamento tra i versanti e il canale. I risultati hanno mostrato un incremento dei valori di IC dopo l'eruzione, dovuto ai cambiamenti di copertura del suolo e all'espansione del canale attivo. Il secondo studio ha affrontato gli effetti di incendi forestali in un bacino del Cile centrale. Per far ciò si è utilizzato un approccio più affinato del primo studio al fine di migliorare lo studio della connettività dei sedimenti nelle aree colpite dagli incendi. I risultati hanno indicato che la severità degli incendi e le variazioni di IC hanno seguito una distribuzione spaziale simile e che i valori di IC sono aumentati di meno dopo il secondo incendio a causa degli effetti residui del primo evento.

Il secondo capitolo presenta un'analisi della risposta idrologica, geomorfologica e sedimentologica di un bacino idrografico alpino ad una tempesta. Nel 2018 la tempesta Vaia ha provocato vasti schianti da vento e inondazioni in tutto il settore montano del Nord-Est d'Italia. Perciò, l'analisi effettuata nel bacino del Rio Cordon è stata fondamentale per documentare i vari effetti che tale perturbazione ha prodotto in un tipico torrente alpino. L'analisi della connettività, sviluppata con IC e Dem of Difference (DoD), ha fatto luce sul ruolo delle nuove fonti di sedimenti nel fornire materiale dai versanti alla rete idrografica. Pertanto, l'IC è stato usato come strumento di supporto per collegare i risultati delle altre analisi.

Nel terzo capitolo e ultimo caso di studio, viene presentato un approfondimento sull'IC. In particolare, la capacità dell'IC di rappresentare la connettività strutturale e di predire la connettività funzionale è stata valutata statisticamente nel Rio Cordon, utilizzando come campioni i collegamenti tra le fonti di sedimenti e la rete di canali. In primo luogo, si è proceduto a valutare lo stato di connettività per ogni fonte di sedimenti. In seguito, la capacità delle mappe di IC di predire tale stato

è stata testata attraverso modelli di regressione logistica. I risultati hanno dimostrato che l'IC è accurato nel convalidare i collegamenti statici ma non riesce a predire i collegamenti basati sui processi. Ad ogni modo, si è derivata una soglia netta tra alto e basso IC, che potrebbe favorire l'uso delle mappe di connettività come strumento di gestione dei bacini montani.

Nel complesso, in questa tesi ho fornito spunti su come indagare la connettività dei sedimenti in diversi contesti. In più bacini colpiti da disturbi naturali, è stato possibile derivare una metodologia utile per rappresentare la connettività dei sedimenti e la sua evoluzione. Inoltre, ho sottolineato che un approccio più quantitativo, fondato sull'IC e sul rilevamento delle variazioni morfologiche, potrebbe sostenere uno studio più olistico. Infine, ho valutato la vera essenza dell'IC, sottolineando i suoi vantaggi e svantaggi, aprendo nuove sfide nel campo della connettività dei sedimenti.

Introduction

River systems are formed according to the composition, structure and behaviour of the surrounding landscape, which represents the template in which physical processes and landforms interact. Understanding these interactions is fundamental to inform about past, present and future conditions of the landscape (Fryirs and Brierley, 2013). Geomorphic systems like river basins are highly dynamic, constantly reshaping and self-regulating their forms and processes after perturbations (Knighton, 1998). Iterative adjustments are observed between subsequent perturbations, with the magnitude of the adjustments decaying over time and becoming asymptotic towards a new steady state of equilibrium (Graf, 1977; Wu et al., 2012). Indeed, the condition of equilibrium, intended as the absence of net change, is reliant on the time scale, thus the same system might appear stable considering a long-time interval but highly unstable in the short term, due to small fluctuation around the steady-state (Wohl, 2020). Therefore, in natural geomorphic systems an equilibrium barely exists and the concept is evanescent.

The perturbations acting on the landscape and influencing the ecosystems are often referred as disturbances, which may differ in spatial distribution, frequency or return interval, severity and intensity (White and Pickett, 1985). Considering a rough distinction between small frequent disturbances and large infrequent disturbances, it is clear how the understanding of the latter has increased slower than the former. Large and infrequent disturbances are known only superficially, mainly because of the lack of long-term data and their wide spatial scale that makes their investigations challenging (Turner and Dale, 1998). Sometimes referred as LIDs, Large and Infrequent Disturbances are documented as major agents of landscape modification even though they were first recognized only for their implications on forest ecosystems and biological legacies (Foster et al., 1998). LIDs are characterized by low frequency and high magnitude and they result in those phenomena like volcanic eruptions, wildfires and floods sometimes named extreme or exceptional events.

In the present thesis, the objectives consider natural disturbances at catchment-scale, thus it becomes clear that the term disturbance is used as a generalized version of LID, still implying large-scale effects. Moreover, the present work overlooks the nomenclature issue, thus it is possible to find extreme/exceptional event used as synonyms to large disturbance or LID.

In fluvial geomorphology, the interaction river system-disturbance has always fascinated scientists who focus their attention on the response, effects and sensitivity to these events. Particularly, the

sensitivity concept has been used to understand the reaction time, i.e. the interval in which the system responds to a change, the relaxation time, i.e. time taken to reach or to return to a new or past condition, and the recovery time, which refers to the period engaged to maintain the new or past condition after a disturbance (Fryirs and Brierley, 2013). Considering one of the first sensitivity frameworks proposed by Brunsden and Thornes (1979), disturbances can manifest themselves as pulsed or ramped inputs. Pulsed inputs refer to episodic events characterized by low frequency, high magnitude but limited duration so that the effects are confined locally (e.g. floods). On the contrary, after ramped inputs, the effects are propagated over time and space causing a permanent change in the boundary conditions (e.g. drought). How the system responds to different inputs depends upon its structure, strength properties, complexity, resilience, shock absorption capacity, transmission of linkages and coupling efficiency (Brunsden, 2001). Notably, transmission of linkages and coupling efficiency are two concepts recalled by many other authors. Harvey (2001; 2002) stressed the importance of coupling between hillslopes and channels in influencing the system after a disturbance. Different coupling mechanisms have implications on the geomorphic response to human-induced, climatically-induced and tectonically induced environmental changes. Coupling mechanisms can manifest in a double-direction: downsystem and upsystem. The former concerns the coarse fraction of sediment reaching the channel network from hillslopes; the latter may relate to the diffusion of an event upstream from channels to hillslopes or through channels. Regarding the transmission of pulses throughout a basin, Brunsden (1993) classified three coupling states: coupled, not coupled and decoupled. Coupled components show free transmission of energy and material (water and/or sediment); not coupled units show no linkages due to the presence of an impediment; decoupled units refer to a previous coupling state, which is now ceased. Increasing attention has been paid to the overall chain of events governing the transport of sediment throughout the fluvial landscape, defined by Burt and Allison (2010) as sediment cascade. In steep mountain catchments, recognized as the sediment production zone (Schumm, 1977), the sediment cascade is fueled by the sediment sources. With particular reference to the transfer between sources to storage areas, like floodplains, alluvial fans, lakes and so on, Ferguson (1981) defined this journey as jerky conveyor belt of sediment delivery. Building within all these concepts, a new term has taken hold in the last two decades: sediment connectivity.

Outside the field of geomorphology, the term connectivity has been widely used in biological disciplines concerning, for instance, the passage of species between habitats or the transfer of genetic material amongst populations (Crooks and Sanjayan, 2006). Definitely adopted from these disciplines, geomorphologists started using connectivity with regard to the transfer of water and

sediment (Wohl, 2017). Particularly, sediment connectivity can distinguish from other two major types of connectivity, indicated as landscape connectivity, related to the coupling of landforms, and hydrological connectivity, referred to the passage of water or to the transfer of matter and energy within the hydrological cycle (Pringle, 2001; Bracken and Croke, 2007). A universal definition of sediment connectivity is not yet documented, essentially because of the many facets the concept can assume. Nevertheless, several authors provided their definition and the framework in which it can be applied. Hooke (2003) mainly focused on river-channel systems, highlighting the physical linkage of sediment through the channel network, hence the potential capability of a sediment particle to move throughout the system. Moreover, five classes of connectivity were defined according to the transport capacity of channel reaches and considering the disturbance component (e.g. partially connected reaches show transfer only during extreme floods). Brierley et al. (2006), underlined the importance of an effective description and explanation of (dis)connectivity to identify sensitive parts of the landscape and to predict future trajectories of geomorphic change. Moreover, they considered three types of linkage still in use: longitudinal, namely in-channel from upstream to downstream; lateral, including slope-channel or channel-floodplain relationships; vertical, referred to surface-subsurface interactions. Developing on these aspects, Fryirs et al. (2007a; 2007b), developed a conceptual framework for analyzing sediment disconnectivity by incorporating the spatial-temporal patterns of buffers, barriers and blankets, hence landform impediments. These features can restrict (buffers; e.g. terraces, alluvial fans), inhibit (barriers; e.g. dams, wood material) or drape (blankets; e.g. bed armor) sediment movement by switching on and off the sediment delivery throughout the various components of the catchment. Therefore, connectivity is implicitly underlying sediment transfer problems and bearing empirical approaches such the sediment delivery ratio, which infers the fraction of sediment transferred to the outlet of a basin (Bracken and Croke, 2007). With particular attention to the triggering factors of sediment transfer, Bracken et al. (2015), proposed a framework emphasizing the need to characterize the distributions, both spatial and temporal, of sediment detachment and transport and detect the feedbacks between these two processes. As the attention towards connectivity boosted in recent years, it became important to conceptualize the response of fluvial systems, in terms of sediment connectivity, to a major type of disturbance, the human impact. Human activity has entered very quickly in the set of factors driving connectivity and originally circumscribed to geology (e.g. parent material permeability), climate (e.g. rainfall event), biota (e.g. vegetation density), geomorphology (e.g. landslides) and soils (e.g. infiltration) (Bracken and Croke, 2007; Keesstra et al., 2018; Wohl et al., 2018). Whether human impacts affect the longitudinal dimension of a channel (e.g. dam construction, sediment removal) or the lateral connectivity of an

entire catchment (e.g. deforestation, urbanization), they trigger system's self-regulatory mechanisms still poorly studied but extremely important from a management point of view (Poeppl et al., 2017). Therefore, understanding where and how a human impact interrupts or enhances connectivity is deemed essential in social-geomorphic frameworks accounting for process-response feedback loops resulting from different types of human disturbance in river systems (Poeppl et al., 2020). The relevance of connectivity in a geomorphic context brought to light an important distinction between structural and functional connectivity, again inherited from ecological interpretations (Turnbull et al., 2008) and nowadays highly debated in any connectivity framework.

Structural connectivity underlies how physical linkages between components of a geomorphic system are spatially arranged and how these linkages can affect the potential sediment transfer regardless the processes. Hence, it represents a static glimpse of the physical template in which interactions between landforms occur. Structural/static/potential connectivity emphasizes the structural properties of the landscape (e.g. topography, grain size, vegetation) that intrinsically influence the sediment cascade without necessarily implying the transfer of sediment from a compartment to another. Within this structural configuration operates the functional connectivity, which, on the contrary, is process-based and investigates the actual transfer of sediment on a time-dependent scale. The functional/dynamic/actual connectivity depends also on external factors of the system (e.g. precipitation, disturbances) that may characterize the frequency-magnitude distribution of sediment detachments (Wainwright, 2011; Bracken et al., 2015; Wohl et al., 2017; Heckmann et al., 2018; Hooke and Souza, 2021). Indeed, both structural and functional concepts are intertwined as the structures influence the processes and vice versa via feedback mechanisms. This means that the sediment moved by a debris flow reaches a specific downstream area due to high connectivity between the detachment area and the sink area; large enough, the debris flow deposit then creates a new landform capable of interrupting the original pathway and consequently decreasing the connectivity. Therefore, a reliable connectivity framework or metric should account for both static and dynamic aspects (Wohl et al., 2018).

The conceptual frameworks and definitions mentioned so far represent only a small part of a widely discussed and evolving field of research. Many authors tried to summarize and provide comprehensive reviews on the topic. Amongst these authors, Heckmann et al. (2018), undertook a deep focus on the available measure of sediment connectivity, specifically indices, and defined hydrological and sediment connectivity as "the degree to which a system facilitates the transfer of water and sediment through itself, through coupling relationships between its component". Wohl et al. (2018), discussed historical, present and future trends of connectivity and presented connectivity

as “an emergent property of geomorphic systems”. The review by Najafi et al. (2021), organized and presented concepts, frameworks and methods extrapolated from an extensive selection of publications while emphasizing the rapid growth of the topic in different countries of the world. A particular focus on the advantages and deficiencies of approaches to description, modelling, quantification and analysis of connectivity is given by Hooke and Souza (2021), while Turnbull et al. (2018), unraveled the main challenges in the topic. Besides the importance of reviewing the information already existing about connectivity in fact, these works provided evidence of major challenges and future trajectories in the field of sediment connectivity. Some of these challenges have surfaced, approached and faced, sometimes marginally and sometimes more thoroughly, also in the present thesis.

In past years, a first inevitable dilemma was how to measure sediment connectivity, especially given the difficulty of determining sediment transfers in the field and to foresee the future behavior of a geomorphic system. Furthermore, if sediment connectivity is so hardly measurable, particularly if the quantification of sediment fluxes is required, is it possible to even try to develop a metric that summarizes all essential aspects of connectivity? Should connectivity be measured directly, or indirect metrics are also sufficient? These types of questions led to the development of connectivity indices (Heckmann et al., 2018). Since the advance of GIS, the approaches relying on raster-based indices have become successful solutions for the characterization and measure of structural sediment connectivity. In this context, the well-known Index of Connectivity (IC) first developed by Borselli et al. (2008), and then refined by Cavalli et al. (2013), is widely used to investigate potential sediment transfer from hillslopes to downstream areas, to identify the preferential sediment pathways and to prioritize sediment source areas. The IC offers a semi-quantitative approach to measure the degree of linkages by exploiting high-resolution Digital Elevation Models (DEMs) (Cavalli et al., 2013). IC computes the logarithmic ratio between two ideal components of a catchment. The upslope component represents the potential for the mobilization of the sediment given the intrinsic characteristics of the contributing area (slope, area and impedance to sediment fluxes). The downstream component, instead, considers the transfer of sediments according to the length of the flow path taken to reach a point under investigation, i.e. the target. Although the IC is a promising tool for assessing sediment connectivity and the number of applications based on the IC (and other indices) has boosted, more issues and challenges have arisen.

Because the properties defining connectivity systematically vary in time and space, defining the most appropriate scale is a recurrent issue when applying raster-based indices. Considering the spatial scale, the problem is mainly related to define the spatial resolution and the area of reference (Heckmann et al., 2018). The problem of defining the spatial resolution often turns in choosing the

optimum raster resolution (in most cases the DEM cell size dimension) for the objective of the analysis. This choice is particularly difficult in large areas or when high-resolution spatial data are recommended but their availability is not always guaranteed. The area of reference, for which an index or a model is computed (e.g. a reach or an entire catchment), is instead related to a more conceptual problem, which concerns the designation of fundamental spatial units. The choice of fundamental units is a complex task and still a highly debated topic: for instance, is a raster cell or a landform the most appropriate unit? In fact, without a prior consideration of the meaningfulness of the fundamental units, no reliable insights about their connectivity can be obtained (Poeppl and Parson, 2018). The temporal scale over which sediment connectivity varies is again another core problem. As consequence, time component is extremely challenging to introduce into metrics such the IC, hence most of the indices are representing only the spatial variation in sediment connectivity rather than temporal-driven sediment dynamics. First approaches in this direction seek to apply the IC reiteratively over a more or less wide temporal scale to capture potential variation of structural linkages driven for instance by land-use changes or other scenarios (e.g. Lopéz-Vicente et al., 2013; Persichillo et al., 2018; Llena et al., 2019). Finally, the issue of scale can be exacerbated in light of large infrequent disturbances capable of changing landforms and processes over wide scales. Hence, it is difficult to estimate a crucial temporal and spatial scale in which such changes are likely to be effective.

Another important challenge is validation. The widespread use of indices as indirect methods to quantify connectivity called the need for validation, which is chiefly based on field surveys (Hooke and Souza, 2021). First, fieldworks and ground truth are recognized for their importance in building a solid and reliable methodology to apply connectivity indices. In other words, field survey may still represent a fundamental procedure to retrieve and enhance the input of a methodological workflow guiding the computation of the index in different scenarios. Involving direct measures made in the field, in fact, would improve the explanatory ability of the metric, thus the representation of the actual sediment linkages and dynamics. However, no universal protocol for field-based assessment of connectivity is available yet, since many properties (e.g. intrinsic or extrinsic) of a geomorphic system can be involved and many methodological approaches are proposed (Turnbull et al., 2018). Validation, in a more common practice, means to double-check the outcomes of an index, or a model, by exploiting traditional mapping or other modelling approaches (Messenzehl et al., 2014; Schopper et al., 2019; Hooke and Souza, 2021). In the case of the IC, Heckmann et al. (2018), pointed out that fieldwork is recommended to investigate the validity of the IC maps and their interpretations, because the variables included in structural connectivity indices are often reflecting "researcher's conceptual

understanding of connectivity". Therefore, exploring the relationship between IC and field observations could represent an important diagnostic process to improve potential deficiencies in the index or other structural-based metrics. However, this is still poorly investigated.

Partially associated to the issue of validation, a more recent source of discussion has emerged. Most of the raster-based indices are basically using structural properties of the catchment to explore sediment connectivity, which in the end can be identified only as structural connectivity. Once, the IC is validated for its capacity in depicting structural connectivity, another question quickly arises: is it also capable of predicting functional connectivity, i.e. actual sediment dynamics? Therefore, the capability of connectivity indices to explain or predict observable processes is reported as a new major research challenge by Wohl et al. (2017) and Heckmann et al. (2018). They recommended considering IC, but in general all the metrics of sediment connectivity, not only as the ultimate objective of the research but a starting point to understand actual sediment transfer throughout a system. This new tendency opens the door to new applications of IC maps, which can be used in combination with field surveys, other maps or spatially distributed properties, as a supportive tool for broader studies aiming at describing also the processes and not only the structural linkages.

The development of approaches accounting for both functional and structural connectivity is not easy, hence most of the studies refer (implicitly or explicitly) to one of the two and, more frequently, to only structural connectivity (Najafi et al., 2021). According to the reviews above mentioned, what is actually needed is the incorporation of the functions and external properties of the system, i.e. water runoff, sediment transport and yield, soil erosion and infiltration capacity, their interaction among different temporal scales, as well as the feedbacks between processes and morphology. However, this brings back to the first dilemma of how to measure sediment connectivity in its entirety. Finally, it is important to underline that these "functional studies" should be developed starting from more advanced structural-based approaches.

Research objectives and thesis structure

The main objective of the present thesis is to investigate the effects of natural disturbances on sediment connectivity in different mountain catchments. Mountain catchments are highly dynamic environments, where connectivity controls the capability of the system to transfer sediment from source areas to downstream areas. Therefore, awareness of how sediment connectivity controls the exchange of material within a river basin could help predicting positive and negative consequences. However, after large and infrequent disturbances, foreseeing the variations of sediment connectivity is a complex task, given the wide array of unexpexted effects that these events can induce.

Specific objectives are designed to achieve the main objective and to support the building of the thesis organized in chapters. The order in which the objectives are presented reflects the increasing level of complexity and consequently the personal scientific development during the PhD project. Therefore, each subsequent chapter of the present thesis addresses specific objectives so that the entire work can fulfil the overall purpose progressively, step by step.

In chapter 1 the first two specific objectives are addressed:

> I) to identify and integrate the factors driving the Index of Connectivity after disturbances;
>
> II) to adapt the methodology of the pre-existing Index of Connectivity geomorphometric approach to different mountain basins.

Hence, the first chapter concerns the use of the Index of Connectivity (IC) in mountain basins to detect potential changes in sediment connectivity induced by the effects of natural disturbances. The hypothesis is that the impact of natural disturbances has a consequence on sediment connectivity and this impact translates into specific effects that can be integrated into a more adaptable and refined IC-based approach. Two study cases were carried out and presented as they tested the hypothesis and tackled the first two specific objectives.

In chapter 2, the third specific objective is addressed:

> III) to provide a reliable tool for supporting the investigation of sediment connectivity in a more holistic context.

Hence, in the second chapter, an adapted IC-based approach is presented not only as the ultimate goal for studying sediment connectivity but as a tool to support the outcomes of a broader and holistic analysis dealing with the effects of a natural disturbance in an alpine catchment. The hypothesis is that IC helps to investigate the role of sediment source areas as suppliers to the channel network

during extreme events. A single study case was carried out to prove this hypothesis and to achieve the third objective.

In chapter 3, the last specific objective is addressed:

> IV) to contribute to the development of a more quantitative approach in the frame of the Index of Connectivity analysis, to better plan watershed management interventions.

Hence, the last chapter represents a deep focus on the IC in order to unravel the true capability of the index in representing sediment connectivity. To reach a more quantitative approach based on the IC, first it is important to understand which are its limitations and then how to move forward towards a more reliable measure of sediment connectivity. The hypothesis is that IC can depict structural connectivity but not predict functional connectivity. Moreover, in the former case, it is possible to derive a more accurate IC map by defining a threshold between high and low connectivity.

Chapter 1.

In this chapter, two case studies are presented dealing with the impact of natural disturbances on sediment connectivity and how to integrate the main effects of these large and infrequent events into the IC, used as the main tool to investigate connectivity. Both studies were carried out in Chilean catchments, where it is possible to find favourable conditions to better isolate the effects of large natural disturbances on natural river basins. Indeed, the first chapter represents the starting point as it introduces the main tool on which the whole thesis is based on: the IC. Nevertheless, although in the two study cases composing this chapter, the IC is indubitably the core, they do not represent mere applications of the geomorphometric approach proposed originally in alpine catchments. Rather than just transplanting the application of IC in Chilean river basins, in chapter 1 it is possible to find methodological workflows designed to adapt and refine a pre-existing methodology to the effects of natural disturbances like volcanic eruptions and wildfires. Understanding how the IC, and sediment connectivity in general, changes over time after such disturbances employing an adaptive methodology will pose the basis for developing the next study cases presented in the next chapters.

1.1 Sediment connectivity changes in an Andean catchment affected by volcanic eruption

Adapted from Martini L., Picco L., Iroumé A., Cavalli M. (2019).
Sediment connectivity changes in an Andean catchment affected by volcanic eruption.
Science of the Total Environment, 692, 1209-1222. https://doi.org/10.1016/j.scitotenv.2019.07.303

Contributions by the PhD candidate: Investigation, conceptualization, methodology, data curation, writing the original draft.

Abstract

River systems are continuously affected by multiple natural and anthropogenic phenomena. Among major natural disturbances, volcanic eruptions have the capability to overthrow the forms and to modify dramatically the morphological setting and sediment connectivity of the system. Moreover, the input of sediments in the channel network can lead to active channel widening, bed aggradation and river scouring, which in turn may affect downstream human settlements. In this context, the present research aims to investigate sediment connectivity by means of a geomorphometric index in a catchment affected by an explosive volcanic eruption in order to assess its variation before and after the disturbance. We developed a workflow exploiting the use of open source data (i.e., Global Digital Elevation Models, satellite imagery) to represent the impedance to the sediment fluxes and to apply the Index of Connectivity (IC) in this context characterized by the lack of high-resolution topographic data. The study area is the Blanco River basin, southern Chile, which was heavily affected by the eruption of Chaitén volcano (2008–2009) that caused the partial destruction of the forest and the profound alteration of Blanco River's morphology. The application of the IC on different land cover scenarios, derived by combining field observations and satellite image classification techniques, showed an increase in sediment connectivity after the volcanic eruption. In addition, the results highlighted different patterns of connectivity according to the expansion of the active channel induced by the massive input of pyroclastic material. The approach proposed in this study case offers a methodology to investigate sediment connectivity in a river catchment affected by natural disturbance where high-resolution data are not available. The results of the study help to improve knowledge on the effect of volcanic eruptions in the hydrologic catchment and to improve watershed management strategies in such kind of environment.

Keywords: Natural disturbances; Chile; Sediment connectivity; Land cover change; Open source data

Introduction

Fluvial systems are continuously reshaping and adjusting their forms and processes to an array of natural phenomena, defined as disturbances, which change the physical environment on a discrete spatial and temporal scale (White and Pickett, 1985). Dynamic environments like rivers have the capability to self-regulate after a disturbance in order to re-establish the balance of water, sediment and energy fluxes (Fryirs and Brierley, 2013). Among the disturbances, extreme natural events such as volcanic eruptions are able to rapidly upset the flow regime, topography, land use, vegetation, the sediment and large wood supply of an entire river system (Ayris and Delmelle, 2012; Swansonet al., 2013; Pierson and Major, 2014; Tonon et al., 2017). In particular, explosive eruptions are responsible for ejecting a huge amount of volcanoclastic particles (tephra), and for triggering and providing sediment for secondary disturbances like Pyroclastic Density Currents (PDCs), lahars, landslides and floods, which may cause severe damages to nearby human infrastructures and communities (Kataoka et al., 2009; Manville et al., 2009; Mazzorana et al., 2019). Moreover, thick but unconsolidated layers of tephra deposited all over the hillslopes, are easily remobilized by erosional processes, becoming additional sources of sediment for the channel network (Major, 2003). The massive sediment input in the river network leads to well-known effects, such as active channel widening, river scouring, bank erosion and an acceleration of aggradation-degradation cycles (Pierson and Major, 2014). In addition, the hydrology at the catchment scale is also affected by the tephra deposits, which causes the reduction of water storage capacity and the consequent alteration of runoff volume and timing (Major and Yamakoshi, 2005). In highly impacted areas, where these effects are often associated with the loss of interception by dead canopies, the occurrence of larger flash floods and lahars is observed even without extreme rainfall (Alexander et al., 2010).

Concerning the ecological effects, volcanic eruptions may deeply affect the land cover of the entire catchment by burying, damaging or removing the living vegetation, then becoming material for massive pulses of dead wood into the river corridor (Swanson et al., 2013). In post-eruption scenarios, river adjustments are primarily responsible for the in-channel mobility of dead wood that may affect downstream settlements (Tonon et al., 2017). In the last decades, the hydro-geomorphic responses to explosive eruptions have been widely studied in several volcanic scenarios: Mount Pinatubo in Philippines (Hayes et al., 2002; Gran and Montgomery, 2005); Mount St. Helens in the USA (Meyer and Martinson, 1989; Major et al., 2000; Major and Yamakoshi, 2005); Chaitén in Chile (Ulloa et al.,

2015; Ulloa et al.,2016); El Chichón in Mexico (Inbar et al., 2001). Moreover, understanding the behaviour of sediments in volcanic environment is fundamental to predict morphological, ecological and hydrological responses and to avoid considerable economic losses (Dale et al., 2005; Pierson and Major, 2014; Ortíz-Rodríguez et al., 2017). In geomorphic systems, the issue of sediment dynamics typically addresses the processes driving sediments from sources to downstream areas (Cavalli et al., 2013). Each of these processes strictly depends upon the intrinsic features of the system and its structure, controlled by vegetation pattern (Cammeraat, 2002; Borselli et al., 2008) and topography (e.g., elevation, slope and roughness) (Heckmann et al., 2018). In the last years, the growing interest in the sediment cascade concept, as well as the need for a deeper characterization of the hillslope-channel (de)coupling state, stimulated the research in the field of sediment connectivity (Harvey, 2001; Hooke, 2003; Fryirs et al., 2007; Bracken et al., 2015). In geomorphology, the sediment connectivity is defined as the degree to which a system facilitates the transfer of sediment through itself, by means of coupling relationships between its components (Heckmann et al., 2018). It represents an emergent system property (Wohl et al., 2019) playing a key role for sediment sources-sinks relationship and, thus, being relevant for the sediment yield assessment (Bracken and Crooke, 2007; Fryirs et al., 2007). Notably, the spatial characterization of sediment connectivity aims at defining the paths, routes and distances of transport through which the sediment can be transferred (Cavalli et al., 2013). Thus, defining the degree of connection infers the potential for a particle to move through the system (Hooke, 2003).

The ongoing interest about the quantification of sediment connectivity called the development of many indices (a comprehensive review on indices is available in Heckmann et al., 2018), designed to overcome traditional qualitative approaches, which typically involve the interpretation of geomorphological maps and multiple field surveys (Harvey,2001; Brardinoni and Hassan, 2006). Among the raster-based connectivity indices, the refined topography-based Index of Connectivity (IC) by Cavalli et al. (2013), developed starting from the seminal work by Borselli et al. (2008), has been widely applied in literature to study connectivity in different contexts (e.g., Evrard et al., 2013; Cavalli et al.,2016, 2019; Tiranti et al., 2016; Nicoll and Brierley, 2017; Schopper et al., 2019; Tarolli et al., 2019). The IC was refined in order to adapt it to the application in mountain environment and to better exploit the high-resolution Digital Terrain Models (DTMs) furnished by LiDAR. For this purpose, the approach of Cavalli et al. (2013) introduced a parameter of surface roughness to derive the weighting factor (W). The Roughness Index (RI) (Cavalli and Marchi, 2008), implemented as W factor in the formula, makes the IC application easy and straightforward since it requires only the DTM as input (Cavalli et al., 2013). It's worth noting that such an approach is only recommended in

areas like high mountain catchments, where vegetation cover is absent or quite homogeneous and thus the surface roughness can be used as a proxy of the impedance of sediment fluxes in place of a land cover weighting factor.

Several IC variants have been suggested afterward to apply the model in different environments and adapt IC to different contexts (Chartin et al., 2017; Heckmann et al., 2018; López-Vicente and Ben-Salem, 2019). In most of the cases, the need to represent the impedance to sediment fluxes in complex and heterogeneous areas promoted the development of many alternative W factors. Chartin et al. (2017) performed the IC analysis in Japan by integrating the USLE Cover and Management factor (C-factor) (Wischmeier and Smith, 1978) with measures of rainfall erosivity to study typhoon-affected catchments. A similar approach was applied by López-Vicente and Ben-Salem (2019) in the Vero River (Spain) with the purpose of modelling both structural and functional connectivity in large catchments. In another Spanish catchment, Lizaga et al. (2017) attempted to combine the C-factor, the RI and the equation for aerial pine biomass estimation to adjust the W factor in pine forests. Moreover, according to Gay et al. (2016), the introduction of a soil infiltration/runoff parameter in the IC formula permits a better characterization of connectivity in the lowlands, in which the soil infiltration properties cannot be neglected. Kalantari et al. (2017) derived W from the curve number method to consider also runoff generation potential along with the topography and thus better adapt IC in lowland areas affected by floods in Sweden. In a burned basin, the sediment and hydrological connectivity were investigated based on the alternative use of C-factors and runoff coefficients (Ortíz-Rodríguez et al., 2019). Finally, connectivity in a Mexican volcano was studied by Ortíz-Rodríguez et al. (2017), which joined the C-factor with the topographic roughness (RI) in order to model IC in both bare soils and forested areas. In most of the cases, the use of C-factor is however limited to agriculture and forested environments typically characterizing Mediterranean environments (Cavalli et al., 2013). For this purpose, another widely recognized method to develop a landcover-based W factor is the use of Manning's n tables in land use change scenarios (Persichillo et al., 2018; Llena et al., 2019). Up to now, to our knowledge, the application of IC has been rarely accomplished in drainage basins affected by extreme events, and only very few in volcanic environments (Ortíz-Rodríguez et al., 2017). In addition, the traditional approach relies only upon post-disturbance analysis, which does not consider the initial topographical conditions of the area under investigation, with the exception of the recent work by Llena et al. (2019). Therefore, the prediction of future scenarios may be uncertain due to the lack of useful pre-disturbance information. Assessing the IC and its limiting or promoting factors before, during and after the eruption could give possible insights about the response of the fluvial system to natural disturbances (Wohl et al., 2019). The main aim of

this work is the application of the IC (Cavalli et al., 2013), in a Chilean basin in order to assess the variation of sediment connectivity induced by the changes in land cover and river morphology generated by a volcanic eruption. Specific objectives regarding the adaptation of IC for its application to Patagonian environment involve: i) the development of a reproducible procedure to estimate a W factor based on the Manning's n by exploiting remotely sensing imagery and its implementation in IC computation; ii) the delineation of a specific workflow to correctly apply IC to investigate a catchment profoundly affected a natural disturbance. Furthermore, iii) given the paucity of high resolution topographic and land use data, the reliability of open source data to create the multi-temporal analysis of IC was also tested. Finally, some considerations on a hypothetical future scenario have been drawn and discussed.

Study area

The study area is the Blanco River (or Rio Blanco) catchment, located in the southern region of Los Lagos, Palena Province (Chile) (Fig. 1.1.1a; b). The drainage basin extends for approximately 70 km^2 and it is eastward confined by the Andes and westward by the Pacific Ocean (Fig. 1.1.1c) (Lara et al., 2013). According to the Chilean Meteorological Office (Dirección Meteorológica de Chile), the precipitations of the Province are >3000 mm $year^{-1}$, with the highest peaks in the winter season. The whole study area (Fig. 1.1.1d) is dominated by the Chaitén volcano (1122 m a.s.l.), a 3-km diameter caldera positioned over a rhyolitic mount (Pallister et al., 2013). The volcano (42°50′16″S; 72°38′52″W) raises on the Southern Volcanic Zone (SVZ) (33°- 46°S), a wide segment of the Quaternary American Volcanic Arc, which is triggered by the subduction of Nazca and Antarctic plates under the South American one (Major and Lara, 2013). Although in the SVZ the volcanic activity primarily releases basalt, Chaitén has been recognized as the only one erupting large quantities of rhyolite (López-Escobar et al., 1993).

The Blanco River is a fourth-order stream that flows for, approximately, 18 km, draining waters from the surrounding steep forested slopes and from the southern flank of the volcano. The latter contributes water to the Blanco River thanks to a small tributary named Caldera Creek (Fig. 1.1.1c) (Major and Lara, 2013). The main stem of the river runs for 6 km into a valley 350 m wide, following a north-south orientation (Ulloa et al., 2015).

The forest cover is mainly composed of old-growth dense stands of natives Nothofagus dombeyi (Coihue), Nothofagus nitida (Chiloé Coihue), Weinmannia trichosperma (Tineo), Aextoxicon punctatum, Drimys winteri, Podocarpus nubigenus and Eucryphia cordifolia (Ulmo) (Donoso, 1981).

Trees with diameters exceeding one meter are common in the native old-growth forest that grows along the slopes. Here, the density ranges from 250 to 550 stems ha^{-1}, and the basal area ranges from 48 to 124 $m^2\,ha^{-1}$. In the river corridor instead, the original forest density ranged between 2100 and 2600 stems ha^{-1} with a basal area ranging between 63 and 83 $m^2\,ha^{-1}$ (Swanson et al., 2013).

The whole catchment was severely affected by the eruption of Chaitén volcano, which, starting in May 2008, experienced an explosive phase, dome construction and a major dome collapse (Pierson et al., 2013). Strong rainfall during the first phases contributed to mobilizing the pyroclastic material, which caused a first massive aggradation pro-cess in the Blanco River. Successively, during the development of the new dome, small collapses caused rockfalls and two major PDCs entering the Blanco River Valley through a breach in the caldera (Major and Lara, 2013). Further information about the eruption and the chain of events can be found in Lara (2009), Alfano et al. (2011), Major and Lara (2013) and Pierson et al. (2013).

The massive collapse of the dome along with lateral blast occurred on the 19th February 2009, wiped out the trees around the caldera, destroying most of the pre-existing vegetation. Moreover, PDCs, lahars and floods affected the main stem of Blanco River, killing the riparian vegetation, destroying vegetated islands, widening and burying the original active channel (Major et al., 2013; Swanson et al., 2013; Ulloa et al., 2015; Ulloa et al., 2016). The rainfall events that occurred just after the explosive phase triggered the massive aggradation of the river-bed, which rose up to 7 m above the original level (Pierson et al., 2013). The consequent stream avulsion and flood inside the Chaitén Village (population around 4600, evacuated on May 6, 2008) produced several structural damages to the existing infrastructures. As previously mentioned, PDCs produced thick layers of sediments in the Blanco River floodplain (average 3–5 m according to Major et al., 2013). Furthermore, recent cascading processes along the slopes include the occurrence of landslides due to the progressive loss of roots' resistance of dead trees (Mazzorana et al., 2019). In order to investigate more in deep sediment availability and connectivity changes, we focused, at a higher detail with respect to the analysis carried out at the whole catchment scale, on a small subcatchment of the Blanco River basin in the proximity of a major landslide. The landslide is 360 m wide at the base with an estimated volume of 0.2×106 m^3 of material delivered into the floodplain (Korup et al., 2019). The subcatchment, extending for approximately 0.94 km^2, with an average gradient of 26° and north-west aspect, is located on the left bank just downstream from the confluence between the Blanco River and the Caldera Creek (Fig. 1.1.1d).

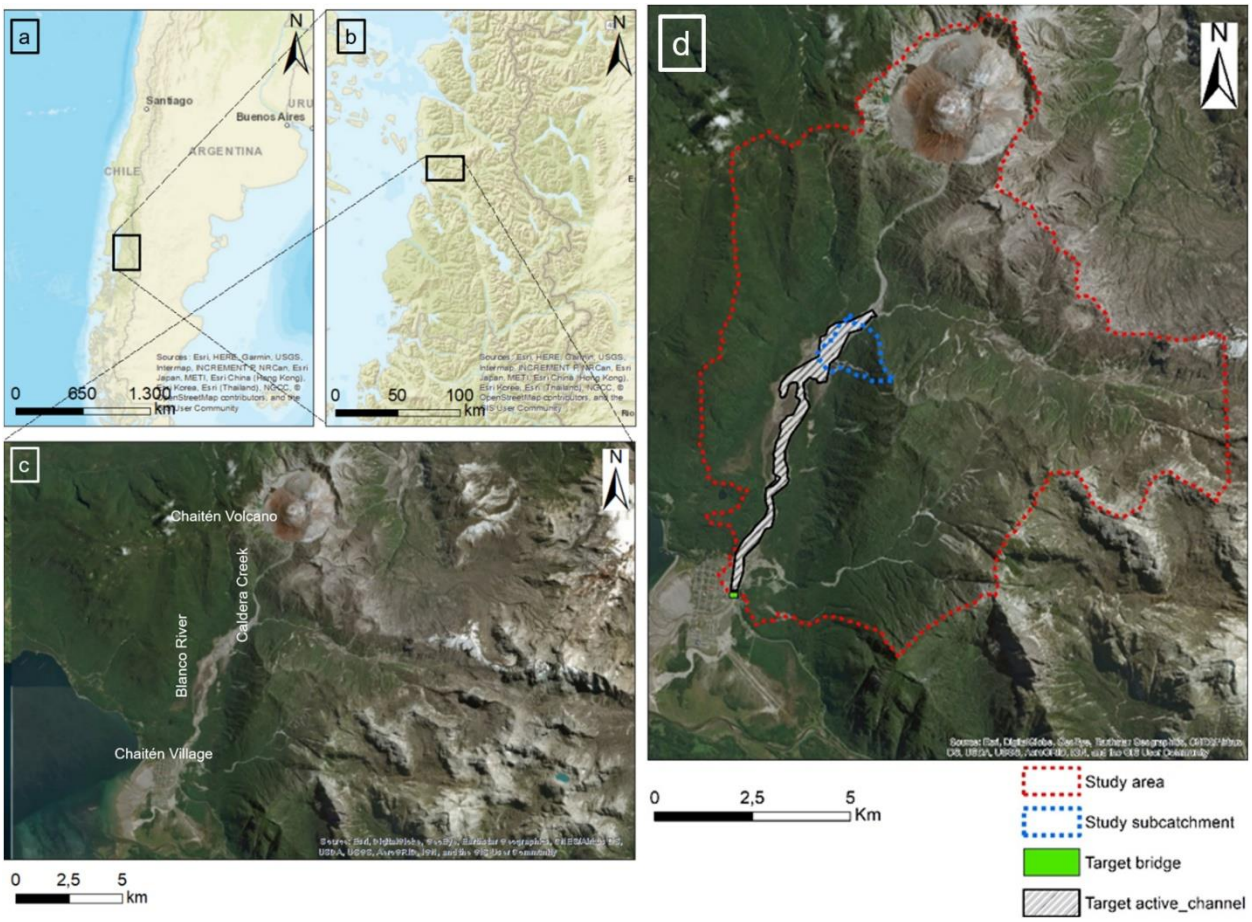

Figure 1.1.1. Geographical framework of the study area: the location of the Blanco River basin in South America (a), in the Los Lagos Region (b) and according to main reference points (c). The extension of the study area and the study subcatchment, involving the targets of the analysis (d).

Material and methods

The application of the IC over the Blanco River catchment was performed using the software SedInConnect 2.3, which operates as a stand-alone application to create connectivity maps (Cavalli et al.,2013; Crema and Cavalli, 2018). The tool, originally developed within the framework of the Alpine Space programme (SedAlp, 2017), is an open source and GIS-independent application (Cavalli et al., 2014). However, in the present analysis, the need for data preparation and implementation required the supporting use of ArcGIS 10.6 software (ESRI). SedInConnect 2.3 application runs a single executable Windows file with its Python source code and license (GPL v 2.0), scripting and exploiting libraries. Moreover, TauDEM (Tarboton, 1997) tool installation is required to run the hydrological functions (Crema and Cavalli,2018). The multi-temporal analysis of connectivity in the Blanco River basin was developed following several steps concerning the choice

and implementation of DEMs, weighting factors and targets (Fig. 1.1.2), which are required in the IC approach. The workflow aims to summarize the possible choices in the application of IC in the Blanco River basin or in similar contexts. Particularly, the choice of weighting factor deals with the Roughness Index and/or the hydraulic-based Manning's n.

Basic of the Index of Connectivity

The original model by Borselli et al. (2008) introduced two components representing the degree of connection between sources and sinks of a catchment. The logarithmic ratio between the upslope (D_{up}) and downslope component (D_{dn}) constitutes the IC, which can range from -∞ to +∞. Eq. (1.1.1) reports the original formula:

$$IC = log_{10}\frac{(Dup)}{(Ddn)} \quad (1.1.1)$$

The upslope component (Eq. (1.1.2)) represents the potential for the mobilization of the sediment according to the characteristics of the upslope areas of the catchment:

$$D_{up} = \bar{W}\,\bar{S}\sqrt{A} \quad (1.1.2)$$

where W is the average weighting factor, which means the average value of the impedance to sediment fluxes in the upslope area, S is the average slope (m/m) and A is the area (m^2) contributing to a specific point under investigation. The downslope component (Eq. (1.1.3)) instead, considers the transport of the sediment according to the length of the flow path taken to reach the point under investigation (e.g. a sink, channel network):

$$D_{dn} = \sum_i \frac{d_i}{S_i W_i} \quad (1.1.3)$$

Where d_i is the length (m) of the flow path along the i^{th}, W_i is the weighting factor and S_i the slope gradient of the i^{th} cell. The refinement by Cavalli et al. (2013), provided three main differences to adapt the model in mountainous environments: (i) the slope factor was computed according to the steepest downslope direction and limited by a lower and upper limit; (ii) the contributing area was computed using the D-infinity multiple flow approach; (iii) a Roughness Index (Cavalli and Marchi, 2008) was introduced as weighting factor.

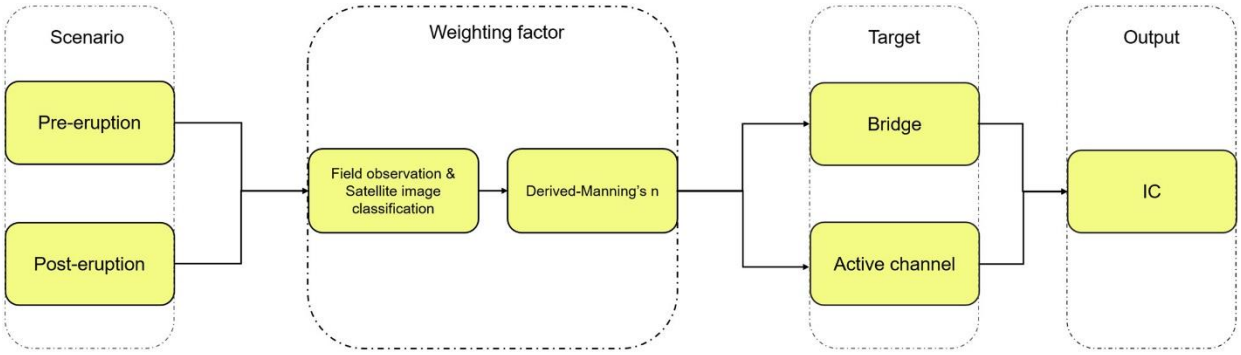

Figure 1.1.2. Workflow of the steps taken into account to apply IC in the Blanco River basin. Bold lines represent the actual path followed to carry out the results.

Digital elevation models

Two DEMs with a spatial resolution of 12.5 × 12.5 m cell size, provided by the open-source website Alaskan Satellite Facility (ASF, 2017; dataset: ASF DAAC, 2007, 2011) were considered sufficiently representative of the topography despite all the limitations of global digital surface models. They constitute the topographic base of the pre and post-eruption scenarios in the connectivity analysis for 15/07/2007 and 21/02/2011, respectively. The two DEMs are part of the ASF's radiometrically terrain-corrected (RTC) Project, which provides SAR-corrected data from the ALOS PALSAR satellite imagery system. RTC Project involves relative high resolution (12.5 m) and low resolution (30 m) RTC product's bundles. The accuracy of terrain-corrected products directly depends on the quality of the DEM used for the correction (Gens, 2015). Alaskan Satellite Facility makes use of the USGS National Elevation Dataset (NED13) to correct their RTC products. More detail about the NED13 overall vertical accuracy can be found in Gesch et al. (2014). The DEMs were hydrologically corrected using a filling algorithm implemented in the ArcGIS 10.6 software (ESRI) to remove local depressions acting as sinks, which could cause bias in the analysis. The area covered by the available DEMs does not include a small portion of the catchment's headwaters, which is therefore excluded from the analysis.

Weighting factors

The choice and implementation of the weighting factor, representing the resistances to sediment flux, varies according to the specific characteristics of the study area (Foerster et al., 2014). According to Crema and Cavalli (2018), the W factor can be freely implemented in the calculation of IC, as long as it is applied equally for the upslope and downslope component and it ranges between 0 and 1.

In this paper, the topographic W factor, derived from the RI (Cavalli and Marchi, 2008), has not been chosen for three particular reasons: i) the global DEMs used do not represent bare earth topography and thus a surface roughness characterization would be affected by a high degree of uncertainty; ii) in any case, the geomorphometric computation of the RI from a 12.5 m resolution DEM would lead to a landform roughness characterization which cannot be reasonably used as an impedance; iii) given the land use cover characteristics of the Blanco River catchment (i.e. dense stands of native species covering the most of the territory), the surface roughness can not be considered the most appropriate variable to be used as a sediment impedance proxy. For this purpose, following the approach by Persichillo et al. (2018) and Llena et al. (2019), an alternative weighting factor based on the hydraulic Manning's coefficient (n) for the overland flow was applied to consider also the main vegetation and micro-morphological characteristics of the catchment. The implementation of the Manning's n was accomplished first through field observations followed by an image classification. Notably, thanks to the field observations it was possible to define the land cover class corresponding to the forest damages, which is afterward implemented in the image classification process finalized to the creation of the multi-temporal weighting maps.

Field observations

Field observations were carried out in the study area in December 2017 to assess the forest settings and to define forest cover classes. The observations were carried out directly into the main areas of interests and by taking multiple pictures with Unmanned Aerial Vehicle (UAV). Based on previous studies by Swanson et al. (2013), the forest damages found during the field surveys mainly concern the burying, debranching and loading of tree canopies by tephra fall. Although in several areas the density of the old-growth forest was univariate, with dead but still standing trees, the simplification of the forest structure determines an important effect on the weighting factor. The removal of intermediate layers and the widespread coverage on tephra in fact, promoted the reduction of the resistance to the sediment fluxes (Pierson and Major, 2014). Considering the classification made by CONAF (1999) prior to the eruption, the most representative classes are native forest, glaciers, sparse vegetation or shrubs. Therefore, the introduction of a new land cover class to include the damaged forest was required. In the end, three land cover classes were defined for the pre-eruption period, and four classes after the eruption.

Figure 1.1.1. Panoramic view of the Blanco River valley with South-North orientation made with a DJI Phantom 4 Quadcopter mounting a 20 Mpx camera. The classification according to field observations and UAV imagery in: (a) old-growth forest; (b) damaged old-growth forest; (c) bare soils and/or glaciers; (d) sparse vegetation. Photo by Sanhueza D., December 2017.

According to Fig. 1.1.3:

- old-growth forest (a), bare soil and/or ice (c), sparse vegetation (d);
- old-growth forest (a), damaged old-growth forest (b), bare soil and/or glaciers (c), sparse vegetation (d).

Based on Cowan's original approach (Cowan, 1956), a modified Manning's n for each land cover class was derived according to the scale of values refined later by Arcement and Schneider (1989). Each Manning's coefficient (n) is given by the sum of the values assigned to the following parameters assessed in the field: a base value for the floodplain's bare soil (n_b); degree of surface irregularity (n_1); effect of obstructions (n_3) and amount of vegetation (n_4). The overall coefficients (n), assigned to each land cover class (Table 1.1.1), were calculated as follow:

$$n_{a,b,c,d} = (n_b + n_1 + n_2 + n_3 + n_4)m \quad (4)$$

where m is a correction factor for the meandering and n_2 a value for variations in shape and size of the floodplain cross section, which in the case of floodplains or hillslope are conventionally set as 1 and 0, respectively (Arcement and Schneider, 1989). This strategy represents a compromise between the access constraints to the Blanco River catchment and the need for a roughness co-efficient that could be adjusted to post-disturbance conditions. On the other hand, the approach relying only on the straightforward use of pre-existing tables (e.g. Persichillo et al., 2018) does not permit the adaptation of the Manning's coefficient for non-conventional roughness conditions.

Table 1.1.1. Weighting factor (W) values by land cover class calculated from the adjustments to the Manning's coefficients for the overland flow (*n*).

Land Cover Classes	**Derived-Manning's *n***	**W factor**
Old-growth forest	0.30	0.70
Damaged old-growth forest	0.15	0.85
Sparse vegetation	0.20	0.80
Bare soil and/or glacier	0.04	0.96

The overall derived values were verified with the ones proposed in the literature and defined by other authors (Engman, 1986; Weltz et al., 1992; Brunner and Bonner, 2010).
Finally, the weighting factor (W) was calculated following the approach by Brardinoni et al. (2015), Persichillo et al. (2018), and Llena et al. (2019) as:

$$W = 1 - n \tag{1.1.5}$$

where, W is the weighting factor for each land cover class and n is the Manning's coefficient derived with the aforementioned approach.

Satellite image classification

To obtain the weighting factor maps used as input in SedInConnect 2.3, 16 satellite images were used as base maps for the image classification tool unsupervised Iso Cluster run by ArcGIS 10.6 (ESRI) software (Table 1.1.2). Each image refers to a unique year between 1999 and 2017 and in particular from the collection 1 of Landsat 4–5 TM, Landsat 7 ETM+ and Landsat 8 OLI/TIRS. Data are freely available thanks to the U.S. Geological Service free satellite data provider EarthExplorer (EarthExplorer, 2018). The data were collected as real-color images with a resolution of 30 m, and only those with a cloud cover ranging from 0% to 10% were used for this research. The Landsat data were chosen over other remote sensing programs mainly due to their long-term availability. However, following the above-mentioned requirements, no images corresponding to the years 2000, 2003 and 2012 were found suitable and therefore these years were not considered in the analysis.

Table 1.1.2. Summary of the dates of the satellite images used to carry out the multi-temporal analysis and arranged according to the respective scenario.

Pre-eruption scenario	**Post-eruption scenario**
10/02/1999	11/01/2009
16/12/2001	15/02/2010
01/02/2002	18/02/2011
11/03/2004	24/12/2013
30/03/2005	17/04/2014
13/02/2006	21/01/2015
06/01/2007	31/01/2016
03/02/2008	10/11/2017

The image classification was then performed over the 16 Landsat images by running the Iso Cluster unsupervised classification in ArcGIS10.6 (ESRI) and then verifying the results with the supervised Maximum Likelihood Classification (MLC) for further control over the classification parameters. Both tools rely upon a pixel-based algorithm but, while the former can be used straightforwardly by the analyst, the latter requires the creation of training examples for the categorization of the image (Lu and Weng, 2007; Li et al., 2014). However, since the MLC is commonly recognized for its robustness and practicality (Settle and Briggs, 1987; Lu and Weng, 2007), it was integrated into the analysis. The resulting land cover maps computed with image classification were then checked using Google Earth Pro software and a previous photo interpretation of the damaged areas (see in Major et al., 2013). Finally, the 16 weighting maps were then derived by assigning the overall Manning's n to the specific land cover class according to Eq. (1.1.5).

Targets

Catchment-scale sediment connectivity commonly involves lateral connectivity (e.g. hillslope-channel) and longitudinal connectivity (e.g. within channel) (Fryirs et al., 2007). The choice of a specific target rep-resents an important step in the IC analysis since the selected target clearly defines which perspective (e.g. hillslope to channel, a specific cross section of the river) the analysis is

focused to. Two alternative tar-gets were set to study the IC for both pre and post-eruption scenarios over the Blanco River catchment: the active channel of the Blanco River and the main bridge upstream of the Chaitén village (Fig. 1.1.1d). The choice of active channel intends to focus on lateral connectivity and thus on the sediment transfer processes acting in a hillslope-to-channel perspective. Conversely, a stable infrastructure close to the watershed's outlet might be affected both by lateral and longitudinal sediment connectivity. It is worth underlying that modelling the latter perspective using a simple geomorphometric index as IC, represents a strong simplification of the processes acting along the channel, but it was chosen to provide a general overview of connectivity at the catchment scale. The computation of IC was then carried out using the two DEMs representing the pre and post-scenarios according to 16 weighting factor maps for both the two alternative targets, for a total of 32 IC and W factor maps, respectively. Among them, the year 2005 (for pre-eruption scenario), and 2016 (for post-eruption scenario) were chosen by way of example to be deeper investigated. In order to test the significant differences between the IC results be-fore and after the eruption, the Wilcoxon test has been carried out. The Wilcoxon signed rank test is a non-parametric test looking for the differences between the medians of two samples that do not show nor-mal distribution (significance level set to p-value <0.05). The statistical analysis was performed in Rstudio version 1.1.463 (RStudio Team,2016). Moreover, a linear regression analysis was performed between the IC mean values and the area covered by active channel or bare soil/ glaciers for each period.

Results

Land cover changes

The satellite image classification pointed out widespread changes inland cover for the analyzed time span. In particular, the eruption affected the forest with different severity mainly according to the distance from the Chaitén volcano as well as from the river corridor hit by PDCs. Two years are selected as an example: 2005 and 2016. As can be observed in the W factors map, the old-growth forest in the pre-eruption period (Fig. 1.1.4a) prevails over the other two land cover classes: 87% against 8% and 5% (Table 1.1.3). The latter are represented by small, scattered areas along the river corridor and slopes (sparse vegetation) or circumscribed on the highest peaks (bare soil/glaciers). In the post-eruption map (Fig. 1.1.4b), the extent of the old-growth forest is greatly reduced due to the introduction of the new class representing the vegetation damages.

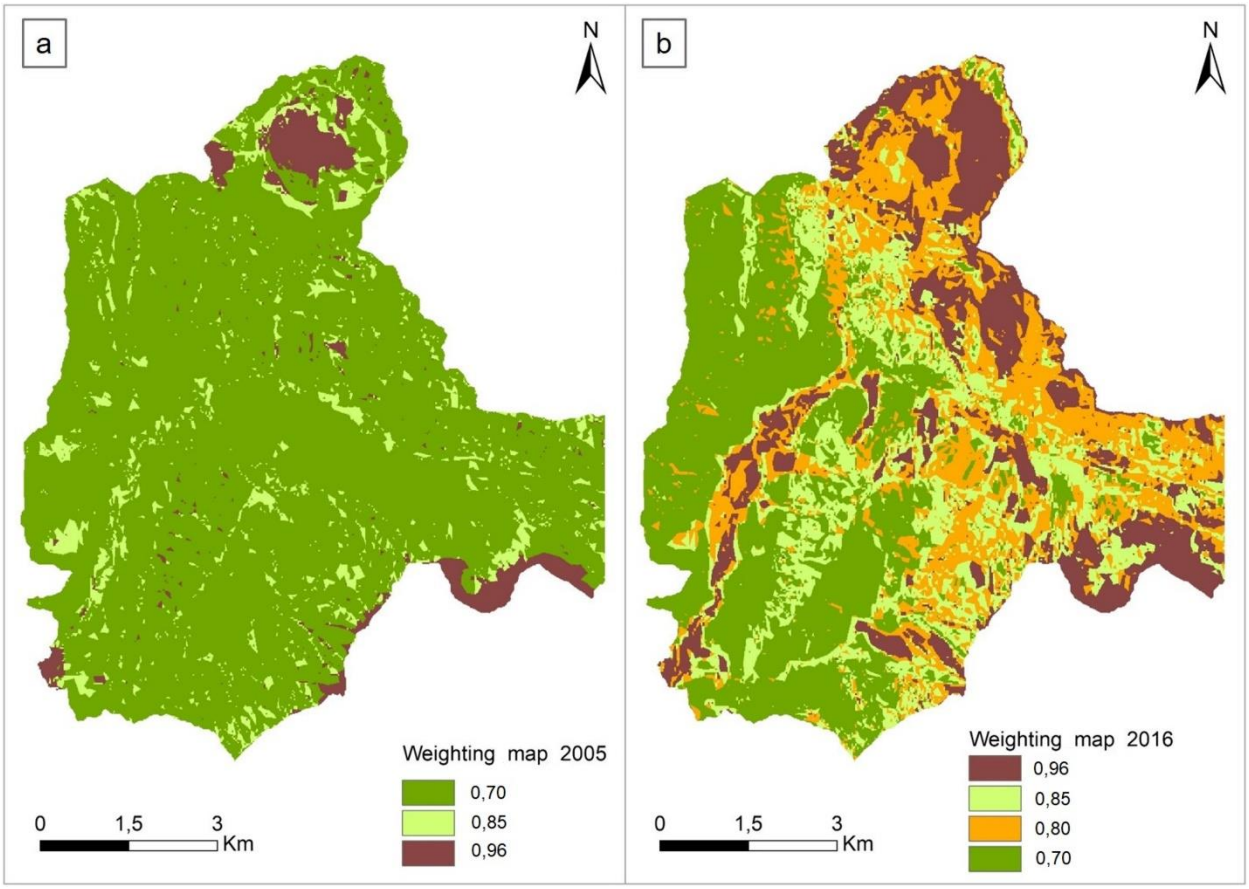

Figure 1.1.2. Weighting maps of a pre-eruption year (a) and post-eruption year (b). Each land cover class include its specific weighting factor derived from field observations and image classification techniques.

Notably, the greater changes are evident near to the caldera and int he north-eastern part of the catchment, where the damaged old-growth forest and bare soils are the most represented land cover classes. Moreover, the Blanco River's active channel is visible by the intertwining of exposed sediments and sparse vegetation, which results in a two-tone strip in the middle of the catchment. Thus, the affected forest accounts for 24% of the total area with an extent of almost 1654 ha (Table 1.1.3). On the other hand, the reduction of the old-growth forest class is outstanding: from 5930 ha to 2434 ha in 2005 and 2016, respectively, with a decrease of about 59%.

Table 1.1.3. Pre and post-eruption extensions of the land cover classes computed from the satellite image classification.

Land Cover Classes	Pre-eruption (2005)		Post-eruption (2016)	
	Area (ha)	Area (%)	Area (ha)	Area (%)
Old-growth forest	5930	87	2434	36
Damaged old-growth forest	-	-	1653	24
Sparse vegetation	567	8	1462	21
Bare soil / Glaciers	361	5	1308	19

Although this decrease is primarily associated with the arising of the new land cover class, the increase of sparse vegetation class, which in 2016 accounts for 21% of the entire catchment, had also a significant role in reducing the old-growth forest cover. After the eruption, the removal of tree canopies progressively offered new growing space for shrubs and herbaceous species, as observed during the field surveys. In addition, the aforementioned amount of deposited and exposed sediments in the valley bottom increased the area classified as bare soil by the classification algorithm. In fact, from 2005 to 2016 the area associated with bare soils and/or glaciers in-creased by 14%, changing from 361 to 1308 ha.

Catchment scale connectivity

Sediment connectivity with regard to the bridge.

According to the changes experienced by the Blanco River catchment, 16 connectivity maps were produced using the adjusted Manning's n and the bridge as a target. The example maps proposed in this section present the result of IC for two specific periods: before (Fig. 1.1.5a), and after the eruption (Fig. 1.1.5b), respectively. At the catchment scale, the variation of connectivity can be hardly appreciated. The patterns of connectivity remain mainly constant in the two maps. Highly connected areas are visible along the slopes close to the bridge (Fig. 1.1.5_1), and, particularly, in the tributary valley that joins the Blanco River just upstream the bridge (Fig. 1.1.5_2). On the contrary, low connectivity sites are located along the floodplain (Fig. 1.1.5_3) and in the uppermost areas of the

catchment, including the area around the caldera (Fig. 1.1.5_4). In this zone, even with the complete absence of vegetation and the presence of exposed sediment, the IC did not appreciably increase and the volcano still presents low values of IC with regard to the bridge. Instead, medium-low IC values are visible in the areas contributing to the upstream part of the river with E-O orientation. In this case, the role of the flat and wide floodplain is evident. As expected in fact, according to the IC, the valley bottom and the wide floodplains act as buffers, reducing the coupling between the more distant hillslopes and the bridge (Fig. 1.1.5_3). The IC maps seem not to capture the weight of the land cover changes along the hillslopes although the Manning's n is applied. Even though there are no visible changes from the maps, the IC slightly changed after the eruption, and the increase of IC in the most-damaged areas is confirmed by the difference of values between the two periods (Fig. 1.1.6).

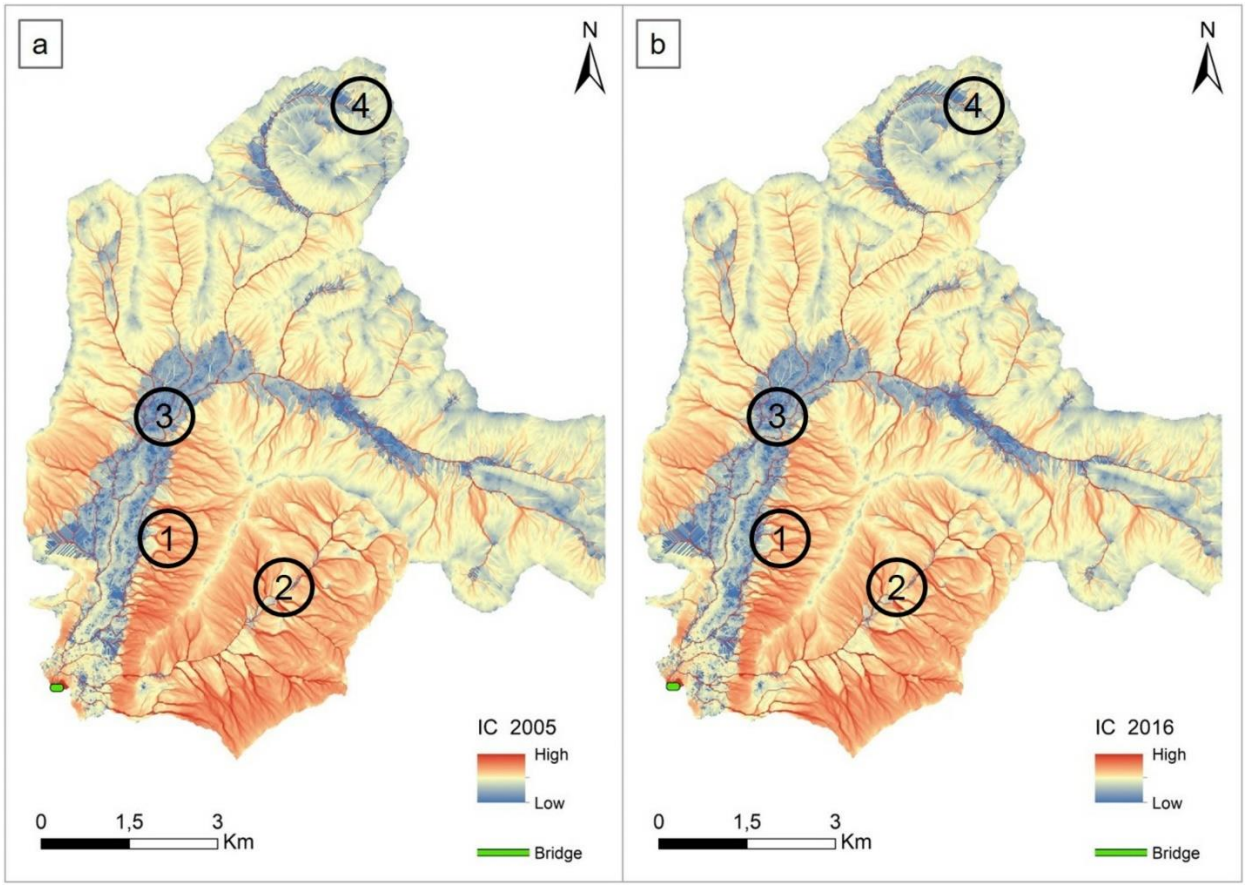

Figure 1.1.3. IC maps for a pre-eruption year (a) and post-eruption year (b) using the derived-Manning's n as weighting factor and the bridge as target. Higher is the IC and greater is the chance for the sediment flux to reach the village of Chaitén. Main areas of interest are marked as: (1) the left slope of the Blanco River valley; (2) the major tributary valley; (3) the floodplain; (4) the Chaitén caldera.

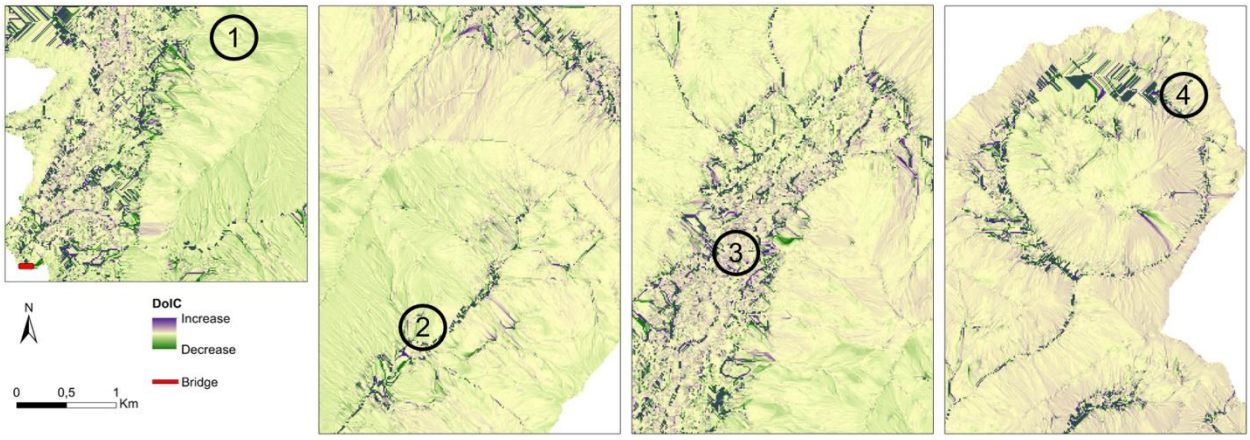

Figure 1.1.4. Difference of the Index of Connectivity (DoIC) between 2016 and 2005 according to the main areas of interest in the hillslopes-bridge scenario. Main areas of interest marked as:(1) the left slope of the Blanco River valley; (2) the major tributary valley; (3) the floodplain; (4) the Chaitén caldera.

Moreover, since the two maps are characterized by the same area itis possible to compare the main descriptive values of IC (Table 1.1.4). Both, the median and the mean values increased from 2005 to 2016, moving from -4.87 and −4,86 (± 0.52 s.d.) to -4.75 and -4.73 (± 0.50 s.d.), respectively. The variation of IC values is also evident looking at the minimum and maximum values, the minimum increased by 0.15, and the maximum decreased by 0.06, respectively. In addition, the results of the Wilcoxon signed rank test for the two samples point out the significant difference between the medians of pre and post-eruption IC values.

Considering the entire database, the increase of IC after the eruption is pointed out in Fig. S1.1.1 The median value grew from -4.86 in 1999 to -4.74 in 2017. Prior to the eruption (period 1999-2007), the median and the interquartile range (IQR) remained almost constant at -4.86 and 0.54 respectively. This fact indicates a condition of stability without major changes in the topography and land cover during that period. Then, the catchment suffered from high instability due to the 2008 explosive eruption and consequent dome collapse (see *study area* section); there by the IC values of the catchment fluctuated right after the disturbance (period 2008–2011). In this time span, the median IC varied between -4.80 (2008), -4.75 (2009), -4.76 (2010), and -4.74 (2011). Successively, during the period 2011–2017, the median IC stabilized between -4.74 and -4.73, while the interquartile range reduced considerably until 0.48 in 2017.

Table 1.1.4. Difference in the main descriptive statistics of the IC analysis considering the hillslope-bridge and hillslope-active channel perspectives.

Statistics	**2005 bridge**	**2016 bridge**	**2005 active channel**	**2016 active channel**
Min	-7.35	-7.20	-6.99	-6.84
Max	3.48	3.42	3.27	3.33
Mean	-4.87	-4.75	-4.28	-4.15
Median	-4.86	-4.73	-4.33	-4.21
SD	0.52	0.50	0.64	0.66
Q1	-5.11	-4.97	-4.61	-4.50
Q3	-4.57	-4.48	-4.02	-3.88

Hillslope to channel

The most evident changes in the IC were observed considering the active channel as the target of the analysis. Considering the coupling hillslope–active channel, in fact, the results show well-delimited pat-terns of high and low IC in the basin and the variations are emphasized with respect to the previous scenario (Fig. 1.1.7). In both pre-eruption and post-eruption years, highly connected areas were visible along the slopes, close to the upstream area of the target, in the correspondence with the confluence of the Caldera Creek (Fig. 1.1.1c). In this particular spot, the active channel is closer to the slopes due to the narrower valley and therefore the connectivity is higher. On the other hand, the down-stream part of the active channel is more distant from the slope because of the persistence of wide floodplains and the connectivity is, also, lower.

Focusing on the differences between pre and post-eruption scenarios, it is evident that the progressive expansion of the active channel had a major role in the alteration of IC from 2005 to 2016. The before-mentioned highly connected areas in the central part of the basin (Fig. 1.1.7a_1) display a wider extension and an even higher level of IC in 2016 (Fig. 1.1.7b_1). Furthermore, a vast sub-basin, located close to the caldera with N-S orientation, appears to be much more connected in 2016 (Fig. 1.1.7b_2) than in 2005 (Fig. 1.1.7a_2). On the contrary, some scattered spots downstream and in the tributary valley show a mild decrease in the IC (Fig. 1.1.7_3).

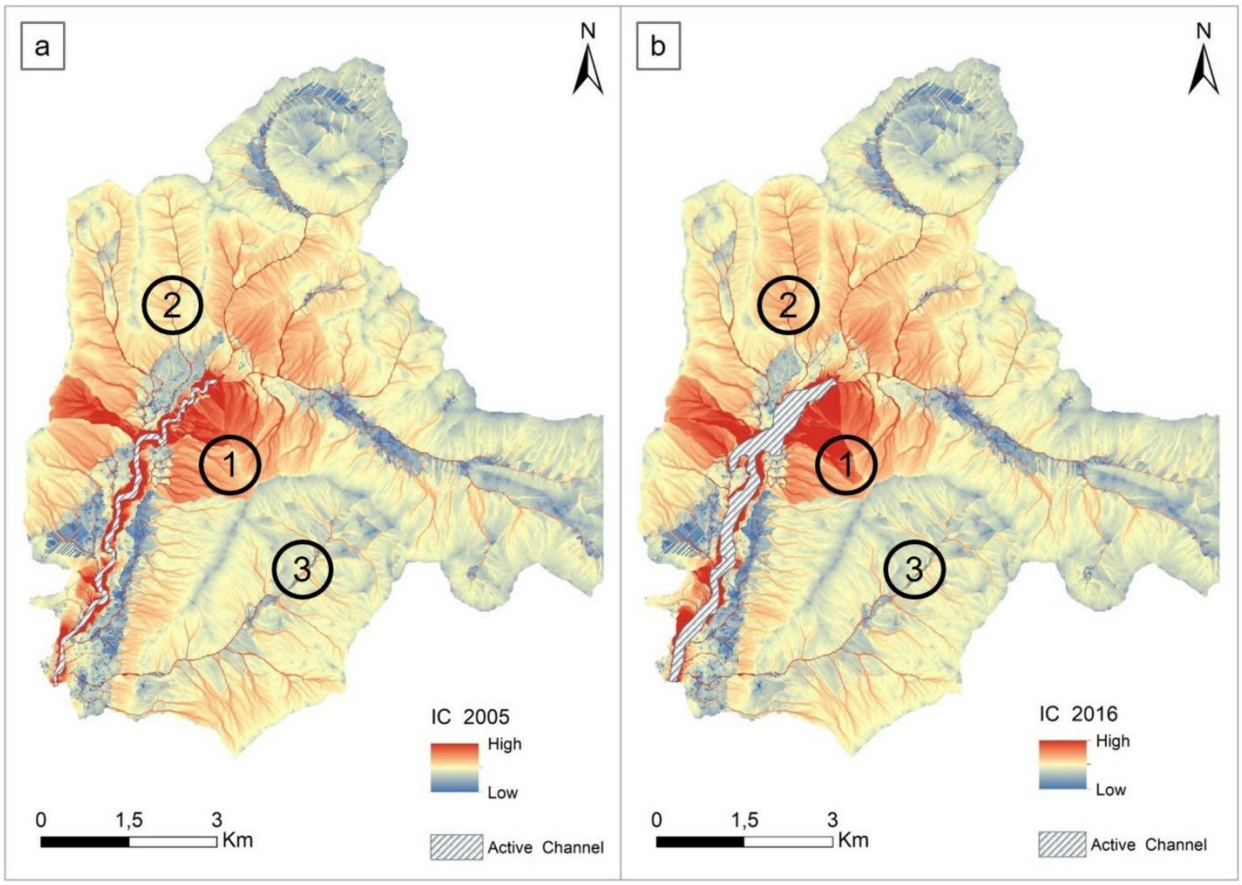

Figure 1.1.5. IC maps for a pre-eruption year (a) and post-eruption year (b) using the derived-Manning's n as weighting factor and the active channel as target. Higher is the IC and greater is the chance for the sediment flux to reach the channel network. Main areas of interest marked as: (1) sub-catchment in the central part of the basin; (2) upstream subcatchment; (3) the major tributary valley.

The IC changes in the aforementioned spots are confirmed by the difference of the IC computed between the two years (Fig. 1.1.8). In the rest of the basin, the IC did not change importantly, because of the distance from the target. The main descriptive parameters underline the changes in the IC of the two sample years (Table 1.1.4): the median and mean values grew from -4.33 and -4.28 (± 0.64 s.d.) to -4.21 and -4.15 (± 0.66 s.d.) respectively. Moreover, the range of values slightly reduced from 10.26 to 10.17 with the increase of the minimum and maximum values by 0.15 and 0.06 respectively. The multi-temporal analysis underlined the post-eruption enhancement of IC described so far. Fig. S1.1.2 exhibits the trend of IC values over the 16 years. Notably, the median value rose from –4.32 in 1999 up to -4.21 in 2017. In support, the results of Wilcoxon signed rank test for the two samples point out the significant difference between the medians of pre and post-eruption IC values.

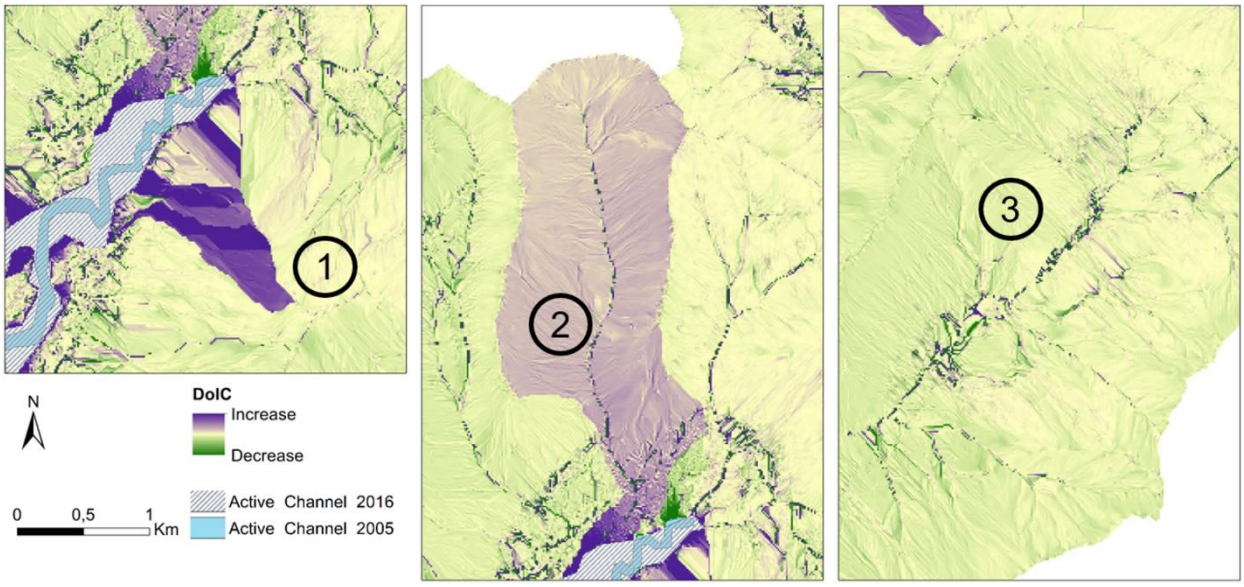

Figure 1.1.6. Difference of the Index of Connectivity (DoIC) between 2016 and 2005 according to the main areas of interests in the hillslope-active channel scenario. Main areas of interest marked as: (1) subcatchment in the central part of the basin; (2) upstream subcatchment; (3) the major tributary valley.

Even in this case, the lack of variations in the interquartile range and median values, which remained remarkably constant between 1999 and 2008, reflects the pre-eruption catchment's stability. After the eruption (period 2009-2017), the sudden expansion of the active channel along with the severe changes in forest cover promoted the sediment connectivity in the hillslope to channel perspective. The major increase of IC occurs only in 2009, when the river valley was definitively buried and the active channel extended. In the post-eruption scenario, the computed IC values are generally higher, with the median peak value of -4.19. Furthermore, the interquartile increased after the eruption, with a peak of 0.63 in 2010. Even though the IC trend over time is similar to the previous case (Fig. S1.1.1), the values are generally higher when considering the active channel as target because the sediment paths are shorter between hillslopes and channel than between hillslopes and bridge. The positive correlation (R = 0.95) between the IC and the active channel area is confirmed by the graph in Fig. 1.1.9a, where the mean IC of the catchment for each year is plotted against the area of the active channel. As the target area enlarged, the distance between sources and the target was lower, resulting in an increase of IC values. As expected, there is also a positive correlation (R = 0.91) between the area of the bare soils and/or glaciers and the mean IC (Fig. 1.1.9b). The changes in forest cover, identified mainly as a simplification of the forest structure and the removal of trees in

large areas, promoted the potential sediment transfer between hillslope and channel network, which leads to high level of sediment connectivity.

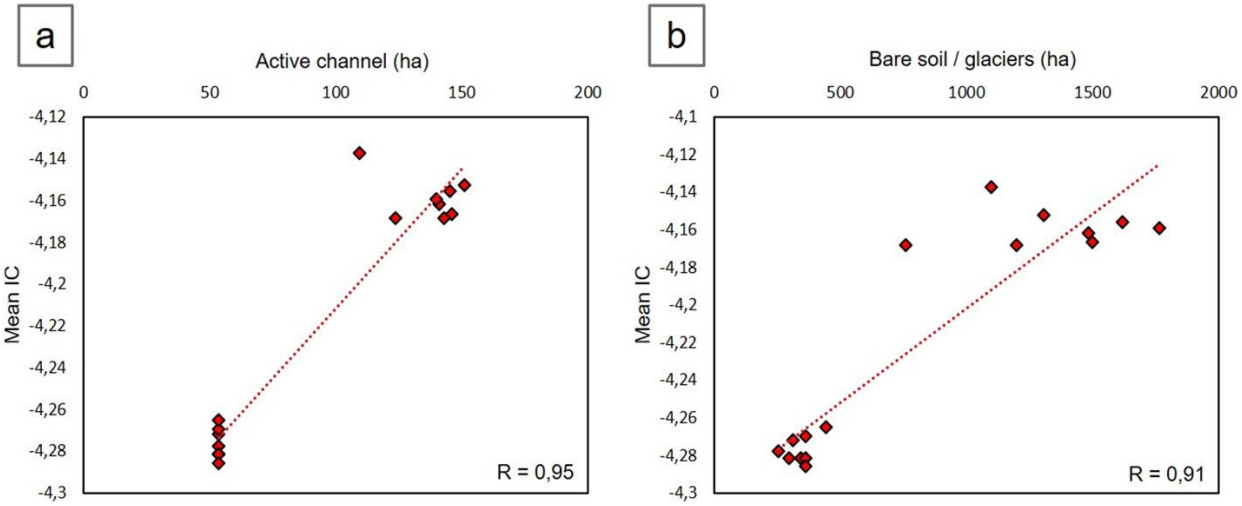

Figure 1.1.7. Relationship between the mean IC, computed with the derived-Manning's n, and the extension of the active channel (a); or between the mean IC and the extension of the bare soil/glaciers land cover class (b).

Subcatchment scale connectivity: hillslopes to channel perspective

Among the several sub-basins, one featuring high instability and high IC was examined. From the previous analysis (*hillslope to channel* section; Fig. 1.1.7b_1), the subcatchment is characterized by the highest value of IC in the entire Blanco River basin and, therefore, it could be an efficient supplier of sediment for the channel network. Moreover, since late 2016 the area features part of the scar of a large landslide, without any vegetation and the bedrock layer exposed in many parts. The trend of the IC performed through the multi-temporal analysis exhibits outstanding changes after 2008 (Fig. S1.1.3). As expected, prior to the eruption (1999-2007) the range of values remained almost constant with the lower limit and the upper limit stationary at -4.24 and -2.36 respectively. Later, during the post-eruption period, the range of values first fluctuated noticeably and then decreased in 2017. The effects of the eruption boosted the subcatchment's median value of IC from -3.00 in 2007 to -2.07 in 2011 but in the last year considered, the median IC fell to -2.29.

Discussion

The analysis of sediment connectivity was performed for the first time in the Blanco River basin, a large and forested area in the Southern Andes that was strongly affected by the Chaitén eruption and its important consequences in 2008–2009. To this end, we applied the IC that was first developed to be applied in alpine catchments where the topography-based index was proved efficient to study the (de)coupling between source areas and channel network (Messenzehl et al., 2014; Brardinoni et

al., 2015; Cavalli et al., 2016; Rainato et al., 2018). However, the application of surface roughness as a proxy of the impedance to sediment fluxes in densely vegetated catchments is not recommended because it does not take into account the impedance operated by the vegetation. In addition, the lack of high-resolution DEM excludes the computation of the RI a priori. In order to develop a workflow for IC application in study areas characterized by paucity of high-resolution data and access constraints, we propose here the use of global DEM sand of a weighting factor based on the Manning's n.

The choice of an adjusted Manning's n as base parameter was sufficiently representative of the post-eruption conditions of the Blanco River catchment, which features wide areas of damaged old-growth forest and exposed ground. In fact, as already proved by Foerster et al. (2014), the spatial configuration of vegetated and bare areas can alter the seasonal and long-term redistribution of sediment sources and connectivity along the hillslopes. This issue is partially confirmed also in the present multi-temporal analysis of connectivity: the changes in landcover increased slightly the values of IC all over the catchment.

Other authors have highlighted the strong relationship between land use changes and IC by applying the C-factor (e.g. Lizaga et al.,2017) or Manning's n (e.g. Persichillo et al., 2018; Llena et al., 2019) as weighting factors. However, contrary to Persichillo et al. (2018), who adopted and applied the Manning's coefficients straight forwardly from the empirical tables available in the literature, the present analysis used a different approach, based on the derivation of the Manning's n from the land cover characteristics suggested by Arcement and Schneider (1989) and implemented through an image classification. The standardization of this approach is indeed the core issue of the present research. A proper and updated protocol for the choice and adaptation of W factors is still lacking in the analysis of IC in complex study areas. The combination of field observations with image classification technique gave positive results for the reproducibility of a coherent W factor that supported the computation of multiple and well-justified IC maps. In accordance with Ortíz-Rodríguez et al. (2017), the great heterogeneity of forms and processes driving sediment connectivity in volcanic environments requires inevitably the modification of pre-existing weighting factors. In this sense, the tendency towards the development of a more robust approach to derive the W factor in various disturbance-affected areas, would let the adequate characterization and comparison of inter-catchment IC results. The spatial configuration of land cover patterns was therefore essential in this type of analysis to define the paths prone to route the sediment fluxes within the IC maps. Nonetheless, field measurements are necessary to validate the predicted sediment paths.

Recent studies have highlighted the benefits of satellite image classification to study the effects of volcanic eruptions (Davila et al., 2007; Ulloa et al., 2015), or to assess changes in the sediment connectivity after (natural) disturbances (Chartin et al., 2017; Ortíz-Rodríguez et al., 2019). The use of satellite images and DEMs to examine large catchments overcome the systematic field observation, which cannot be accomplished all over the area (Theler et al., 2010). On the other hand, working with satellite images often arise issues related to the spatial scale. Dealing with the IC means to define a proper spatial resolution and a suitable area of reference for the purpose of the analysis (Heckmann et al., 2018). The use of DEMs with different spatial resolution have strong effects on the resulting IC: increasing the DEM resolution results in lower IC values due to the simplification of flow paths (Brardinoni et al., 2015). In a Belgian experiment, Cantreul et al. (2018), suggested the use of 1 m DEM with an area of reference of 1.24 km^2, while López-Vicente and Álvarez (2018) found the resolution of 0.20 m to be the best representative spatial scale for a catchment of 0.274 km^2. In the present study, any specific topographic survey (e.g., LiDAR, SfM) allowing a high resolution was unavailable and thus the use of global DEMs with a resolution of 12.5 m was tested: the analysis in the Blanco River basin aims at providing a homogenous multi-temporal information of sediment connectivity by taking advantage of open source data. The results suggested that the 12.5 m resolution was suitable to conduct a multi-temporal analysis of sediment connectivity, if an accurate methodological workflow like the one developed in this study, is adopted. As an example, it should be remembered that, with global DEMs at coarse resolution, the use of surface roughness is not recommended for two main reasons: i) lack of representativeness of bare earth morphology and ii) too coarse resolution to compute a meaningful RI as a proxy of the impedance to sediment fluxes through a geomorphometric approach.

The issue of coarse resolution also concerns the Landsat images collected for the image classification. According to Lu and Weng (2007), in complex and heterogeneous landscapes the image classification of coarse resolution images can be responsible for biases in the analysis because of the mixed pixels, in this sense Fig. S1.1.4 represents a clear example of possible biases in the classification outcomes.

For instance, the marked increase of sparse vegetation areas found in 2016 (see *land cover changes* section), could address either ecological causes related to re-generation or colonization or errors related to the low resolution of the images. However, the multi-temporal changes in land cover highlighted a clear and unquestionable increase of bare soils, damaged forests and sparse vegetation areas, which are responsible for the changes in the IC. Concerning the effects of volcanic eruptions upon the fluvial geo-morphology, in the hillslope-channel network perspective, the active channel

played the key role. The overall enhancement of IC values, is a function of the progressive widening of the active channel after the eruption. The same alteration is confirmed by a previous study in the Blanco River by Ulloa et al. (2015), which calculated a widening of 211% between pre and post-eruption, but we observed that this widening phase is still ongoing. The differences in the IC patterns found between the two coupling perspectives (hillslope-bridge and hillslope-active channel) mainly depend upon the topography of the catchment that is the main driving force of the Index. However, due to its intrinsic limitations (topography-based nature), the IC can not fully represent the real sediment behavior all over the area. Despite the low IC shown by the caldera in all the maps, there is evidence of the high amount of sediment transported to the outlet due to the formation of huge delta in the months following the eruption (Pierson et al., 2013; Major et al., 2016). Furthermore, the wide and flat floodplain acting initially as a buffer, as also low IC values seem to suggest, represents in turn an active sediment source area capable to deliver the unconsolidated pyroclastic sediment till the outlet during flood events. Indeed, computing the IC with a different target, such as the active channel, avoided this sink effect, which typically interrupts the lateral linkages within the catchment (Fryirs et al., 2007).

Although the patterns of high and low connectivity are clearly different between the two perspectives, a similar behavior can be appreciated in all the multi-temporal trends presented in the results. The increase of IC values is concentrated in the triennium 2009–2010–2011, when first the dome collapse and then PDCs and lahars took place. The analysis of sediment connectivity at the catchment scale provides a general portrait of how the sediment could behave in the system. However, to plan focused management actions for localized processes, it is important to study the driving processes at smaller scale. For this reason, the catchment has been divided into sub-basins in order to highlight IC information for local areas. At subcatchment scale, the IC trend throughout the study period is easily comparable to the one developed by Pierson and Major (2014) about the response of fluvial systems to the volcanic eruptions. The IC behave similarly to other geomorphic variables measured during a post-eruption period: the value is constant during the steady state (1999–2007), then it shapes a steep ascendant limb right after the disturbance (2008–2010) with a peak of values (in 2011). Moreover, evidence of recover is represented by the IC values in the last study year (2017), where the notable decrease of sediment connectivity suggests the beginning of the relaxation period. In geomorphic systems, like river basins, the relaxation period typically involves a series of adjustments towards a new steady state. In the case of Blanco River catchment, this particular trend of IC is somehow observable only in the subcatchment under investigation (section *subcatchment scale connectivity: hillslopes to channel perspective*). The response of any geomorphic variable to

disturbances is indeed different from one part of the system to another (Graf, 1977). In post-disturbance conditions, the IC could constitute the starting step in the prediction of future developments for the study area because it summarizes some of the main geomorphic changes. However, it is worth underlying that the predictive capacity of this kind of indices can be only ensured with further steps dealing with the direct measurements of system behavior.

In the Blanco River catchment, the increase of IC is driven by the reduction and simplification of forest cover in combination with the hydro-geomorphic changes that affected the active channel widening. The rapid decrease of the distance between the slopes and active channel established a coupling state, which may be responsible for new sediment inputs to the channel network. As a matter of fact, the Blanco River is shifting towards the highlighted subcatchment by eroding the unconsolidated banks. Furthermore, the subcatchment is prone to deliver sediment to the channel thanks to the progressive formation of anew sediment path, which can be observed from the Fig. S1.1.5. It is important to point out that the chance of new sediment inputs coming from the subcatchments is associated with the two combined conditions: the increase of real sediment connectivity and the activation of new sediment source areas due to the degenerative effects of the eruption.

In river systems, the awareness of the degree of connectivity is be-coming a fundamental issue to understand the response to natural and human disturbances (Wohl et al., 2019). Considering the outcomes of the present research, we encourage the use of IC, as an efficient and adaptable tool for the assessment of the evolution of sediment connectivity. IC helps to identify what are the most impactful driving factors for the systems and how to prioritize the affected areas for management interventions. The correct use of multi-temporal maps with future scenarios assessment of sediment connectivity could constitute a fruitful instrument for territorial management strategies. In the case of Blanco River, the understanding of sediment source areas, priority paths of sediment fluxes and their degree of connection with downstream infrastructure could be extremely helpful for land owners and the local administration. The improvement of local awareness would help to mitigate the exposure to hazards and to reduce the vulnerability of critical infrastructures like the bridge or the port of Chaitén (Mazzorana et al., 2019). In the same way, worldwide, the assessment of connectivity trends is crucial for a holistic comprehension of how the catchment impedes or promotes sediment hazards (James, 2010; Wohl, 2015; Wohl et al., 2019).

Conclusions

The Index of Connectivity was successfully applied in a Chilean catchment in order to assess the variation in sediment connectivity driven by the Chaitén explosive eruption. For this purpose, the implementation of an alternative weighting factor, adaptable to the characteristics of a river basin after a major disturbance, was successfully carried out. In this work, a workflow based on the use of freeware global DEMs and satellite images has been developed. This approach can be easily followed to carry out multi-temporal IC analysis in other study areas characterized by paucity or lack of high-resolution data. Nevertheless, the use of freely available data can lead to spatial scale problems: typically, low-resolution data are the cause of overestimation in the IC assessment and they can provide biases in the outcomes of land cover classification. In any case, the IC has proved promising to furnish a rapid insight on post-eruption main effects.

More incentives to develop further research in the field of sediment connectivity are required, especially in relation to exceptional natural disturbances that are becoming more and more frequent. Enhanced awareness on sediment fluxes and their connectivity would help local land managers to mitigate the risk associated with extreme natural events. For this purpose, the ongoing tendency towards the development of functional connectivity could be particularly important in com-plex and heterogeneous landscapes. Finally, field measurements as supportive tools for the numerical computation of sediment connectivity are still needed to validate and comprehensively represents the sediment transfer in dynamics environments.

1.2 Assessing the effect of fire severity on sediment connectivity in central Chile

Adapted from Martini L., Faes L., Picco L., Iroumé A., Lingua E., Garbarino M., Cavalli M. (2020). Assessing the effect of fire severity on sediment connectivity in central Chile. *Science of the Total Environment*, 728, 139006. https://doi.org/10.1016/j.scitotenv.2020.139006

Contributions by the PhD candidate: Conceptualization, methodology, data curation, writing the original draft.

Abstract

Chilean territory is recurrently affected by severe wildfires, which drastically reduce the forest cover and promote runoff, soil erosion and slope instabilities. To understand how the geomorphic system responds to wildfires in terms of sediment dynamics, the assessment of sediment connectivity, i.e. the property describing the relation-ships between compartments of a geomorphic system, is crucial. This study aims to quantify the spatial linkages between fire severity and sediment connectivity to identify common patterns and driving factors. The compound use of field data and open-source satellite imagery helped to apply the Relative differenced Normalized Burn Ratio (RdNBR) and the Index of Connectivity (IC) in the context of two consecutive wildfires, occurred in 2002 and 2015, in the Rio Toro catchment (Chile). The fire severity assessment showed that the 2002 event affected 90% of the catchment, with high severity areas representing around 70%. The 2015 wildfire instead, affected 76% of the catchment with moderate severity around 42%. Accordingly, as result of the sudden reduction in forest cover in severely affected areas, the IC changed after both wildfires with an overall increase of 1.07 and 0.54, respectively. However, only for the second disturbance, it was possible to observe a clear relationship between the RdNBR and the IC variations. The different degree of vegetation cover heterogeneity between the two pre-wildfire scenarios contributed to different fire severity and IC variability between the two disturbances. The use of open-source satellite data and the development of a weighting factor (W), to be used in IC and able to capture the land cover change driven by the wildfires, could make the application of this approach straightforward, promoting its reproducibility in other catchments for land management and risk mitigation purposes.

Keywords: Sediment connectivity; Wildfire; Fire severity; Natural disturbance; Rio Toro

Introduction

Landscape configuration is determined by the interaction of natural disturbances, geomorphic processes and landforms expressed at multiple spatial and temporal scales. Wildfires are recognized as major agents of land and soil degradation (Shakesby, 2011) and geomorphological changes (Neary et al., 2005). In burned catchments, the interaction among vegetation, fire severity and hydro-geomorphic components needs to be deeply investigated to understand the variety of observed responses. The high amount of burned material (e.g., charcoal and ashes) deposited on the soil surface can modify soil properties by increasing and then reducing soil infiltration capacity according to the time since the fire (Woods and Balfour, 2008; Shakesby, 2011). As result, these effects often promote water repellency (Swanson, 1981; Certini, 2005; Shakesby and Doerr, 2006; Larsen et al., 2009). Therefore, the alteration of soil properties often leads to the increase of runoff, soil erosion and sediment yield, which can be detected even at a long-term scale (Benavides-Solorio and MacDonald, 2001; Neary et al., 2005). Furthermore, fire effects are different in terms of hydrological (e.g. overland flow generation) and erosional (e.g. sediment loss) responses. As stated by Vieira et al. (2015) in fact, the latter is more evident because of the role played by the changes in soil aggregate stability and organic matter content, which indirectly favours erosive capacity of the runoff. Direct effects on river systems have been documented concerning the increase of in-channel wood recruitment (Benda and Sias, 2003), the alteration of channel stability (e.g. channel aggradation, DeBano et al., 1998), the speed of riparian vegetation recovery, and the rapid relocation of the channel heads along the hillslopes (Wohl and Scott, 2017). Indirect effects mainly concern the alteration of annual water yields (Hallema et al., 2019) and hillslope instabilities given the higher occurrence of landslides and debris flows (Neary et al., 2005).

Many classification systems and change detection methods of multi-spectral data, such as the Relative differenced Normalized Burn Ratio (Miller and Thode, 2007), have been adopted to map and measure the overall effect of fire on vegetation and surficial soil, i.e. burn severity (DeBano et al., 1998). It is widely recognized that this overall effect strongly depends on the fire intensity and pre-fire disturbance history, which determines variable sensitivity across the landscape and overtime (Brogan et al., 2019). Further intrinsic factors such as the area, topography, vegetation, geology and climate, affect the magnitude of changes caused by the natural disturbance (Swanson, 1981). Notably, topography shows strong relationships with fire severity because it in-fluences biophysical gradients

(e.g., moisture, solar radiation) and characteristics of the fuel. For instance, upper slope positions and steep slopes are typically increasing the pre-heating of fuels, whereas different orientations cause high variability in fuel's drying out (Iniguez et al., 2008; Carmo et al., 2011).

In this context, the assessment of fire severity, which often encompasses the properties of intensity and duration, is essential to quantify the fire-related impact. The determination of fire severity and related impacts would help to: i) protect sensitive ecosystems from reduction of soil organic matter, modification of population dynamics; ii) to safe-guard local forest and water users from the reduction of forest productivity and touristic value, and from the sudden release of chemicals into the stream network; iii) to prevent economic losses for downstream areas caused by mass failure and floods (Neary et al., 2005).

Framing the response of an entire catchment to natural disturbances in terms of variation of sediment supply, routing and deposition is still a controversial issue due to the variety of factors involved (e.g., disturbance properties, sediment characteristics, topography, land cover, hydrological regime). In post-wildfire conditions, if a great amount of sediment is available for sudden mobilization, the awareness of how a catchment facilitates the transfer of sediment between source areas and channel network is vital to predict future scenarios and reduce the associated risk (Mazzorana et al., 2019). To this end, the geomorphic property known as connectivity (Wohl et al., 2019) is gaining interest from the scientific community especially concerning major disturbances. Specifically, sediment connectivity underlies the sediment transfer between the compartments of a geomorphic system and their relationships, which control the sediment cascade and geomorphic response to disturbance events (Bracken and Crooke, 2007; Fryirs, 2013). Several metrics of sediment connectivity have been proposed to overcome the more traditional field measurement and to exploit the high amount of topographic data available nowadays (Heckmann et al., 2018). Following this trend, the topography-based Index of Connectivity (hereinafter IC), proposed by Borselli et al. (2008) and refined by Cavalli et al. (2013), has become a sound and accessible instrument to assess the degree of linkage between sources and sinks of sediment in various contexts. Therefore, many authors grasped the opportunity to map sediment connectivity using the IC in different environments and considering plenty of numerical approaches: Gay et al. (2016) and Kalantari et al. (2017) mapped connectivity in lowlands by integrating catchment infiltration/runoff properties and precipitation-runoff variability, respectively; López-Vicente and Ben-Salem (2019) developed a new aggregated index based on the RUSLE2 equation; Rainato et al.(2018), analyzed the (de)coupling relationships of a small dolomitic catchment.

Mapping the IC with respect to major natural disturbances is becoming paramount to understand the variation of sediment connectivity's spatial patterns, their evolution and to predict downstream adjustments (Cavalli et al., 2019). In post-disturbance scenarios, sensitivity is defined as the rate of response to the change, so that highly connected systems tend to respond faster than less-connected ones (Brunsden and Thornes, 1979). Geomorphic systems affected by volcanic eruptions (Martini et al., 2019), land-use change (Persichillo et al., 2018; Llena et al., 2019), typhoons and monsoons (Chartin et al., 2017; Singh and Sinha, 2019), and wildfires (Williams et al., 2016; Estrany et al., 2019; Ortíz-Rodríguez et al., 2019) are closely monitored for their sensitivity in terms of sediment connectivity. However, still strong efforts need to be made to standardize a process to consider the land cover change and its effect on the IC and to make such an accessible tool fully applicable. In other terms, is it possible to convey the essential information about land cover changes into a single parameter, such as the IC, to explain or predict catchment-scale responses to natural disturbances? It often occurs that in order to investigate sediment connectivity changes in post-disturbance areas, the two components are treated separately and much more attention is paid to either IC or the effects of disturbances. However, a multi-disciplinary approach is indeed required to consider the same issue from different standpoints to better support catchment management decisions.

Accordingly, the present study aims at defining how multiple wildfires interact with catchment-scale sediment connectivity by analysing fire severity and sediment connectivity spatial patterns and by identifying common driving factors and interlinked relations in an Andean catchment. The general objectives of the work are to improve awareness about the fire-related impacts from a multidisciplinary perspective, by linking the ecological and geomorphic response and to provide a methodological approach helpful to prioritize areas of hillslope instabilities in wildfire-affected river basins. The specific objectives are: i) to investigate interlinked relationship between fire severity and sediment connectivity changes induced by wildfires; ii) to move towards the standardization of a procedure to apply the IC after major disturbances; iii) to rely upon open source data so the application of the proposed methodology could be replicated in other contexts.

Study area

The study area is the Rio Toro catchment, located in Chile (Fig. 1.2.1A), close to the north-eastern border of the Araucanía Region (IX Región) (Fig. 1.2.1B) and affected by two wildfires in 2002 and 2015. The area extends for 18 km^2, entirely comprised in the Malleco National Reserve, with elevation ranging from 760 to 1810 m a.s.l. and a mean slope of 24°. The climate is classified as temperate warm humid (Fuenzalida, 1965), strongly influenced by the presence of the Andean

Cordillera (E) and the Pacific Ocean (W). The average annual precipitation is about 2480 mm (Comiti et al., 2008), with a monthly maximum and minimum of 490 mm and 62 mm in June and January, respectively (average rainfall calculated for the period 2000–2018; source: http://explorador.cr2.cl/). Bedrock layer is primarily composed of pyroclastic rocks generated by the high volcanic activity of the Southern Andes Volcanic Zone (SVZ, 33°S–46°S) and triggered by the Nazca-South American plate convergence (Cembrano and Lara, 2009). The Rio Toro channel network, which features a pluvial/nival hydrological regime (Comiti et al., 2008), develops mainly with south-north direction with a total length of 11 km from the upstream ridges to the downstream Rio Niblinto, where the outlet of the study catchment is established (Fig. 1.2.1C). The main channel, receiving water from two branches divided by the central ridge, is classified as a third-order stream featuring a step-pool/cascade bed morphology with a mean channel slope of 0.05 m/m (Comiti et al., 2008; Iroumé et al., 2015). The forest is mainly composed of endemic species of Araucaria Araucana and Nothofagus spp. (southern beech). The two species naturally form mixed forests along the Andes Cordillera in the South-Central Chile and western Argentina (Veblen,1982). The understorey of Araucaria-Nothofagus forests hosts Chusquea spp. (quila), a fast-growing bamboo plant reaching high densities, especially after major natural disturbances that typically affect this type of landscape (Gunckel, 1948; Veblen et al., 1981). Until 2002, when the first wildfire occurred, the Rio Toro catchment was almost completely covered by forests. At lower elevation (below 1200 m.a.s.l.) the main species were Nothofagus dombeyi and Nothofagus nervosa while Araucaria Araucana stands dominated the landscape above 1200–1300 m a.s.l. The 2002 fire, occurred in late February, affected both the Malleco National Reserve and the near Tolhuaca National Park, with an overall burned area of about 11.660 ha (Assal et al., 2018), greatly contributing to the 20.000 ha burned in the region in the summer fire season (González et al., 2005). Besides, during the fire season of 2014–15, which counted 1344 wildfires and almost 46,000 ha burned in the Araucanía Region alone (CONAF, 2019), another wildfire affected the same area in late February 2015.

In central Chile, land use practices and extreme climatic conditions are exacerbating wildfires effects (Bowman et al., 2019). For this reason, there is growing interest in monitoring future developments for this and similar areas, where slope instabilities could be expected. Event though no instabilities were reported by other studies after the 2002 wildfire (Comiti et al., 2008; Iroumé et al., 2015), the re-occurrence of the 2015 event may have increased their likelihood.

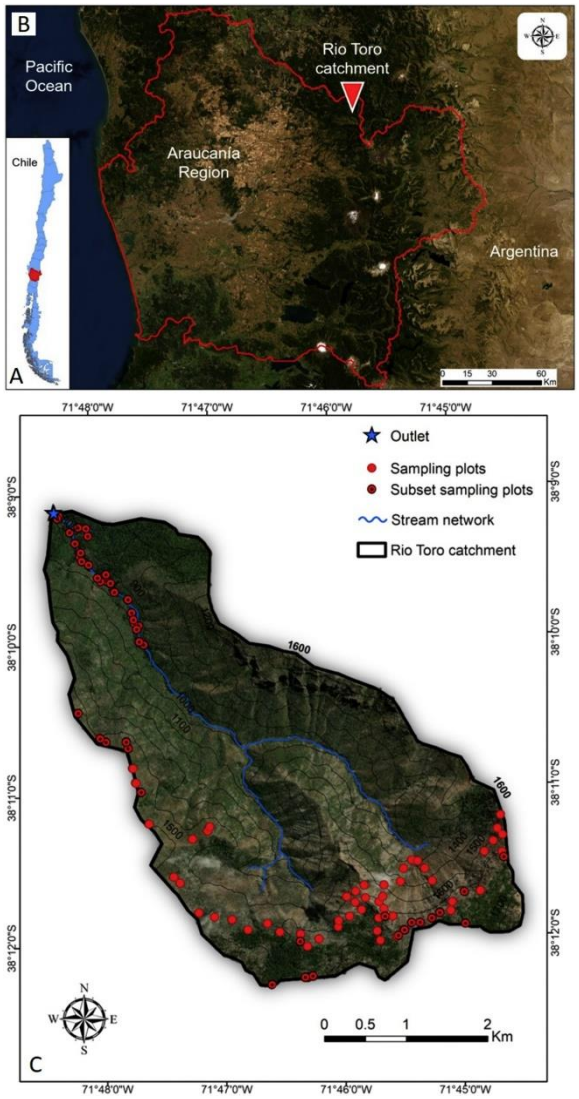

Figure 1.2.1. Location of the Rio Toro within (A) Chilean territory, (B) Araucanía Region and (C) catchment. Source: Esri, DigitalGlobe.

Material and methods

The present study was carried out following a methodological workflow with two parallel phases regarding i) the assessment of severity of the two wildfires occurred in 2002 and 2015, and ii) the mapping of sediment connectivity changes following the aforementioned events (Fig. 1.2.2). The development of both activities relies on field data, acquired during field campaigns carried out in 2019, and freely available satellite Landsat data provided by open-source websites.

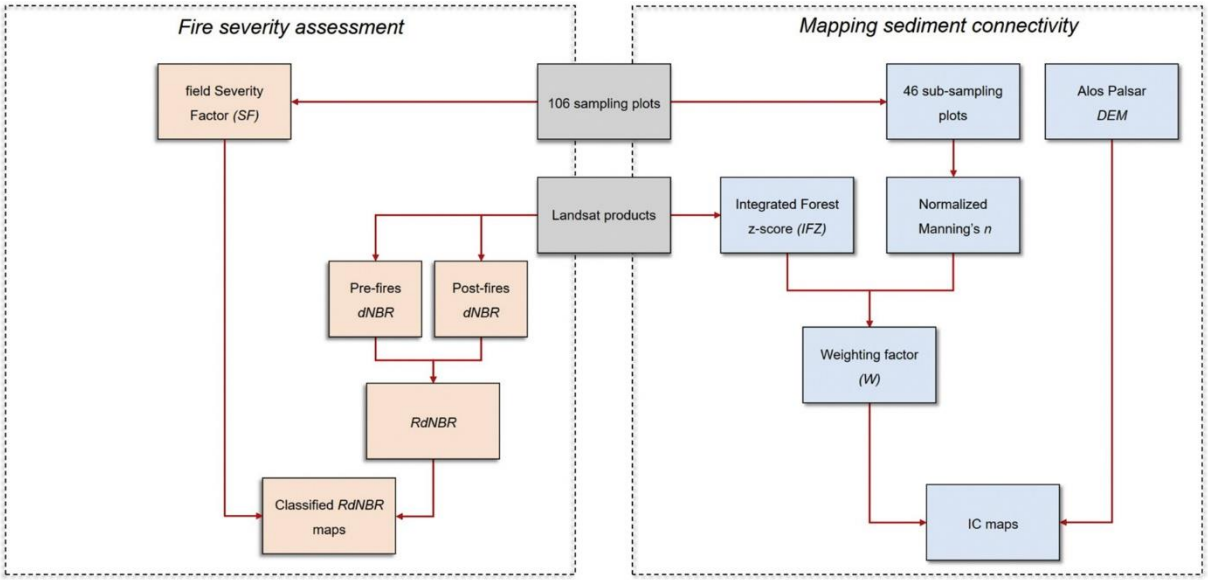

Figure 1.2.2. Methodological workflow to derive fire severity and IC maps. Field data and Landsat products were involved in both activities.

Satellite data

The need for multi-temporal images and consistency among the two methodological phases drove the attention towards Landsat missions, which offer long time series and sufficient global coverage at 30 m resolution (Banskota et al., 2014). Two Landsat 7 ETM+ images corresponding to periods pre- and post-2002 wildfire (01/02/2002, 20/02/2003) and two Landsat 8 OLI images corresponding to the pre- and post-2015 wildfire (28/01/2015, 31/01/2016) periods were selected from the U.S. Geological Service free satellite provider EarthExplorer (EarthExplorer, 2019). After the selection, Landsat products were ordered and obtained from the Earth Resources Observation and Science Center (EROS) Science Processing Architecture On Demand Interface (ESPA). The ESPA allows the processing of Landsat data beyond the standard Landsat Level-1 processing level. Therefore, the four images were provided atmospherically corrected at surface reflectance to account for sensor, solar and atmosphere distortion (Young et al., 2017). In addition, we applied transformations to guarantee continuity among the Landsat 7 ETM+ and Landsat 8 OLI bands in order to avoid misinterpretations of the outcomes (Roy et al., 2016). The topographic information required for developing the sediment connectivity analysis is represented by the Global Digital Elevation Model (DEM) with a spatial resolution of 12.5 × 12.5 m cell size derived by the ALOS PALSAR satellite imagery system. The data were processed and redistributed by the Alaska Facility Service (ASF, 2019; dataset: ASF DAAC, 2009), which provides Radiometrically Terrain-Corrected (RTC)

products. Detailed information about the accuracy of ASF's products can be found in Gesch et al. (2014).

Field data

During January 2019, multiple field campaigns were carried out in the Rio Toro catchment to collect land cover data. We established a total of 106 square sampling plots of about 400 m^2, in which the percentage of area covered by understorey, bare soil and rocks, grassland, deadwood (standing and/or lying on the ground) and trees was visually determined (Fig. 1.2.3). In particular, the understorey was defined as the vegetation layer including bamboo, Araucaria and Nothofagus seedlings, and shrubs developing under the trees. The latter category in-stead, includes only living trees taller than 1.30 m.

In addition, we also evaluated specific ground characteristics on a subset of 46 sampling plots regarding the number of standing dead and living trees and the number of obstructions on the ground (Table S1.2.1). The distribution of the plots within the study catchment was highly constrained by the scarce accessibility due to steep slopes, lack of roads and presence of fallen logs. The position of each sampling plot was taken measuring the centroid using a GPS Trimble Juno 5 (Fig. 1.2.1C).

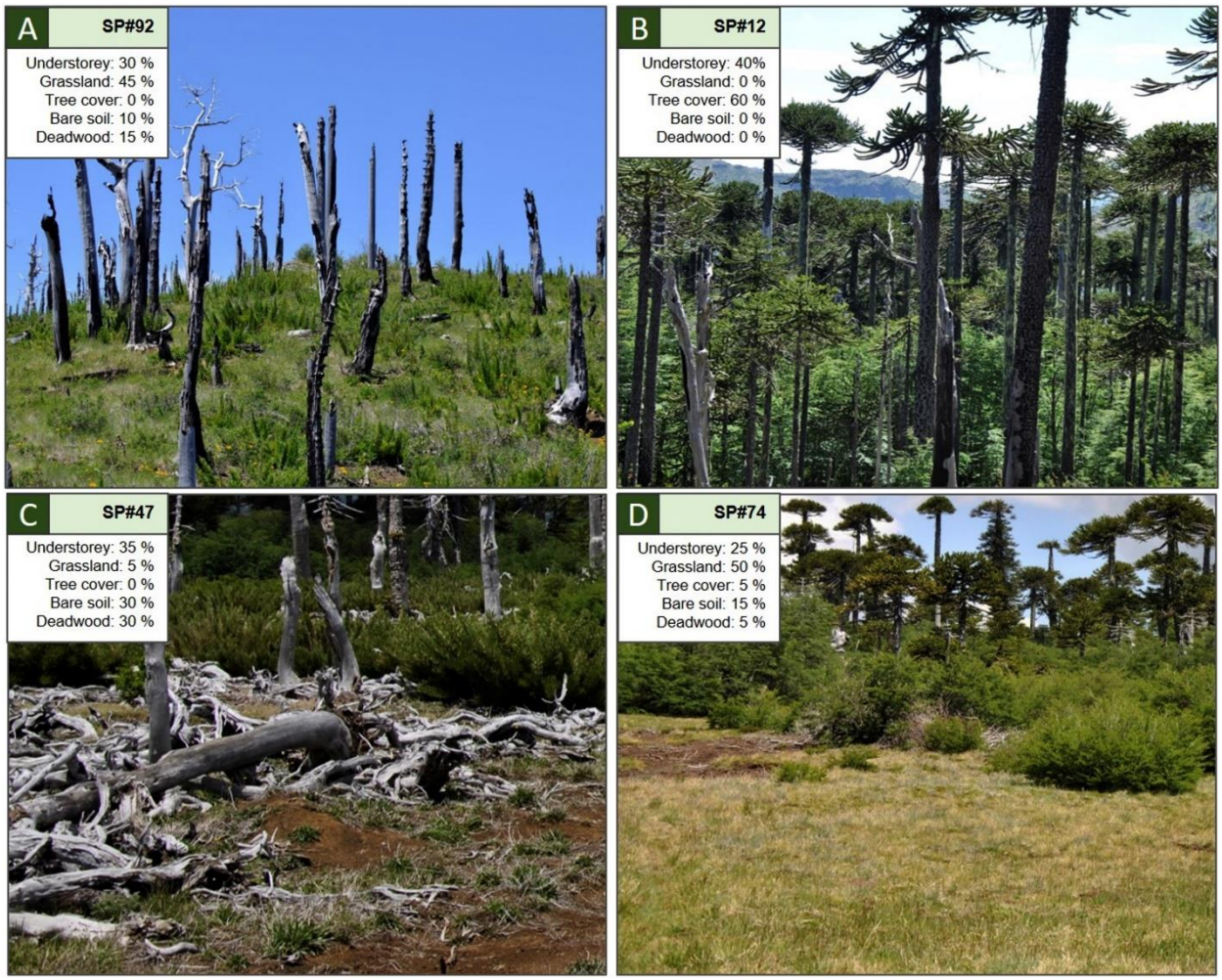

Figure 1.2.3. Examples of four sampling plots assessed during the field campaign of January 2019. For each sampling plot the percent land cover was visually estimated, according to 5 classes (understorey, grassland, tree cover, bare soil and deadwood). (A) Plot presenting high percentage of vegetation regrowth from the fires; (B) Plot presenting undamaged native forest; (C) Plot presenting high amount of deadwood within a scarcely vegetated area; (D) Plot presenting predominantly grassland.

Fire severity assessment

Using the multispectral satellite data described in the section *satellite data*, we first calculated the Normalized Burn Ratio (NBR) for each pre- and post-wildfire year (2002, 2003; 2015, 2016) according to the following formula:

$$NBR = \frac{NIRSWIR2}{NIR+SWIR2} \quad (1.2.1)$$

where, *NIR* is the Near InfraRed band and *SWIR2* is the ShortWave InfraRed band, which are the two wavelengths most sensitive to wildfires (Key and Benson, 2006). In order to provide a quantitative measure of change, the NBR calculated after the fire was subtracted from the NBR calculated before the fire. The resulting delta NBR (dNBR) was calculated as follows:

$$dNBR = \left(\left(NBR_{prefire} - NBR_{postfire}\right) * 1000\right) - dNBR_{offset} \quad (1.2.2)$$

where, the dNBR is conventionally scaled up by a factor of 1000 to obtain an integer output (Miller et al., 2009) and dNBR offset is obtained by averaging dNBR values calculated outside the wildfires-affected areas in order to avoid reflectance biases given by the natural phenological effect (Parks et al., 2014a, 2014b; Morresi et al., 2019). Given the occurrence of two wildfires in the Rio Toro catchment, multiple dNBRs were calculated as the difference between the years 2003–2002; 2016–2015 and 2016–2002. The latter aims at detecting the spectral changes given by the sum of the two wildfires and it has been considered only as a proxy variable in the function used to classify the severity of the two separate wildfires. Furthermore, to improve the accuracy of wildfire severity assessment we calculated the Relative dNBR (RdNBR), following Eq.(1.2.3):

$$RdNBR = \frac{dNBR}{\sqrt{|NBR_{prefire}|}} \quad (1.2.3)$$

where the absolute sign in the denominator avoids unreal numbers as results.

Choosing the relative ratio (RdNBR) instead of the absolute one (dNBR) permits to enhance the classification accuracy for high severity categories especially in more heterogeneous environments and to compare fires across time and spatial scales (Miller and Thode, 2007). The resulting three RdNBR maps (2002–2003, 2015–2016 and 2002–2016) were then classified using field data.

From the sampling plots, we tested the combination of field metrics that best fitted with RdNBR values corresponding to the period 2002–2016, which summarizes all the changes in reflectance caused by both wildfires. The ratio between areas of bare ground and bare ground plus tree cover area (hereinafter defined as Severity Factor, SF) reported the strongest relationship with RdNBR values, according to a second-order polynomial function (R^2= 0.65). Using the natural breaks algorithm, the SF was grouped into four classes corresponding to un-burned, low, moderate and high severity. Using the polynomial function it was possible to carry out the four RdNBR classes' thresholds, which determine the classification scheme used in the wildfire severity maps 2002–2003 and 2015–2016 (Fig. S1.2.1). The classification accuracy calculated between measured and predicted severity of sampling plots was 62% with a Cohen's Kappa coefficient (κ) of 0.45, indicating moderate agreement between the raters.

The final wildfire severity maps were then compared in terms of spatial patterns, with particular focus on the eventual changes or similarities among different severity areas between the two events. Similarity analysis was performed thanks to the Jaccard Index, calculated specifically between areas with the same severity (e.g. unburned 2002 - unburned 2015). On the contrary, the variation was evaluated through the transition matrix (or cross-tabulation matrix), to highlight gains and losses among the classes.

To improve awareness on how the topographic features of the Rio Toro affected the fire severity in the two events, two Generalized Linear Models (GLMs) were carried out. The effect of slope, elevation (continuous), slope position (Guisan et al., 1999), aspect (categorical) were tested on the RdNBR with a significance level of at least 0.05. We applied simple random sampling with a 95% confidence interval to select the most appropriate number of samples to be used in the GLMs.

Mapping sediment connectivity

The analysis of sediment connectivity was performed through the IC, applied to four periods corresponding to 2002, 2003, 2015 and 2016. The IC in the Rio Toro catchment was computed using the open-source, stand-alone software SedInConnect 2.3 (Crema and Cavalli, 2018), which operates using TauDEM tool for hydrological functions (Tarboton, 1997). Following the original formula by Borselli et al. (2008), the IC relies upon two components that describe the linking relationships between sediment sources and downstream areas, so:

$$IC = log_{10}\left(\frac{D_{up}}{D_{dn}}\right) = log_{10}\left(\frac{\overline{W}\,\overline{S}\sqrt{A}}{\sum_i \frac{d_i}{S_i W_i}}\right) \quad (1.2.4)$$

where, D_{up} is the upslope component representing the potential for downward routing of the sediment according to the catchment's upslope area features. Hence, $\overline{W}$ and $\overline{S}$ are the average value of the impedance to sediment fluxes and the average slope (m/m) in the upslope catchment, respectively, and A is the contributing area (m^2) of the specific point under investigation. On the denominator, D_{dn} is the downslope component including the characteristics that could affect the transfer of sediment: d_i is the length (m) of the flow path along the i^{th} cell, W_i is the weighting factor and S_i the slope gradient of the i^{th} cell.

In the present study, we made use of a unique DEM as the main source of topographic information for the computation of the IC for the four wildfire scenarios. This choice was constrained by the lack of representative DEMs for the two events and by the assumption that no major morphological

changes, detectable at 12.5 m resolution, occurred during the period between the two wildfires. On the contrary, an adaptive weighting factor has been developed to represent the differences of impedance to sediment fluxes likely to be caused by the large variability in land cover due to the wildfires. Finally, to highlight the linkages between hillslopes and the Rio Toro (i.e. lateral connectivity of the system), we set the whole stream network as target of the IC computation.

Weighting factor

To derive the weighting factor for the IC, the Manning's n for the overland flow was selected over the original USLE C-factor (Wischmeier and Smith, 1978) and its variants (see Chartin et al., 2017; Lizaga et al., 2017; López-Vicente and Ben-Salem, 2019) since we consider it a better proxy of sediment impedance in natural catchments. Following the additive method provided by Arcement and Schneider (1989), an ad-hoc Manning's coefficient was computed foreach of the 46 sub-sampling plots according to the ground characteristics collected during field campaigns and described in the section *field data*. From the plot-derived Manning's n, a new approach has been adopted, based on the abrupt land cover changes at the pixel scale, in order to produce four catchment-scale weighting factor maps (hereinafter W factor maps). The four W factor maps were generated starting from the correlation between the Manning's n and the spectral vegetation index known as Integrated Forest Z-score (IFZ) calculated from the four Landsat images (Eq. (1.2.5)). The IFZ is a threshold-based index aiming at identifying the likelihood of a pixel to be not forested so that it represents a strong index to track vegetation changes and recovery after wildfires (Huang et al., 2010; Morresi et al., 2019).

$$IFZ = \sqrt{\frac{1}{NB}\sum_{i=1}^{N}\left(\frac{b_i-\bar{b}_i}{SD_i}\right)^2} \quad (1.2.5)$$

where, NB is the number of spectral bands employed (in this work SWIR and SWIR2) b_i is the spectral value of the pixel of band i, $\bar{b}_i$ and SD_i are respectively the mean and standard deviation of random pixel samples of the band i. Hence, the IFZ and Manning's n are inversely related: higher is the chance for a pixel to be not forested and lower is the impedance to sediment fluxes. More information about the fitting model IFZ-Manning's n are present in the supplementary material (Fig. S1.2.2).

Although similar approaches, combining land use-based roughness and spectral indexes, have been proposed in the field of connectivity (e.g. Mishra et al., 2019), they mainly focused on the use of NDVI that is less sensitive to the sudden changes in reflectance than the IFZ (Huang et al., 2010; Chu, et al., 2016; Morresi et al., 2019). Once the Manning's n was extended for the whole catchment

and the four periods, the final weighting factor maps (W) were generated following the normalization equation originally proposed by Trevisani and Cavalli (2016) for the topographic roughness:

$$W = 1 - \frac{\ln(n) - \ln(n_{min})}{\ln(n_{max}) - \ln(n_{min})} \quad (1.2.6)$$

where n_{min} and n_{max} are the minimum and maximum Manning's coefficients included within the range 0.001 -1 and converted in the logarithmic form. The main advantages of this operation are: i) to preserve the adimensionality of IC, as also stressed by Zanandrea et al. (2020), ii) to offer a wider range of W factor values, otherwise constrained by the additive method of Arcement and Schneider (1989), and allowing an enhancement of the spatial variability in the final IC maps and iii) to move towards the full standardization of land use-based W factor.

In the present work, differences among datasets were analyzed for their statistical significance using the non-parametric Kruskal-Wallis (KW) test; the comparisons were considered statistically significant if $p < 0.001$ (given the high statistical power from the high number of pixels). All statistical procedures were carried out with the support of Rstudio version 1.2.5019 (Rstudio Team, 2016) and Statgraphics 18.

Results

Wildfire severity maps

Two severity maps based on RdNBR classification for 2002 (Fig. 1.2.4) and 2015 (Fig. 1.2.5) wildfires in the Rio Toro catchment are presented. After the 2002 event, significant burned areas accounted for 1657 ha, which corresponds to the 90.9% of the whole study catchment. Particularly, high severity represents the most widespread class, occupying 68.9%, whereas moderate and low severity classes characterize 14.7% and 7.3% of the study area, respectively. On the contrary, the area classified as unburned covers 9.1% of the catchment area and it is mainly located in the further upstream and downstream positions. The 2015 fire severity map shows 1384 ha of burned areas (75.9%), with the prevalence of moderate severity areas, covering the 42.2% of the total study catchment. Less represented are the high and low severity patches, which covers 23.4% and 10.2% of the total area, respectively. The map shows a major presence of high severity areas, mainly located on the left slopes facing North-East and, conversely, moderate and low severity spread along the right slope, facing South-West. However, unburned areas are the second most represented class with 24.1%. The areas unaffected by the fire can be found at lower and upper elevations as well as in the higher and steeper ridges on the right slope.

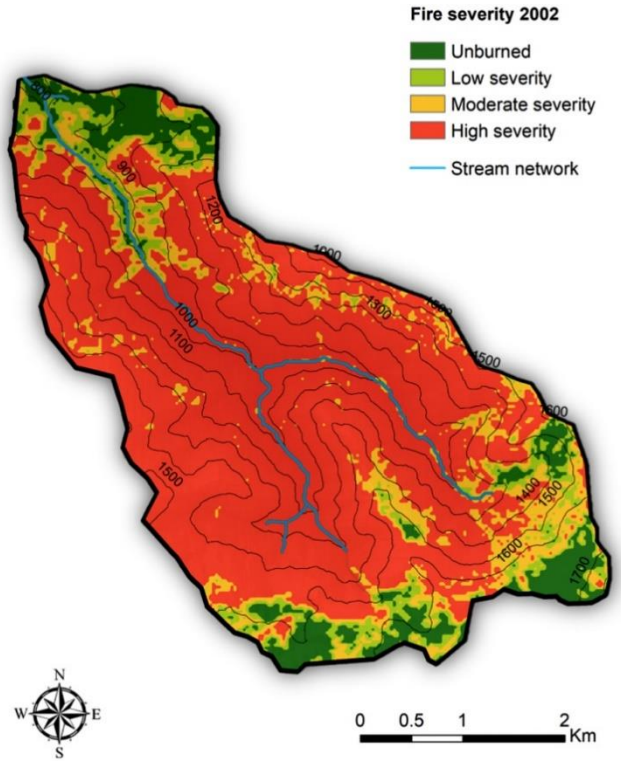

Figure 1.2.4. The 2002 wildfire severity map shows the distribution of severity classes within the Rio Toro catchment.

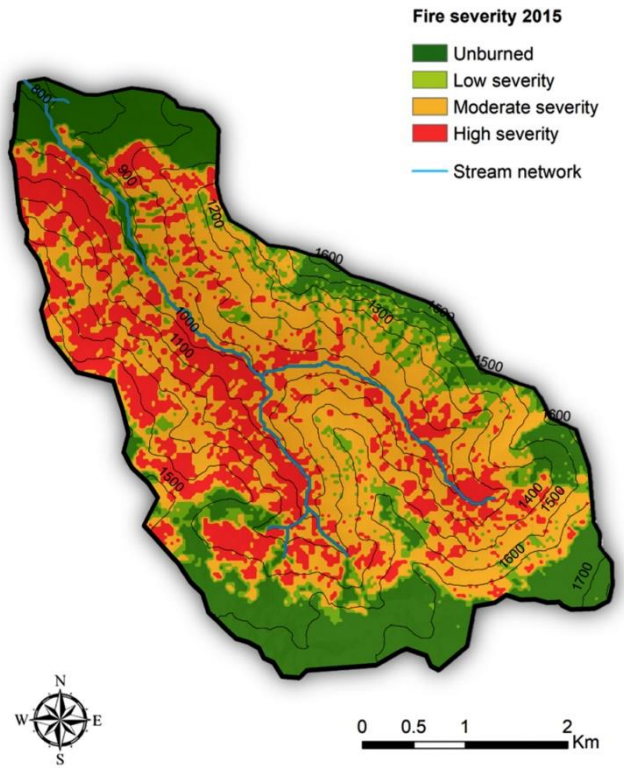

Figure 1.2.5. The 2015 wildfire severity map shows the distribution of severity classes within the Rio Toro catchment.

Despite the major difference in high severity areas, similar patterns can be observed in the two maps: unburned areas near the northern and southern borders; high and moderate severity areas in the central part. The Jaccard Index demonstrates poor similarity in the overlap for the low and moderate severity classes, with outcomes of 0.06 and 0.12, respectively. The higher similarity was found for the extreme classes with outcomes of 0.30 (High severity) and 0.35 (Unburned). The comparison between the 2002 and 2015 fire severity maps led to the development of the transition matrix (Table 1.2.1), which points out the percentage of catchment within each combination of severity classes as well as the total for each period. Diagonal entries show the percent-age of severity that did not change throughout the years, suggesting that highly burned (21.4%) and unburned (8.7%) areas are the ones that persisted the most after the events. On the other hand, low (1.1%) and moderate (6.5%) severity areas are the classes that show lower persistence and therefore higher changes. The gain and losses from 2002 to 2015 exhibits that moderate severity class gained the 35.8% of the catchment, whereas high severity class lost the 47.6% of the catchment. Lowest gains were experienced by the low severity class, 9.1% of the landscape, whereas lowest losses were experienced by the unburned class.

Table 1.2.1. Transition matrix showing the fire severity persistence and changes between the two wildfires. The area is expressed as percentage of the total catchment area. Total is the sum of rows and columns, representing the overall area of each class for 2002 and 2015, respectively. Loss is the area of each class that did not persisted from 2002 to 2015. Gain is the area of each class that persisted from 2002 to 2015.

Area (%)	**Wildfire 2015**				**Total**	**Loss**
	Unburned	Low severity	Moderate severity	High severity		
Wildfire 2002						
Unburned	8.7	0.3	0.1	0.0	9.1	0.4
Low severity	5.0	1.1	1.0	0.2	7.3	6.2
Moderate severity	3.9	2.4	6.5	1.9	14.7	8.2
High severity	6.5	6.4	34.6	21.4	68.9	47.6
Total	24.1	10.2	42.2	23.4	~100	
Gain	15.4	9.1	35.8	2.0		

Table 1.2.2. Statistical results from the Generalized Linear Models for the effects of topographic variables on RdNBR of the two wildfires. Significant results at p <0.05 or p <0.001 are indicated with * or **, respectively.

	RdNBR 2003-2002			RdNBR 2016-2015		
Variable	**d.f.**	***F***	***p***	**d.f.**	***F***	***p***
Aspect	3	18.586	<0.001**	3	17.815	<0.001**
Slope	1	50.023	<0.001**	1	80.103	<0.001**
Slope position	3	4.228	0.040*	3	6.691	0.009*
Elevation	1	2.303	0.129	1	58.350	<0.001**
Aspect × Slope position	9	2.134	0.144	9	0.117	0.731

The results of the GLMs showed that RdNBR values are statistically related to slope, aspect (p-value <0.001) and slope position (p-value <0.05) variables in both wildfires. On the contrary, elevation did not show a statistical relation with fire severity (p-value >0.05) in the first wildfire, whereas in the second one did (Table 1.2.2). Since slope position is derived from the combination of slope and elevation, it showed a weaker but still significant effect on fire severity in both cases. Besides, the analysis regarding the combined effect of the two categorical variables (slope position and aspect) gave negative results due to non-significance (p-value >0.05).

Sediment connectivity

Peculiar spatial patterns can be observed in the IC maps (Fig. 1.2.6). In 2002, high IC areas were located mainly on the left slopes and streambanks, whereas low IC values characterize the small sub-catchment close to the outlet as well as the high and flat areas along the southern border (Fig. 1.2.6A). Following the 2002 wildfire, the IC map show high values of the index also near the channel heads of the two main branches of the Rio Toro (Fig. 1.2.6B). Apparently, the IC remained constant also for 2015 (Fig. 1.2.6C) and 2016 (Fig. 1.2.6D) maps. Although the multi-temporal assessment points out similar patterns of high and low IC in all the scenarios, the degree of linkage between slopes and channel net-work, enhanced in post-wildfire scenarios.

To emphasize the IC changes, the difference of IC (hereinafter DoIC) between post-wildfire and pre-wildfire scenarios was computed for the two events. The DoIC maps are presented in Fig. 1.2.7, where darker the colour, higher the increase in IC after the wildfire. It is important to mention that

the classification of the two maps varies according to the value range of each map, except for the decrease class, since this class consistently refers to negative values. The 2003–2002 DoIC map (Fig. 1.2.7A) shows a clear upward trend, with a mean value of 1.07 (±0.38) and observed minimum and maximum of -1.56 and 2.88 respectively. Low, moderate and high increase of IC values cover 24.1%, 51.8% and 23.4% of the whole catchment, with mean values of 0.57, 1.11, 1.52. Notably, high positive DoIC values are detectable near the junction of the two main streams and in the proximity of areas of convergence of flows and channel heads. On the contrary, areas showing decreasing IC values are covering the 0.7% of the catchment (mean -0.28). After the second wildfire, the 2016–2015 DoIC map (Fig. 1.2.7B) shows again an upward trend but with a lower mean values than the first event for the overall catchment (0.53 ± 0.22) and DoIC classes (-0.11, 0.20, 0.51, 0.75).

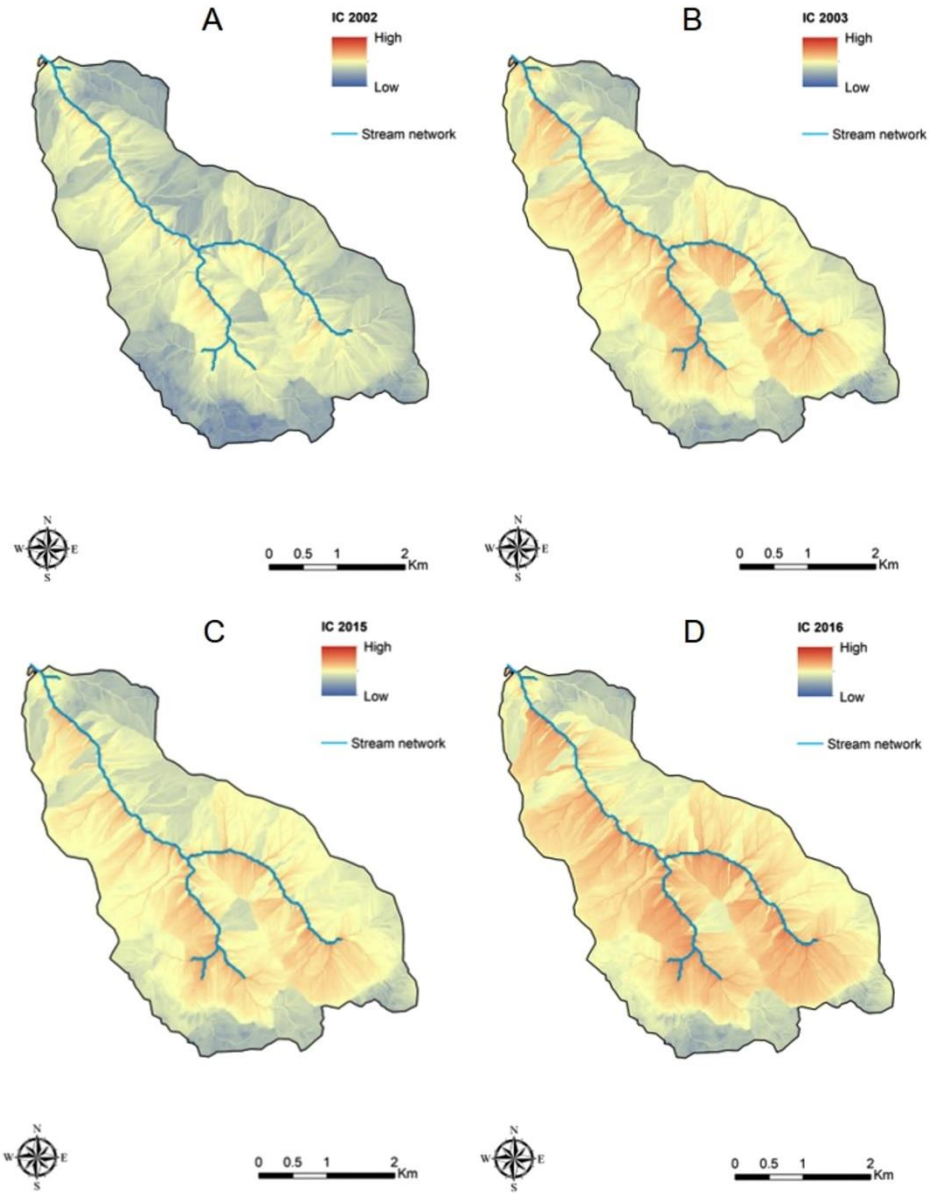

Figure 1.2.6. Maps of IC calculated for scenarios pre (A, B) and post (C, D) wildfires.

.

Nonetheless, the representativeness of each DoIC class is: decrease areas 1.3%; low increase areas 20.7%; moderate increase areas 40% and high increase 38%. The spatial arrangement of the classes shows high increase IC areas close to the stream network and they are mainly located in the central part of the basin rather than at the channel heads. Decreasing IC areas are instead confined to small spots near the outlet and on the high and flat areas along the southern border, already characterized by low IC in the pre-wildfire scenario (Fig. 1.2.6C).

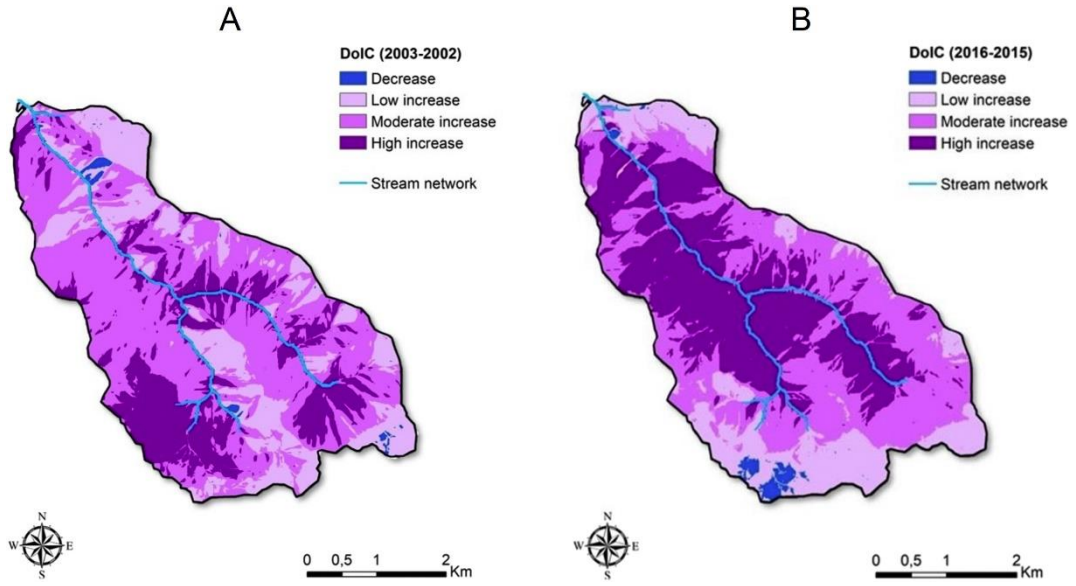

Figure 1.2.7. Maps of DoIC showing increasing and decreasing patterns of IC after the (A) 2002 wildfire and (B) 2015 wildfire.

Linking fire severity and sediment connectivity

The comparison between fire severity and sediment connectivity can help to shed light on the effect of how a wildfire can affect sediment connectivity. As expected, from a first qualitative assessment of the maps, the spatial patterns are very similar. Areas of lower DoIC (decrease and low increase) located where the fire severity is lower (unburned and low severity) and areas of higher DoIC (moderate and high increase) where the fire severity is higher (moderate and high severity). Quantitatively, the overlap between the connectivity and severity component is expressed as the area (%) of DoIC class that partly covers the corresponding fire severity class (Table 1.2.3).

Table 1.2.3. Overlap between fire severity classes and DoIC classes for the second wildfire. The area is expressed as percentage of the total DoIC class.

		DoIC 2003-2002			
	%	Decrease	Low increase	Moderate increase	High increase
Fire severity 2002	Unburned	24.9	23.7	4.3	2.2
	Low severity	17.3	12.6	6.3	3.1
	Moderate severity	17.0	17.0	15.3	10.0
	High severity	40.8	46.8	74.1	84.7

Table 1.2.4. Overlap between fire severity classes and DoIC classes for the second wildfire. The area is expressed as percentage of the total DoIC class.

		DoIC 2016-2015			
	%	Decrease	Low increase	Moderate increase	High increase
Fire severity 2015	Unburned	94.5	82.1	10.8	0.9
	Low severity	1.6	9.3	17.4	3.4
	Moderate severity	3.8	7.0	54.3	52.4
	High severity	0.1	1.6	17.6	43.4

Particular attention was given to the diagonal values, representing the overlap of counterparts. After the first wildfire, only the 84.7% overlap confirms what previously observed between the two maps: high DoIC spatial patterns extensively corresponds to high fire severity. On the contrary, the correspondence between decrease IC areas and unburned areas is only the 24.9%. Indubitably, the huge extent of high severity class causes most of the DoIC areas to be greatly overlapped by it. Even the decrease IC areas, in fact, are constituted by high severity areas for the 40.8%. After the second wildfire, the highest correspondence is between decrease IC areas and unburned areas (Table 1.2.4), with an overlap of 94.5%, which confirms what can be seen in the maps. Moderate overlap is visible among higher classes, i.e. moderate-moderate, high-high, with a 54.3% and 43.4% respectively.

Fig. 1.2.8A shows the DoIC distributions for the period 2003–2002 and Fig. 1.2.8B the DoIC distributions for the 2016–2015 time window. The medians of DoIC values according to the four severity classes were 0.68, 0.91, 1.05, 1.19 for the first event and 0.22, 0.49, 0.62 and 0.70 for the second one, respectively. While for the second wildfire the results suggest that higher the fire severity and higher is the increase in IC values, in the 2002 event, the relation is less clear due to the higher data Fig. 1.2.6. Maps of IC calculated for scenarios pre (A, B) and post (C, D) wildfires. dispersion. However, in both cases, the distributions of each group were found statistically different among each other (KW test, p-value <0.001).

The distribution of DoIC values, fire severity and topography is presented in Fig. 1.2.9, where the three most significant topographic variables (Table 1.2.2) are used. Generally, among all fire severity classes, the higher DoIC values correspond to high severities but, again, the DoIC values for the first event show higher data dispersion than the second. After the 2002 wildfire, the higher DoIC values are found in areas facing North, whereas the lowest values in areas facing West, and they are both statistically different (KW test, p-value <0.001) from the others (Fig. 1.2.9A). The DoIC values for the 2015 wildfire instead do not show a clear pattern among the aspects and there is no statistical difference (KW test, p-value >0.001) between North and West for the high fire severity classes (Fig. 1.2.9B). The interaction with slope position for the first event (Fig. 1.2.9C) shows that the highest and lowest DoIC interquartile ranges are observed for the lower slope positions, in which the DoIC distributions are also the only statistically different from the others. In 2015, again unburned areas located on lower slopes positions show the lowest DoIC values and the highest increase characterizes the areas of high severity on upper slopes (Fig. 1.2.9D).

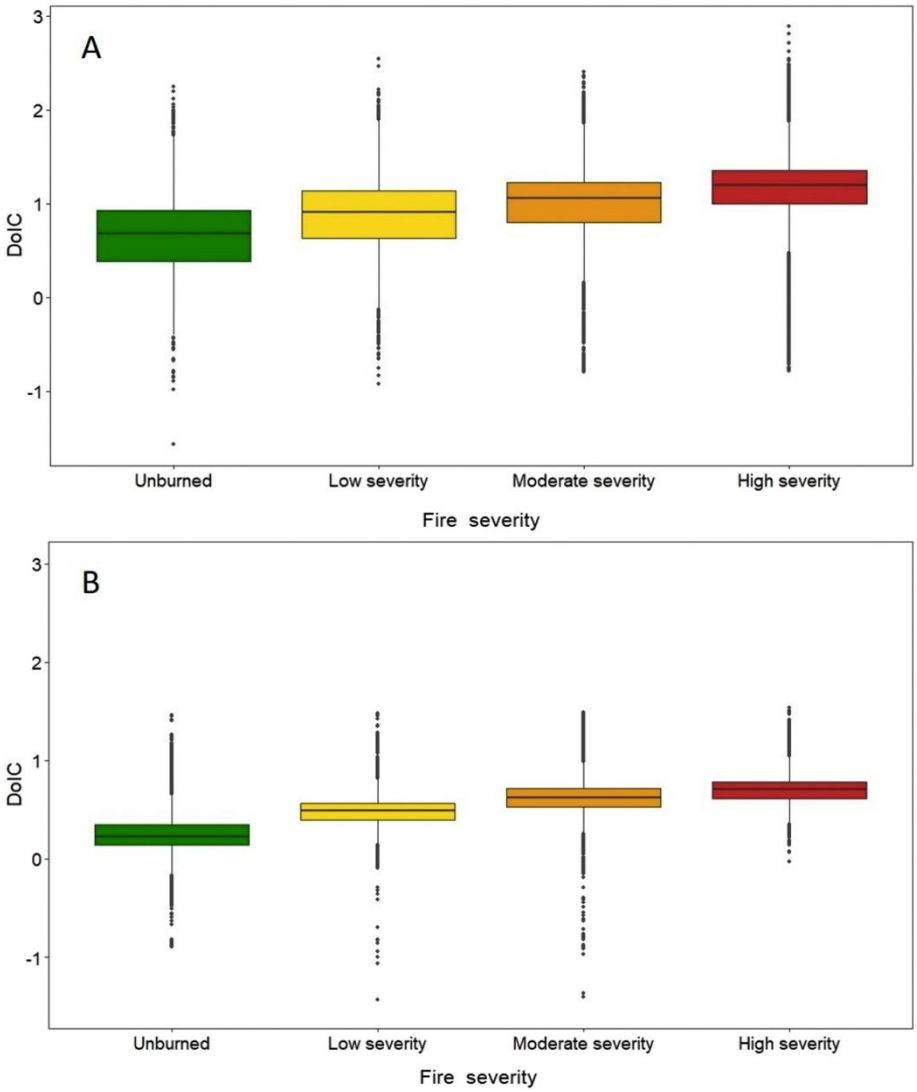

Figure 1.2.8. The DoIC value distribution according to the four fire severity classes for the (A)first wildfire and (B) second wildfire. Box indicates the interquartile range, whiskers the values included within 1.5 times the interquartile range.

Finally, the variation of DoIC as function of slope indicates that a higher increase in IC values is detected at minor slope degrees in the first event (Fig. 1.2.9E) but, the opposite trend, in the second event (Fig. 1.2.9F). Notably, after the first wildfire, DoIC values strongly differ be-tween unburned and other classes on steep slopes (45–60°), while after the second wildfire no IC increments were found in unburned areas on the steepest slopes (60–75°).

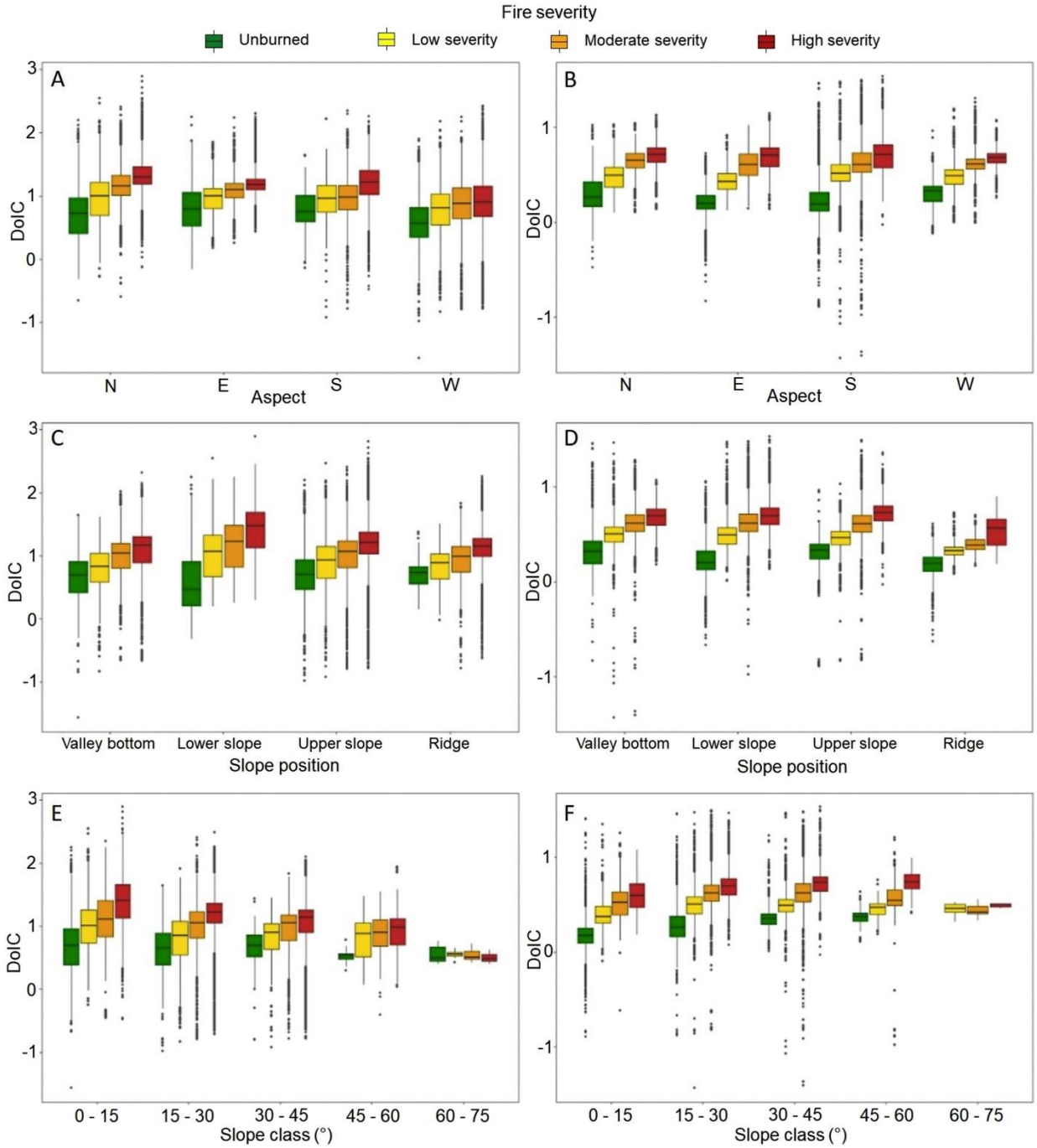

Figure 1.2.9. The DoIC value distribution according to driving topographic factors for the (A, C, E) first wildfire and (B, D, F) second wildfire showed for each of the four fire severity classes. Box indicates the interquartile range, whiskers the values included within 1.5 times the interquartile range.

Discussion

In the Rio Toro catchment, two major wildfires occurred in 13 years, causing severe changes to the land cover and vegetation structures. The assessment of fire severity showed that most of the catchment was hit by wildfire of moderate and high severity. Indeed the first wildfire strongly affected the vegetation community of the catchment and surrounding territory, as observed by other authors (Comiti et al., 2008; Iroumé et al., 2015; Assal et al., 2018; Mazzorana et al., 2019). On the other hand, the second wildfire showed lower severity but similar spatial patterns, for instance, demonstrated by the persistence of unburned areas at the northern and southern borders. The result of lower severity after previous high severity events is in contrast with some studies developed in the south-west of the US (Holden et al., 2010; Parks et al., 2014a, Parks et al., 2014b) but shared by Stevens-Rumann et al. (2016), who found this divergence as caused by slower vegetation recover after the prior disturbance. In our study area, the first fire had much more fuel's availability compared to the second one, which occurred after 13 years only. In the assessment of the second event, the use of a relative vegetation index, such the RdNBR, helped to avoid the bias of the low amount of 2015 pre-fire vegetation caused by the first wildfire. However, the difference between the two fire severity maps could be caused by the classification procedure, which relies upon field surveys carried out four years after the second wildfire, or by the RdNBR values used in the polynomial function and associated to total changes after both wildfires (RdNBR 2016–2002, see section *fire severity assessment*). The resulting 62% of classification accuracy, obtained from the measured and predicted severity, can affect model outcomes. In the end, the choice of an appropriate spectral index for fire severity assessment is fundamental. We selected the SWIR-based NBR, for its higher sensitivity to fire damages and post-disturbance forest structure recovery (Pickell et al., 2016). Although Ortíz-Rodríguez et al. (2019) found good classification agreement using the NDVI for fire severity assessment, the peculiar condition of fire recurrence in the Rio Toro catchment led us to avoid indexes with lower disturbance response, such as the NDVI, which proved to overestimate recovery rates (Schroeder et al., 2011; Morresi et al., 2019).

As proved in several case studies (Iniguez et al., 2008; Oliveras et al., 2009; Estes et al., 2017), topography plays a fundamental role in the distribution patterns of burned areas. In the Rio Toro catchment, slope more than other variables showed a relation with fire severity. Nonetheless, other fire drivers like wind, temperature and fuel's characteristics must not be neglected for their growing importance in the context of climate change and particularly in south-central Chile, where a strong decrease in precipitation is expected in the next years (CONAMA, 2006; Úbeda and Sarricolea, 2016).

The analysis of sediment connectivity highlighted a general increase of IC values after the wildfires, with high IC increase mainly located in the headwaters in 2002 and in the central part of the catchment in 2015. This suggests that, after the second wildfire, potential loose sediment could have higher chances to enter the channel network and being transported downstream thanks to their proximity to the outlet.

Moreover, the DoIC average values observed for the two wildfires, reflected the difference in fire severity: higher overall increase of IC values after the first wildfire than the second one (i.e. higher DoIC values for the 2002 disturbance). However, the lower increase observed in the second scenario could be associated with the estimation of the Manning's n, which primarily drives the IC in our study case. While for the fire severity assessment we made use of a relative index for burn detection, the IC calculation was based on the IFZ, which enhances the detection of forest recovery and thereby higher impedance to sediment fluxes. Hence, the difference in the DoIC between the two events can be associated to: i) lower severity of the 2015 wildfire, ii) IFZ overestimation of the 2015 pre-fire vegetation cover iii) actual fast recovering rate in the Araucaria-Nothofagus forest after the first wildfire. The last hypothesis is also supported by field evidence. Just four years after the 2015 wildfire, shrubs species such the endemic *Chusquea* spp. re-occupied large patches of the study area and blocking many pathways (Fig. S1.2.3). Therefore, in our study area, shrubs might represent the conjunction between the ecological and geomorphological response, since their encroachment can enhance rapidly the storage capacity and reduce sediment connectivity.

Despite the overall higher increase of IC after the 2002 wildfire, the results demonstrated stronger relation between fire severity and sediment connectivity after the 2015 event. The first wildfire was characterized by poorer spatial patterns overlap due to the huge extent of the high fire severity class: contrary to DoIC, the fire severity variable was almost saturated by the highest class. In addition, IC values showed higher IC variability than for the second event. The cause of such different variability of IC values found after the two events may be attributable to the different degree of land cover heterogeneity in the pre-2002 scenarios. While before 2002 the catchment showed high variability of forest structures, hence high vegetation heterogeneity, before the 2015 the vegetation was far more homogeneous. Since the severity of 2002 disturbance was high on the majority of the study area, successional dynamics driving the vegetation recovery started from similar conditions (i.e. complete mortality of canopy trees and consumption of shrub and herb layers) and the short time period between the two disturbances was not enough to differentiate fuel load and structure among different sites.

The application of the IC permitted to capture the main changes in possible sediment sources, routes and deposits at the catchment scale. In post-disturbance scenarios the IC has been used to summarize the sediment dynamic changes but, according to the characteristics of the disturbance and environment, different W factors would have been used. In forested mountain catchments, neither the standard Roughness Index (Cavalli et al., 2013) nor the C-factor are suggested since they are more focused on applications to high altitude headwater catchments characterized by lack of forest cover and agricultural catchments where the role of crop management systems in terms of soil loss is pivotal. On the contrary, Manning's n is becoming much more used (e.g. Persichillo et al., 2018; Llena et al., 2019), especially with high land-use heterogeneity. Nonetheless, the Manning's n causes low distribution in W factor values and requires tabled data. We tried to overcome the first issue, which has been proved to impact negatively the IC (Zanandrea et al., 2020), by normalizing the W factor. To avoid the mere use of tabled data, we implemented a methodology that exploits field observations and remote sensing data in order to adapt the W factor to specific post-disturbance conditions without yielding too much subjectivity. Zanandrea et al (2020), offered an alternative W factor that properly preserved adimensionality and emphasized the role of forests but without the chance to adjust the methodology to dynamic environments. Therefore, with this work we tried to progress towards the standardization of the W factor without neglecting the importance of field data and considering the role of regeneration in post-wildfire scenarios by using the IFZ over the NDVI.

The choice of the appropriate W factor also depends on the data availability as well as temporal and spatial scales. For instance, Mishra et al. (2019) calculated the impedance according to a simple remote assessment of vegetation, based on the C-factor and NDVI, to study major sediment connectivity patterns in a large basin; Estrany et al. (2019), used the traditional Roughness Index to study plot-scale vegetation-sediment structures in micro-catchments; Kalantari et al. (2017), proposed a W factor based on runoff generation potential, having different land use and group of soil types within the lowland study area.

The compound analysis of fire severity and sediment connectivity highlighted the main areas of interest, where presumably the land cover changes were exacerbated and so characterized by high severity and high increase in IC. It is worth mentioning that the increase of IC at the pixel scale is not the mere result of the adopted weighting factor but it is also the outcome of the propagation of changes due to land cover variations in the catchment. Considering also the intrinsic characteristics of the catchment, it was possible to identify where the IC increased the most for each fire severity class. Therefore, it appeared that during the first wildfire, lower slope positions and on gentle slopes facing North promoted fire severity; hence the IC. These results can be seen partially in contradiction with

literature data. In fact, while on northern aspects, in the southern hemisphere, temperature and fuel conditions are usually suitable for increasing wildfire occurrence and severity, lower slope positions on gentle slopes are not (Carmo et al., 2011; Estes et al., 2017). These areas were actually covered by *Nothofagus* spp., species that do not present resistance traits and can be deeply affected even at intermediate fire intensity (González et al., 2005). On upper slope positions the *Araucaria* stands were greatly damaged when high-intensity crown fires affected the stand, while with lower intensity the severity was lesser due to the resistance traits of the species, such as thick bark and a crown displaced several meters above the ground in mature trees (Burns, 1993; González et al., 2010).

To provide useful information for management decisions, the results of the present study should be considered as a whole. Hence, the prioritization of catchment areas after wildfires would rely on: i) the fire severity maps, describing where overland flow, soil erosion and sediment yields could be suddenly boosted, ii) the most recent IC map, showing where there is higher degree of connectivity to sensitive targets, and iii) the DoIC map, demonstrating where the connectivity suddenly increased. Monitoring vegetation decay is also important since in post-fire scenarios falling dynamics of damaged and standing dead trees can last for decades and, depending on species and snag size (Marzano et al., 2012; Molinas et al., 2017), they can either provide elements able to enhance microsite for regeneration on the slopes (Marzano et al., 2013) or be recruited as large wood in river systems. (Benda and Sias, 2003).

Finally, it is important to point out that the IC offers only semi-quantitative information of the potential sediment transfers, while for accurately predicting sediment displacement and dynamics, a different analysis considering also other driving factors is indeed required. Notably, in post-wildfire scenarios these factors are associated with the reduction of soil infiltration parameters, changes in soil physicochemical properties and the presence of ashes, which are all responsible of alteration in runoff and sediment transfer (Shakesby, 2011). Considering also these variables would have required dedicated field campaigns and would have moved simple approaches based on geomorphometric indices to more complex and sophisticated models with all the uncertainties related to the different variables estimations. Aware of all the limitations of our approach, in the present work, the aforementioned factors have been overlooked to restrict the variables involved and focus on the topography and land cover based ones. We used land cover changes as the only proxy for sediment impedance. This choice is justified by the lack of multi-temporal DEMs and by the absence of major morphological changes occurred between the two wildfires. In addition, although our work exploited open-source data, which can be used to replicate and standardize the procedure in different post-disturbance contexts, much attention has been paid to their spatial resolution to consider the most

appropriate scale for the results. Sediment connectivity outcomes can cause serious misinterpretations if there is an imbalance between the scale of data and objectives. According to Cantreul et al. (2018), 1 m is the best resolution for the IC application in a crop-managed watershed of 1.24 km^2, while López-Vicente and Álvarez (2018) suggested a 0.20 m resolution to study soil displacement in a 0.274 km^2 area. Different resolutions have been chosen in other contexts. It is our opinion that the choice of the spatial resolution has to consider the objectives of the sediment connectivity analysis and, turning this concept over, the available spatial resolution poses a limit to geomorphometric analysis that could be carried out. High-resolution DEMs are fundamental to investigate fine-scale processes (Cantreul et al., 2018; López-Vicente and Álvarez, 2018; Tarolli et al., 2019) and allows to derive important parameters as local surface roughness to characterize sediment dynamics at these scales. Different and simplified approaches can be devised when only coarse DEMs are available and the aim of the study is focused on large scale processes as coarse material sediment transport in large catchments. Accordingly, we found that a Global DEM at 12.5 m resolutions suitable for detecting major spatial patterns of IC in an Andean catchment. The proposed workflow could be effectively applied to investigate post-disturbance scenarios in other areas where high-resolution data are not available.

Conclusions

The interaction between wildfire severity and sediment connectivity has been presented in order to map the ecological and geomorphological effects of multiple wildfires on the Rio Toro catchment (Chile). The proposed method combines field data and open source satellite imagery to identify the spatial patterns of sediment connectivity variations driven by two subsequent wildfires. In the study catchment, the wildfire severity assessment pointed out the different severity patterns between the two events. The 2002 wildfire affected the 90% of the catchment, of which almost 70% was classified as high severity, while the 2015 wildfire significantly affected the 76%, of which only the 23% was classified as high severity. These results are mainly ascribed to the different fuel's availability and land cover heterogeneity between the two pre-fire scenarios. The sediment connectivity maps showed large areas of high IC increase located at the headwaters, after the first wildfire, and in the central part of the catchment after the second wildfire. The IC values varied according to the difference in fire severity: catchment's average increase of 1.07 after the first wildfire, 0.53 after the second one. However, the response of IC to fire severity was less evident in the first event, being the overlap between fire severity and DoIC spatial patterns levelled off by the vastity of high severity areas.

Therefore, the relationship between wildfire severity and sediment connectivity was weaker when the severity classification approached saturation.

The methodology proposed represents a good compromise between the reliability of the results and the limited availability of high-resolution data in inaccessible areas. The integration between geomorphometric analysis based on open-source satellite products and field work can definitely promote sediment connectivity spatial patterns characterization and the study of its relationship with wildfire severity, although more efforts can be made to improve the classification accuracy. In addition, the computation of a normalized W factor helped to better capture the main effects of the wildfires on the IC thanks to appropriate land cover change detection indices.

Finally, we suggest that further research in this field may consider also the integration of soil and ashes properties in the analysis, which be source of significant alterations of the sediment impedance, as well as the use of multiple topographic surveys if available.

Chapter 2.

Chapter 2 consists in a single study case carried out in an Alpine catchment, where the response to a large disturbance is analysed in all its main components. Two characters are introduced in this chapter, the Rio Cordon catchment and the Vaia storm, which will be again considered in chapter 4. The Rio Cordon catchment is well documented in literature, due to its long-lasting monitoring programme carried out for more than 30 years that permitted the measure of water and sediment fluxes. The Vaia storm instead, was a disturbance that deeply affected the North-East of Italy in late October 2018, causing massive forest windthrows and exceptional flood events in mountain streams. In this context, a deep and holistic analysis of the response of a mountain catchment to a large natural disturbance was found suitable, also considering its potential relevance for communities of the territory. Analysing the hydrological, geomorphic and sedimentological responses of the Rio Cordon represented a rare opportunity to study the whole sediment cascade of a mountain basin.

Sediment connectivity represented a key aspect underlying the chain of events documented in the study. Particularly, the analysis of sediment connectivity was developed to understand the role of sediment sources during the event. The analysis was carried out using a combination of the IC and Dem of Difference (DoD) technique in order to discriminate which sediment source acted as sediment supplier during the event and to estimate the volume of sediment supplied. In this way, it was also possible to support the outcomes concerning the sedimentological response.

Therefore, in chapter 2 the IC represented a supportive tool for a wider study instead of the core of the research. Nevertheless, the use of the index was not limited to its straightforward application but it was integrated in a methodological workflow involving a quantitative measure of the sediment mobilized. In this way, it is possible to contribute to a more quantitative approach by addressing the functional component of sediment connectivity.

Hydrological, geomorphic and sedimentological responses of an alpine basin to a severe weather event (Vaia storm)

Adapted from Rainato R., Martini L., Pellegrini G., Picco L. (2021).
Hydrological, geomorphic and sedimentological responses of an alpine basin to a severe weather event (Vaia storm).
Catena, 207, 105600. https://doi.org/10.1016/j.catena.2021.105600

Contributions by the PhD candidate: Methodology and data curation (geomorphic response parts), investigation and writing the original draft (all parts).

Abstract

To achieve a reliable analysis of the impacts induced in mountain basins by large and infrequent floods, all their main components, from the spatial-temporal distribution of meteorological agents to the hydrological, geomorphic and sedimentological response should be considered. Comprehensive study of the hydro-geomorphic responses is extremely valuable to increase the awareness of large floods, especially, in highly populated mountain areas. Such type of investigation requires a solid and wide dataset, which is why only few studies had the chance to describe the response in such a holistic way. This work comprehensively analyzed the high magnitude/low frequency Vaia event, a severe storm that affected northeastern Italy in October 2018 and thus the Rio Cordon study basin. The 80 h precipitation registered in the basin showed a total rainfall equal to 29.8% of the mean annual precipitation. The temporal distribution of rainfall presented two phases, i.e., a first characterized by moderate but persistent precipitation and a second more intense, exhibiting recurrence intervals over 50 years. A combination of indirect methods permitted the reconstruction of the hydraulic forcing acted in the Rio Cordon. Despite the implicit uncertainty, these methods clearly highlighted the high magnitude expressed by October 2018 flood, which generated a unit peak discharge equal to 3.3 $m^3 s^{-1} km^{-2}$ and a peak of unit stream power of 3865 W m^{-2}, i.e., the highest hydraulic forcing conditions ever observed in 34 years. In terms of geomorphic changes, the use of pre- and post-event LiDAR data stressed out a moderate response of the hillslopes, where the (re)activation of the sediment sources was limited. Only few of these acted as sediment supplier to the main channel. The channel network instead, exhibited an evident response, with the Rio Cordon severely altered by wide lateral widening, deep streambed incision and armouring removal. The hydraulic and geomorphic forcing generated by October 2018 flood caused extensive streambed remobilization and boulder

mobility that, in turn, induced the transport of a massive sediment volume. In this sense, the match between bedload observed and bedload predicted suggested the outstanding hydraulic forcing occurred and the quasi-unlimited supply conditions acted during the flood. The long-lasting monitoring program maintained in the Rio Cordon basin provided the rare opportunity to compare two high magnitude/low frequency floods and their induced effects. The September 1994 and October 2018 events were caused by different rainfall conditions, which resulted in different hydrological- and, especially, geomorphic- and sedimentological-responses. Particularly, the October 2018 flood induced an unprecedented alteration on the fluvial system, the effects of which could persist over the long-term.

Keywords: Vaia storm; Mountain basin; Large flood; Geomorphic changes; Sediment transport; Boulder mobility.

Introduction

Large and infrequent floods are hydrological events characterized by high magnitude and low frequency occurrence, which can impact mountain basins and their fluvial systems over large temporal and spatial scales. In alpine environments, these flood events can be induced by intense summer thunderstorms (Shakti et al., 2017), prolonged rainfalls (Brogan et al., 2019), rapid snowmelt (Friele et al., 2020), rain-on-snow event (Pomeroy et al., 2016) and sudden water release from glacier sources (Bohorquez and Darby, 2008). All these triggering factors converge in a main effect that is the generation of massive runoff characterized by high water discharges and stream power peaks. An extensive literature found these conditions associated to flash floods, i.e., rapid and severe floods (McEwen and Werritty, 1988, Batalla et al., 1999, Borga et al., 2014, Marchi et al., 2016, Lucía et al., 2018), whereas they were observed less frequently in large floods of long duration (Cassandro et al., 2002, Sholtes et al., 2018, Bucała-Hrabia et al., 2020). The characterization of the hydraulic forcing conditions expressed by high magnitude/low frequency events can be challenging, with the frequent need to rely on indirect methods as post-flood measurements, dendrogeomorphic analysis, paleoflood estimation and hydraulic modelling in order to reconstruct hydrographs and peak discharges (Rico et al., 2001, Stoffel and Bollschweiler, 2008, Victoriano et al., 2018, Wyzga et al., 2020). In this sense, a delineation of large and infrequent events based on peak of water discharge or unit peak discharge appears not fully defined, with values

spanning over several orders of magnitude (Marchi et al., 2016, Amponsah et al., 2018), while a minimum threshold of 300 $W\ m^{-2}$ was reported in terms of unit stream power (Miller, 1990, Magilligan, 1992). However, it is worth noting that this threshold was based on geomorphic effectiveness of floods and that mountain basins responses are highly variable. Indeed, the geomorphic response to a high magnitude/low frequency flood can include: (i) the formation of rockfalls (Heckmann and Schwanghart, 2013), debris flows (Pastorello et al., 2020) and landslides (Korup, 2005) along the hillslopes; (ii) bedforms alteration (Lenzi, 2001), channel narrowing (Liébault and Piégay, 2002), chute cutting and channel migration (Gorczyca et al., 2013), reach straightening (Bauch and Hickin, 2011), lateral widening with floodplain erosion (Wicherski et al., 2017) or increase in channel bars extent (Hajdukiewicz et al., 2016) along the fluvial system. The investigation of these geomorphic changes is traditionally accomplished by multi-temporal geomorphological mapping, using both field and remote sensing products, such Digital Elevation Models (DEMs) and aerial photos (Messenzehl et al., 2014, Carrivick et al., 2016, Vericat et al., 2017). Additionally, geomorphic variations in mountain streams are quantified using the widely known DEM of Difference (hereinafter DoD) technique, which can be also used to infer in-channel sediment transfer's efficiency (Lane et al., 2003, Vericat et al., 2014, Cucchiaro et al., 2019, Calle et al., 2020). In mountain basins, the hydraulic forcing and geomorphic changes generated by high magnitude/low frequency floods can intensify the ordinary sediment transfer processes, altering the sediment cascade from source areas to the fluvial system (Brierley et al., 2006, Burt and Allison, 2010, Fryirs, 2013). However, during and after a large infrequent event, the capability of a catchment to promote or impede the sediment cascade depends on the impact of such event on the degree of (dis)connectivity. Specifically, highly connected catchments react transmitting a sediment pulse throughout the system, whereas in disconnected catchments the pulse is stopped by landform impediments (Fryirs et al., 2007). Along the fluvial system, the sediment dynamics promoted by high magnitude/low frequency floods can stretch over various time scales. Typical effects induced at event scale are streambed remobilization (Piton and Recking, 2017), boulder mobility (Turowski et al., 2009, Gob et al., 2010), high transport rates (D'Agostino and Lenzi, 1999, Pagano et al., 2019) and massive transported volumes (Rickenmann, 1997, Baewert and Morche, 2014). Nonetheless, the induced effects can also act on longer time scales, augmenting the transport rate of subsequent floods and favoring a memory effect on the sediment dynamics (Rainato et al., 2017, Uchida et al., 2018, Rickenmann, 2020, Korup, 2005).

High magnitude/low frequency floods caused by severe weather events were poorly investigated and rarely analyzed from the rainfall-runoff conditions to geomorphic and sedimentological effects.

A recent example of severe weather event was the Vaia storm, which affected the Northeast Italy on October 27–30, 2018. This storm generated extremely high wind gusts, storm surges and heavy precipitation that caused landslides, floods, interruption of electric supply, road traffic disruption and the worst forest loss ever documented in Italy, consisting of about 8.5 million m^3 of growing stock felled over 41,000 ha (Biolchi et al., 2019, Cavaleri et al., 2019). This work aims at defining the responses of an alpine basin to the Vaia storm, focusing on: (i) the determination of rainfall and hydraulic forcing conditions, (ii) the analysis of the geomorphic and sedimentological responses showed by hillslopes and main channel, (iii) the comparison of these responses with those exhibited by the alpine basin over the last three decades.

Material and methods

Study area

Study basin

The Rio Cordon basin (Fig. 2.1) is a mountain basin extending for 5 km^2 in the eastern Italian Alps (Dolomites). It is characterized by typical alpine climatic conditions with a mean annual precipitation of 1180 mm (1986–2018). The runoff regime can be defined as nivo-pluvial due to the predominance of snowfalls between November-April, while short rain showers and persistent precipitations prevail in summer and autumn, respectively. The basin is part of the Southern Limestone Alps with the geological substrate mainly composed by dolomites, limestones, volcanic conglomerates (Wengen group) and calcareous-marly rocks (Buchenstein group). A rugged topography can be appreciated throughout the basin, which exhibits an average slope of 27°. Due to the basin elevation between 1763 and 2763 m a.s.l., spruce and larch forest covers merely 7% of catchment area, while bare rock (14%), shrubs (18%) and grassland (61%) are more widespread. In the basin, the third-order Rio Cordon stream flows on a rough channel bed, featuring boulder-cascade and step-pool morphologies (*sensu* Montgomery and Buffington, 1997). In 2014, the surface streambed material resulted poorly sorted with $D_{16}/D_{50}/D_{84}/D_{90}$ of grain size distribution (GSD) equal to 29/114/358/455 mm, respectively, and a well-developed armour layer (Rainato et al., 2018a). The main channel (hereinafter Rio Cordon) had an average slope of 17% with a mean bankfull width equal to 5.3 m and a bankfull discharge (Q_{Bf}) = 2.30 $m^3\ s^{-1}$ (Lenzi et al., 2006a, Mao and Lenzi, 2007). Along the basin, the Rio Cordon is interrupted by a waterfall, which represents a topographic knickpoint that conventionally divides the whole basin into the upper part (upper plateau) and lower part (Rainato et al., 2018b). In 2016, 420 sediment source areas were detected throughout the basin, classified in

debris flow channel/deposit, erosional area, stream bank erosion, landslide, rockfall deposit and active talus (Ferrato et al., 2017). From the sources, the sediment can be transported downstream and eventually deposited at the outlet (1763 m a.s.l.), where a permanent monitoring station is built.

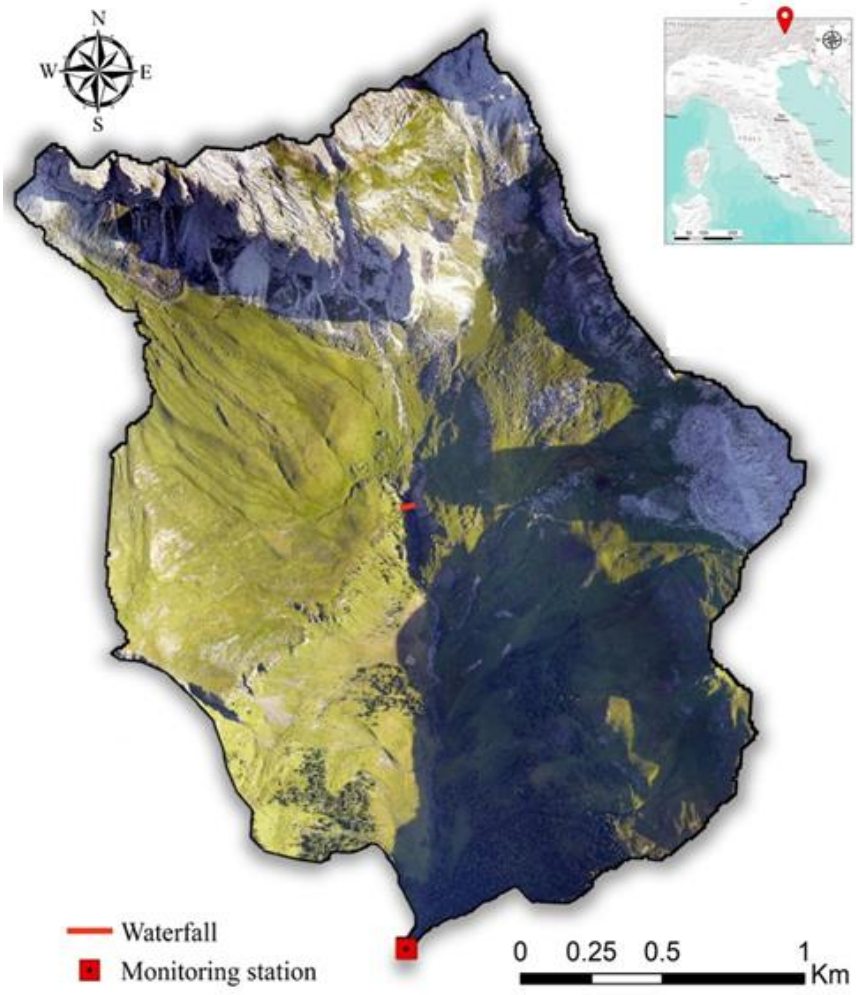

Figure 2.1. The Rio Cordon basin, located in the eastern Italian Alps. The waterfall represents the topographic knickpoint that divides the upper part (upper plateau) and lower part of the basin.

Long-lasting monitoring program

In 1985, the Rio Cordon basin was instrumented thanks to a collaboration between University of Padova and Veneto Region, and operating since 1986 under the ARPA Veneto management (Regional Department for Land Safety). Specifically, a permanent monitoring station was set up at the basin outlet with the aim of continuously monitor water discharge (*Q*), suspended sediment load (*SSL*) and bedload (*BL*). In 1994, the monitoring station was provided with a meteorological station, which measure continuously air temperature, wind speed and precipitations through a heated rain gauge. Between September 1986 and September 2018, the monitoring station recorded 33 flood events (Supplementary S1). Overall, these events mobilized 1850 m^3 of coarse material, corresponding to a bedload yield of 3154 t. Considering instead the total sediment yield (*BL* + *SSL*), the Rio Cordon basin delivered ~15125 t. Among the 33 events recorded, the highest magnitude was expressed by the September 1994 flood, when an intense summer shower triggered a flash flood with a peak of water discharge (Q_P) equal to 10.40 $m^3\ s^{-1}$ (Rainato et al., 2017). This event altered the basin by modifying the streambed configuration, creating new sediment sources throughout the catchment and causing the transport of about 900 m^3 of coarse material, which corresponds to ~50% of the total bedload volume observed between September 1986 and September 2018.

Rainfalls

Consistently to the previous flood event investigations realized in the Rio Cordon basin (Lenzi and Marchi, 2000, Rainato et al., 2018a, Oss Cazzador et al., 2020), to describe the rainfalls induced by the Vaia storm the data from the heated rain gauge were used. This sensor measures every 5 min with an accuracy of 0.2 mm, permitting to determine the total precipitation and the rainfall intensities exhibited by the storm event. Specifically, the maximum rainfall intensities in 5, 15, 30 min and 1, 3, 6, 12, 24, 48, 72 h were determined and named, I_{5min}, I_{15min}, I_{30min} and I_{1h}, I_{3h}, I_{6h}, I_{12h}, I_{24h}, I_{48h}, I_{72h}, respectively. To better comprehend the magnitude expressed by Vaia storm in the Rio Cordon basin, the measured rainfall intensities were compared to the rainfall depth-duration-frequency (DDF) curves compiled by ARPA Veneto for the "Passo Falzarego" meteorological station. This was chosen as the nearest rain gauge with a long-lasting monitoring. In fact, it is located 9.4 km north-west of the Rio Cordon basin, at 2040 m a.s.l., and operates since 1985.

Hydrological conditions

The wind and rainfall generated by the Vaia storm caused the arrest of the water level gauges installed in the Rio Cordon monitoring station. Therefore, no discharge measurement was realized during the Vaia induced flood event (hereinafter October 2018 event). In light of this, to describe the hydraulic forcing conditions that acted in the Rio Cordon, indirect methods were used. To reconstruct the , the nearest gauging station operating during the Vaia storm was tested. This was the "Sottorovei" Arpa Veneto gauging station (5.2 km south-west of the Rio Cordon basin), which recorded the discharge of the Fiorentina Stream (Q_{Fi}). Worth noting is that the Rio Cordon is a sub-basin of the Fiorentina basin (58 km^2). To test the capacity of Fiorentina discharge (Q_{Fi}) to describe the Rio Cordon discharge (Q_{Rc}), two recent floods (November 2012 and November 2014) recorded in the sub-basin were isolated and the measured Q_{Rc} were compared to the Q_{Fi} simultaneously recorded. Using linear regression and comparing 1762 discharge measurements, it was possible to observe that Q_{Fi} and Q_{Rc} were statistically correlated ($R^2 = 0.897$, p-value < 0.01). Therefore, the Q_{Fi} measured during the Vaia storm were scaled according to the linear equation obtained, permitting to reconstruct the hydrograph of the October 2018 flood in the Rio Cordon. However, it should be stressed that this reconstruction was affected by a certain degree of uncertainty as based on the analysis of near-bankfull events. In fact, in terms of Q_P, the November 2012 and November 2014 floods ranged between 2.06 and 2.10 $m^3 s^{-1}$ in the Rio Cordon, while in the Fiorentina Stream spanned between 23.60 and 32.00 $m^3 s^{-1}$. Therefore, given the high magnitude expressed by October 2018 flood, a specific investigation about Q_P was made in order to integrate the hydrograph reconstructed with a portion devoted to describing the peaking part. The latter was intended as the hydrograph part simulated between the maximum discharges estimated by hydrograph reconstruction ($Q_{Fi} - Q_{Rc}$ relationship) and the Q_P estimated. A simple triangular shape was used to describe this peaking part, according to the hydrograph shapes generated in mountain basins by high magnitude/low frequency floods (Lenzi et al., 1999, Turowski et al., 2009).

The value of Q_P was calculated through two different approaches. Firstly, post-event surveys permitted to clearly identify high-water marks along a cross section located in the final straight reach of Rio Cordon and embanked on the right side, i.e., the best conditions for Q_P definition by the slope conveyance method (Gaume and Borga, 2008, Marchi et al., 2016). A differential Global Position System (dGPS) device, featuring an average vertical and horizontal accuracy <0.05 m, was used to survey this cross section, which was used to compute Q_P through the Manning-Strickler equation (Eq. (2.1)):

$$Q = \frac{A\,R^{\frac{2}{3}}\,S^{\frac{1}{2}}}{n} \quad (2.1)$$

in which Q is the water discharge ($m^3\ s^{-1}$), A the flow area (m^2), R the hydraulic radius (m), S the stream slope ($m\ m^{-1}$) and n the Manning roughness coefficient. Based on field observation of the boundary roughness conditions and on the n observed in mountain streams (Reid and Hickin, 2008, Zink and Jennings, 2014, Oss Cazzador et al., 2021) a Manning roughness coefficient = 0.125 $s^{-1}\ m^{-1/3}$ was applied.

Secondly, the equation (Eq. (2.2)) proposed by Bravard and Petit (1997) to determine Q_P through a basin area scaling ratio was used:

$$q = Q(a/A)^c \quad (2.2)$$

in which q is the water discharge occurred in a sub-basin (in $m^3\ s^{-1}$), Q the water discharge measured at the basin outlet (in $m^3\ s^{-1}$), a is the sub-basin area (in km^2), A the basin area (in km^2), while c is a site specific coefficient that in literature varies between 0.4 and 1.0 (Gob et al., 2010). The maximum Q_{Fi} recorded during the Vaia storm were used as Q, while c equal to 0.8 was applied according to Liébault et al., 2012, Oss Cazzador et al., 2021.

Once determined the hydrograph and its peaks, the bedload duration (T_{Bl}) and the effective runoff (ER) were estimated. These describe the hydrograph-duration and -volume exceeding the threshold for bedload motion. To this end, the critical discharge (Q_C) for motion of coarse streambed material observed in the Rio Cordon during the period 2012–2018 was used, which corresponds to Q_C = 2.06 $m^3\ s^{-1}$ (Rainato et al., 2020). This is consistent with the observations made in the Rio Cordon by Lenzi et al. (1999), who documented Q_C constantly around Q = 2.00 $m^3\ s^{-1}$ in the flood events of 1987–1994.

The hydraulic forcing conditions were expressed even in terms of unit stream power (ω), through Eq. (2.3):

$$\omega = \frac{\rho g Q S}{w} \quad (2.3)$$

where ρ is the fluid density ($kg\ m^{-3}$), g the acceleration due to gravity ($m\ s^{-2}$), Q the water discharge ($m^3\ s^{-1}$), S the stream slope ($m\ m^{-1}$) and w is the flow width (m). Specifically, to calculate the peak of unit stream power (ω_P) acted during the October 2018 flood, the flow width was determined by analyzing the Digital Terrain Model (DTM) of the Rio Cordon dated 2006 (see *remote sensing data* section), which suggested a w = 6.30 m.

Geomorphic setting

Remote sensing data

To investigate the geomorphic response induced in the Rio Cordon basin by the Vaia storm, two LiDAR surveys dated, respectively, 2006 and 2019 were exploited. Both surveys produced classified point clouds and orthophotos. The latter with resolution of 0.5 m and 0.2 m, for 2006 and 2019, respectively. From the point clouds, only the ground points were used to derive the DTMs for the following analyses. The post-processing was carried out using CloudCompare software (www.danielgm.net/cc; version 2.10.2 Zephyrus), with the primary aim of co-registering the point clouds. The co-registration was performed using a combination of automatic Iterative Closest Point (ICP) algorithm and manual definition of point correspondences. The compound use of these methods wants to provide a suitable solution to reduce unrealistic differences between the point clouds that often exist in rugged environments (Cucchiaro et al., 2020). The orthophotos were exploited for different purposes: from the qualitative assessment of the changes throughout the basin to the analysis of the variations along active channel and sediment source areas. However, due to the time interval between the two LiDAR surveys, other events might have contributed to alter the geomorphic setting of the catchment. To distinguish the alterations induced by these events from the October 2018 effects, an additional pre-event orthophoto and previous studies were used. Specifically, the 2015 orthophoto (Web Map Service service for AGEA, 0.20 m resolution) and the geomorphic effects documented in Rainato et al., 2017, Rainato et al., 2018a, Oss Cazzador et al., 2020 were taken advantage of. Instead, the two DTMs permitted to determine the topographic differences and, then, any significant geomorphic change related to the Vaia storm.

Geomorphic change detection

The topographic differences were determined by comparative analysis between the 2006 and 2019 DTMs, using the DEM of Difference, hereinafter DoD, technique. The old-2006 DTM was subtracted to the new-2019 DTM using the Geomorphic Change Detection 7.4.4, AddIn for ArcGIS (Wheaton et al., 2010). To overcome the mere representation of all the changes, hence to distinguish those changes produced by noise from the real ones, a widely used approach accounting for spatially distributed elevation uncertainty was adopted. Also, this approach overcomes spatially uniform methods, i.e. minimum level of detection (minLOD), in which real geomorphic changes risk to be removed. The methodology proposed by Wheaton et al. (2010) mainly regards three steps to generate a robust DoD output: (i) computation of cell-by-cell DEM uncertainty (spatial distribution of

elevation uncertainty) using the Fuzzy Inference System (FIS); (ii) propagation of the uncertainty into the DoD; (iii) statistical significance of the propagated uncertainty based on probabilistic thresholding. The first step was accomplished using a three inputs-FIS, i.e., point density, slope and roughness. Particularly, the roughness information was derived using the Roughness Index, proposed by Cavalli and Marchi (2008), and already applied in other geomorphological studies as part of the three inputs-FIS (Oss Cazzador et al., 2021). The second step regards the propagation of the uncertainty from the individual DEM into the DoD, still on cell by cell basis. This step was accomplished by applying the well-known combined error formula proposed by Brasington et al. (2000). The third step assessed the statistical significance of the DoD output using a 95% probabilistic thresholding, which means that all the elevation changes that do not fit within a confidence interval of 95% were discarded. The application of such probabilistic thresholding relies upon the choice of the corresponding *t*-value, as proposed by Taylor (1997) and then by Brasington et al., 2003, Lane et al., 2003. In this work, a conservative 95% confidence interval (*t*-value = 1.96) was assigned because of the high values of elevation uncertainty and the willingness to quantify the minimum compatible volume of sediment mobilized in the Rio Cordon basin. The DoD was performed to investigate sediment displacement occurred along the hillslope, within the lower Rio Cordon and at the bedload storage area of the monitoring station. Specifically, for the hillslopes, the aim was to outline potential new sediment sources that may or not have contributed to supply sediment in the channel network. At the bedload storage area, the DoD was performed over a polygon of 4200 m^2, which includes also the lateral and downstream zones buried by sediment. However, an area of ~500 m^2 was affected by the presence of a bridge that passes over the deposit. Here, no suitable LiDAR data were found so that the 2006 and 2019 DTMs have been roughly interpolated causing an estimated source of error of about 11%.

Sediment sources

The detection of the new sediment sources was accomplished through orthophotos and DoD interpretation with a focus to the lower part of the basin. In addition, a previous sediment source inventory (Ferrato et al., 2017), was used to help the detection of those areas (re)activated only during the Vaia storm. The sediment sources were then grouped according to the classification already proposed for the Rio Cordon basin in: landslide, debris flow channel/deposit, surficial erosion, stream bank erosion, rockfall and active talus. Knowing the coupling state of the sediment sources, it is possible to have an idea of the volume of sediment supplied to the channel network and eventually to

the outlet. To assess the coupling state and the potential supply from sources to active channel, an approach based on the Index of Connectivity (IC) (Cavalli et al., 2013) and the DoD was proposed. First, using the 2019 orthophoto, the sources that did not reach the active channel and, therefore, visibly decoupled were excluded. Then, the IC map was computed with SedInConnect 2.3 (Crema and Cavalli, 2018), using the pre-event (2006) DTM, selecting the active channel as target. The mean IC value for each sediment source was extracted and only those having a value higher than a threshold were considered. The threshold was set as the median (50th percentile) of all the mean IC values of each area. In other terms, a boundary based on the central value was set, to distinguish areas of high- and low-IC. Finally, the sediment sources showing predominant erosion (negative net volume difference) were selected. In this way, we assumed that only the sediment sources highly coupled with the active channel supplied a significant volume of sediment. Conversely, the decoupled or balanced (erosion and deposition balanced) sediment sources were not considered suppliers. In particular cases, e.g. landslides recharging debris flow channels/deposits, the balance was obtained as the overall DoD result of the single areas composing the same potential supplier.

Active channel

The active channel variations were first investigated through qualitative analysis of orthophotos. To further investigate the geomorphic changes as well as its causes and effects along the Rio Cordon, the active channel was segmented into sub-reaches. The segmentation, which draws part of the criteria from Rinaldi et al. (2013), considered homogeneous sub-reaches based on stream slope, channel width and confluences with tributaries. Stream slope was derived from the 2006 DTM, while channel width and confluences from the orthophotos. Hence, six sub-reaches (1–6) ranging from 154 m to 623 m in length were identified in the lower basin, resulting in 2023 m totally investigated along the active channel. Upper Rio Cordon was excluded from this analysis due to its semi-colluvial nature and sediment disconnectivity documented during Vaia storm (Oss Cazzador et al., 2021). The width ratio (*Wr*), the peak of unit stream power (ω_{Pi}) acted during the October 2018 event and the DoD segregation (Wheaton et al., 2013) were calculated for each sub-reach. *Wr* is intended as the ratio between the post- and pre-flood average channel width (Scorpio et al., 2018), which were assessed on the 2019 and 2006 orthophotos, respectively. The peak of unit stream power occurred in the sub-reaches ($\omega_{P1} - \omega_{P6}$) was determined according to Eq. (2.3). To this end, each *S* and *w* were calculated analyzing the 2006 DTM and considering the stream slope and the channel width averaged on the upstream channel portion. Instead, the maximum water discharge flowed in each sub-reach

(i.e. Q in Eq. (2.3)) was determined using the Eq. (2.2), with Q equal to the Q_P calculated for the Rio Cordon outlet (see *hydrological conditions* section), while a and A were the basin area subtended by the sub-reach and the whole basin, respectively. Finally, the potential correlations between Wr, ω_{Pi} and DoD were investigated through linear regression.

Sedimentological setting

The sedimentological response of the study basin to the Vaia storm was explored by investigating the variation in the grain size distribution of the main channel and by characterizing and quantifying the coarse material transported. To determine the post-flood GSD of the Rio Cordon, 202 particles were collected and measured along the main channel using the grid by number method. The same method was used to describe the GSD of bedload transported to the monitoring station, which was estimated by sampling 224 particles. Also, the ten largest boulders deposited at the bedload storage area were characterized in terms of *a*-, *b*- and *c*-axis in order to describe the boulder mobility triggered by the October 2018 flood. To determine the volume of coarse material mobilized by the event (BL_{Obs}), the bedload storage area of the monitoring station was surveyed. Therefore, using the DoD technique (see *geomorphic change detection* section) it was possible to quantify a reliable volume resulting from the elevation difference between the post-event storage unit (2019 DTM) and the pre-event one (2006 DTM). The reconstruction of hydraulic forcing conditions occurred during the October 2018 event enabled the volume of coarse material transported to be predicted (BL_{Pred}) as well. To this end, consistently with previous Rio Cordon flood investigations (D'Agostino and Lenzi, 1999, Lenzi et al., 1999, Lenzi et al., 2006b, Rainato et al., 2017), the bedload equation (Eq. (2.4)) proposed by Schoklitsch (1962) was used:

$$Q_S = \frac{2.5}{\rho_s/\rho} S^{\frac{3}{2}} (Q - Qc) \quad (2.4)$$

where Q_S is the bedload rate ($m^3\ s^{-1}$) and ρ_s is the sediment density ($kg\ m^{-3}$), respectively. The use of Schoklitsch equation permitted to calculate BL_{Pred} but also to analyze its performance under the different hydrological conditions examined in the Rio Cordon over the last decades.

Results

Rainfall characterization

In the Rio Cordon basin, the Vaia storm induced a rainfall event that lasted about 80 h, starting on October 27th at 06:55 (CET) and ending on October 30th at 14:45 (Table 1). During this time interval, a total precipitation of 352.0 mm was recorded, corresponding to the 29.8% of the mean annual precipitation. The rainfall event was not continuous but exhibited a hiatus of ~9 h (Fig. 2.2). Therefore, it is possible to identify a first and a second phase, hereinafter Phase 1 and Phase 2. The Phase 1 lasted 36.8 h with 199.8 mm, while 152.0 mm were recorded in the 34.2 h of Phase 2. The event registered a mean rainfall intensity equal to 4.4 mm h^{-1}, while Phase 1 and Phase 2 expressed an average of 5.4 and 4.4 mm h^{-1}, respectively (Table 2.1). Phase 1 showed a higher mean intensity due to the more continuous precipitation over time compared to Phase 2 that exhibited an abrupt decrease after peaking (Fig. 2.2). However, the highest intensities between I_{5min} and I_{12h} were constantly observed during Phase 2, particularly, between 8:30 and 21:30 of October 29th. In this sense, the maximum rainfall intensities recorded ($I_{5min} - I_{72h}$) were compared to the DDF curves of the "Passo Falzarego" meteorological station. Fig. 2.2b and 2.2c show that I_{5min}, I_{15min} and I_{30min} resulted lower than DDF curve estimated for recurrence interval (*RI*) of 2 years, while from I_{1h} progressively exceeded the DDF curves by culminating in $I_{6h} - I_{72h}$ that showed *RI* clearly higher than 50 years.

Table 2.1. Main characteristics of the first and second phase of the rainfall event recorded by the Rio Cordon rain gauge during the Vaia storm, as well as of the entire rainfall event. I_{5min}, I_{15min}, I_{30min} describe the maximum rainfall intensities measured in 5, 15 and 30 minutes, respectively. I_{1h}, I_{3h}, I_{6h}, I_{12h}, I_{24h}, I_{48h} and I_{72h} are the maximum intensities recorded, respectively, in 1, 3, 6, 12, 24, 48 and 72 hours.

	Phase 1	Phase 2	Event
Time of rainfall initiation (CET)	27/10/2018 06:55	29/10/2018 04:30	27/10/2018 06:55
Time of rainfall end (CET)	28/10/2018 19:45	30/10/2018 14:45	30/10/2018 14:45
Total precipitation duration (h)	36.8	34.2	79.8
Total precipitation (mm)	199.8	152.0	352.0
Mean rainfall intensity (mm h^{-1})	5.4	4.4	4.4
Time of I_{5min} (CET)	28/10/2018 07:15	29/10/2018 19:05	29/10/2018 19:05
I_{5min} (mm/5 min)	2.2	4.2	4.2
I_{15min} (mm/15 min)	5.6	7.0	7.0
I_{30min} (mm/30 min)	9.2	12.4	12.4
I_{1h} (mm/1 h)	14.6	20.4	20.4
I_{3h} (mm/3 h)	34.8	42.0	42.0
I_{6h} (mm/6 h)	74.4	85.2	85.2
I_{12h} (mm/12 h)	111.2	111.8	111.8
I_{24h} (mm/24 h)	176.6	142.8	176.6
I_{48h} (mm/48 h)	-	-	295.0
I_{72h} (mm/72 h)	-	-	343.2

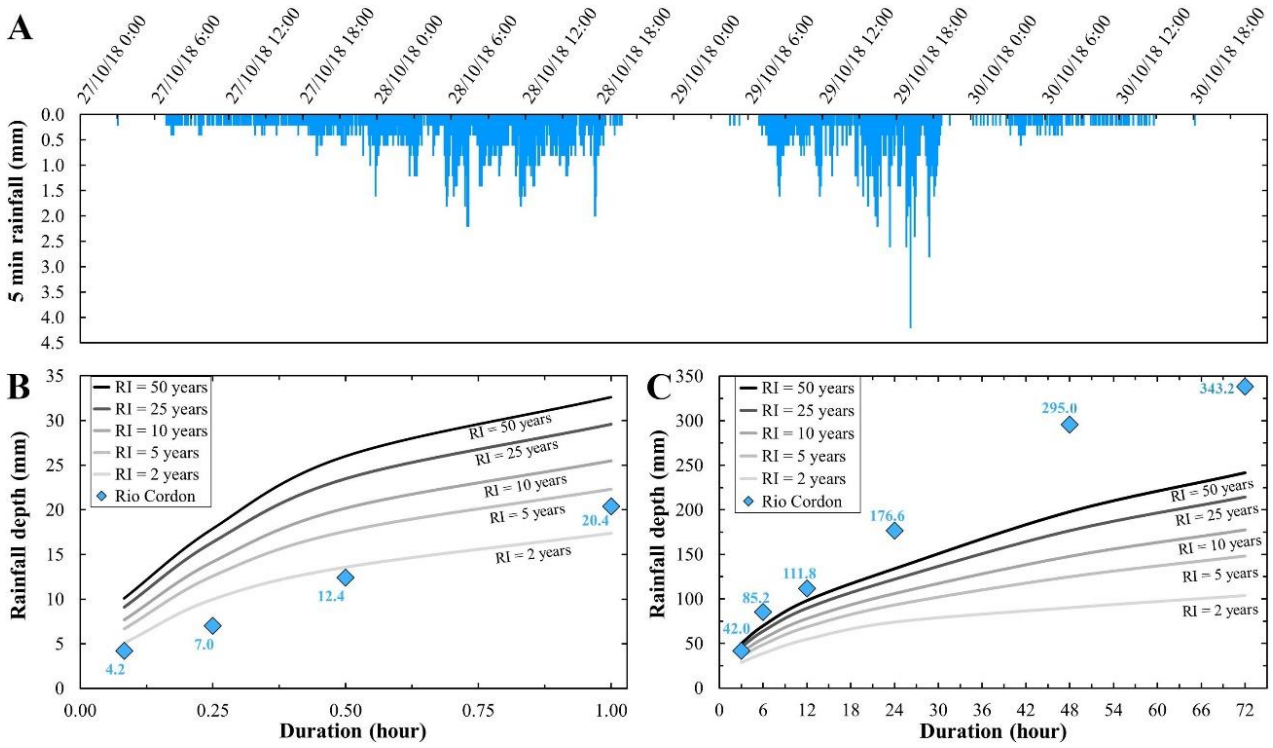

Figure 2.2. (A) Rainfall recorded by Rio Cordon meteorological station during Vaia storm; (B) Maximum rainfall intensities recorded in 5 (I_{5min}), 15 (I_{15min}), 30 (I_{30min}), 60 (I_{1h}) minutes and (C) in 3 (I_{3h}), 6 (I_{6h}), 12 (I_{12h}), 24 (I_{24h}), 48 (I_{48h}) and 72 (I_{72h}) hours compared to the rainfall depth-duration-frequency curves of Passo Falzarego rain guage.

Hydraulic forcing conditions

The reconstructed hydrograph suggested Q_P for the Phase 1 and Phase 2 equal to 2.31 $m^3 s^{-1}$ and 8.24 $m^3 s^{-1}$, respectively. Interestingly, the maximum discharge exhibited a delay respect to the maximum I_{5min} of 55 min (Table 2.2). The high-water marks detected in the post-flood surveys enabled to calculate, via Eq. (2.1), a maximum peak flowed = 17.50 $m^3 s^{-1}$. Such peak was related to the maximum discharge occurred, i.e., Q_P of Phase 2. No field evidences permitted to determine the Q_P of Phase 1. For both phases, the peak of water discharge was estimated through the basin area scaling ratio (Eq. (2.2)) applied to the maximum Q recorded in the Fiorentina Stream. Thus, the Q_P estimated were 3.43 $m^3 s^{-1}$ and 15.21 $m^3 s^{-1}$ for Phase 1 and Phase 2, respectively (Table 2.2). These peaks resulted roughly consistent to those estimated for the Phase 1 by the hydrograph reconstruction (lower by a factor of 0.67) and for the Phase 2 by the post-flood surveys (higher by a factor of 1.15). Therefore, considering the uncertainty and limits associated to each method used, the average between Q_P estimated by hydrograph reconstruction (2.31 $m^3 s^{-1}$) and the one determined by basin area scaling ratio (3.43 $m^3 s^{-1}$) was considered representative in describing the water discharge

peak of Phase 1. About Phase 2, the average between Q_P obtained by post-flood surveys (17.50 $m^3 s^{-1}$) and the one resulted by application of basin area scaling ratio (15.21 $m^3 s^{-1}$) was considered. Hence, Phase 1 and Phase 2 expressed Q_P = 2.87 (±0.56) $m^3 s^{-1}$ and Q_P = 16.36 (±1.14) $m^3 s^{-1}$, respectively (Fig. 2.3).

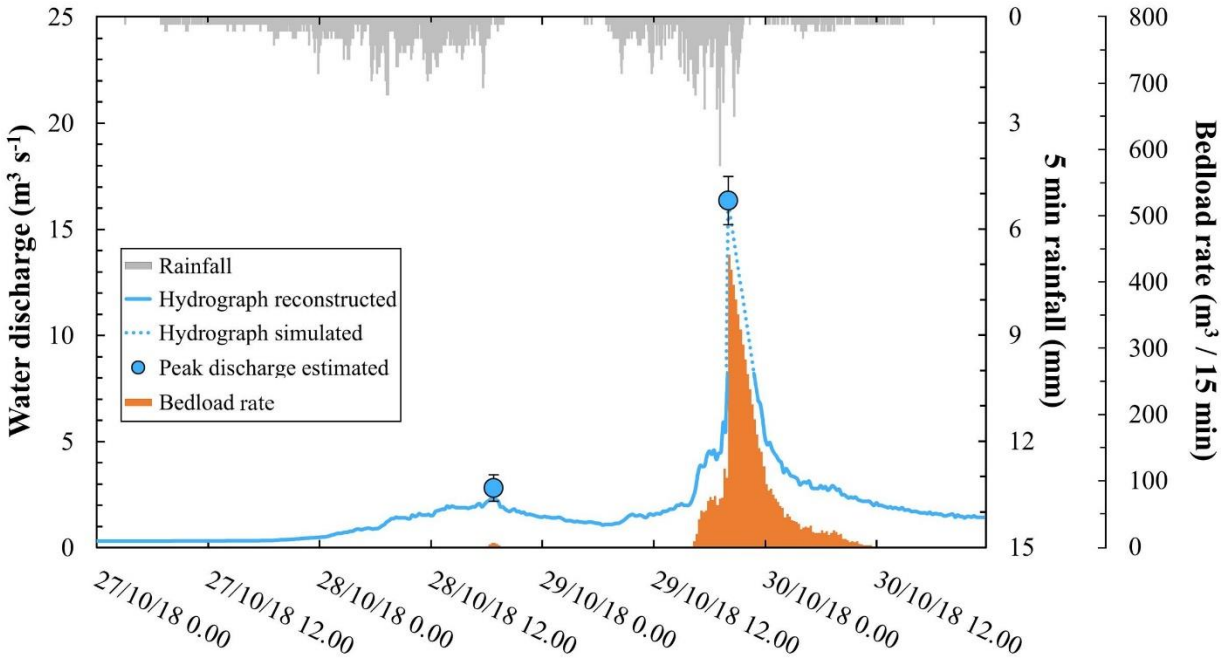

Figure 2.3. Rainfall, water and bedload discharges estimated for the October 2018 event. The blue line represents the hydrograph reconstructed starting from the Fiorentina discharge measurements; the blue dotted line are the parts of hydrograph simulated between the maximum values estimated by discharge reconstruction ($Q_{Fi} - Q_{Rc}$ relationship) and the peaks discharge estimated for the first and second phase of flood event. The peaks discharge are represented by the blue circles, the error bars are the lower and upper bounds of the Q_P considered. The orange lines express the bedload rate calculated by the Schoklitsch (1962) equation.

Table 2.2. Main characteristics of first and second phase of the flood event induced in the Rio Cordon by Vaia storm, and of the entire flood. Q_{Bf} indicates the Rio Cordon bankfull discharge (i.e., 2.30 m^3 s^{-1}), while Q_{2Bf} and Q_{3Bf} represent discharges, respectively, two and three fold larger. T_{Bl} is the estimated bedload duration, while ER is effective runoff. BL_{Pred} and BL_{Obs} describe the bedload volume calculated by applying the Schoklitsch (1962) equation and by DoD analysis, respectively.

	Phase 1	Phase 2	Event
Duration of $Q > Q_{Bf}$ (h)	0.50	17.75	18.25
Duration of $Q > Q_{2Bf}$ (h)	-	5.75	5.75
Duration of $Q > Q_{3Bf}$ (h)	-	3.50	3.50
T_{Bl} (h)	1.75	20.25	22.00
ER (10^3 m^3)	1.0	200.0	201.0
Time of Q_P (CET)	28/10/2018 18:45	29/10/2018 20:00	29/10/2018 20:00
Q_P (hydrograph reconstructed[a]; m^3 s^{-1})	2.31	8.24	8.24
Q_P (post-flood survey; m^3 s^{-1})	-	17.50	17.50
Q_P (basin area scaling ratio[b]; m^3 s^{-1})	3.43	15.21	15.21
BL_{Pred} (m^3)	32	6858	6890
BL_{Obs} (m^3)	-	6656	6656

In terms of unit stream power, these peaks corresponded to 678 W m^{-2} and 3865 W m^{-2}. The resulted hydrograph shows a Phase 1 characterized by a lower magnitude compared to Phase 2. In terms of flow duration, in Phase 1 about 0.50 h with $Q > Q_{Bf}$ and 1.75 h of bedload duration (T_{Bl}) were assessed. Such conditions led to an effective runoff (ER) equal to 1.0×10^3 m^3 (Table 2.2). Phase 2 exhibited a clear higher magnitude: over-bankfull discharge for ~18 h was observed and Q two- and three-fold higher than Q_{Bf} were noted for 5.75 h and 3.50 h, respectively. In Phase 2, $ER = 200 \times 10^3$ m^3 and T_{Bl} equal to 20.25 h were estimated, leading the total bedload duration for the October 2018 flood to 22 h (Table 2.2). Overall, the October 2018 flood expressed the largest Q_P (16.36 m^3 s^{-1}) and ER (201×10^3 m^3) ever documented in the Rio Cordon basin, with a unit peak discharge equal to 3.3 m^3 s^{-1} km^{-2}.

Geomorphic effects

Sediment source areas and sediment connectivity

The detection of the sediment sources led to the mapping of 9 newly formed instabilities and 17 source areas reactivated or enlarged during the October 2018 flood (Fig. 2.4A). The new sediment sources were exclusively located in the lower part of the Rio Cordon basin, covering a total area of 31,179 m^2, with a minimum extent of 49 m^2 and a maximum of 4927 m^2. According to the sediment sources' classification used in the Rio Cordon basin, 5 sources were classified as debris flow channels/deposits, 20 as landslides and 1 as stream bank erosion.

The sediment connectivity analysis pointed out the presence of 6 sources coupled to the channel network and potentially sediment suppliers (Fig. 2.4A). Conversely, 20 sources were classified as non-supplier, either because decoupled to the active channel or because they did not show net erosion. This result agrees with the historic knowledge of the basin and with post-event observations. The estimated volume of sediment eroded from the 6 coupled sources was 1219 m^3, mostly conveyed by the landslides-debris flow system located close to the outlet (Fig. 2.4A). This volume was reduced, subtracting the bedload yields expressed by November 2012 and June 2014 events (Supplementary S2.1) to avoid double counting, thus obtaining a potential volume supplied during the October 2018 flood of 1140 m^3.

Active channel

Between pre- and post-event conditions, over the 2023 m analyzed, the active channel widened from an average width of 6.30 m to 10.60 m, expanding from 8607 m^2 to 38696 m^2. Considering the geomorphic change detection, the DoD analysis computed a total net erosion of 6979 $m^3 \pm 2059$ m^3 unevenly distributed along the reach (Fig. 2.4A). The average depth of surface lowering (erosion) was 1.06 m, while the average depth of surface raising (deposition) was 0.63 m. Many of the deeper erosional areas were located along the banks (Fig. 2.4B). Notably, the deepest erosion of 4.70 m was located in the downstream part of the basin, along banks affected also by windthrows. Conversely, the depositional areas were predominantly located in the middle of the stream and the highest deposit was 3.10 m. The DoD segregation pointed out that all the sub-reaches were eroded and the downstream sub-reach has the highest average net thickness of difference with -0.45 m (Table 2.3). Therefore, sub-reach 6 presented the highest averaged rate of erosion (averaged to the area of the sub-reach), followed by sub-reaches 3, 4 and 1 with remarkable erosion rates.

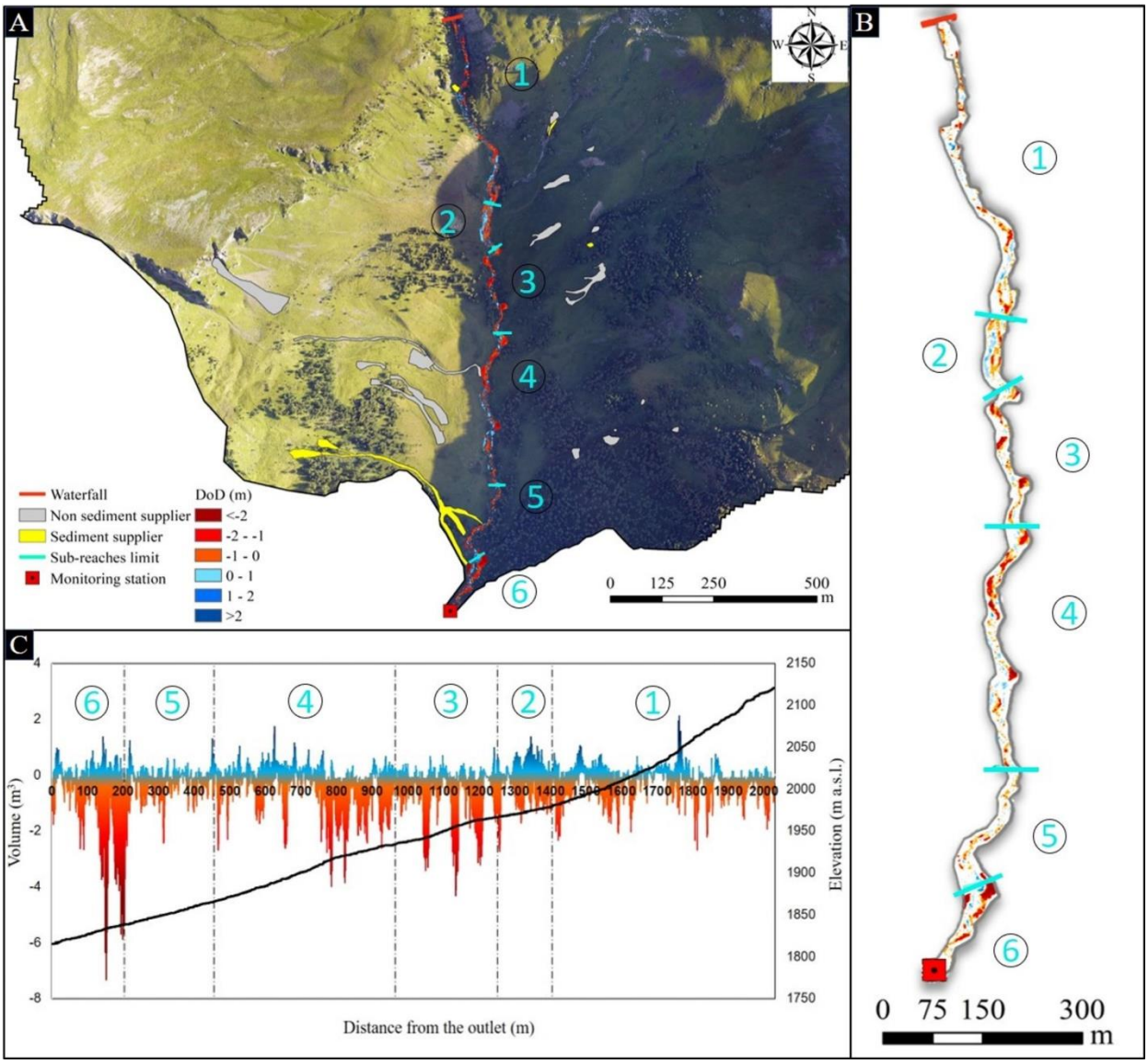

Figure 2.4. The geomorphic response of the lower Rio Cordon basin: A) location of the source areas and their potential role as sediment supplier to the active channel (sub-reaches 1–6); B) zoom of the spatial pattern of geomorphic changes along the Rio Cordon obtained from the DoD; C) DoD represented as the sum of eroded (red) and deposited (blue) volume along the longitudinal profile of the active channel.

Differently, sub-reaches 2 and 5 exhibited the lower average net thickness of difference with −0.07 m and −0.08, respectively, stressing that they were closer to balancing the erosional and depositional volumes than other sub-reaches. These results were confirmed in the DoD profile (Fig. 2.4C), in which the DoD was presented as the sum of all the values hydrologically equidistant from the outlet. Sub-reach 6 exhibited predominant erosion values, whereas sub-reach 2 and 5 showed erosion values almost balanced with deposition ones.

Table 2.3. Summary of the results for each sub-reach concerning unit stream power (ω_{Pi}), width ratio (Wr) and average net thickness of difference (DoD).

Sub-reach	Contributing area (km^2)	Length (m)	ω_{Pi} (W m^{-2})	*Wr*	*DoD* (m)
1	2.30	623	2487	1.21	- 0.12
2	3.37	154	2971	1.79	- 0.07
3	3.50	288	2984	1.39	- 0.24
4	4.28	510	3534	2.44	- 0.19
5	4.47	251	3586	2.01	- 0.08
6	5.00	197	3865	3.76	- 0.45

As proven by the elevation profile, sub-reach 2 corresponds to a flatter part of the Rio Cordon. The unit stream power acted in each sub-reach (ω_{Pi}) showed a progressive increase by moving from upstream to downstream, spanning from ω_{P1} = 2487 W m^{-2} to ω_{P6} equal to 3865 W m^{-2}. Interestingly, sub-reach 1 expressed a width ratio (*Wr*) close to 1, while sub-reach 6 experienced major planimetric variations with a *Wr* equal to 3.76 (Table 2.3). In this sense, the width ratio scaled roughly linearly with the unit stream power (R^2 = 0.749, p-value < 0.05), while a weak relationship was observed between ω_{Pi} and DoD values (R^2 = 0.293, p-value > 0.05). Therefore, the results suggest that stream power variation led to a linear variation in the channel width but not in the streambed elevation.

Sedimentological effects

The post-flood GSD of Rio Cordon resulted slightly finer than pre-event, with $D_{16}/D_{50}/D_{84}/D_{90}$ that varied from 29/114/358/455 mm, respectively, to 26/78/302/423 mm (Fig. 2.5). Particularly, it should be stressed the reduction of about a third experienced by D_{50}. The coarse material transported to the monitoring station exhibited a GSD comparable to that expressed by the streambed material, with D_{16} = 38 mm, D_{50} = 90 mm, D_{84} = 248 mm and D_{90} equal to 381 mm (Fig. 2.5).

The ten largest elements were characterized measuring the axis and, thus, estimating the weight. These boulders had a *b*-axis between 400 and 1100 mm, corresponding to an estimated weight between 0.11 and 1.75 t. Field evidence suggested that these elements were recruited primarily from banks and cascade/step-pool sequences, being then transported for tens of meters. The relationship observed in the period 2012–2018 between critical unit water discharge (q_c) and particle size (Rainato et al., 2020) permitted to roughly determine the hydraulic forcing that caused the boulder entrainment.

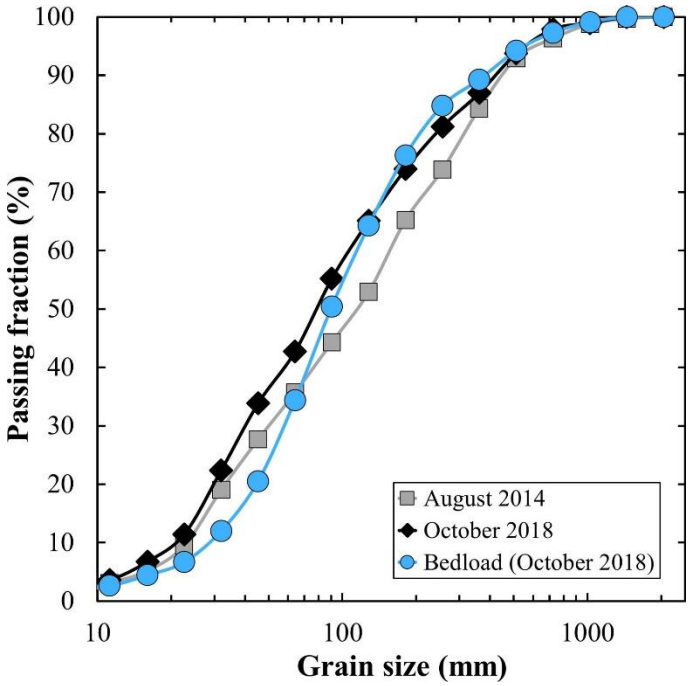

Figure 2.5. Comparison between grain size distributions of pre- (August 2014) and post-flood (October 2018) Rio Cordon streambed as well as of October 2018 bedload.

Considering the ten largest elements, the analysis suggested q_c between 0.68 $m^2 s^{-1}$ and 1.51 $m^2 s^{-1}$.

The bedload storage area located at the measuring station was completely filled with coarse sediment (Fig. 2.6). In this area, the DoD analysis determined a bedload volume (BL_{Obs}) equal to 6656 m^3 ± 769 m^3, over an extent of about 4200 m^2. Therefore, the average net thickness of difference was 1.58 m, with the maximum elevation change reaching 5.96 m of deposition. The reconstruction of the hydrograph also permitted to determine the bedload volume predicted (BL_{Pred}) by bedload equation. The application of the Schoklitsch (1962) equation suggested a bedload volume of 6890 m^3, of which 32 m^3 were associated to Phase 1 and 6858 m^3 to Phase 2 (Fig. 2.3). Interestingly, the total 6890 m^3 resulted higher by a factor of 1.04 respect to the *BL* calculated by DoD analysis. Thus, the bedload volume expressed by the October 2018 flood was considered as the average between BL_{Obs} and BL_{Pred}, i.e., equal to about 6800 m^3.

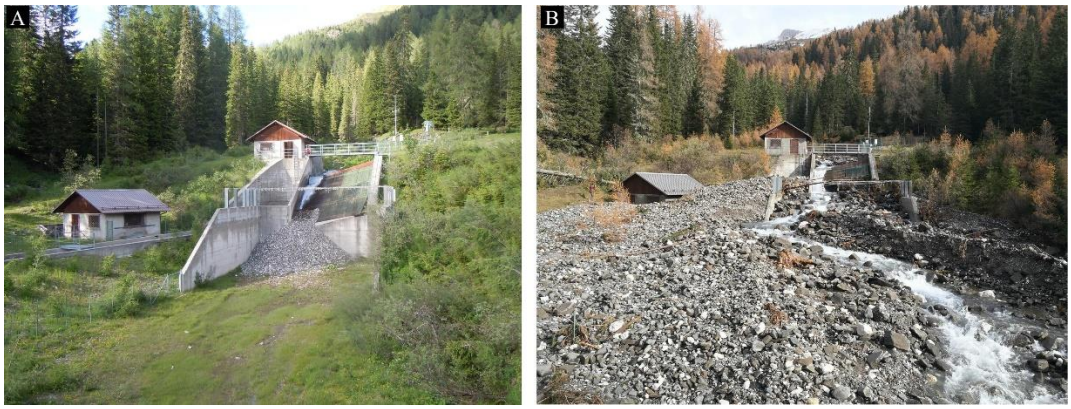

Figure 2.6. Bedload storage area (A) pre- and (B) post-October 2018 flood.

In terms of *BL*, the October 2018 flood appeared the largest event recorded in the last 34 years (1986–2018), resulting greater than the second flood by a factor of ~7.5, i.e., the September 1994 event (*BL* = 900 m^3), and by a factor of 3.68 than the cumulative bedload volume generated by the 33 previous events. Moreover, the bedload was transported over a T_{Bl} of 22 h, corresponding to a transport rate equal to 309 $m^3\ h^{-1}$. In terms of bedload yield, the October 2018 flood delivered 11,713 t of coarse material, accounting for 99% of the annual bedload recorded in 2018 and 79% of total bedload observed in the period 1986–2018 (Fig. 2.7). Considering this period and accounting the October 2018 event, the Rio Cordon basin therefore exhibited a total sediment yield = 26840 t, which corresponds to a mean sediment yield of 162.6 t $km^{-2}\ y^{-1}$. It is worth bearing in mind that this estimate does not account for the suspended sediment load generated by October 2018 event.

Considering the 34 floods recorded in the Rio Cordon basin in the period 1986–2018, it is possible to note a power law relationship between Q_P and *BL* (R^2 = 0.719, p-value < 0.01), in which the October 2018 flood represents the upper bound (Fig. 2.8a). In addition, the bedload GSD seems to be described by Q_P, with the transported $D_{16}/D_{50}/D_{84}/D_{90}$ well predicted by the peak of water discharge. Notably, the relationship performance increases with the coarsening of the percentiles (Fig. 2.8b). In fact, the relationships $Q_P - D_{90}$ and $Q_P - D_{84}$ showed R^2 = 0.842 (p-value < 0.01) and R^2 = 0.813 (p-value < 0.01), respectively, with the larger elements mobilized by October 2018 flood. Differently, $Q_P - D_{50}$ (R^2 = 0.677, p-value < 0.01) and $Q_P - D_{16}$ (R^2 = 0.421, p-value < 0.05) resulted more scattered, with October 2018 event that transported D_{50} and D_{16} similar to those entrained by lower magnitude floods. Overall, a progressive increase of both the factor *a* and exponent *b* can be noticed with the coarsening of the percentile considered (Fig. 2.8b).

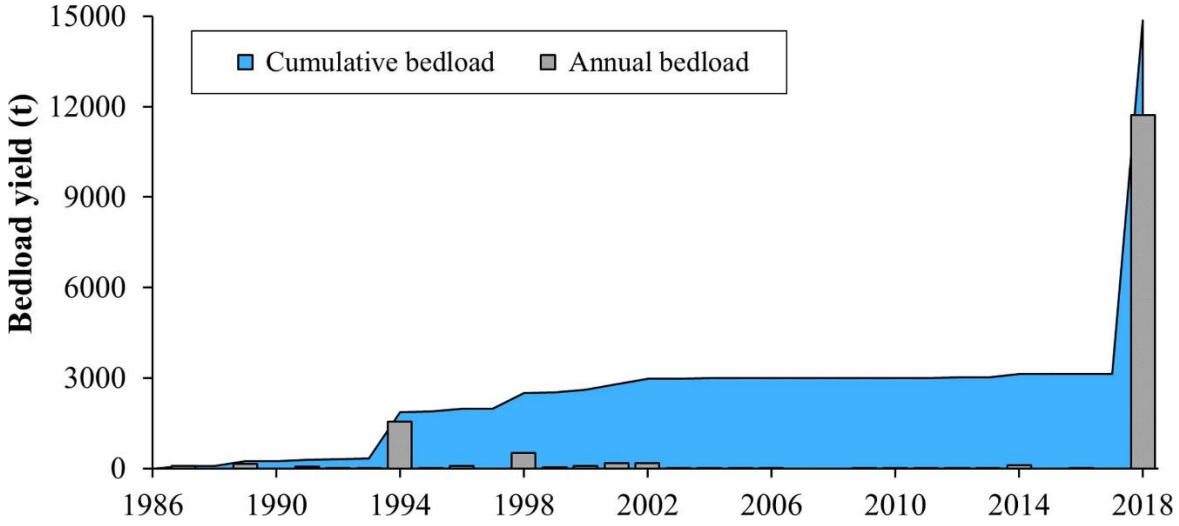

Figure 2.7. Annual and cumulative bedload yields in the Rio Cordon between 1986 and 2018.

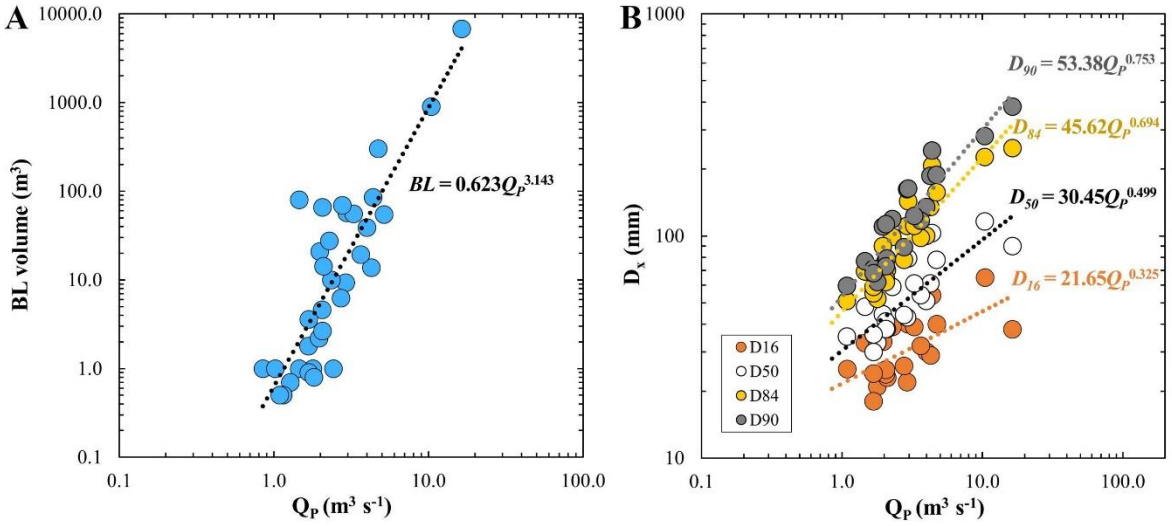

Figure 2.8. Relationship between Q_P and (A) BL volume, and (B) D_{16}, D_{50}, D_{84}, D_{90}, transported by the 34 flood events recorded in the Rio Cordon (1986–2018). The dotted lines are the best-fit lines for each relationship investigated.

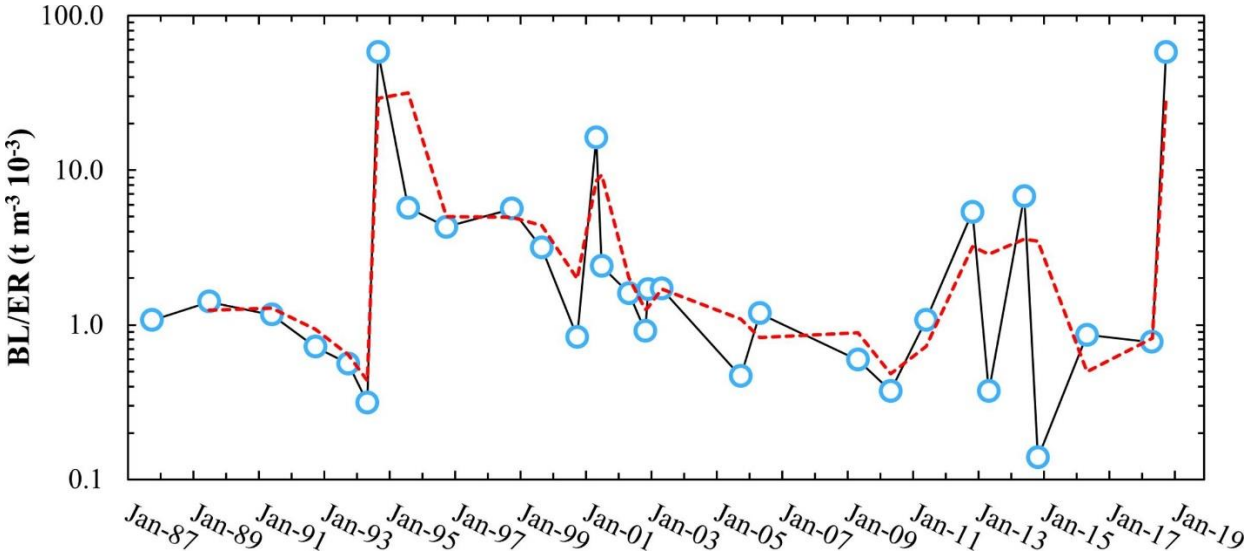

Figure 2.9. Temporal trend expressed by the BL/ER ratio over the 34 flood events recorded in the Rio Cordon (1986–2018). The red dotted line is the 2-event moving average.

The ratio between *BL* (in t) and *ER* expressed by each flood recorded (1986–2018) enabled to investigate the temporal trend of transport efficiency. Fig. 2.9 shows a general decreasing trend over the long-term period, with most of the events characterized by a *BL*/*ER* ratio between 0.1 and 10.0. The only floods that clearly deviate from the general trend were the September 1994 (*BL*/*ER* = 58.0) and the October 2018 (*BL*/*ER* = 58.3).

Discussion

Rainfall conditions

The heavy precipitation generated in the study basin by the Vaia storm was not continuous but exhibited a hiatus of about 9 h, permitting the identification of a Phase 1 and a Phase 2 in the rainfall event (Table 2.1). This temporal distribution is consistent to what was shown by Vaia storm over northeastern Italy (Davolio et al., 2020, Giovannini et al., 2021). The maximum rainfall intensities recorded in 5, 15, 30 min (I_{5min}, I_{15min}, I_{30min}) were characterized by *RI* < 2 years, while considering longer time intervals ($I_{6h} - I_{72h}$) the *RI* resulted well over 50 years, emphasizing the persistence of rainfall occurred in the Rio Cordon basin. These results agree with Giovannini et al. (2021) who, investigating the main characteristics of the Vaia storm, reported 72 h accumulated precipitation with *RI* > 200 years in most of the eastern Italian Alps.

Table 2.4. Main characteristics of the high magnitude/low frequency event analyzed in this work, compared with those observed in mountain basins by other authors. A is the basin area; S the mean channel slope; Rainfall description indicates the precipitation type triggering the flood event (PP = persistent precipitation, ST = summer thunderstorm); Basin responses describes the main effects induced by the high magnitude/low frequency event in each study basin (CC = channel changes, BM = boulder mobility, HF = Hyperconcentrated flow, DF = debris flows, LA = landslides).

Study basin	Event	*A* (km^2)	*S* ($m\ m^{-1}$)	Rainfall description	Mean rainfall intensity ($mm\ h^{-1}$)	Unit peak discharge ($m^3\ s^{-1}\ km^{-2}$)	Unit stream power ($W\ m^{-2}$)	Basin responses	Reference
Rio Cordon	October 2018	5.0	0.17	PP	4.4	3.3	2487-3865	CC, BM	This work
Arás	August 1996	18.0	0.14	ST	250.0	20.0	–	CC, HF, BM	Batalla et al. (1999)
Emme	July 2014	94.0	0.02	ST	~ 87.0	2.7 – 4.7	–	CC, DF, LA	Ruiz-Villanueva et al. (2018)
Erlenbach	July 1984	0.7	0.18	ST	21.3	17.1	–	CC, BM	Turowski et al. (2009)
Erlenbach	July 1995	0.7	0.18	ST	12.9	14.0	–	CC, BM	Turowski et al. (2009)
Erlenbach	June 2007	0.7	0.18	ST	36.8	20.9	–	CC, BM	Turowski et al. (2009)
Fourmille	September 2013	65.0	0.03[a]	PP	~ 2.6	–	2500	CC, BM, DF	Wicherski et al. (2017)

Grimmbach	May 2016	30.0	0.02	–	~ 6.4	22.6 – 25.1	–	CC, LA	Lucía et al. (2018)
Jamne	July 2018	8.9	–	ST	~ 2.0	4.6 – 4.8	770 –2769	CC	Bucała-Hrabia et al. (2020)
Jaszcze	July 2018	11.4	–	ST	~ 2.0	4.1 – 4.5	767 –2703	CC	Bucała-Hrabia et al. (2020)
Orlacher Bach	May 2016	6.0	0.06	–	~ 6.4	20.0	–	CC, LA	Lucía et al. (2018)
Rio Cordon	September 1994	5.0	0.17	ST	16.0	2.1	–	CC, BM, LA	Lenzi et al. (1999)
Selška Sora	September 2007	29.8	0.02	–	~ 20.0	4.4	–	CC, DF, LA	Marchi et al. (2009b)
Tegnas	October 2018	52.0	0.03	PP	5.7	3.3	–	CC, DF, LA	Pellegrini et al. (2021)

The moderate but persistent pattern of rainfall was further stressed by the comparison of other high magnitude/low frequency events documented in mountain basins. Batalla et al. (1999) documented, in the Arás basin, a flash flood associated to boulder mobility and massive sediment transport and caused by a brief but intense summer thunderstorm that featured a mean rainfall intensity of 250 mm h^{-1} (Table 2.4). Similarly, Turowski et al. (2009) analyzed three high magnitude floods that affected the Erlenbach basin with large bedload and boulder mobility, identifying intense summer thunderstorms as triggering factor.These events were characterized by I_{1h} (40.4–61.3 mm) and mean rainfall intensity (12.9–36.8 mm h^{-1}) clearly higher than those observed in the Rio Cordon basin during the Vaia storm, but associated to a total precipitation (45.3–106.7 mm) and a total precipitation duration (1.5–5.0 h) notably lower. Few authors described high magnitude/low frequency events triggered by persistent precipitation. In the Fella River basin, Marchi et al. (2009a) analyzed a convective storm (I_{12h} = 390 mm) which caused a massive debris flow with a mobilized volume of ~78,000 m^3, while a 6 days rainfall event with a total precipitation of 501.0 mm and daily rainfall between 27.2 and 246.4 mm led to a flood with RI > 200 years in the Ligurian Alps (Nannoni et al., 2020).

Hydraulic forcing

The use of indirect methods to estimate the hydraulic forcing acted in the Rio Cordon led to an implicit uncertainty, which needs to be considered. In fact, the hydrograph reconstruction was based on the use of the discharge measured in the Fiorentina basin to describe what occurred in the Rio Cordon sub-basin. The $Q_{Fi} - Q_{Rc}$ relationship was statistically significant and based on 1762 discharge measurements recorded during floods triggered by persistent precipitation, i.e., same rainfall conditions that led to the October 2018 flood. However, it is worth noting that these floods were near-bankfull events and, therefore, the $Q_{Fi} - Q_{Rc}$ relationship may have allowed a better description of under- and near-bankfull discharge than over-bankfull conditions. Nevertheless, the reconstructed hydrograph seems reliable since it reflected the temporal distribution of rainfall registered. Thus, specific analyses were made to determine the corresponding Q_P using the slope conveyance method (Gaume and Borga, 2008) and the basin area scaling ratio proposed by Bravard and Petit (1997). This latter indirect method is characterized by an implicit source of uncertainty due to the basin to sub-basin discharge extrapolation. This uncertainty may have been somewhat reduced by means of the site specific coefficient *c* (see *hydrological conditions* section) already used and tested in the Rio Cordon (Oss Cazzador et al., 2021). Thus, the Q_P inferred for Phase 1

(2.87 ± 0.56 m^3 s^{-1}) and Phase 2 (16.36 ± 1.14 m^3 s^{-1}) were associated to the hydrograph reconstructed and, in particular, in the Phase 2 the hydrograph was integrated by a part simulated to describe the peaking portion of flood. This simulated part involved 3 h of the 90 h investigated (October 27th–October 30th) and it was described as a triangular shape according to the hydrograph shape observed in mountain basins during high magnitude/low frequency floods (Lenzi et al., 1999, Marchi et al., 2009a, Turowski et al., 2009). Interestingly, this shape was consistent to the hydrograph generated by the Vaia storm in another basin of eastern Italian Alps, i.e., the Tegnas catchment (Pellegrini et al., 2021). The hydraulic forcing conditions estimated clearly stressed the high magnitude expressed by the October 2018 flood event (Table 2.2). This high magnitude can be ascribed to the amount and intensity of rainfall but also to their temporal distribution and soil moisture. The soil conditions may have also influenced the perifluvial areas, where important windthrows were observed (Picco et al., 2020) likely to the high wind gusts of October 29th acting on a saturated and softened terrain.

In the Rio Cordon, the October 2018 flood resulted in a unit peak discharge of 3.3 m^3 s^{-1} km^{-2}. This value was lower than those described in the Erlenbach by Turowski et al. (2009), who observed a unit peak discharge between 14.0 and 20.9 m^3 s^{-1} km^{-2} in large floods due to intense thunderstorms (Table 2.4). Higher unit peak discharges were documented even in the Fella River basin by Marchi et al. (2009a) and in Grimmbach and Orlacher Bach by Lucía et al. (2018), who reported 20.0 m^3 s^{-1} km^{-2} and 20.0–25.1 m^3 s^{-1} km^{-2}, respectively. Hydraulic forcing comparable to that observed in the Rio Cordon were detected by Marchi et al. (2009b) in the Selška Sora basin, where a flash flood expressed 4.4 m^3 s^{-1} km^{-2}, and by Ruiz-Villanueva et al. (2018) that reported a unit peak discharges between 2.7 and 4.7 m^3 s^{-1} km^{-2} ascribed to heavy and extensive summer precipitation in the Emme River basin (Table 2.4). Particularly, the unit peak discharge calculated in the Rio Cordon resulted consistent to the 3.3 m^3 s^{-1} km^{-2} experienced in the Tegnas catchment during the Vaia storm (Pellegrini et al., 2021). Also, the peaks of unit stream power inferred along the main channel ($\omega_{P1\text{-}6}$ = 2487–3865 W m^{-2}) appeared comparable, although at the upper limit, to those reported in literature. In fact, the small Jamne and Jaszcze basins, located in the Western Polish Carpathians, experienced ω between 767 and 2769 W m^{-2} as a consequence of flood due to heavy summer precipitation (Bucała-Hrabia et al., 2020). In Fourmille Creek, Wicherski et al. (2017) documented a precipitation event of 350 mm in seven days, which generated over-bankfull discharge for 120 h and a maximum ω of about 2500 W m^{-2} (Table 2.4). Instead, the range of unit stream power determined in the Rio Cordon appeared in line to what observed by Yochum et al. (2017) in the Colorado Front

Range as consequence of persistent heavy rainfall (~460 mm in 10 days). These authors analysed 531 stream reaches, estimating maximum ω between 30 and 7000 W m^{-2}.

Hillslopes and main channel responses

The limited response of hillslope and the only 26 sediment sources (re)activated could be attributed to the moderate rainfall intensity that, in combination with the hiatus in precipitation, may have precluded an extensive slope instability. Also, the lack of other high magnitude events in the period 1994–2018, might have reduced the erosional processes and favoured a consequent stabilization trend along the hillslopes (Ferrato et al., 2017). Differently, in the Tegnas catchment characterized by a similar geological substrate, the Vaia storm caused a marked increase of sediment sources with the catchment area covered by instabilities, such as debris flows and landslides, augmented from 0.33% to 0.83% (Pellegrini et al., 2021), whereas in the Rio Cordon basin this extent increased only from 0.13% to 0.14%. The sediment sources were investigated as potential suppliers in the lower basin. According to Dalla Fontana and Marchi (1994), the lower Rio Cordon belt shows predominant erosion areas (e.g., landslides, debris flows, stream bank erosions), where the sources are potentially more capable of transferring sediment to the downstream outlet in respect to the upper basin (Cavalli et al., 2016). In this sense, recent analyses performed on the upper plateau by Oss Cazzador et al. (2021) demonstrated that, although the October 2018 flood caused the reconfiguration of the upper reach (estimated BL = 86.0–133.2 m^3), it did not effectively transferred sediment to the downstream part of the basin. According to the IC-DoD analysis, only few sources acted as sediment suppliers to the main active channel during the event. Although it proved to be sufficiently reliable, this approach can be further improved. First, the DoD should consider more frequent surveys, second the IC analysis could involve a deeper and extensive field analysis to derive a more accurate threshold (see *sediment sources* section). However, the analyses stressed that the Rio Cordon basin showed evidence of limited lateral connectivity, since only few sediment sources supplied material to the channel network. On the contrary, it showed high longitudinal connectivity due to the evident linkage between active channel and outlet (Fryirs et al., 2007). The DoD analysis suggested that the moderate but persistent rainfall caused greater hydraulic forcing along the main channel than along the slopes, leading to a predominant alluvial response of the Rio Cordon basin. This hypothesis was supported by a volume eroded from Rio Cordon (6979 m^3) clearly larger than the potential volume supplied by sediment sources (1140 m^3). In fact, the DoD pointed out that along the active channel the October 2018 flood resulted in severe erosion processes, with large streambed incisions and banks scouring. Particularly, an evident widening was observed along the 2023 m analyzed, with the average channel

width that varied from 6.30 m, pre-event, to 10.60 m post-event. In this sense, it is worth noting that the geomorphic changes measured can be affected by uncertainty due to: (i) the error range in the active channel DoD, corresponding to ±2059 m^3 (29.5%); (ii) the inaccuracies related to the channel width measuring by means of orthophotos interpretation. Despite these sources of uncertainty, the results seem to suggest that the sediment transport benefited by quasi-unlimited sediment supply conditions mainly due to an extensive alteration of active channel, where the armoured layer was removed. From the DoD analysis a longitudinal pattern along the channel was hardly detectable as many avulsions caused the variation of the stream pathway and no clear erosional/depositional alternation can be used to infer in-channel sediment transfers (Calle et al., 2020). However, the subdivision in sub-reaches helped to reconstruct the linkage between the hydraulic forcing and the geomorphic response. As supported by Marchi et al. (2016), unit stream power was able to describe the major geomorphic changes at channel reach scale. In particular, consistency between ω_{Pi} and lateral geomorphic changes (*Wr*), rather than vertical (DoD), was found. This result appeared in line with Krapesch et al. (2011), who successfully predicted channel widening, caused by extreme floods in alpine gravel bed rivers, by using ω determined by means of the pre-event channel width. In the Rio Cordon basin, the definition of the hydraulic forcing conditions and the induced geomorphic changes supported also the hypothesis that the high magnitude/low frequency floods are the only events that can severely alter the rough boulder streams (Baker and Costa, 1987).

Sedimentological response

The hydraulic forcing and erosive processes triggered by October 2018 flood resulted in a massive sediment transport. The GSD investigation stressed that the entire streambed grain size, from fine gravel to large boulders, was mobilized (Fig. 2.5). This finding supports the hypothesis that the Rio Cordon experienced structural bedload, condition under which a complete streambed remobilization occurred (Piton and Recking, 2017). Consistently, the mobility of large boulders was also observed, highlighting the outstanding hydraulic forcing expressed by October 2018 event. In this sense, it is interesting to note that, in literature, the transport of boulders was generally documented for higher unit peak discharges (Table 2.4). However, Wicherski et al. (2017) observed boulder mobility in the Fourmille Creek as a consequence of ω comparable to that exerted in the Rio Cordon by October 2018 flood. Therefore, these outcomes stressed out the need to better comprehend the boulder mobility, a condition that can strongly impact the mountain streams but that was only rarely investigated. The approaches used to determine the bedload volume, i.e.,

DoD analysis and bedload prediction, provided very similar volumes, with a BL_{Obs}/BL_{Pred} ratio equal to 0.97. In the Rio Cordon, this ratio was always lower due to the overestimation of BL_{Pred} by Schoklitsch (1962) equation and, in general, by bedload equations, with respect to BL_{Obs} (D'Agostino and Lenzi, 1999, Rainato et al., 2017). Therefore, the good match between BL_{Obs} and BL_{Pred} emphasized the high hydraulic forcing of October 2018 flood coupled with a high sediment supply, conditions under which the bedload equations can provide the highest predictive performance (D'Agostino and Lenzi, 1999, Recking, 2012, Rickenmann, 2020). However, it is worth noting that both BL_{Pred} and BL_{Obs} might be affected by a certain degree of uncertainty. On the one hand, BL_{Pred} was calculated by means of the Schoklitsch equation applied to the hydrograph reconstructed (see *hydraulic forcing* section). Therefore, the intrinsic uncertainty affecting the discharges estimated may have propagated in the predicted bedload. On the other hand, the BL_{Obs} determined by DoD analysis presented an error range of ±769 m^3, corresponding to about 11.5% of the volume observed. Finally, BL_{Obs} might be affected by a partial underestimation as the October 2018 flood caused the complete filling of the bedload storage area, up to its maximum capacity (Fig. 2.6), and therefore a certain portion of bedload may have been transported further downstream.

Large and infrequent floods in Rio Cordon basin

The two-high magnitude/low frequency floods occurred in the catchment were caused by markedly different rainfall conditions. The intense summer thunderstorm that triggered the September 1994 flash flood exhibited $I_{5min}/I_{15min}/I_{30min}$ about twice the Vaia storm's values but lasted 12 h, i.e., a total precipitation duration considerably shorter than the 79.8 h estimated in October 2018 (Table 2.1). The prolonged rainfalls of October 2018 produced the highest hydraulic forcing conditions among the 34 floods recorded in the Rio Cordon since 1986 (Supplementary S1). Particularly, the estimated water discharge peak (Q_P = 16.36 ± 1.14 $m^3 s^{-1}$) and effective runoff (ER = 201.0 × 10^3 m^3) were higher by a factor of 1.57 and 7.56, respectively, than those exhibited by September 1994 flood. Despite this outstanding hydraulic forcing, the hillslope response to the October 2018 event was modest. In particular, the number of newly formed sediment source areas was relatively low compared to what produced by the September 1994 flood (Dalla Fontana and Marchi, 1994, Lenzi and Marchi, 2000). This diverse response appears to be due to the different rainfall intensity showed by the flood events (Table 4). However, in both high magnitude/low frequency floods, the main sediment source was identified in the active channel and, particularly, in the streambed that

experienced armoured layer removal. In October 2018, the alteration faced by the main channel was clearly larger than in 1994, with unprecedented lateral widenings and avulsions. This finding confirmed that, with similar unit stream power and peak discharge, long-lasting floods can produce larger geomorphic changes than flash floods (Costa and O'Connor, 1995, Magilligan et al., 2015, Marchi et al., 2016). The hydraulic and geomorphic forcing exerted by October 2018 flood triggered boulder mobility in the Rio Cordon main channel, a condition that was previously observed only in the September 1994 event. In this sense, according to Rainato et al. (2020), the largest element (*b-axis* = 1100 mm) recovered in the bedload storage area after the October 2018 flood suggests a critical unit water discharge (q_c) of 1.51 $m^2 s^{-1}$, thus, higher than q_c = 1.25 $m^2 s^{-1}$ observed in the September 1994 flood (Lenzi et al., 2006b). Also in terms of bedload volume, the October 2018 flood (*BL* = 6800 m^3) was the largest event recorded in the Rio Cordon basin, and about one order of magnitude larger than the September 1994 event (*BL* = 900 m^3). Interestingly, the two high magnitude/low frequency events showed comparable transport rate, i.e., 309 $m^3 h^{-1}$ in October 2018 flood and 323 $m^3 h^{-1}$ in September 1994 event but the latter lasted 3 h, while, during the former, bedload persisted 22 h. The *BL* magnitude expressed by October 2018 flood was also clearly noticeable in terms of sediment yield, accounting for 79% of the total bedload delivered during the period 1986–2018 and, then, leading to an abrupt increase over the annual trend (Fig. 2.7). In light of climate change, because of which a higher frequency of heavy rainfall event is expected (Fischer and Knutti, 2015, Peleg et al., 2020), the observed relationships Q_P-*BL* volume and Q_P-GSD transported seem to suggest that in the near future, in the Rio Cordon, other massive bedload transport accompanied by the mobilization of coarse grain size could be awaited. Additionally, the October 2018 flood induced a peak in the temporal trend of *BL*/*ER* ratio, similarly to what was caused by the September 1994 event, i.e., a condition that favoured about a decade of increased transport efficiency (Rainato et al., 2017).

Conclusions

In alpine basins, severe rainfall events and induced large floods can influence erosion processes, sediment dynamics and landscape evolution over large spatial and temporal scales. However, given the high magnitude/low frequency, these events and their effects are difficult to measure and, thus, to be documented. Additionally, even rarer are the studies proposing a comprehensive approach that encompasses all the main responses to the events. This work analyzed the hydrological, geomorphic and sedimentological responses of an alpine basin (Rio Cordon basin) to the Vaia storm, a severe

weather event that affected northeastern Italy in October 2018. In the Rio Cordon basin, the Vaia storm resulted as a severe and persistent rainfall event, during which the rainfall intensities for sub-hourly intervals were ordinary, while for longer time intervals expressed $RI > 50$ years. The combination of different indirect methods helped the hydraulic forcing quantification. Despite the uncertainty associated to this approach, the analyses clearly stressed the outstanding hydraulic forcing occurred during the flood, pointing out the largest Q_P and ER ever recorded in 34 years. These conditions induced a moderate hillslope response, with only few new sediment sources capable of acting as sediment suppliers to the main channel. Instead, the precipitation favored a predominant alluvial response of the basin, with the Rio Cordon severely altered by lateral widening, deep streambed incision and armouring removal. In terms of sedimentological response, the hydraulic forcing and the erosive processes induced by the Vaia storm resulted in streambed remobilization, boulder mobility and in a bedload volume about four times the one produced cumulatively by the 33 previous events. Thanks to a monitoring program maintained over three decades, the Rio Cordon basin offered the uncommon chance to compare characteristics and effects of two high magnitude/low frequency floods. These two events exhibited different rainfall and hydraulic forcing conditions that favored in the September 1994 flash flood a hillslope response larger than in the October 2018 event, which instead altered the main channel more extensively. These conditions resulted in a different sedimentological response of the basin, clearly evident in terms of bedload volume, supporting the hypothesis that floods featuring high Q_P (or ω_P) combined with a long duration can severely influence the mountain fluvial systems. Therefore, bearing in mind the long-lasting effects induced by the previous large and infrequent event, what can be expected for the future? Has the October 2018 event represented the new ground zero for the Rio Cordon basin? To answer these questions, also in the framework of climate change, it will be fundamental to continue investigating over the long-term this and other alpine basins to understand how they will respond to forthcoming ordinary and high magnitude/low frequency events.

Chapter 3.

The last chapter presents a study case carried out again in the Rio Cordon catchment affected by the Vaia storm. Chapter 3 concludes the thesis by facing some of the most recent issues and challenges in the field of sediment connectivity. In chapter 2, a simple but useful workflow based on IC and DoD was developed to investigate sediment connectivity between new sediment sources and the Rio Cordon stream. Starting from that, it seemed essential to test the true capability of IC to validate the static linkages between sediment sources and channel network (i.e. structural connectivity) and to predict the occurrence of new linkages temporarily triggered by an event (i.e. functional connectivity). In this way, it is possible to test the reliability of the IC in a real case study. The methodology proposed highlights the importance of integrating traditional field surveys with observations and analysis from remote sensing.

This chapter embraces a more recent perspective in the field of sediment connectivity, which poses the implementation of IC, or any other metric of connectivity, as the starting point and not the ultimate goal for studies related to sediment dynamics. Moreover, thanks to the outcomes of this chapter it is possible to understand the advantages and disadvantages of the IC and to provide a threshold capable of distinguishing between high and low connectivity with a certain level of accuracy. Even though the threshold is derived specifically for the Rio Cordon catchment, the methodology can be transferred to be applied to other catchments.

Predicting sediment connectivity in a mountain basin: a quantitative analysis of the Index of Connectivity

Adapted from Martini L., Cavalli M., Picco L. (2022). Predicting sediment connectivity in a mountain basin: a quantitative analysis of the Index of Connectivity.
Earth Surface Processes and Landforms. https://doi.org/10.1002/esp.5331

Contributions by the PhD candidate: Investigation, conceptualization, methodology, data curation, writing the original draft.

Abstract

Sediment connectivity underlies the relationships between sediment source areas and stream network and the use of topography-based indices, such as the Index of Connectivity (IC), has become a common approach to investigate these relationships. However, few studies have tested the potential of the IC as an independent variable for predicting observable processes. In this study, the aim is the validation of IC as semi-quantitative tool for depicting structural connectivity and for predicting sediment dynamics linking sediment sources to the channel network after a large infrequent disturbance in the Rio Cordon catchment (Italy). First, the assessment of lateral connectivity was carried out using a combination of remote sensing data and field observations. In this way, it was possible to classify the sediment sources into disconnected, connected or functionally connected. Second, logistic regression analyses were performed using different IC variants, with different weighting factors and spatial resolutions as independent variables and the connectivity status as dependent variable. Hence, the predictive capacity of IC was tested and a threshold was derived to distinguish between low and high sediment connectivity. The results showed that only 15% of the sediment sources are connected to the stream network. Moreover, IC proved to be a reliable tool for depicting structural connectivity when using surface roughness as weighting factor and high-resolution Digital Terrain Models. On the contrary, it failed at predicting sediment dynamics as it did not classify correctly the functionally connected areas, so it can not infer functional sediment connectivity in this case study. As consequence, it was possible to obtain an IC threshold of -2.32, capable of differentiating between low and high structural sediment connectivity and useful to future management decisions. The threshold in fact, represents an objective boundary between disconnected and connected sources in the Rio Cordon catchment.

Keywords: Sediment connectivity; Index of Connectivity; Mountain basin; Sediment source areas; Logistic regression.

Introduction

In the last decades, the interest in connectivity has soared and many authors provided frameworks to support definitions, methodological approaches, and case studies (Najafi et al., 2021). In the investigation of the processes operating on the Earth's surface, connectivity can refer to the role of sediment as a major agent of the landscape's evolution. Considering the classification proposed by Bracken and Croke (2007), a clear distinction is made between landscape, hydrological and sediment connectivity, with the latter specifically addressing the transfer of sediment in geomorphic systems. A widely accepted definition was proposed by Heckmann et al. (2018), who outlined sediment connectivity as the degree to which a geomorphic system facilitates the transfer of sediment through its components. Indeed, in the framework of the sediment cascade, the transfer depends upon the relationships between these components, which in drainage basins are hillslopes, channel networks, and valley bottoms (Burt and Allison, 2010; Fryirs, 2013; Fryirs and Brierley, 2013). Depending on the coupling mechanism, Brierley et al. (2006) distinguished connectivity in longitudinal (along the channel network), vertical (surface-subsurface) or lateral (hillslope-channel).

Furthermore, two major aspects of sediment connectivity have been identified. Structural sediment connectivity regards the physical linkages among sediment sources, channels, and valley bottoms, i.e. their spatial arrangement in the catchment. In other words, it represents a static snapshot of the catchment's spatial configuration (Wohl et al., 2018). On the contrary, functional sediment connectivity denotes the dynamics of the sediment transfer as it describes also the external forcings acting on the sediment fluxes (e.g. precipitation, water discharge, sediment inputs from slope failures) (Wainwright, 2011; Heckmann et al., 2018). Therefore, functional connectivity is process-based and investigates the actual transfer of sediment by considering the time component and the frequency-magnitude distributions of sediment detachments (Bracken et al., 2015). Recently, a few authors proposed integrated approaches of both concepts in order to achieve a deeper understanding of the sediment cascade (Croke et al., 2013; Wester et al., 2014; Liu and Fu, 2016; Kalantari et al., 2017; Lopéz-Vicente and Ben-Salem, 2019; Zingaro et al., 2019). However, this remains a complex task.

Measuring sediment connectivity is one of the ongoing major challenges. This is primarily due to the complexity of the concept and the difficulty of directly measuring sediment fluxes in multiple temporal and spatial scales, i.e. functional connectivity (Heckmann et al., 2018). The lack of

standardized protocols for field-based investigation (Turnbull et al., 2018), the impossibility to summarize all factors involved in one metric, and the incomparability of results across scales exacerbate the issue. Despite the problem of measuring connectivity in the field, several improvements have been made to measure structural connectivity indirectly, which is fundamental to represent the spatial configuration of the linkages.

Among raster-based indices, the Index of Connectivity (IC) first developed by Borselli et al. (2008), and then refined by Cavalli et al. (2013), has been widely applied to infer potential sediment transfer from hillslopes to downstream areas, to identify the preferential sediment pathways and to prioritize sediment source areas. The IC provides a semi-quantitative approach to investigate structural connectivity by exploiting high-resolution Digital Elevation Models (DEMs). Hence, the spatial resolution of the topography is fundamental because it directly affects the IC outcomes. Brardinoni et al. (2015), comparing three different DEM resolutions (2.5 m, 5 m, and 10 m), found that IC slightly increases with the increasing of pixel size. This result was found also by Cantreul et al. (2018), who compared different DEM resolutions (between 0.25 and 10 m) in an agricultural site of 1.24 km^2 and recommended a 1 m DEM because it provided the suitable compromise between accuracy and processing time. Low resolution DEMs were successfully used to compute IC at large scales for instance by Martini et al. (2019), Singh et al. (2017), and Nicoll and Brierley (2017), who computed IC with 12.5 m, 30 m and 90 m satellite-derived DEMs, respectively. Therefore, even though high-resolution DEMs are recommended, the choice must also consider the extent of the area of interest, the processes and spatial units under investigations (Heckmann et al., 2018).

Increasing attention is given to the adaptation of the IC in different environments. In this context, the way impedance to sediment fluxes is represented, i.e. weighting factor (W factor) in the IC formula, is fundamental. The choice of the most appropriate W factor in function of the local characteristics of the study area is still highly debated. As proposed by Cavalli et al. (2013), surface roughness is preferred in steep mountain areas lacking vegetation. In a large Himalayan area, Mishra et al. (2019) used NDVI to implement the cover and management factor (C factor) as W factor, whereas in a wildfire-affected catchment, Martini et al. (2020), adopted the Manning's n. When multiple disturbances affect forested catchments, Jautzy et al. (2021) propose a parameter based on forest stand characteristics and snowmelt rate to transform multi-temporal forest disturbance maps into W factor maps.

In mountain catchments, where typically sediment sources are fueling the sediment cascade, the IC is computed to investigate lateral sediment connectivity and thus hillslopes to channel linkages. When using IC maps to infer sediment transfer from sediment sources originated along the hillslopes

to the channels, qualitative or semi-quantitative analyses are typically performed. Persichillo et al. (2018), used the mean IC values of shallow landslides to investigate changes in sediment connectivity driven by anthropic activities. Using a 50 m buffer between channel network and sediment sources located in high IC areas, Tiranti et al. (2018), evaluated the potential decoupling of debris flow processes. In the upper Fella River basin, Schopper et al. (2019), found that IC is able to characterize the patterns of processes (e.g. debris flows) reaching the main channel rather than predicting the occurrence of those not reaching the river. In fact, although the concept of predictability is implicitly addressed in the IC approach, as it represents the potential sediment connectivity, a temporal component is not involved. To move forward the use of IC as a predictor of sediment dynamics (Pellegrini et al., 2021) a more quantitative and comprehensive approach must be carried out with direct measures of structural connectivity (Turnbull et al., 2018). However, few studies have used the information collected in the field to test the reliability of IC, and even less tested thresholds of IC to discriminate actual sediment connectivity from source to channel. For instance, Calsamiglia et al. (2018), pointed out an overlap between spatial patterns of high IC and the collapse of terrace walls surveyed in a Mediterranean area. As matter of fact, the investigation of IC as an independent variable is becoming critically important due to its potential capacity of predicting observable processes (Wohl et al., 2017; Heckmann et al., 2018).

In this work, the main objective is the validation of the IC as semi-quantitative tool to infer sediment transfer between sediment sources and channel network in a mountain catchment. We aim at i) identifying the most appropriate IC when trying to depict lateral sediment connectivity by testing a combination of IC variants, computed using different spatial resolutions and W factors, ii) establishing a threshold between high and low IC that may be helpful to enhance the use of IC maps for catchment management purposes. The accomplishment of these goals will also entail a deeper awareness of the limits of structural-based indices.

Material and methods

The study was conducted in the Rio Cordon, an alpine catchment located in the Dolomites, Italy (section *study area*). The methodology can be divided into two parts. The first concerns the assessment of lateral sediment connectivity, hence the linkages between existing sediment sources (section *sediment source areas inventory*) and channel network. The assessment of lateral sediment connectivity was made using remote sensing data (orthophotos, DEM of Difference-DoD, section *remote sensing data*) and field surveys, and it is further described in section *assessment of lateral connectivity*. The second part, instead, regards the computation of the IC maps using different DTM

spatial resolutions and different W factors. The predictive capacity of the IC was evaluated using binary logistic regression analysis, testing each IC variant as the main independent variable. The most appropriate IC variant was then used to identify an IC threshold. Further information in sections *computation of the Index of Connectivity* and *logistic regression analysis.*

Study area

The Rio Cordon is a small catchment (5 km^2) located in the eastern Italian Alps (Figure 3.1). The basin is characterized by a rugged topography with elevation ranging from 1763 to 2763 m a.s.l. and an average slope of 27°. The geological substrate is mainly composed of dolomites, limestones, volcanic conglomerates (Wengen group), and calcareous-marly rocks (Buchenstein group). Due to the high elevation, the area is covered by grassland, bare rock, and woody vegetation, composed of shrubs and larch-spruce forest. The average annual precipitation is around 1150 mm with the prevalence of short rain showers in summer and persistent rainfall in autumn. Furthermore, given the typical alpine winter conditions, the snowmelt represents a significant component of the Rio Cordon hydrological regime, hence classified as nivo-pluvial. The channel network develops for almost 7 km, featuring cascade and step-pool morphologies (Montgomery and Buffington, 1997). Particularly, the third-order main channel is interrupted by a waterfall, which conventionally divides the whole basin into the upper part and lower part. In the upper part, a wide plateau prevents the sediment originated from the uppermost rock walls to be transferred into the lower part of the basin. At the outlet, a permanent monitoring station, implemented with a storage area, was built to continuously monitor the water and sediment fluxes (Rainato et al., 2017).

Like many other catchments in the surroundings, the Rio Cordon was deeply affected by the Vaia storm, a large infrequent disturbance that hit the NE of Italy from the 28th to the 30th of October 2018. The event was characterized by strong wind gusts and persistent rainfall (RI > 50 years), that triggered a severe hydro-geomorphic response. Along the hillslopes, 26 sediment sources were (re)activated but only a few were actually contributing to the stream network. Considerable morphological changes were registered along the main channel, resulting in a massive sediment deposition in the storage area at the outlet (more information can be found in Rainato et al., 2021).

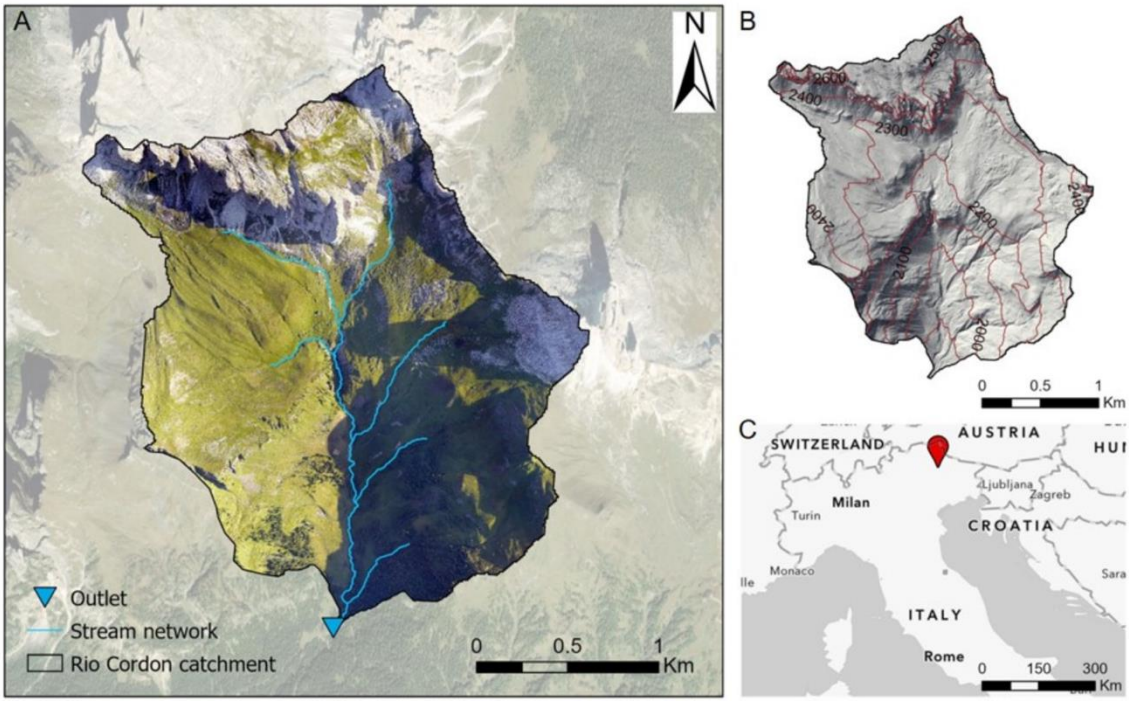

Figure 3.1. The aerial view (A), topography (B) and location (C) of the Rio Cordon catchment. The aerial view shows the condition of the catchment in August 2019. In the aerial view, the eastern part is partially covered by shadows.

Sediment source areas inventory

The sediment source areas in the Rio Cordon catchment have been monitored since 1994, when the first inventory was carried out by field-based measurements and aerial photographs interpretation (1:25.000 scale). Later, the 1994 inventory was digitized, georeferenced and re-worked to be used in the GIS environment. In 2006, an inventory was performed using contemporary onsite surveys, 1 m resolution DTM, and a 0.5 m orthophoto (Cavalli et al., 2016).The sources were classified in active talus, surficial erosion, stream bank erosion, debris flow channel/deposit, and landslide. Also, stabilized areas and wetlands were surveyed although not responsible for sediment production. From 1994 to 2006, 127 more sources were identified, increasing the total number up to 419 with a total surface of about 648554 m^2 (Cavalli et al., 2016). After 10 years, the catchment was again surveyed and a new inventory was obtained supported by a dataset of photos (Ferrato et al., 2017). The 2016 inventory presented 420 sediment sources and a total surface of about 652100 m^2. The major differences regarded: the presence of a large rockfall deposit (20676 m^2), the stabilization of surficial erosions, increased number of landslides and debris flows channels. After the Vaia storm, in 2019 the geomorphic response of the basin was assessed and 9 newly formed instabilities were added to the inventory (Rainato et al., 2021). Moreover, 17 sources were also reactivated by the event and thus

their shape was modified and their features updated. Therefore, the resulting 2019 inventory is an update of the previous one (2016), considering only the variations induced by Vaia.

For the purposes of this work, we used the 2019 inventory with the following adjustments: i) obliterated, stabilized and wetland areas were excluded; ii) debris flow channels and deposits were merged into a single class (debris flow); iii) sediment sources largely outside the watershed were removed. The resulting inventory consists in 431 areas with an overall extension of 675692 m^2 and classified as follows: 219 landslides, 86 surficial erosions, 80 debris flows, 26 active talus, 19 stream bank erosions, and 1 rockfall.

Remote sensing data

Two LiDAR surveys were used in the present research, dated 2006 and 2019, respectively. From the LiDAR surveys orthophotos and point clouds were made available. The 2006 (pre-event) orthophoto had a resolution of 0.5 m, while the 2019 (post-event) orthophoto had a resolution of 0.2 m but it presents a large part of the eastern catchment in the shadow (Figure 3.1A). The co-registration of point clouds was performed in CloudCompare (software version 2.19.2 Zephyrus), using a combination of automatic Iterative Closest Point (ICP) algorithm and manual definition of stable point correspondences. First, two Digital Terrain Models (DTMs) at the highest resolution (0.5 m) were derived to perform a catchment-scale Dem of Difference. The DoD was used to support the assessment of the lateral sediment connectivity made via orthophotos and field surveys (see section *assessment of lateral sediment connectivity*). Specific information about the DoD computation can be found in Rainato et al. (2021). Second, multiple 2006 DTMs were computed with different spatial resolutions in order to derive multiple IC maps to be used in the analysis of predictability. Hence, the DTMs were interpolated at 0.5 m, 1 m, and 2.5 m resolution. We chose these grid sizes as representative of the maximum spatial resolution achievable (0.5 m), the most common spatial resolution for LiDAR data (1 m), and five times the maximum spatial resolution (2.5 m). Larger grid sizes would represent an unnecessary loss of detail for a 5 km^2 catchment.

Moreover, a 2015 orthophoto was exploited as it represented the pre-event land cover condition and it was used to carry out the 2016 inventory. The orthophoto was downloaded at 0.2 m resolution from the Web Map Service for AGEA (Italian Agricultural Payments Agency).

Assessment of lateral sediment connectivity

The sediment source areas of the post-event inventory were classified according to their relationship to the channel network. In accordance with Bracken et al. (2015) and Thomas (2001), we termed this relationship as (dis)connectivity status. In this paper, we defined three different connectivity status: disconnected, connected, and functionally connected. Specifically, disconnected sources do not show any linkage with the streams (Figure 3.2A); connected sources are in contact with the stream, so that we assume the sediment eventually reaches the channel (Figure 3.2B); functionally connected also consider a type of contact with the stream, but they specifically refer to an event-based type of linkage (Figure 3.2C). Functionally connected areas show field evidence of sediment transfer associated with the 2018 event rather than a permanent interface. These sources of sediment do not show an evident contact with the stream but a pathway (i.e., deposition of fine sediment or rill) that probabily will stabilize in the near future. For these reasons, functionally connected areas represent a sub-group of connected sources only attributable to the 26 post-event areas.

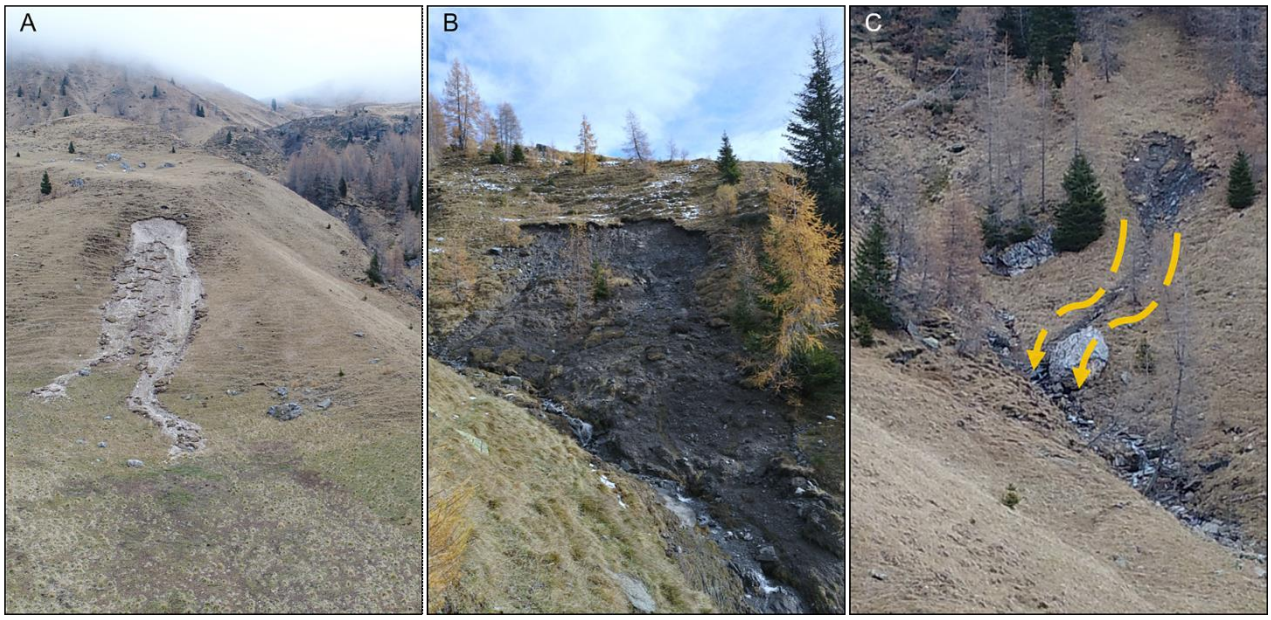

Figure 3.2. Examples of sediment source areas classified as disconnected (A), connected (B) and functionally connected (C), in which the sediment pathway is highlighted within the two red dashed arrows.

The classification was accomplished following the schematic procedure outlined in Figure 3.3. First, the post-event orthophoto was examined to decide whether or not the sources are directly in contact with the stream network. If they show direct contact with the stream network they were classified as connected. In the opposite case, and especially when it was impossible to decide from aerial view, we analyzed their status using a two-steps assessment in order to discriminate between disconnected and functionally connected sources: i) The DoD highlighted potential sediment mobilization (erosion) not visible with the aerial view, ii) Targeted field inspections were carried out to determine if the erosion reached the stream. During the field campaigns, we looked for pieces of evidence of sediment pathways and evaluated the traceability to the Vaia event. If the sediment reached the channel, the source was classified functionally connected, in the opposite case disconnected. As result, the inventory was classified into disconnected, connected or functionally connected features.

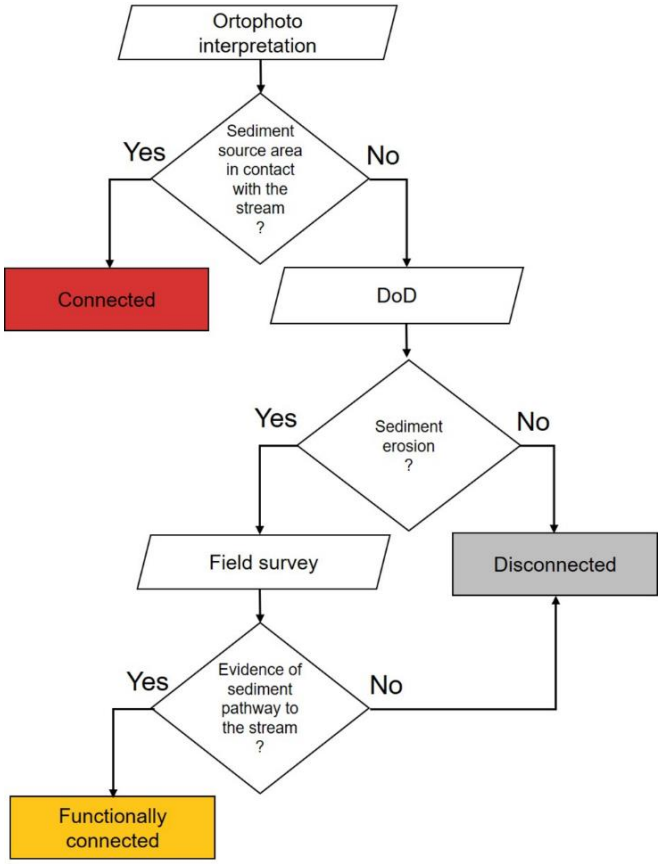

Figure 3.3. Decisional flowchart implemented to classify the sediment source areas in disconnected, connected and functionally connected. Trapezoids indicate the materials needed, diamonds indicate decisions to be taken and rectangles indicate process steps, i.e. the classification outcome.

Computation of the Index of Connectivity

The IC maps were derived using the open-source, stand-alone executable SedInConnect 2.3 (Crema and Cavalli, 2018), which exploits TauDEM tool for hydrological functions (Tarboton, 1997). According to the original formula by Borselli et al. (2008), the IC is composed by two components:

$$IC = log_{10}\frac{(Dup)}{(Ddn)} = log_{10}\frac{(\overline{W}\,\bar{S}\sqrt{A})}{(\sum_i \frac{d_i}{S_i W_i})} \quad (3.1)$$

where, D_{up} is the upslope component, in which the features about the catchment's upslope area are reported. Hence, $\overline{W}$ and $\bar{S}$ are the average value of weighting factor and the average slope (m/m) of the upslope area, respectively, and A is the contributing area (m^2) of the specific raster cell under investigation. The D_{dn} instead, represents the downslope component, in which the features affecting the sediment transfer are reported: d_i is the length (m) of the path along the i^{th} cell, W_i is the weighting factor and S_i is the slope gradient along the i^{th} cell. The logarithmic ratio between the upslope and downslope components returns the IC value for each cell.

For the purpose of the present study we evaluated three of the most common W factors: the Roughness Index (RI), the Mannings' n, and the C factor. The RI represents the topographic surface roughness and it exploits the DTM as the only input (Cavalli and Marchi, 2008). The RI was already implemented in the refined version of the IC by Cavalli et al. (2013) and in SedInConnect 2.3. It estimates the weight objectively and it is straightforwardly computed. The W factor is calculated from the RI as follow:

$$W_{RI} = 1 - \frac{(RI)}{(RI_{max})} \quad (3.2)$$

On the contrary, both Manning's n and the C factor are derived from pre-existing tabled data and they require a land cover mapping of the study area to be applied. In the Rio Cordon catchment, three major land cover classes can be distinguished: forest, grassland and bare rock. To achieve high-resolution land cover classification, otherwise impossible with pre-existing regional maps, the image classification technique was carried out. The 2015 orthophoto (0.2 m) was chosen for image classification as it offered the best quality: higher resolution than the 2006, fewer shadows than the 2019. Supervised classification was accomplished through ArcGIS Pro 2.4.1 maximum likelihood algorithm, using 224 training sample areas. To each land cover class Manning's n and C-factor values were assigned. The Manning's n is a parameter of hydraulic roughness; thus it offers an advantage for modeling impedance to water and sediment fluxes. The values were extracted from empirical

tables as in Persichillo et al. (2018), and Zanandrea et al. (2020). The W factor is calculated from the Manning's n as follows:

$$W_n = 1 - n \tag{3.3}$$

The cover and management factor (C factor) proposed in the USLE/RUSLE formula (Wischmeier and Smith, 1978; Renard et al., 1997) was originally implemented in the IC formula by Borselli et al. (2008). This parameter is used to model the soil erosion rates associated to different land cover and management practices. The correct C factor for each land cover class was extracted from Panagos et al. (2015), who estimated mean values in 28 countries of the European Union based on pan-European datasets such the CORINE Land Cover. The W factor is derived from the C factor straightforwardly:

$$W_{CC} = C \tag{3.4}$$

Indeed, the choice of the W factor influeces the final IC output because the RI, Manning's n and C factor show a different distribution of values as they are computed or extrapolated from different souces. Finally, the land cover map, enriched with appropriated W_n and W_{CC} for each class, was converted to individual W factor maps and resampled at the three resolutions. Considering also the W_{RI} maps automatically computed by SedInConnect 2.3., we obtained nine different W factor maps as a proxy for impedance to sediment fluxes in the IC computation (Figure S3.1, supplementary information). The nine IC maps were calculated setting the stream network of the Rio Cordon as a target. We included the whole stream network (Figure 3.1A) in order to investigate only the lateral connectivity and overlooking the transport capacity of the channel, which is not object of the present work.

The nine IC maps were hereinafter termed as presented in Table 3.1.

Table 3.1. The codification adopted to distinguish the IC variants according to spatial resolution (rows) and W factor (columns).

Spatial resolution (m)	W factor		
	Roughness Index	**Manning's *n***	**C factor**
0.5	IC_RI_0.5	IC_Wn_0.5	IC_Wcc_0.5
1	IC_RI_1	IC_Wn_1	IC_Wcc_1
2.5	IC_RI_2.5	IC_Wn_2.5	IC_Wcc_2.5

Logistic regression analysis

The logistic regression analysis lies in the basic principle that a dependent factor, in the form of a binary categorical variable (e.g. 0 and 1, false and true, absence and presence), is a function of one or more independent factors (Ayalew and Yamagishi, 2005). Therefore, the logistic regression finds the best fitting model to describe the relationship between dependent and independent factors. The fitting model has the following form:

$$Y = logit(p) = ln\left(\frac{p}{1-p}\right) = \beta_0 + \beta_1 X_1 + \beta_2 X_2 \ldots \beta_n X_n \quad (3.5)$$

where p is the probability of occurrence of the dependent variable (Y), β_0 is the intercept, and β_1, β_2, ... β_n are the coefficients of the independent variables X_1, X_2, ... X_n (Menard, 1995).

In this study, the application of the logistic regression consisted of: i) training nine logistic regression models considering connectivity status as dependent variable and one by one each IC variant as independent variables; ii) select the model with the highest performance; iii) using the most performant model to identify the IC threshold with the optimal cutoff; iv) validation of the model and associated IC threshold on an independent dataset.

First, median values for each sediment source were extracted from the nine IC maps. Using the median value, we summarized the IC avoiding the biases of outliers that may occur in large areas or due to computational errors. Moreover, the extrapolation of median values can be easily performed in GIS environment, making the procedure highly reproducible. Therefore, the inventory was enriched with nine IC median values per sediment source area. The 431 samples were split into two groups: the pre-event sources and post-event sources. Specifically, 405 pre-event sediment sources were used in the training phase, while the 26 post-event sources (see section *sediment source areas*

inventory) were used for model testing and validation as independent dataset. Second, the connectivity status, representing the dependent variable, was considered as a binary variable: disconnected and connected. Connected sources also included functionally connected ones, which were considered partitioned only for discussing the final results. Data preparation was carried out in ArcGIS Pro 2.4.1.

For each model variant, the training phase was carried out using repeated 10-k-fold cross validation, in which the dataset is split into 10 subsets (folds) and while one subset is held out, the model is trained over the remaining 9. This process is repeated 10 times, where the data sample is shuffled at each repetition until the mean model accuracy is returned. As the dataset was highly imbalanced, the repeated k-fold cross validation guaranteed the same proportion of connected and disconnected sources in each fold. Confusion matrices were produced for each of the 9 model variants.

Receiver operating characteristic (ROC) curve is largely used to assess performance of logistic regression models. Moreover, with imbalanced dataset, also precision-recall (PR) curves can be adopted. While the former considers recall (true positive rate) against specificity (true negative rate), the latter takes into account plots precision (positive prediction value) against recall. The computation of the area under ROC curve (AUC) and precision-recall curves (AUPRC) are used to evaluate the performance of the 9 model variants: the closer the AUC and AUPRC values are to 1, the better their predictive capability (Bradley, 1997). In addition, the McFadden pseudo R^2 for logistic regression was used to compare the models (McFadden, 1973). In conclusion, for this step, the best model was chosen as the one with the highest AUC, AUPRC, and R^2.

Once the best model was identified, the IC threshold was determined according to the optimal probability cutoff along the ROC curve. The cutoff (range 0 to 1) was determined among those having the highest Youden's J statistic (Youden's index, range 0 to 1) and the F-measure (F-score, range 0 to 1). The Youden's J maximizes sensitivity and specificity, while the F-measure is the harmonic mean of recall and precision. From the optimal probability cutoff, the corresponding IC value was derived using the inverse function (eq. 3.5). Finally, the best model with optimal cutoff was validated on the independent dataset made by the 26 post-event sediment sources. Confusion matrix was produced and the results discussed. All the statistical procedure was conducted in RStudio 1.2.5019 (R Core Team, 2020).

Results

The assessment of sediment connectivity pointed out a notable difference between the number of disconnected and connected areas. In the Rio Cordon after the Vaia storm, we identified 369 disconnected and 64 connected sediment source areas, of which 7 were classified as functionally connected sources, thereby showing a connectivity status strictly related to the event (Figure 3.4). Therefore, the 26 areas reactivated after the Vaia storm are distributed in 7 functionally connected, 7 connected, and 12 disconnected sediment sources. The total surface area classified as disconnected, connected, and functionally connected was 620574 m^2 (91%), 44088 m^2 (7%), and 11110 m^2 (2%), respectively.

Among the 57 connected areas 28 were landslides, 16 stream bank erosions, 10 surficial erosions, 2 debris flows, and 1 rockfall. However, to determine which typology is the most connected, the relative number of connected sources for each typology was calculated: 100% of the rockfalls (1/1); 84% of the stream bank erosions (16/19); 13% of the landslides (28/219); 12% of the surficial erosions (10/86); 2% of the debris flows (2/80) and 0% of the active talus (0/26). Moreover, among the 7 functionally connected, 5 landslides and 2 debris flows were detected. Several connected areas were found in the middle part of the catchment, in correspondence with the gorge, where steep and active sources are directly overhanging the main Rio Cordon channel. Other smaller connected areas are present along the tributaries developing on the eastern part of the catchment. On the contrary, functionally connected areas, were found in the south-western part of the catchment, where the presence of tributaries is limited.

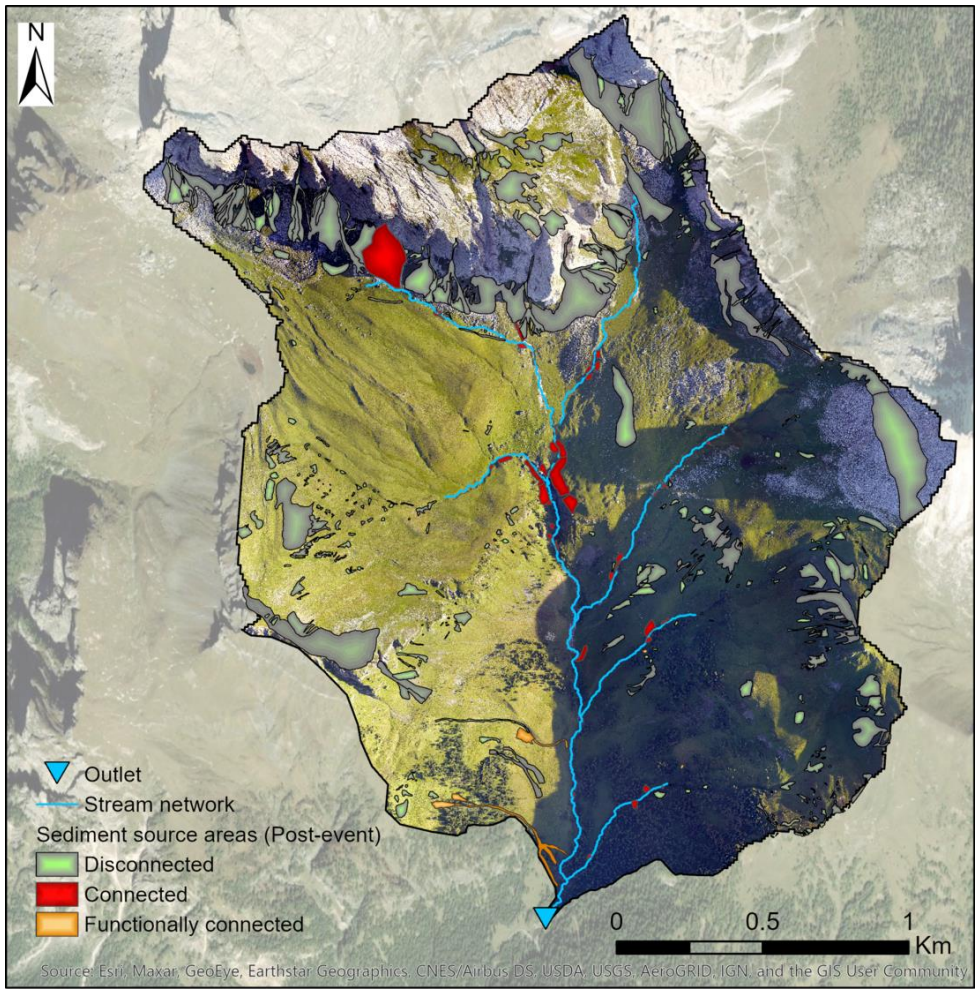

Figure 3.4. The location of the sediment source areas of the post-event inventory classified in disconnected, connected and functionally connected.

The IC maps are presented in Figure 3.5, considering the channel network as a target, three different raster cell dimensions, and three different W factors. In all the maps, high IC areas are visible in the center of the maps, in correspondence to the steep gorge, and in the upper Rio Cordon catchment, where the almost vertical rock walls are close to the channel network. However, major differences can be observed especially among the IC computed with different W factors. Moving from left to right maps in Figure 3.5, it is possible to identify a substantial increase in low IC areas. Notably, the IC_Wcc maps (Figure 3.5C-F-I) show an overall lower IC pattern compared to the IC_RI maps (Figure 3.5A-D-G) and IC_Wn maps (Figure 3.5B-E-H). In all scenarios, the lowest IC areas are located in the upper plateau and the upper part of the tributaries.

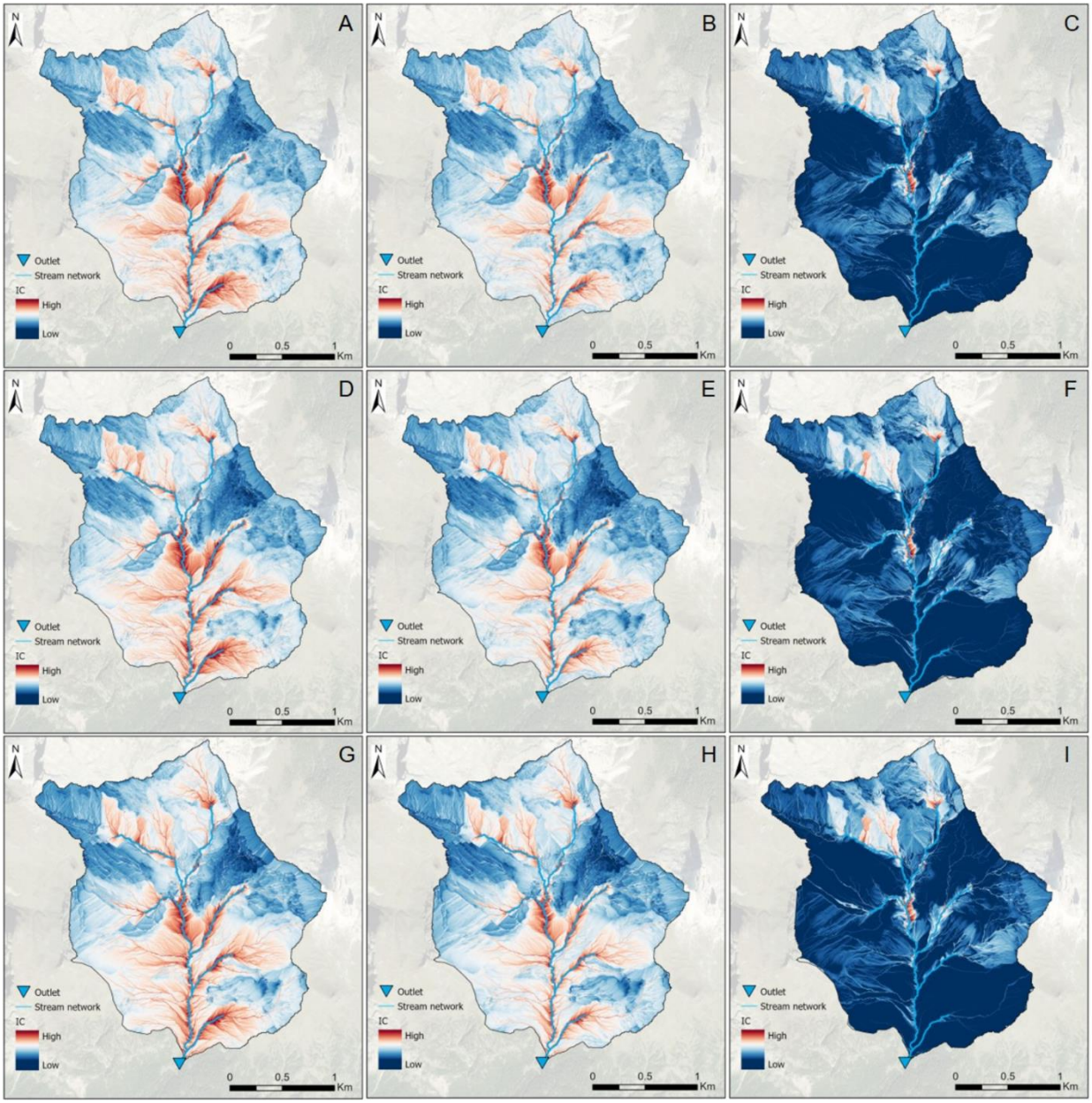

Figure 3.5. The nine IC maps computed according to different spatial resolution (rows) and W factors (columns). Specifically: IC_RI_0.5 (A); IC_Wn_0.5 (B); IC_Wcc_0.5 (C); IC_RI_1 (D); IC_Wn_1 (E); IC_Wcc_1 (F); IC_RI_2.5 (G); IC_Wn_2.5 (H); IC_Wcc_2.5 (I). The IC values are represented with stretched classification (blue ~ low / red ~ high).

Table 3.2. Main descriptive statistic of the nine IC variants. Particularly, mean, min and max, median and interquartile ranges (IQR) are reported.

	Mean	**Min / Max**	**Median**	**IQR**
IC_RI_0.5	-3.60	-7.56 / 2.38	-3.65	1.24
IC_Wn_0.5	-3.80	-7.51 / 2.30	-3.67	1.23
IC_Wcc_0.5	-5.77	-12.09 / 2.21	-5.57	1.56
IC_RI_1	-3.22	-7.26 / 2.40	-3.23	1.23
IC_Wn_1	-3.41	-7.16 / 2.35	-3.42	1.18
IC_Wcc_1	-5.35	-11.67 / 2.29	-5.35	1.66
IC_RI_2.5	-2.75	-6.53 / 2.51	-2.70	1.20
IC_Wn_2.5	-2.92	-6.68 / 2.48	-2.89	1.15
IC_Wcc_2.5	-4.84	-11.26 / 2.45	-4.84	1.67

Quantitative differences are highlighted in Table 3.2, where main descriptive statistics are reported. First, it is possible to verify that the lowest IC median, min, max, and mean values are obtained using the IC_Wcc with all three spatial resolutions. For instance, considering the median at decreasing resolution, IC_Wcc values are -5.57 -5.35 and -4.84, while IC_RI values are -3.65, -3.23 and -2.70 and IC_Wn values are -3.67, -3.42, and -2.89. On the contrary, in fact, IC_RI variants show the highest IC values, while IC_Wn variants exhibit the lowest dispersion, having, the lowest interquartile ranges (IQR). Worth noting is the close difference between IC_RI and IC_Wn values , indicating similar distributions of the two W factor values, Roughness Index and Manning's n in the study area. On the contrary, IC_Wn and IC_Wcc have larger difference. Second, an increasing trend is observable considering the differences in spatial resolution: the coarser the resolution, the higher the IC values.

Differences among the IC variants are also visible when considering the distribution of all values extrapolated from the sediment source areas. Particularly, the IC values of all the nine combinations, of the source areas classified as disconnected, connected, and functionally connected are presented in Figure 3.6. The main difference is again evident when using different W factors: lower IC values for the IC_Wcc variants (Figure 3.6A-B-C). Still, with coarser resolution, an overall increase of IC values is registered for all the three connectivity analyses. Nevertheless, the main focus is the difference in the connectivity status in order to provide insights on the predictive capacity of the IC. The results indicates a distinction of IC among disconnected, connected, and functionally connected sources at

least in three cases. Connected areas have always the highest IC values, followed by functionally connected areas in six cases.

Differences among the IC variants are also visible when considering the distribution of all values extrapolated from the sediment source areas. Particularly, the IC values of all the nine combinations, of the source areas classified as disconnected, connected, and functionally connected are presented in Figure 3.6. The main difference is again evident when using different W factors: lower IC values for the IC_Wcc variants (Figure 3.6A-B-C). Still, with coarser resolution, an overall increase of IC values is registered for all the three connectivity analyses. Nevertheless, the main focus is the difference in the connectivity status in order to provide insights on the predictive capacity of the IC. The results indicate a distinction of IC among disconnected, connected, and functionally connected sources at least in three cases. Connected areas have always the highest IC values, followed by functionally connected areas in six cases.

Therefore, disconnected areas exhibit the lowest IC values except in three cases, characterized by the Wcc, where functionally connected areas show the lowest distributions. Furthermore, functionally connected areas show the lowest IQR concerning the IC_1 with all three different W factors (Figure 3.6B). Finally, the differences among the three connectivity status are reduced with coarser resolution (Figure 3.6C), suggesting that using IC_2.5 variants for predicting sediment dynamics could be less suitable due to a potential overlap. Anyway, from visual assessment, the distinction between disconnected and connected sources can be always detected, at approximately -2.5 - -3, depending on the chosen W factor and resolution.

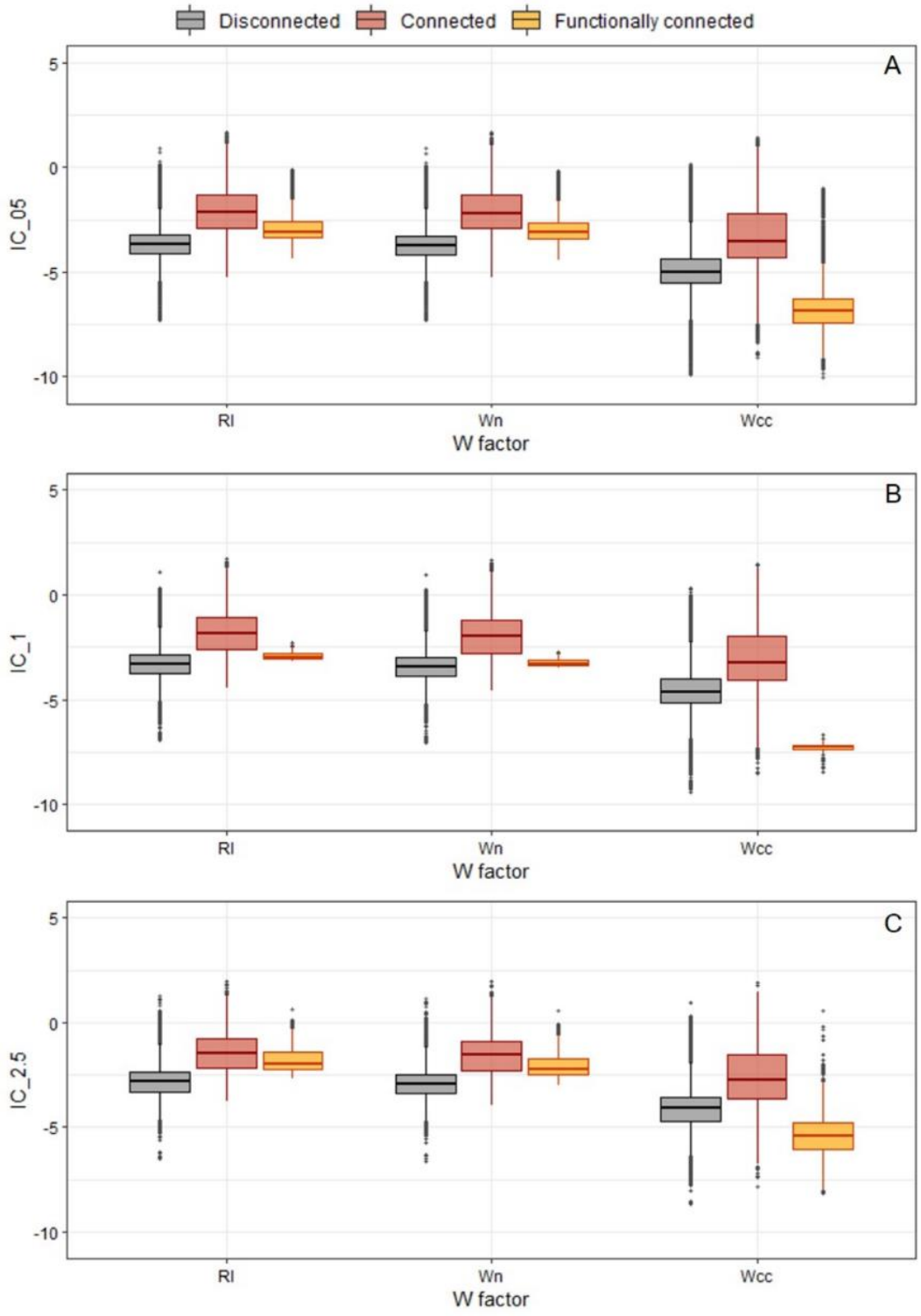

Figure 3.6. The IC value distributions of the post-event sediment sources grouped according to connectivity status (colours), W factors (x axis) and spatial resolution (A-B-C). Specifically, box indicates the interquartile range, whisker the values included within 1.5 times the interquartile range.

The logistic regression analysis pointed out a statistically significant relationship between the connectivity status and the IC in all nine models. However, in order to identify the best IC variant, first ROC curves were plotted (Figure 3.7) in order to visualize the model with the highest performance in terms of sensitivity and specificity. As clearly visible, all nine curves show good performance but six curves are highly intertwined and close to the top-left corner, indicating very high performance. On the contrary, three curves are at lower position, indicating lower performances.

Hence, from a visual assessment, models with IC_RI and IC_Wn variants are interchangeable and offer higher predictive performance than IC_Wcc-based models. Furthermore, these results are confirmed by the AUC, AUPRC, and pseudo-R^2 values (Table 3.3). The model with the highest parameters is the IC_RI_0.5 with 0.99 AUC, 0.84 AUPRC and 0.76 pseudo R^2. Nevertheless, very high performance is also showed by IC_RI_1, IC_Wn_0.5 and IC_Wn_1, since they have close values to IC_RI_0.5. However, it is clear that the three IC_Wcc variants show lower performance and their associated models are less preferable for depicting lateral sediment connectivity.

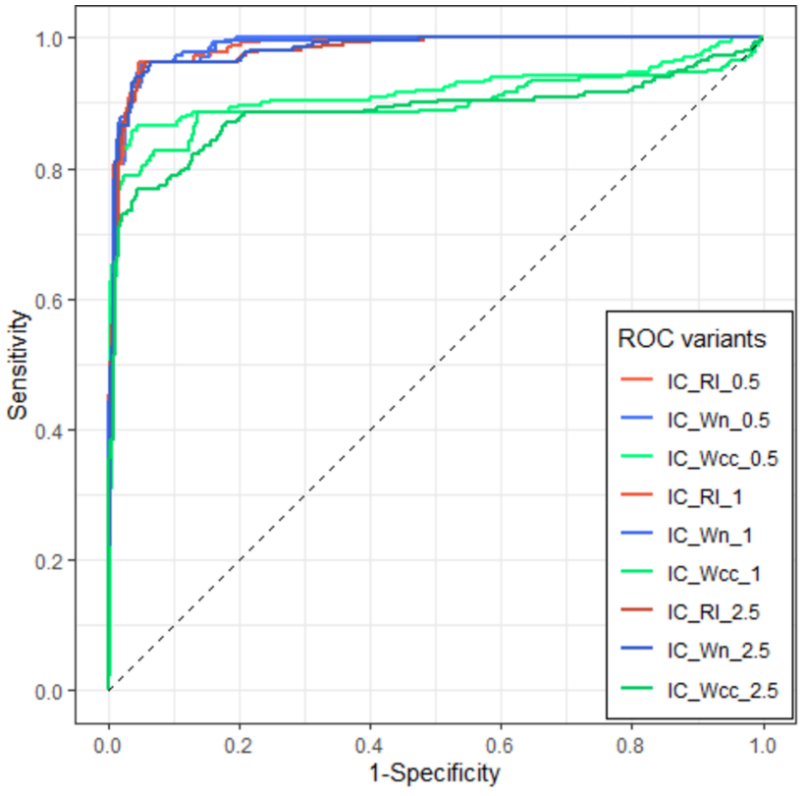

Figure 3.7. ROC curves of the nine models derived from the binary logistic regressions. Different colours refer to different W factors and different shades of the same color refer to different spatial resolutions.

Considering the IC_RI_0.5 as the most appropriate model, the calculated optimal probability cutoff is 0.15, which maximized the Youden's J and F-measure, with values of 0.89 and 0.82, respectively. The corresponding IC threshold, calculated using the RI at 0.5 m resolution, is -2.32, which represents the discriminating factor between disconnected and connected sediment sources. Using the probability cutoff of 0.15, the prediction was made on the 26 post-event sediment sources in order to validate the IC_RI_0.5 model. The confusion matrix gives the following results: 9 true positives, 11 true negatives, 1 false positive, and 5 false negatives (Table 3.4). Hence, the model correctly predicts 20 sediment sources and fails to predict 6 sediment sources, which does not indicate high predictability performance. Particularly, the confusion matrix highlights primarily type 2 error (false negatives) rather than type 1 error (false positive). In other terms, the model fails in predicting 5 connected sources, as they were wrongly classified as disconnected. Considering the characteristics of these 5 areas, it emerges that they correspond to only functionally connected sediment sources. Hence, among the 7 functionally connected sources observed in the Rio Cordon after Vaia storm, 5 were not correctly classified by the logistic regression model IC_RI_0.5.

Table 3.3. Results of the Area Under Curve (AUC), Area Under Precision-Recall Curve (AUPRC) and McFadden pseudo R^2 obtained for the models under evaluation. The highest values are marked (*).

Model IC variants	AUC	AUPRC	Pseudo R^2
IC_RI_0.5	0.99*	0.84*	0.76*
IC_Wn_0.5	0.99*	0.83	0.76*
IC_Wcc_0.5	0.92	0.76	0.64
IC_RI_1	0.99*	0.81	0.73
IC_Wn_1	0.99*	0.82	0.74
IC_Wcc_1	0.90	0.71	0.56
IC_RI_2.5	0.98	0.81	0.71
IC_Wn_2.5	0.98	0.82	0.73
IC_Wcc_2.5	0.89	0.69	0.52

Table 3.4. Confusion matrix for binary classification of the 26 connected and disconnected sediment sources reactivated during the event.

Predicted	**Observed**	
	Connected	Disconnected
Connected	9	1
Disconnected	5	11

Discussion

Wohl et al. (2017), and Heckmann et al. (2018), suggested and emphasized the need of considering parameters measuring sediment connectivity as a starting point rather than the aim of research. This shift of attention makes the computation and adaptation of indices, such the IC, not the ultimate outcome but a tool for depicting structural sediment connectivity and predicting real sediment dynamics. Testing the use of IC as a predictive tool in mountain catchments was already recommended by Pellegrini et al. (2021), which found onsite correspondence between spatial patterns of high IC and actual sediment transfer before and after a large infrequent disturbance. More detailed was the analysis by Calsamiglia et al. (2018), who surveyed collapses of terrace walls and found that more than 70% were located in areas of very high IC values based on quantile distribution.

In this paper, we validated and measured the capability of IC to depict lateral sediment connectivity and to predict hillslope to channel sediment dynamics by exploiting the sediment source area inventory of the Rio Cordon catchment and applying logistic regression analysis. The assessment conducted with remote sensing and field observations showed that 15% of the sediment sources was connected to the stream network. Apart from the single rockfall located in the upper channel network, as expected the most connected typology is the stream bank erosion due to its inherent proximity to the stream. On the contrary, most of the debris flows and active talus were found disconnected. Although active talus cover large areas in the upper Cordon, they historically have a limited role in the basin sediment yield (Dalla Fontana and Marchi, 2003). Therefore, the sediment originated in the upper rocky walls has very low chances of reaching the outlet because of i) the disconnection between the sources and the stream network, ii) absence of an efficient sediment transfer within stream network in the upper plateau (Oss Cazzador et al., 2021), and iii) the overall topographic disconnectivity between upper and lower basin (Cavalli et al., 2016; Rainato et al., 2017). The assessment was accomplished thanks to a stepwise method using remote sensing data and targeted field inspections. Even if the method requires multi-temporal data and a solid knowledge of the study area and considering the potential errors by the operators, like for instance in the construction of the land cover map, it provided a realistic and expeditious system to evaluate the connectivity status. Furthermore, it is worth recalling that the location of the connected and disconnected areas is strictly dependent upon the branching of the stream network. For instance, as the eastern slope is crossed by more tributaries than the west one, it is likely to find more connected sources.

Different IC variants were compared to evaluate the effect of two major user-defined factors: weighting factor and spatial resolution. The choice of the W factor depends upon the aim of the study and the characteristics of the study area. As expected, the C-factor provided the worst results in terms

of predictability. In steep mountain catchments, where forest cover is not predominant, parameters of surface roughness are recommended over land-use-based ones (Cavalli et al., 2013; Llena et al., 2019). Nevertheless, the IC computed with Manning's n showed good results despite that it was derived from land cover maps and tabled data subjectively selected (Zanandrea et al., 2020). Hence, in this study, the poor results associated with the C-factor are to be found in the distribution and variability of the values rather than in the land cover map and in the method used to derive it. The spatial resolution had also an important effect on the predictability, with the highest pixel size (2.5 m) less suitable for the analysis. In agreement with Brardinoni et al. (2015) and Cantreul et al. (2018), an increasingly coarser resolution results in an overall higher IC. This trend reduced the discrepancy between the IC values of disconnected, connected, and functionally connected sediment sources, thus limiting the performance of the models carried out with IC at 2.5 m resolution. Sensitivity to pixel size is clearly a factor to be considered as it highly affects the results of sediment connectivity (Cantreul et al., 2018). The optimal resolution cannot be defined a priori because it depends on the size of the catchment, the scale of landforms and processes involved, and the objectives of the research. Nevertheless, to establish the optimal spatial resolution, field assessments must not be neglected to cross-check the results or to set the reference. Finally, it is important to underline that apart from the IC computed with the C- factor or the 2.5 m resolution, the other variants obtained notable results in terms of predictability. The models' comparison pointed out that these four IC variants (with RI or Manning's n at 0.5 m or 1 m) are still suitable for predicting structural sediment connectivity of the sediment sources in the Rio Cordon. This conclusion can be helpful because it gives leeway to future researches in the catchment. Considering a scenario with lower data availability, still it will be acceptable to use an IC calculated at a pixel size lower than 2.5 m with either the RI or the Manning's n as W factor.

On the contrary, the results showed that the IC was not able to successfully predict the sediment sources classified as functionally connected. This is not surprising since by definition IC is mainly derived from the topographic characteristics, thus intrinsically incapable of providing information about event-based sediment fluxes (Turnbull et al., 2018). In practice, in our study, we found that this issue was already visible from the boxplots (Figure 3.6), where in most cases functionally connected areas had overlapping distributions with connected and disconnected areas. As consequence, this affects the capability of the logistic model to distinguish the two classes and fails to predict them correctly. Therefore, in accordance with Baartman et al. (2020), to represent sediment connectivity in a more complete way, other indices incorporating the functions external events, should be adopted. In this work, we tested the IC also as predictor of sediment dynamics but more controlling factors,

could have been added in the logistic models to provide a more comprehensive analysis. Event rainfall, lithology, soil properties (e.g., moisture, infiltration and saturation capacity) are some of the spatially distributed features worth considering in future research.

Many logistic regression studies are widely used in machine learning problems such landslide susceptibility (Budimir et al., 2015; Youssef et al., 2016; Chen et al., 2017). Fewer applications for gully (Conoscenti et al., 2014) and riverbank erosion susceptibility (Atkinson et al., 2003), and no one for connectivity-related issues. The results presented in this study were developed thanks to an ad-hoc statistical procedure, in which three main critical issues were found. First, the extrapolation of IC from each sediment source was made using the median, which is highly reproducible but perhaps simplistic. Second, the imbalanced training dataset (15% connected, 85% disconnected) forced the computation of other parameters to compare the models' fitting. Using only the ROC curves and AUC, as typically done, it was impossible to find the best model, so that the AUPRC and pseudo-R^2 were used in addition. Third, the independent dataset, used for the models' validation, was based only on 26 samples. We think that these issues shall be addressed in order to seek maximum reproducibility of the statistical procedure.

Mapping sediment connectivity was defined crucial to understand the sediment spatial patterns and their evolution (Cavalli et al., 2019). Traditionally the IC maps are recommended for catchment management purposes, since they highlight the areas with a potential higher chance to deliver sediment to a specific downstream target (Cavalli et al., 2013). Moreover, with the accessibility and extensive use of remote sensing techniques in modern mapping (Pereira et al., 2018), the computation of the IC and the production of IC maps is becoming easier and straightforward. However, the typical representation of high and low connectivity that characterizes the most common IC maps is suitable for a rapid qualitative/semi-quantitative evaluation of the main spatial patterns of connectivity. In most cases the transition between low and high IC, or between decrease and increase in case of IC multitemporal analyses, is fuzzy and the user decides how to classify the maps based on natural breaks (Kalantari et al., 2017; Cucchiaro et al., 2019; Martini et al., 2020), quantiles (Calsamiglia et al., 2018; Jautzy et al., 2021) or normalized distributions (Nicoll and Brierley, 2017) of the values. To move a step forward, our results showed the possibility to derive a site-specific threshold that could objectively discriminate between high and low IC areas. Therefore, the prioritization of the areas likely to be connected to the streams is based on a well-defined methodology that accounts for field-based investigation and statistical analysis. An example of the application of such threshold in the Rio Cordon is presented in Figure 3.8, where high connectivity areas are highlighted. The map shows the areas with IC values higher than the threshold and it can provide a rapid information on the most

important areas to be considered for catchment management purposes. Certainly, this map is subjected to uncertainty due to the assumptions and errors already discussed, but it also represents more faithfully the structural sediment connectivity in the Rio Cordon catchment.

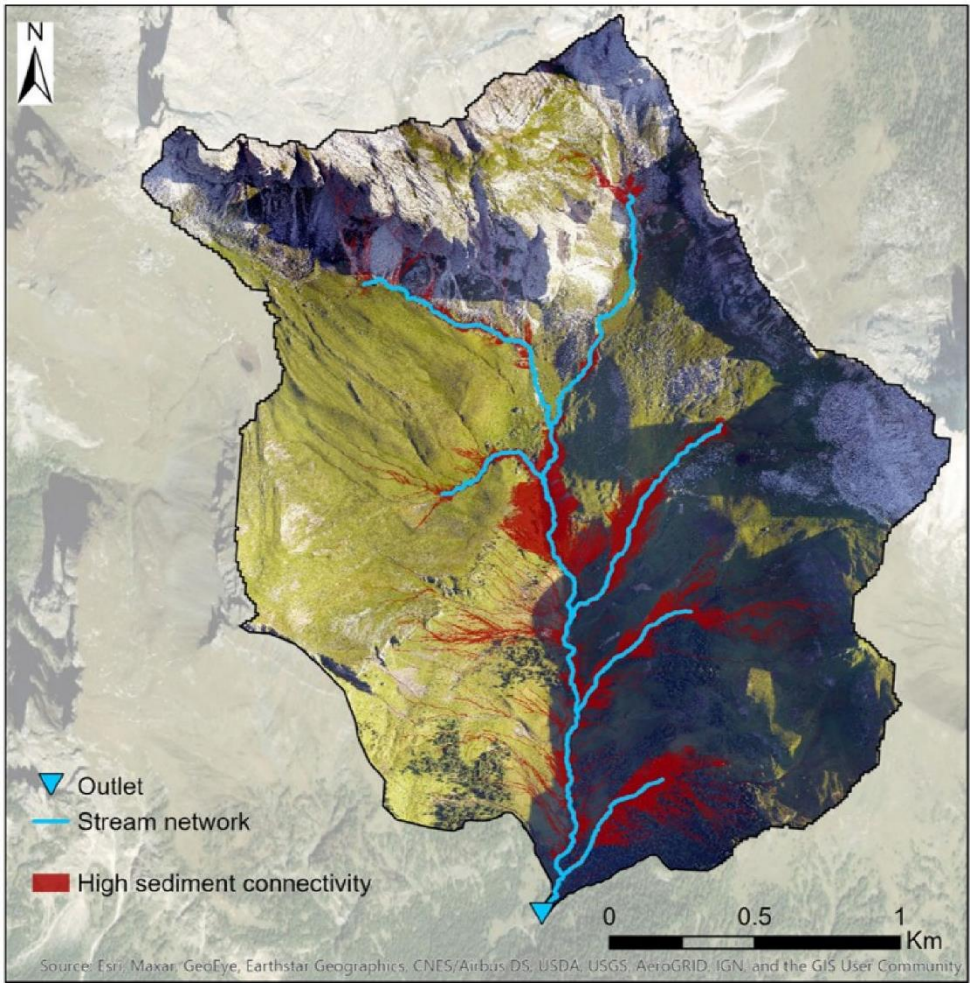

Figure 3.8. High sediment connectivity in the Rio Cordon is highlighted in areas where the IC threshold is exceeded.

Conclusions

In the Rio Cordon catchment, understanding the role of sediment source areas is vital to predict the sedimentological response of the stream to disturbances. In this area, the long-term history of hydrological, geomorphic, and sedimentological analyses has been always supported by a qualitative notion of sediment connectivity through IC maps. However, starting from the traditional and qualitative interpretation of the maps, we proposed a statistical approach able to differentiate high to low sediment connectivity based on the actual lateral connectivity sources-streams found in the catchment. The results showed that it is feasible to derive an accurate IC threshold able to classify connected and disconnected sediment sources. In this way, it is possible to make use of IC maps to represent and communicate the areas to be considered for a potential connection to the stream network. Considering the methodological approach proposed in this study, the IC was proven to be a useful and practical tool for depicting structural sediment connectivity. It was also demonstrated that, in a mountain basin characterized by low vegetation cover and a small drainage area, the most suitable IC is derived using high-DTM resolutions and surface roughness as weighting factor. On the contrary, to infer functional connectivity other approaches must be adopted in order to include event-based variables capable of representing the processes besides the static linkages. In conclusion, this study tested to the potential advantages and disadvantages of using IC to infer sediment connectivity in mountain catchments. In this way, we feel that we shed more light on the most appropriate IC applications, avoiding speculation over structural-based indices.

General discussion

The outcomes of this thesis tackled specific challenges and issues in the field of connectivity and, together, they provided relevant sources of discussion. Common sources of discussion can be identified within the studies presented in chapter 1, but also amongst different chapters. Nevertheless, all study cases presented various objectives, methodological approaches and results, hence different and peculiar arguments have been raised.

The different characteristics of the catchments affected by disturbances, and the peculiar effects provoked by these disturbances, required the adaptation of the topography-based IC (Cavalli et al., 2013). Starting from pre-existing approaches and knowledge of IC, first new modifications and workflows have been proposed, implemented, and refined in two different study cases in Chile (chapter 1). In the Blanco River catchment, the explosive eruption that occurred between 2008 and 2009 led to significant changes in the structural properties of the basin at different temporal and spatial scales. For this reason, it was important to carry out a multi-temporal analysis of IC as a proxy for documenting potential changes in sediment connectivity over time and to highlight the role of the disturbance in producing those changes. It became clear that the impact of the eruption, driving the variation of sediment connectivity, could be traced back to two main effects: land cover changes and widening of the active channel.

Long-term perturbations, like land cover changes, affect sediment connectivity directly by altering the water runoff and increasing/reducing the impedance to sediment fluxes, or indirectly by changing the structural configuration of the hydrological/sedimentological controlling features (Lopéz-Vicente et al., 2013; Lizaga et al., 2017; Llena et al., 2019). Defined by Brunsden and Thornes (1979) as ramps, this type of disturbances is propagated over time and space, potentially inducing permanent variations in the boundary conditions of the system. Interestingly, in the context of the Chaitén volcano eruption, the land cover changes are the immediate result of another large infrequent disturbance, rather than the effect of long-lasting perturbations, such land abandonment, deforestation and urbanization. Therefore, the response of sediment connectivity could be studied in a relative medium period (16 years) and following two scenarios: pre-eruption and post-eruption. In addition, the eruption and subsequent cascading processes conveyed a huge amount of material that modified the entire floodplain, enlarging the active channel and consequently promoting lateral migration of the Rio Blanco. Hence, the fluvial adjustments were included because of their role in promoting or

preventing the coupling between new sediment source areas and the channel network, i.e. lateral sediment connectivity (sensu Brierley et al., 2006).

In the Rio Toro case, the impact of the wildfires was limited to the land cover, which suffered major forest reduction as pointed out by the fire severity assessment and field surveys. Differently from the Rio Blanco, in which fluvial morphological changes had to be considered to better represent the multi-temporal variation of sediment connectivity, in the Rio Toro catchment channel adjustments were not detected. The topography and the configuration of the channel network were completely different in the two catchments, with the Rio Blanco draining a larger watershed, developing in a wider valley and thus showing a wandering/braided planform (Ulloa et al., 2016). On the other hand, the Rio Toro shows characteristics of mountain river system, with a narrow stream network and plane-bed/step-pool morphology (Comiti et al., 2008). Moreover, in the first case, the Chaitén eruption was responsible of large sediment input that triggered river adjustments, while in the second case the wildfires did not directly affect the sediment dynamics within channels. Therefore, in both catchments, a similar strategy was required to integrate the spatial-temporal land cover changes into the geomorphometric approach based on IC. This strategy was primarily built around the weighting factor.

The weighting factor (W factor) is the most adaptable factor in the IC formula, as it represents the impedance to sediment fluxes according to the needs of the user. The choice and implementation of the W factor was always a critical step in the methodology and a wide source for discussion. To involve the effects of land cover before and after the disturbances, an ad-hoc W factor was derived and implemented thanks to a workflow based on a combination of satellite images and field surveys. In the Chilean study cases, the Manning's n was preferred over other parameters, such as the Roughness Index (RI) of Cavalli and Marchi (2008), and the C factor of the USLE formula (Wischmeier and Smith, 1978), to derive the W factor. This decision was deeply discussed in each study case and it can be summarized in three main points: i) the Manning's n can be adapted by the user according to the characteristics of the study area by using the additive method by Arcement and Schneider (1989); ii) the RI, although objectively derived, requires high-resolution DTMs and low forest cover to perform accurately; iii) the C factor is more suited to agricultural areas and has a limited distribution of values. However, it is important to underline that, when the conditions are favourable for the other parameters, the choice has to be rethought. In this sense, in the Alpine catchment Rio Cordon, the three W factors were used to derive IC maps that were then tested for their capability in depicting structural sediment connectivity. The results confirmed that in this environment, characterized by steeper slopes with lower forest cover than the Chilean catchments, a

terrain roughness-based parameter (RI) performs better than the Manning's n and the C factor, although the former achieved good results as well.

Hence, it is fundamental to know the characteristics of study area, be aware of the data available and consider the objective of the research before choosing the W factor. In other terms, instead of using the most known or ready-to-use W factor, in line with other authors who investigated how different W factors affect IC after disturbances (Ortíz-Rodríguez et al., 2017; López-Vicente et al., 2020; Zanandrea et al., 2020), we preach critical thinking to implement the most appropriate W factor for each situation.

The computation and implementation of the W factor constitutes a major step of the methodological workflows presented in the studies. Given the array of variables involved in all studies, it became essential to organize the analyses in subsequent phases, blocks or steps. Furthermore, the presence of a workflow helps the reproducibility of the research providing also a track for further improvements. Without any suitable land cover map to derive W factor maps in the Rio Blanco catchment, i) field surveys were carried out to classify the land cover and assess on-site roughness characteristics and ii) open-source satellite images were adopted to perform image classification, thus implementing the Manning's coefficient into W factor maps. The workflow was applied 16 times to derive a consistent multi-temporal analysis for the whole study period. Reproducibility was also attested in the Rio Cordon (chapter 3), using a simplified version of the approach. Here, the methodological approach was used to implement different W factors and to compute different IC variants, constituting the independent variables in multiple logistic regression models. Nevertheless, a reproducible workflow is also helpful for developing further improvements. In central Chile, in fact, the response to wildfires was integrated into IC using an adapted and refined version of the approach first proposed in the Rio Blanco. Indeed, important upgrades were applied to better represent the potential effect of fires on sediment connectivity and, more specifically, to exploit the spectral index IFZ, which tracks vegetation recovery after the disturbances.

The reproducibility of the workflow depends also on another aspect, already mentioned before and related to data availability. In this sense, there is a net distinction between the first chapter and the other two. In chapter 1, the IC maps were computed thanks to freely available satellite products, precisely the DEM and the satellite images (real colour and multi-spectral). These study areas, lacking coverage of free high-resolution products or with acquisition costs too high given the size of the catchments, open-source data were found a good compromise to study catchment-scale patterns of sediment connectivity. In the Rio Cordon instead, the presence of LiDAR-derived DTMs and orthophotos was clearly a deal breaker but they do not guarantee the reproducibility of the analyses

everywhere, yet. However, despite the issue of reproducibility, paid high-resolution data have indubitably greater advantages than free of charge coarse resolution data. At coarse resolution, it was possible to identify only macro changes of IC, thus giving only large-scale insights. Therefore, in both Rio Blanco and Rio Toro, the objectives were more oriented on how to assess the overall impact of disturbances on sediment connectivity rather than focusing on the single source-to-channel relationship. Conversely, in the analysis of the geomorphic response to the Vaia storm (chapter 3), thanks to high-resolution IC maps and DoD it was possible to inquire about the role of sediment sources in supplying sediment to the channel network. In this way, it was feasible to link the hydrological and sedimentological responses and carry out an integrated analysis with a coherent spatial scale. Considering a study case in which high-resolution data are not available, the same analysis of sediment connectivity would not have been adequate to support the outcomes of the study and to reconstruct the whole sediment cascade.

Working with an appropriate spatial data resolution is essential when investigating sediment connectivity. Sediment connectivity outcomes can be source of severe misinterpretations when the scale of data, analysis and objectives is unbalanced. Especially, in methodologies exploiting the IC, the spatial scale has to be coherent with the planned objectives and the results expected. For instance, a 30 m DEM is not suitable to derive IC map to study potential sediment transfer within rill or gullies. The actual width of sediment route has to be at least equal to the cell size of the DEM. With coarser resolution, in fact, the pathways are oversimplified and the disconnectors omitted, thus increasing the overall connectivity as already reported by some authors (Brardinoni et al., 2015; Nicoll and Brierley, 2017) and supported by the results of the last chapter in this thesis. On the other hand, it has been demonstrated that increasing too much the resolution heavily affects the geoprocessing time, only heading to a small improvement in the fine-scale features representation and, sometimes, even causing spurious disconnections (Cantreul et al., 2018). Finally, what emerges is how difficult it is to define the most appropriate spatial resolution a priori. Many factors are in play, like for instance, the scale of landforms, the size of the phenomenon under investigation, DEM uncertainty, processing time and the purpose of the study.

A fundamental boost to the rapid increase of connectivity-related studies is given by the even faster growth of remote sensing techniques. Thanks to remote sensing data and consequent processing operations, the application of indirect measures of connectivity, like Effective Catchment Area (ECA), Sediment Delivery Ratio (SDR) or IC, is more straightforward and doable at catchment-scale. Accordingly, in this work, it has been proved that different products obtained from different remote sensing platforms definitely help the characterization of sediment connectivity in multiple catchments

of different dimensions and under different conditions. Furthermore, the wide range of sources for topography and imagery, is making such applications easier for anyone interested in the subject. If, on one hand, this tendency clearly leads to benefits, on the other hand, it may cause the proliferation of analyses that overlook important ground rules. That is why in the previous paragraphs the importance of undertaking careful choices to ensure a correct implementation of the IC was stressed out (e.g. selection of the W factor), to build a reproducible approach (e.g. a workflow coherent but also adaptable to specific contexts) and to improve the reliability of the outcomes (e.g. setting the appropriate spatial scale). Therefore, although remote sensing data are now an essential prerequisite for developing an IC-based study, critical thinking alongside a minimum knowledge of the study area are, once again, to be preferred. In this sense, field surveys are still considered good practices and large consensus around this conclusion is well documented. Messenzehl et al. (2014), argued that traditional field mapping remained fundamental to validate and improve the results obtained from IC maps "in our modern pixel-dominated world". Nicoll and Brierley (2017), stressed the incapability of IC in differentiating activity levels of sediment storages that were, however, evident in the field. Nevertheless, their assessment was probably vitiated by the coarse spatial scale considered (> 30 m), which is not indicated for a straightforward application of IC. To detect flat areas acting as disconnectors for sediment connectivity, Hooke et al. (2021) underlined the importance of field observations for further validation even when using high-resolution data, like UAV products. Therefore, as part of the validation process, field-based approaches are still recognized as important if not essential (Lexartza-Artza and Wainwright, 2009; Mahoney et al., 2018; Hooke and Souza, 2021). For these reasons, field activities were carried out in all four study cases. In Chilean catchments, the goal was to assess the land cover conditions as part of the process building the ad-hoc Manning's coefficient. Without ground validation, it would have been impossible to adapt the W factor and to characterize the post-disturbance scenarios. Regarding the third study case, many field surveys were carried out to i) reconstruct the hydrograph of the flood; ii) validate the outcomes of the sediment connectivity analysis; iii) estimate the sediment transport and boulder mobility. With particular attention to the sediment connectivity, the evidence from the field helped to validate the results obtained from IC-DoD analysis, permitting the distinction between the six source areas that did supply sediment and the twenty sources that did not. In the last chapter, field mapping represented a fundamental procedure in order to assess the connectivity status between sediment sources and the stream network. The integration of on-site and remote assessments allowed the classification of all the sources in disconnected, connected or functionally connected, throughout the whole basin. With

only one of the two sources of information available, the assessment would have been inaccurate or too much time-consuming.

Finally, measuring and quantifying sediment connectivity are still major challenges. Recently, several authors recommended the integration of structural and functional aspects of connectivity to overcome this challenge. From the outcomes of this thesis, it appears that still more efforts need to be done to include also the functions and the external properties of the catchment into the IC-based approaches. However, the four studies have more or less directly contributed to this end. In the first two study cases, the incorporation of multi-years scenarios has definitely helped to describe connectivity more dynamically. Although not directly addressing typical event-based or process-based parameters, like, for instance, precipitation, water runoff, soil erosion, soil infiltration capacity, sediment discharge, the integration of land cover changes and river adjustment to IC maps permitted to move a step forward towards that direction. In the third and fourth study, the quantification of sediment transfer was attempted using the DoD, which measured the erosional and depositional volumes of sediment mobilized by the Vaia storm. With the advance and discount of remote sensing technologies, DoDs, or repeated topographic surveys, are now becoming an important tool to quantify sediment transfer and infer functional connectivity (Heckmann and Vericat, 2018; Calle et al., 2020). In fact, the use of a spatial distributed information on geomorphic changes through time as the DoD, can support a more comprehensive knowledge of sediment connectivity and support more successful approaches (Wohl et al., 2018). Last chapter offered evidence that IC, as applied in that context, is not primarily suitable to predict functional connectivity but it is highly reliable to produce structural connectivity maps. The use of threshold-derived sediment connectivity maps can be widely applied for watershed management intervations. A more reliable detection of hot spots could define where to act in terms of hillslope stabilization (e.g. live stacking) and/or retention structure building (e.g. check dams).

Conclusion

The main objective of this thesis was to study sediment connectivity in relation to natural disturbances affecting the properties of mountain catchments. Specifically, I focused on the Index of Connectivity (IC) as a tool to analyse the potential changes in sediment connectivity caused by large natural disturbances occurring in different catchments. The thesis developed three chapters, designed to help facing such wide and complex objective and to test specific hypothesis.

In the first chapter, the hypothesis was that the impact of natural disturbances has consequences on sediment connectivity and this impact translates into specific effects that can be implemented in a more adaptable IC-based approach.

Therefore, I reported the findings of two studies carried out in Chilean basins, where the effects of a volcanic eruption and wildfires were matter of research. In the Rio Blanco and Rio Toro catchments, I carried out multi-temporal analyses using an approach that allowed the implementation of an adaptive IC for post-disturbance conditions. In this way, the factors recognized as potential drivers of sediment connectivity were integrated into a methodological workflow that adapted and refined the geomorphometric approach based on IC, originally recommended for Alpine areas. In particular, in both case studies, the land cover changes were found responsible for remarkable variations in sediment connectivity. The implementation of land cover changes was accomplished by means of ad-hoc W factors, representing the impedance to sediment fluxes and derived by a combination of free remote sensing data and field surveys. Furthermore, the two catchments showed also different characteristics so that the methodology could not be applied identically. In the Rio Blanco catchment, affected by volcanic eruption, the expansion of the active channel had to be included, whereas, in the Rio Toro catchment, affected by wildfires, the fire severity and vegetation recovery had to be addressed. Hence, although the two studies sought to establish a standardized workflow to analyse sediment connectivity after natural disturbances, this task was only partially achievable. Ultimately, a common methodology was used but, to be able to describe faithfully the changes in sediment connectivity in every scenario, it was also necessary to adapt the approach according to all the key factors in play. Finally, another conclusion is that the results of IC analysis, with proper refinements and within a suitable spatial-temporal scale, can be used also as a variable for monitoring the catchment's sensitivity to natural disturbances.

In the second chapter, the hypothesis was that IC can be used also as supportive tool to investigate the role of sediment source areas as suppliers to the channel network.

Therefore, an integrated analysis of the different responses of a mountain catchment to a storm was carried out. In 2018, the Vaia storm severely affected the mountain sector of the North-East of Italy with remarkable effects for the mountain river basins. In light of this, I presented a study case in which the hydrological, geomorphic, and sedimentological responses of a small dolomitic basin to the Vaia storm were considered. Particularly, sediment connectivity analysis was adopted to reconstruct the geomorphic response of the hillslopes during the event and to investigate the role of sediment source areas in supplying sediment to the main channel. A two-steps approach using the IC and DoD computed at catchment scale was used to classify sediment sources in suppliers and non-suppliers. In this study, three take-home messages can be inferred from the thesis. First, IC computed at high resolution and supported by other spatially distributed measures, can represent a useful supportive tool to decipher the geomorphic response of a catchment to a disturbance. Second, the analysis of sediment connectivity was fundamental to link and justify the outcomes of the other analyses in a comprehensive study describing the whole sediment cascade, from sources to outlet. Last, IC combined with DoD, permitted to reconstruct the dynamics of the sediment transfer from sources to channel and not only their structural linkages. Thus, this combination of metrics might represent a key starting point to progress towards functional connectivity approaches.

In the last chapter, the hypothesis was that IC can depict structural connectivity but not functional connectivity.

To test the hypothesis, I had to overcome important challenges highlighted in the literature review but scarcely tackled in practice. The validation of the IC means exploring its capacity in describing the actual linkages between sediment sources and downstream areas in mountain catchments. With the increasing number of IC applications and other indices, I found myself questioning the actual reliability of these indices in representing sediment connectivity. However, as the IC is intrinsically a static index, primarily accounting structural characteristics of the system, a distinction had to be made. Therefore, in the Rio Cordon, the capability of the IC in depicting structural connectivity and predicting functional connectivity was evaluated thanks to field surveys and logistic regression analyses. The results showed that, as expected, the IC is a valuable tool for describing the static linkages of lateral connectivity but it is not primarily suitable to predict the disturbance-driven sediment dynamics, i.e. functional connectivity. Nevertheless, it is possible to derive a threshold between connected and disconnected sources that could help improving the IC maps. Using the approach proposed in this last case study, a clear threshold is eventually drawn to separate high and low connectivity in the IC maps. In this way, a more useful and reliable instrument can be provided to stakeholders involved in watershed management.

With this thesis, I found existing issues and I answered few questions but, more importantly, I was able to identify and foresee knowledge gaps that were hidden before and now representing incentives for further research. Some of these gaps have emerged during the development of this PhD project but were faced only in the last chapter and study, which therefore represents more a new beginning than the end. Altogether, the three chapters provide an idea of how deep and complex is the analysis of sediment connectivity after disturbances. Developing each case study, I encountered more and more issues related to the specific topic under investigation and even to other disciplines outside geomorphology. Even though it seemed a very circumscribed and specific research topic, the present thesis proved that a multi-disciplinary perspective, recalling knowledge from forestry, remote sensing, hydrology and geology is required to overcome the challenges in the field of connectivity. Moreover, with the increasing occurrence of large natural disturbances all over the world, much more can be done in relation to these events, hence the present thesis is probably only one of the several starting points for still a fruitful field of research.

Appendix

Appendix 1. Supplementary material

1.1. Sediment connectivity changes in an Andean catchment affected by volcanic eruption

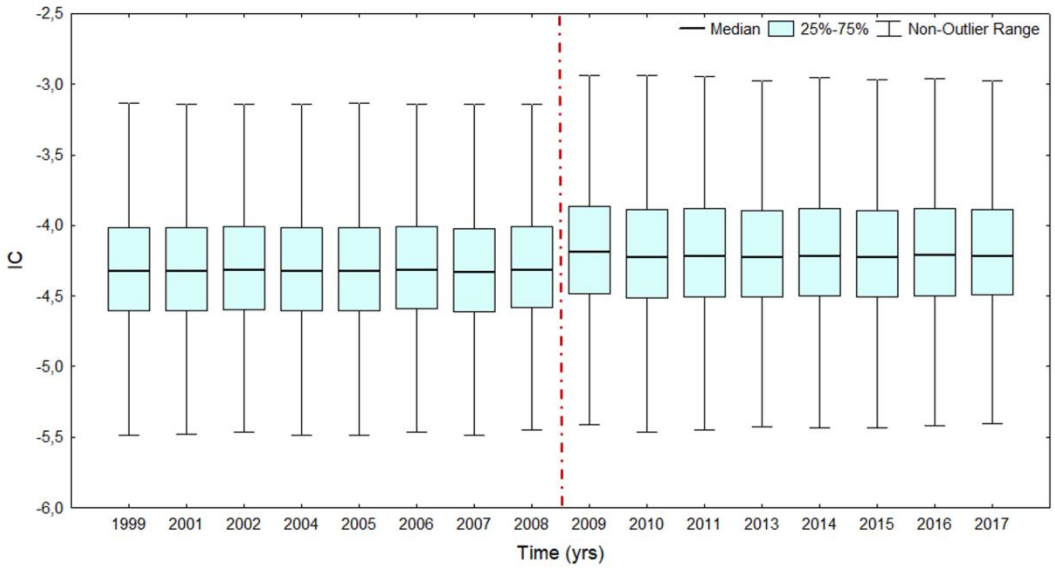

Figure S1.1.1. Multi-temporal variation of the IC computed with the derived-Manning's n and bridge. Whiskers represents the samples included within 1.5 times the interquartile range. The red-dashed line indicates the volcanic eruption.

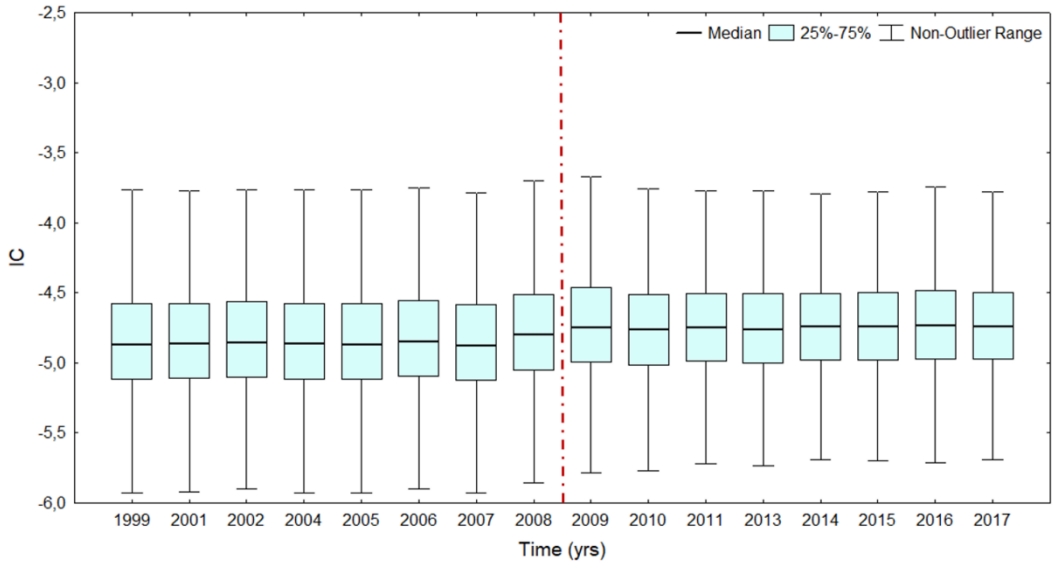

Figure S1.1.2. Multi-temporal variation of the IC computed with the derived-Manning's n and the active channel. Whiskers represents the samples included within 1.5 times the interquartile range. The red-dashed line indicates the volcanic eruption.

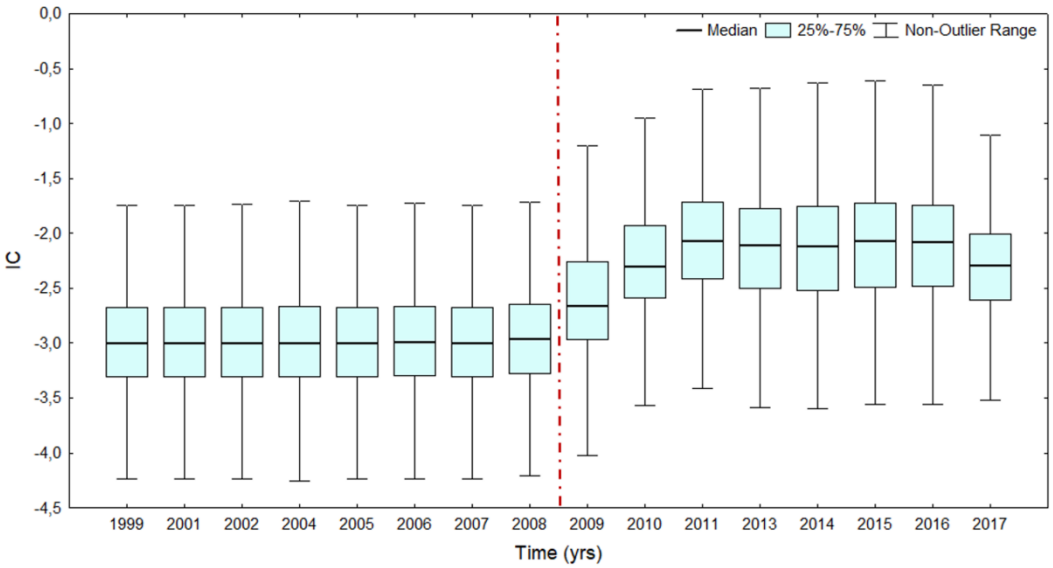

Figure S1.1.3. Multi-temporal variation of the IC, limited to the study subcatchment, computed with the derived-Manning's n and the active channel. Whiskers represents the samples included within 1.5 times the interquartile range. The red-dashed line indicates the volcanic eruption.

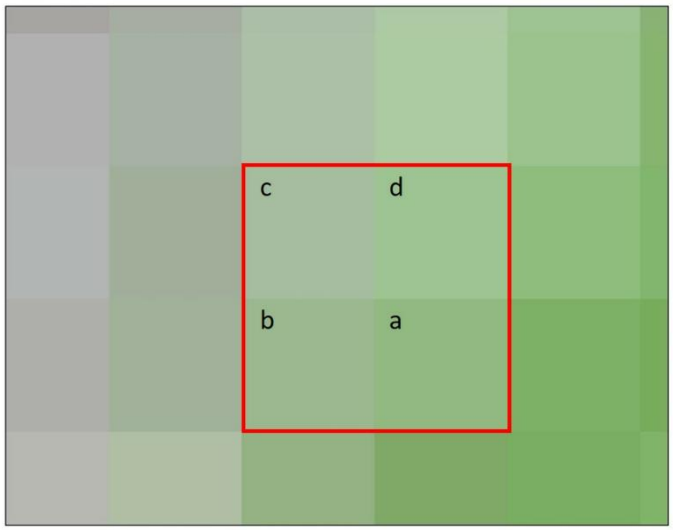

Figure S1.1.4. Detail of coarse spatial resolution used for the land cover classification; pixel size 30 x 30 m. The classification in the four classes is showed in the red frame: (a) old-growth forest, W factor = 0.70; (b) damaged old-growth forest, W factor = 0.80; (c) bare soil/glaciers, W factor =0.96; (d) sparse vegetation, W factor= 0.85.

Figure S1.1.5. Post-eruption development of the Blanco River from 2012 (a) to 2016 (b). The lateral shift of the channel occurs along with the formation of the new sediment path from the slope. Images taken by Google Earth Pro.

1.2. Assessing the effect of fire severity on sediment connectivity in central Chile

Table S1.2.1. Subset of sampling plots visually evaluated to be used for both the Severity factor and Manning's n computation.

Sampling plot	Understorey (%)	Grassland (%)	Deadwood (%)	Tree cover (%)	Bare soil (%)	Standing living trees	Standing dead trees	Amount of obstructions (%)
1	60	0	10	30	0	3	15	2
2	0	65	0	30	5	9	10	2
3	0	6	2	90	2	7	2	0
4	40	0	5	5	50	1	5	3
5	75	0	10	0	15	1	10	2
6	60	0	5	30	5	6	5	2
7	100	0	0	0	0	0	0	0
8	0	75	2	0	23	0	2	0
9	35	0	10	55	0	6	10	0
10	33	0	2	65	0	6	5	0
11	60	0	15	20	5	3	15	2
12	40	0	0	60	0	3	0	0
13	10	14	1	75	0	5	1	0
14	30	0	15	45	10	5	20	0
15	50	0	15	30	5	3	15	2
16	40	0	15	10	35	2	15	2
17	18	0	2	80	0	9	5	1
18	5	15	0	80	0	6	0	0
19	35	0	5	50	10	5	5	2

20	63	0	2	30	5	5	2	2
21	90	0	5	0	5	0	5	4
22	88	0	2	10	0	3	2	4
23	40	0	20	0	40	0	20	0
24	50	0	15	0	35	0	15	4
25	45	50	5	0	0	0	5	3
26	80	0	10	0	10	0	10	2
27	30	0	60	0	10	0	35	4
28	50	0	15	10	25	3	15	3
29	45	0	15	0	40	0	15	3
30	15	0	2	80	3	4	2	0
31	10	0	20	0	70	0	15	5
32	30	0	15	0	55	0	15	4
33	20	0	15	50	15	2	15	1
34	10	0	15	15	60	2	15	1
35	40	0	20	10	40	1	20	1
36	15	0	5	5	75	1	5	0
37	25	0	10	5	60	1	10	3
38	35	0	10	0	55	0	10	1
39	30	0	60	0	10	0	60	1
40	70	0	15	0	15	0	15	4
41	5	0	10	40	45	6	10	3
42	80	0	10	0	10	0	10	2
43	70	0	5	0	25	0	5	2

44	10	0	2	85	3	7	2	0
45	20	0	5	70	5	4	5	0
46	85	0	0	15	0	2	0	1

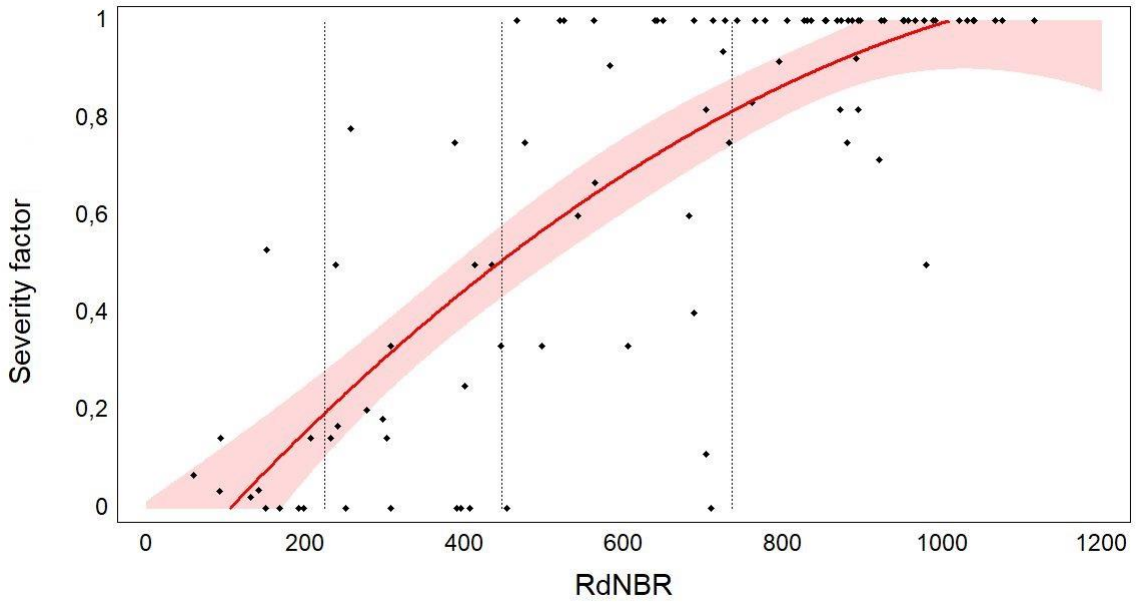

Figure S1.2.1. The relationship between field-based Severity factor and 2002-2016 RdNBR is used to determine the classification scheme for the wildfire severity maps. The solid red line represents the polynomial function within a 95% confidence interval. Black dotted vertical lines represent the severity thresholds.

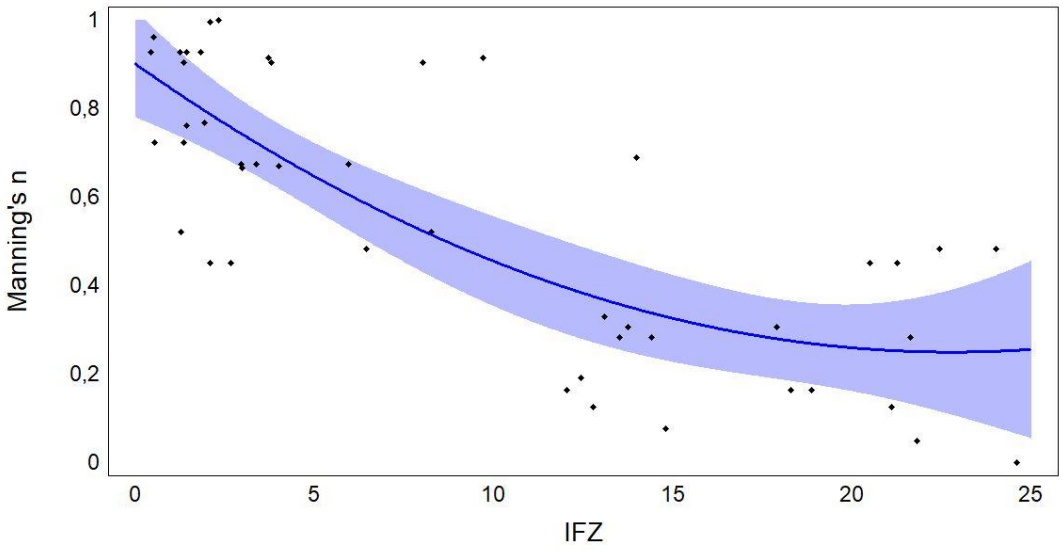

Figure S1.2.2. The relationship between the field-based Manning's n and the IFZ is used to extend the information of hydraulic roughness to the four weighting factor maps. Blue solid line represents the polynomial function within a 95% confidence interval.

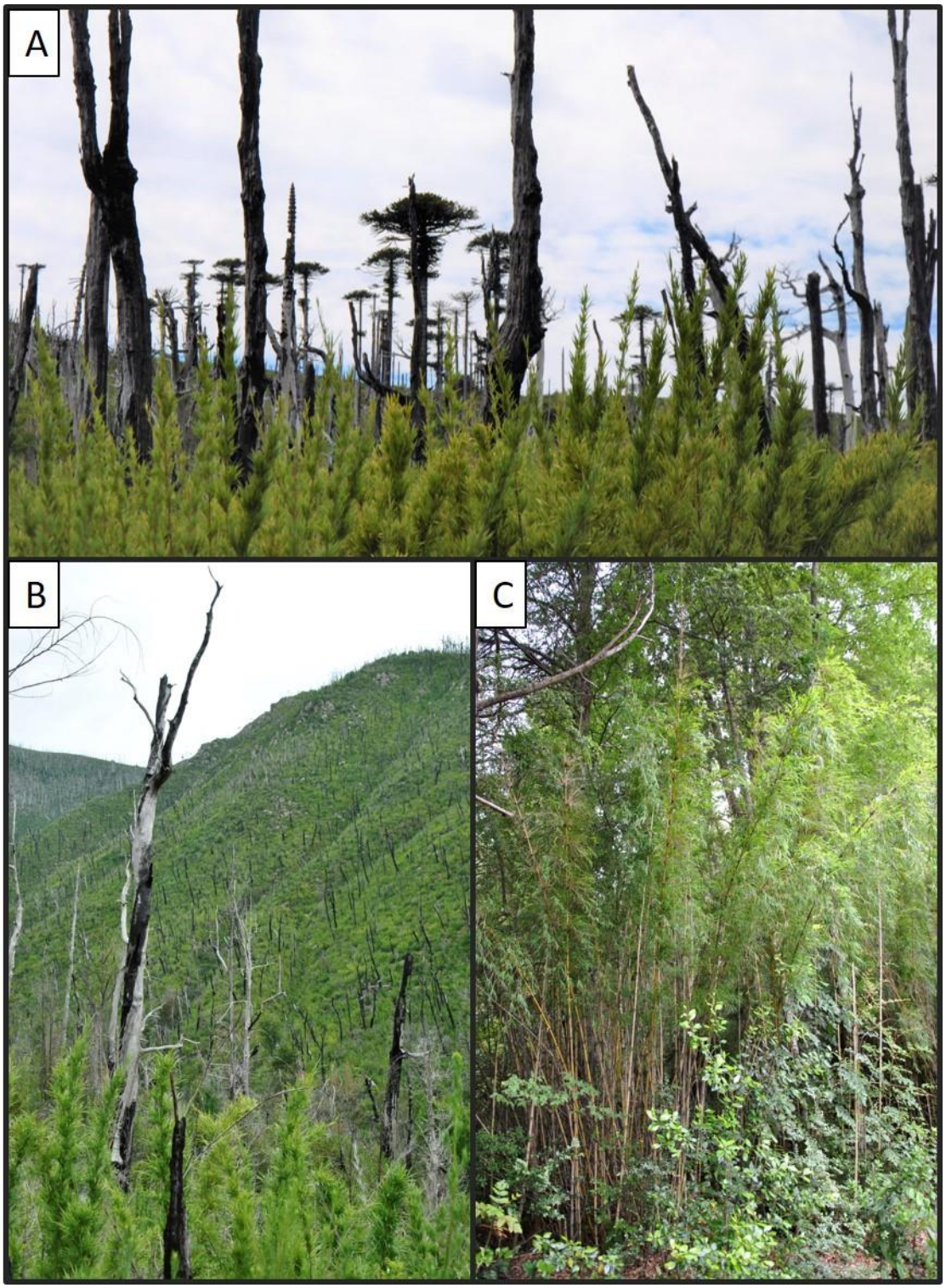

Figure S1.2.3. Endemic species of Chusquea spp. are growing fast under burned canopies in flat areas (A) and along the slopes (B), eventually reaching high density (C)

.

Appendix 2. Supplementary material

Hydrological, geomorphic and sedimentological responses of an alpine basin to a severe weather event (Vaia storm)

Table S2.5. Main features of the flood events recorded by the Rio Cordon monitoring station between September 1986 and September 2018: Q_P is the water discharge peak (in $m^3\ s^{-1}$), RI the recurrence interval estimated (in years), BL the amount of coarse material transported at the monitoring station (both in m^3 and tons), SSL the suspended sediment load measured (in tons), ER is the effective runoff volume (in $10^3\ m^3$), BLr the bedload transport rate (in $m^3\ h^{-1}$), while D_{16}, D_{50}, D_{84} and D_{90} are, respectively, the 16th, 50th, 84th and 90th percentiles of the bedload grain size distribution.

	Q_P ($m^3\ s^{-1}$)	RI years	BL (m^3)	BL (t)	SSL (t)	ER ($10^3\ m^3$)	BLr ($m^3\ h^{-1}$)	D_{16} (mm)	D_{50} (mm)	D_{84} (mm)	D_{90} (mm)
11 October 1987	5.15	11.5	54.8	85.6	131.7	79.9	6.9	-	-	-	-
15 July 1988	2.43	2.0	1.0	1.7	-	-	-	-	-	-	-
3 July 1989	4.39	7.1	85.0	145.6	223.9	103.4	3.1	54	103	207	242
22 May 1990	0.85	1.0	1.0	1.7	-	-	-	-	-	-	-
17 June 1991	4.00	5.5	39.0	67.2	68.1	57.9	2.0	30	51	100	135
5 October 1992	2.91	2.7	9.3	15.5	4.8	21.5	0.9	22	43	111	162
2 October 1993	4.28	6.6	13.7	17.2	41.1	30.7	2.3	29	61	135	186
18 May 1994	1.79	1.4	1.0	1.7	2.7	5.4	0.1	21	33	52	62
14 September 1994	10.42	> 100	900.0	1541.7	2435.1	26.6	323.6	65	116	226	281
13 August 1995	2.72	2.4	6.2	10.3	98.3	1.8	6.2	-	-	-	-
16 October 1996	2.96	2.8	57.0	94.7	294.4	22.0	3.8	40	79	143	163
27 June 1997	1.46	1.2	1.0	1.7	-	-	-	-	-	-	-
7 October 1998	4.73	8.8	300.0	516.8	393.5	91.8	17.6	40	78	157	188
20 September 1999	3.65	4.4	19.2	32.7	50.9	10.4	3.0	32	54	98	117

13 October 2000	3.28	3.5	55.6	92.2	142.0	110.6	1.6	39	61	111	123
11 May 2001	1.46	1.2	80.0	137.8	1017.6	8.5	6.2	33	48	69	77
20 July 2001	1.98	1.6	20.9	36.0	119.8	15.0	4.4	-	-	-	-
04 May 2002	2.29	1.8	27.4	47.2	123.0	29.4	1.4	39	59	99	119
16 November 2002	2.35	2.0	10.0	17.2	54.3	18.9	0.7	-	-	-	-
27 November 2002	2.77	2.5	69.1	119.0	373.7	70.3	2.3	26	44	78	89
03 May 2003	1.02	1.1	1.0	1.7	0.2	1.0	0.3	-	-	-	-
01 November 2004	2.05	1.6	4.6	7.9	7.6	-	-	25	38	62	77
6 October 2005	1.68	1.4	0.9	1.6	1.2	3.3	0.1	18	30	55	71
19 May 2006	1.28	1.1	0.7	1.2	5.1	1.0	0.1	-	-	-	-
24 May 2009	1.67	1.3	1.8	3.1	19.3	5.2	0.1	-	-	-	-
5 May 2010	1.82	1.5	0.8	1.4	14.2	3.7	0.1	-	-	-	-
8 June 2011	1.15	1.1	0.5	0.9	0.6	0.8	0.2	-	-	-	-
11 November 2012	2.10	1.7	14.2	24.4	60.8	4.6	2.3	23	38	70	79
17 May 2013	1.96	1.5	2.2	3.8	13.7	10.2	0.1	33	44	90	110
9 June 2014	2.06	1.7	65.6	113.0	76.8	16.6	4.7	24	41	64	113
5 November 2014	2.06	1.7	2.7	4.6	84.3	33.3	0.1	25	38	62	73
27 May 2016	1.09	1.0	0.5	0.9	-	1.0	-	25	35	51	60
24 May 2018	1.68	1.3	3.6	6.2	-	8.0	0.1	24	36	59	68

Appendix 3. Supplementary material

Predicting sediment connectivity in a mountain basin: a quantitative analysis of the Index of Connectivity

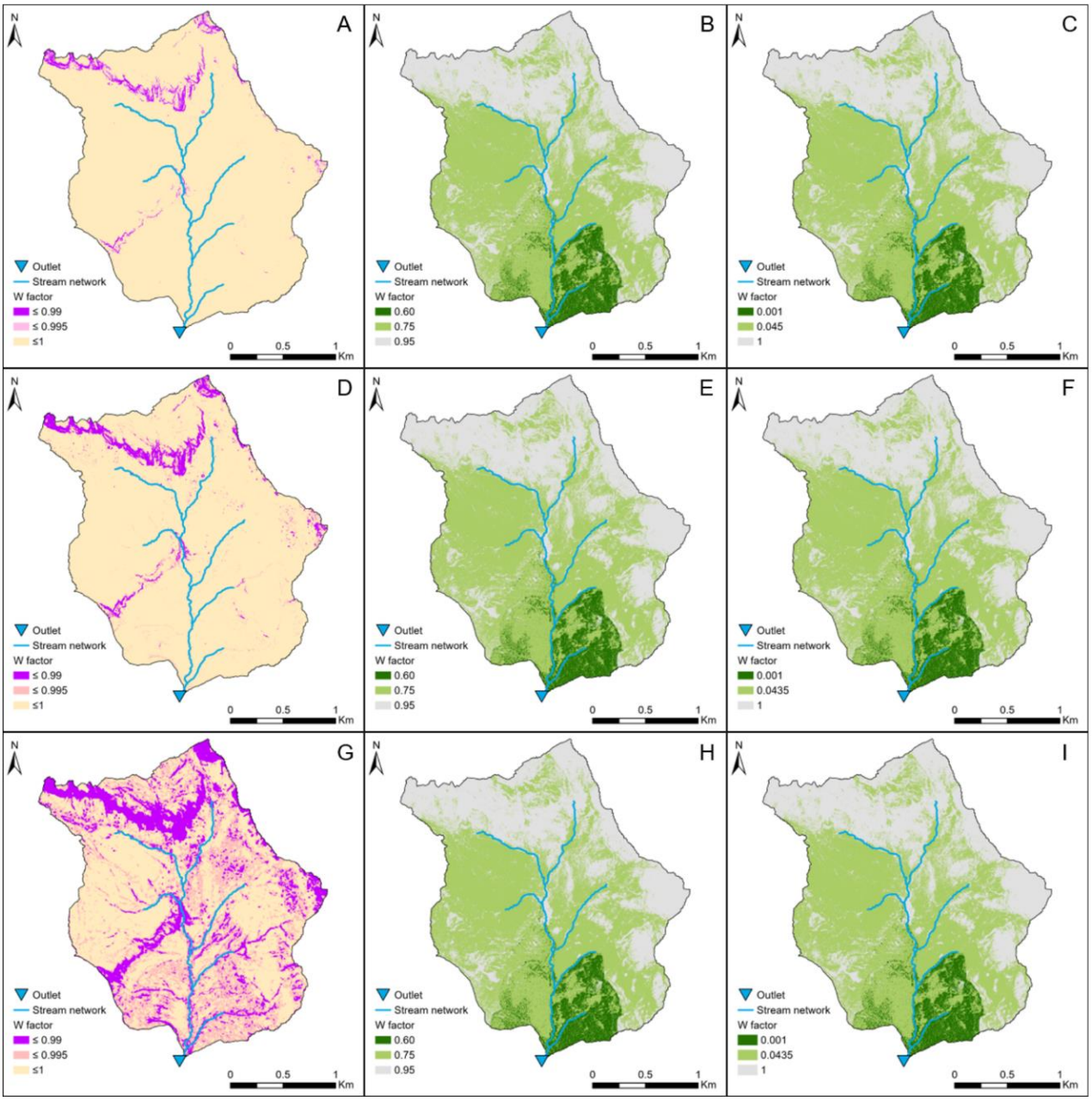

Figure S3.1. The nine W factor maps computed following eq.3.2, eq.3.3, eq.3.4. and according to different spatial resolution (rows) and coefficients (columns): RI_0.5 (A); Wn_0.5 (B); IWcc_0.5 (C); RI_1 (D); Wn_1 (E); Wcc_1 (F); RI_2.5 (G); Wn_2.5 (H); Wcc_2.5 (I). Each map is then used in the computation of IC, resulting in nine different IC maps.

References

Alexander, J., Barclay, J., Sušnik, J., Loughlin, S.C., Herd, R.A., Darnell, A., Crosweller, S., 2010. Sediment-charged flash floods on Montserrat: the influence of synchronous tephra fall and varying extent of vegetation damage. J. Volcanol. Geotherm. Res. 194 (4), 127–138. https://doi.org/10.1016/j.jvolgeores.2010.05.002.

Alfano, F., Bonadonna, C., Volentik, A.C.M., Connor, C.B., Watt, S.F.L., Pyle, D.M., Connor, L.J., 2011. Tephra stratigraphy and eruptive volume of the May, 2008, Chaitén eruption, Chile. Bull. Volcanol. 73 (5), 613–630. https://doi.org/10.1007/s00445-010-0428-x.

Amponsah, W.A., Ayral, P.A., Boudevillain, B.B., Bouvier, C., Braud, I., Brunet, P., Delrieu, G., Didon-Lescot, J.F., Gaume, E., Lebouc, L., Marchi, L., Marra, F., Morin, E., Nord, G., Payrastre, O., Zoccatelli, D., Borga, M., 2018. Integrated high-resolution dataset of high-intensity European and Mediterranean flash floods. Earth Syst. Sci. Data 10, 1783–1794.

Arcement, G.J., Schneider, V.R., 1989. Guide for selecting manning's roughness coefficients for natural channels and flood plains United States geological survey water-supply paper 2339. United States Geological Survey Water-Supply 2339(2339), 39. https://doi.org/Report No. FHWA-TS-84-204.

ASF, 2019. ASF - Alaska Satellite Facility. Available at. https://www.asf.alaska.edu/.

ASF DAAC 2011, ALOS PALSAR_AP_27045_FBS_F6310_RT1_Radiometric_Terrain_correcter_high_res: Includes Material © JAXA/METI 2011. Accessed through ASF DAAC 23 November 2017. DOI: https://doi.org/10.5067/Z97HFCNKR6VA.

Assal, T.J., González, M.E., Sibold, J.S., 2018. Burn severity controls on postfire Araucaria-Nothofagus regeneration in the Andean cordillera. J. Biogeogr. 45 (11), 2483–2494.

Atkinson, P. M., German, S. E., Sear, D. A., Clark, M. J., 2003. Exploring the relations between riverbank erosion and geomorphological controls using geographically weighted logistic regression. Geographical Analysis 35(1), 58–82. https://doi.org/10.1111/j.1538-4632.2003.tb01101.x.

Ayalew, L. Yamagishi, H., 2005. The application of GIS-based logistic regression for landslide susceptibility mapping in the Kakuda-Yahiko Mountains, Central Japan. Geomorphology 65, 359-368.

Ayris, P.M., Delmelle, P., 2012. The immediate environmental effects of tephra emission. Bull. Volcanol. 74 (9), 1905–1936. https://doi.org/10.1007/s00445-012-0654-5.

Baartman, J. E. M., Nunes, J. P., Masselink, R., Darboux, F., Bielders, C., Degré, A., Cantreul, V., Cerdan, O., Grangeon, T., Fiener, P., Wilken, F., Schindewolf, M., Wainwright, J., 2020. What do models tell us about water and sediment connectivity? Geomorphology, 367, 107300. https://doi.org/10.1016/j.geomorph.2020.107300.

Baewert, H., Morche, D., 2014. Coarse sediment dynamics in a proglacial fluvial system (Fagge River, Tyrol). Geomorphology 218, 88–97.

Baker, V.R., Costa, J.E., 1987. Flood power. In: Mayer, L., Nash, D. (Eds.), Catastrophic Flooding. Allen & Unwin, Boston, pp. 1–20.

Banskota, A., Kayastha, N., Falkowski, M.J., Wulder, M.A., Froese, R.E., White, J.C., 2014. Forest monitoring using Landsat time series data: a review. Can. J. Remote. Sens. 40 (5), 362–384.

Batalla, R.J., De Jong, C., Ergenzinger, P., Sala, M., 1999. Field observations on hyperconcentrated flows in mountain torrents. Earth Surf. Proc. Land. 24, 247–253.

Bauch, G.D., Hickin, E.J., 2011. Rate of floodplain reworking in response to increasing storm-induced floods, Squamish River, south-western British Columbia, Canada. Earth Surf. Proc. Land. 36 (7), 872–884.

Benavides-Solorio, J., MacDonald, L.H., 2001. Post-fire runoff and erosion from simulated rainfall on small plots, Colorado front range. Hydrol. Process. 15 (15), 2931–2952.

Benda, L.E., Sias, J.C., 2003. A quantitative framework for evaluating the mass balance of in-stream organic debris. For. Ecol. Manag. 172 (1), 1–16.

Biolchi, S., Denamiel, C., Devoto, S., Korbar, T., Macovaz, V., Scicchitano, G., Vilibić, I., Furlani, S., 2019. Impact of the October 2018 Storm Vaia on coastal boulders in the Northern Adriatic Sea. Water 11 (11), 2229.

Bohorquez, P., Darby, S.E., 2008. The use of one- and two-dimensional hydraulic modelling to reconstruct a glacial outburst flood in a steep Alpine valley. J. Hydrol. 361 (3–4), 240–261.

Borga, M., Stoffel, M., Marchi, L., Marra, F., Matthias, J., 2014. Hydrogeomorphic response to extreme rainfall in headwater systems: flash floods and debris flows. J. Hydrol. 518, 194–205.

Borselli, L., Cassi, P., Torri, D., 2008. Prolegomena to sediment and flow connectivity in the landscape: a GIS and field numerical assessment. Catena 75 (3), 268–277. https://doi. org/10.1016/j.catena.2008.07.006.

Bracken, L.J., Crooke, J., 2007. The concept of hydrological connectivity and its contribution to understanding runoff-dominated geomorphic systems. Hydrol. Process. 21 (November 2008), 1749–1763. https://doi.org/10.1002/hyp.

Bracken, L.J., Turnbull, L., Wainwright, J., Bogaart, P., 2015. Sediment connectivity: a framework for understanding sediment transfer at multiple scales. Earth Surf. Process. Landf. 40 (2),177–188. https://doi.org/10.1002/esp.3635.

Bradley, A. P., 1997. The use of the area under the ROC curve in the evaluation of machine learning algorithms. Pattern Recognition 30(7), 1145–1159. https://doi.org/10.1016/S0031-3203(96)00142-2.

Brardinoni, F., Hassan, M.A., 2006. Glacial erosion, evolution of river long profiles, and the organization of process domains in mountain drainage basins of coastal British Columbia. Journal of Geophysical Research: Earth Surface 111 (1), 1–12. https://doi. org/10.1029/2005JF000358.

Brardinoni, F., Cavalli, M., Heckmann, T., Liébault, F., Rimböck, A., 2015. Guidelines for Assessing Sediment Dynamics in Alpine Basins and Channel Reaches. Retrieved from http://www.sedalp.eu/download/dwd/reports/WP4_Report.pdf.

Brasington, J., Rumsby, B.T., McVey, R.A., 2000. Monitoring and modelling morphological change in a braided gravel-bed river using high-resolution GPS-based survey. Earth Surf. Proc. Land. 25, 973–990.

Brasington, J., Langham, J., Rumsby, B., 2003. Methodological sensitivity of morphometric estimates of coarse fluvial sediment transport. Geomorphology 53, 299–316.

Bravard, J.P., Petit, F., 1997. Les cours d'eau. In: Dynamique du systeme fluvial. Armand Colin, Paris, p. 222.

Brierley, G., Fryirs, K., Jain, V., 2006. Landscape connectivity: The geographic basis of geomorphic applications. Area 38 (2), 165–174. https://doi.org/10.1111/j.1475- 4762.2006.00671.x.

Brogan, D.J., MacDonald, L.H., Nelson, P.A., Morgan, J.A., 2019. Geomorphic complexity and sensitivity in channels to fire and floods in mountain catchments. Geomorphology 337, 53–68.

Brunner, G., Bonner, V., 2010. HEC River Analysis System (HEC-RAS) Hydraulic Reference Manual. Version 4.1. (January), p. 411.

Brunsden, D., Thornes, J.B., 1979. Landscape sensitivity and change. Trans. Inst. Br. Geogr. 4, 463–484.

Brunsden D., 1993. Barriers to geomorphological change. In Landscape Sensitivity, Thomas DSG, Allison RJ (eds). John Wiley & Sons: Chichester; 7–12.

Brunsden, D., 2001. A critical assessment of the sensitivity in geomorphology. Catena 42, 99-123.

Bucała-Hrabia, A., Kijowska-Strugała, M., Bryndal, T., Cebulski, J., Kiszka, K., Kroczak, R., 2020. An integrated approach for investigating geomorphic changes due to flash flooding in two small stream channels (Western Polish Carpathians). J. Hydrol.: Reg. Stud. 31, 100731.

Budimir, M. E. A., Atkinson, P. M. Lewis, H. G., 2015. A systematic review of landslide probability mapping using logistic regression. Landslides, 12(3), 419–436. https://doi.org/10.1007/s10346-014-0550-5.

Burns, B.R., 1993. Fire-induced dynamics of Araucaria araucana-Nothofagus antarctica forest in the southern Andes. J. Biogeogr. 20, 669–685.

Burt, T.P., Allison, R.J., 2010. Sediment Cascades: An Integrated Approach. John Wiley & Sons, Ltd, Chichester, UK.

Calsamiglia, A., Fortesa, J., García-Comendador, J., Lucas-Borja, M. E., Calvo-Cases, A., Estrany, J., 2018. Spatial patterns of sediment connectivity in terraced lands: Anthropogenic controls of catchment sensitivity. Land Degradation and Development, 29(4), 1198–1210. https://doi.org/10.1002/ldr.2840.

Cammeraat, L.H., 2002. A review of two strongly contrasting geomorphological systems within the context of scale. Earth Surf. Process. Landf. 27 (11), 1201–1222. https:// doi.org/10.1002/esp.421.

Cantreul, V., Bielders, C., Calsamiglia, A., Degré, A., 2018. How pixel size affects a sediment connectivity index in central Belgium. Earth Surf. Process. Landf. 43 (4), 884–893. https://doi.org/10.1002/esp.4295.

Carmo, M., Moreira, F., Casimiro, P., Vaz, P., 2011. Land use and topography influences on wildfire occurrence in northern Portugal. Landsc. Urban Plan. 100 (1–2), 169–176.

Carrivick, J.L., Smith, M.W., Quincey, D.J., 2016. Structure from Motion in the Geosciences. John Wiley & Sons Ltd, Chichester, UK.

Cassandro, C., Loglisci, N., Gandini, D., Qian, M.W., Niu, G.Y., Ramieri, P., Pelosini, R., Longhetto, A., 2002. The flood of November 1994 in Piedmont, Italy: A quantitative analysis and simulation. Hydrol. Process. 16, 1275–1299.

Cavaleri, L., Bajo, M., Barbariol, F., Bastianini, M., Benetazzo, A., Bertotti, L., Chiggiato, J., Davolio, S., Ferrarin, C., Magnusson, L., Papa, A., Pezzutto, P., Pomaro, A., Umgiesser, G., 2019. The October 29, 2018 storm in northern Italy – an exceptional event and its modeling. Prog. Oceanogr. 178, 102178.

Cavalli, M., Marchi, L., 2008. Characterisation of the surface morphology of an alpine alluvial fan using airborne LiDAR. Natural Hazards and Earth System Science 8 (2), 323–333. https://doi.org/10.5194/nhess-8-323-2008.

Cavalli, M., Trevisani, S., Comiti, F., Marchi, L., 2013. Geomorphometric assessment of spatial sediment connectivity in small alpine catchments. Geomorphology 188, 31–41. https://doi.org/10.1016/j.geomorph.2012.05.007.

Cavalli, M., Crema, S., Marchi, L., 2014. Guidelines on the Sediment Connectivity ArcGis Toolbox and Stand-Alone Application Release: 1.0, (June), pp. 0–30. https:// doi.org/10.13140/RG.2.1.3243.5361.

Cavalli, M., Tarolli, P., Dalla Fontana, G., Marchi, L., 2016. Multi-temporal analysis of sediment source areas and sediment connectivity in the Rio Cordon catchment (Dolomites). Rend. Online Soc. Geol. Ital.39 (April), 27–30. https://doi.org/10.3301/ROL.2016.39.

Cavalli, M., Heckmann, T., Marchi, L., 2019. Sediment Connectivity in Proglacial Areas. In: Heckmann, T., Morche, D. (Eds.), Geomorphology of Proglacial Systems: Landform and Sediment Dynamics in Recently Deglaciated Alpine Landscapes, Geography of the Physical Environment. Springer International Publishing, Cham, pp. 271–287 https://doi.org/10.1007/978-3-319-94184-4_16.

Cavalli, M., Vericat, D., Pereira, P., 2019. Mapping water and sediment connectivity. Sci. Total Environ. 673, 763–767.

Cembrano, J., Lara, L., 2009. The link between volcanism and tectonics in the southern volcanic zone of the Chilean Andes: a review. Tectonophysics 471 (1–2), 96–113.

Certini, G., 2005. Effects of fire on properties of forest soils: a review. Oecologia 143, 1–10. https://doi.org/10.1007/s00442-004-1788-8.

Chartin, C., Evrard, O., Laceby, J.P., Onda, Y., Ottlé, C., Lefèvre, I., Cerdan, O., 2017. The impact of typhoons on sediment connectivity: lessons learnt from contaminated coastal catchments of the Fukushima Prefecture (Japan). Earth Surf. Process. Landf. 42 (2), 306–317. https://doi.org/10.1002/esp.4056.

Chen, W., Xie, X., Wang, J., Pradhan, B., Hong, H., Bui, D. T., Duan, Z., Ma, J., 2017. A comparative study of logistic model tree, random forest and classification and regression tree models for spatial prediction of landslide susceptibility. Catena, 151, 147–160. https://doi.org/10.1016/j.catena.2016.11.032

Chu, T., Guo, X., Takeda, K., 2016. Remote sensing approach to detect post-fire vegetation regrowth in Siberian boreal larch Forest. Ecol. Indic. 62, 32–46.

Comiti, F., Andreoli, A., Lenzi, M.A., Mao, L., 2008. Wood storage in three mountain streams of the southern Andes and its hydro-morphological effects. Earth Surf. Pro- cess. Landf. 33, 244–262.

CONAF, 1999. Informe Nacional con Variables Ambientales. Corporación Nacional Forestal, Birf, Universidad Australia de Chile, Pointificia Universidad Católica de Chile, Unversidad Católica de Temuco Catastro y evaluación de los recursos vegetacionales nativos de Chile, Santiago, Chile.

CONAF, 2019. Estadísticas - Resumen Regional Ocurrencia (Número) y Daño (Superficie Afectada) por Incendios Forestales 1977–2019.

CONAMA, 2006. Estudio de la variabilidad climática en Chile para el siglo XXI. Informe Final. Chile. CONAMA, Santiago, Chile.

Conoscenti, C., Angileri, S., Cappadonia, C., Rotigliano, E., Agnesi, V., Märker, M., 2014. Gully erosion susceptibility assessment by means of GIS-based logistic regression: A case of Sicily (Italy). Geomorphology, 204, 399–411. https://doi.org/10.1016/j.geomorph.2013.08.021.

Costa, J.E., O'Connor, J.E., 1995. Geomorphologically effective floods. In: Costa, J.E., Miller, A.J., Potter, K.P., Wilcock, P.R. (Eds.), Natural and Anthropogenic Influences in Fluvial Geomorphology (The Wolman Volume) AGU Geophysical Monograph 89. American Geophysical Union, Washington, D.C., pp. 45–56.

Cowan, W.L., 1956. Estimating hydraulic roughness coefficients. Agric. Eng.37 (7), 473–475.

Crema, S., Cavalli, M., 2018. SedInConnect: a stand-alone, free and open source tool for the assessment of sediment connectivity. Comput. Geosci. 111 (September 2017), 39–45. https://doi.org/10.1016/j.cageo.2017.10.009.

Croke, J., Fryirs, K., Thompson, C., 2013. Channel-floodplain connectivity during an extreme flood event: Implications for sediment erosion, deposition and delivery. Earth Surface Processes and Landforms, 38(12), 1444–1456. https://doi.org/10.1002/esp.3430.

Crooks, K.R., Sanjayan, M., 2006. Connectivity Conservation. Cambridge University Press, New York.

Cucchiaro, S., Cavalli, M., Vericat, D., Crema, S., Llena, M., Beinat, A., Marchi, L., Cazorzi, F., 2019. Geomorphic effectiveness of check dams in a debris-flow catchment using multi-temporal topographic surveys. Catena 174, 73–83.

Cucchiaro, S., Maset, E., Cavalli, M., Crema, S., Marchi, L., Beinat, A., Cazorzi, F., 2020. How does co-registration affect geomorphic change estimates in multi-temporal surveys? GIScience Remote Sens. 57 (5), 611–632. https://doi.org/10.1080/ 15481603.2020.1763048.

D'Agostino, V., Lenzi, M.A., 1999. Bedload transport in the instrumented catchment of the Rio Cordon: Part II: Analysis of the bedload rate. Catena 36, 191–204.

Dale, V.H., Swanson, F.J., Crisafulli, C.M., 2005. Ecological Responses to the 1980 Eruption of Mount St. Helens. https://doi.org/10.1007/0-387-28150-9.

Dalla Fontana, G., Marchi, L., 1994. Sediment source areas in a small alpine basin. International Symposium on Forest Hydrology, October 24–28, Tokyo, Japan, 455–462.

Dalla Fontana, G., Marchi, L., 2003. Slope-area relationships and sediment dynamics in two alpine streams. Hydrological Processes, 17(1), 73–87. https://doi.org/10.1002/hyp.1115.

Davila, N., Capra, L., Gavilanes-Ruiz, J.C., Varley, N., Norini, G., Vazquez, A.G., 2007. Recent lahars at Volcán de Colima (Mexico): drainage variation and spectral classification. J. Volcanol. Geotherm. Res.165 (3–4), 127–141. https://doi.org/10.1016/j.jvolgeores.2007.05.016.

Davolio, S., Della Fera, S., Laviola, S., Miglietta, M.M., Levizzani, V., 2020. Heavy precipitation over Italy from the Mediterranean storm "Vaia" in October 2018: Assessing the role of an atmospheric river. Mon. Weather Rev. 148, 3571–3588.

DeBano, L.F., Neary, D.G., Ffolliott, P.F., 1998. Fire's Effects on Ecosystems. John Wiley and Sons, Inc, New York (333 p).

Donoso, C., 1981. Tipos forestales de los bosques nativos de Chile. Doc. De trabajo No 38. Investigación y Desarrollo Forestal (CONAF, PNUD-FAO). FAO Chile, Santiago de Chile.

EarthExplorer, 2019. U.S. Geological Service EarthExplorer. Available at. https:// earthexplorer.usgs.gov/.

Engman, E.T., 1986. Roughness coefficients for routing surface runoff. J. Irrig. Drain. Eng. 112 (1), 39–53.

Estes, B.L., Knapp, E.E., Skinner, C.N., Miller, J.D., Preisler, H.K., 2017. Factors influencing fire severity under moderate burning conditions in the Klamath Mountains, northern California, USA. Ecosphere 8 (5).

Estrany, L., Ruiz, M., Calsamiglia, A., Carriquí, M., García-comendador, J., 2019. Sediment connectivity linked to vegetation using UAVs: high-resolution imagery for ecosystem management. Sci. Total Environ. 671, 1192–1205.

Evrard, O., Chartin, C., Onda, Y., Patin, J., Lepage, H., Lefèvre, I., Ayrault, S., Ottlé, C., Bonté, P., 2013. Evolution of radioactive dose rates in fresh sediment deposits along coastal rivers draining Fukushima contamination plume. Sci. Rep. 3, 1–6. https://doi.org/ 10.1038/srep03079.

Ferguson, R.I., 1981. Channel form and channel changes. In: Lewing, J. (Ed.) British Rivers. Allen and Unwin, London, 90-125.

Ferrato, C., De Marco, J., Tarolli, P., Cavalli, M., 2017. An updated source areas inventory in the Rio Cordon catchment (Dolomites). Rendiconti Online Societ`a Geologica Italiana 42, 10–13.

Fischer, E.M., Knutti, R., 2015. Anthropogenic contribution to global occurrence of heavy-precipitation and high-temperature extremes. Nat. Clim. Change 5, 560–564.

Foerster, S., Wilczok, C., Brosinsky, A., Segl, K., 2014. Assessment of sediment connectivity from vegetation cover and topography using remotely sensed data in a dryland catchment in the Spanish Pyrenees. J. Soils Sediments 14 (12), 1982–2000. https:// doi.org/10.1007/s11368-014-0992-3.

Foster, R., Knight, D., Dennis, F.J., 1998. Landscape patterns and legacies resulting fromlarge, infrequent forest disturbances. Ecosystems 1, 497–510.

Friele, P., Millard, T.H., Mitchell, A., Allstadt, K.E., Menounos, B., Geertsema, M., Clague, J.J., 2020. Observations on the May 2019 Joffre Peak landslides, British Columbia. Landslides 17 (4), 913–930.

Fryirs, K.A., Brierley, G.J., Preston, N.J., Kasai, M., 2007a. Buffers, barriers and blankets: The (dis)connectivity of catchment-scale sediment cascades. Catena 70 (1), 49–67. https://doi.org/10.1016/j.catena.2006.07.007.

Fryirs, K.A., Brierley, G.J., Preston, N., Spencer, J., 2007b. Catchment-scale (dis)connectivity in sediment flux in the upper Hunter catchment, New South Wales, Australia. Geomorphology 84, 297-316. https://doi:10.1016/j.geomorph.2006.01.044.

Fryirs, K.A, 2013. (Dis)Connectivity in catchment sediment cascades: A fresh look at the sediment delivery problem. Earth Surface Processes and Landforms, 38(1), 30–46. https://doi.org/10.1002/esp.3242.

Fryirs, K.A, Brierley, G.J., 2013. Geomorphic Analysis of River Systems: an approach to reading the landscape. Wiley-Blackwell, West Sussex.

Fuenzalida, H., 1965. Geografía Económica de Chile. CORFO, Santiago de Chile.

Gaume, E., Borga, M., 2008. Post-flood field investigations in upland catchments after major flash floods: proposal of a methodology and illustrations. J. Flood Risk Manage. 1, 175–189.

Gay, A., Cerdan, O., Mardhel, V., Desmet, M., 2016. Application of an index of sediment connectivity in a lowland area. J. Soils Sediments 16 (1), 280–293. https://doi.org/ 10.1007/s11368-015-1235-y.

Gens, R., 2015. ASF Radiometric Terrain Corrected Products. Algorithm Theoretical Basis Document.

Gesch, D.B., Oimoen, M.J., Evans, G.A., 2014. Accuracy assessment of the U.S. Geological Survey National Elevation Dataset, and comparison with other large area elevation datasets SRTM and ASTER. U.S. Geological Survey Open File Report 2014–1008, p. 10 (Shimada).

Giovannini, L., Davolio, S., Zaramella, M., Zardi, D., Borga, M., 2021. Multi-model convection-resolving simulations of the October 2018 Vaia storm over Northeastern Italy. Atmos. Res. 253, 105455.

Gob, F., Bravard, J.P., Petit, F., 2010. The influence of sediment size, relative grain size and channel slope on initiation of sediment motion in boulder bed rivers. A lichenometric study. Earth Surf. Proc. Land. 35, 1535–1547.

González, M.E., Veblen, T.T., Sibold, J.S., 2005. Fire history of araucaria-Nothofagus forests in Villarrica National Park, Chile. J. Biogeogr. 32 (7), 1187–1202.

González, M.E., Veblen, T.T., Sibold, J., 2010. Influence of fire severity on stand development of Araucaria araucana – Nothofagus pumilio stands in the Andean cordillera of south-central Chile. Austral Ecology 35, 597–615.

Gorczyca, E., Krzemień, K., Wrońska-Wałach, D., Sobucki, M., 2013. Channel changes due to extreme rainfalls in the Polish Carpathians. In: Loczy, D. (Ed.), Geomorphological Impacts of Extreme Weather, Case Studies from Central and Eastern Europe. Springer, Dordrecht, pp. 23–35.

Graf, W., 1977. The rate law in fluvial geomorphology. Am. J. Sci. 277, 178–191. Gran, K.B., Montgomery, D.R., 2005. Spatial and temporal patterns in fluvial recovery following volcanic eruptions: channel response to basin-wide sediment loading at Mount Pinatubo, Philippines. Bull. Geol. Soc. Am. 117 (1–2), 195–211. https://doi. org/10.1130/B25528.1.

Guisan, A., Weiss, S.B., Weiss, A.D., 1999. GLM versus CCA spatial modeling of plant species distribution. Plant Ecol. 143, 107–122.

Gunckel, L.H., 1948. La floracion de la quila y del colihue en la Araucania. Ciencia e Investigacion 4, 91–95.

Hajdukiewicz, H., Wy˙zga, B., Miku´s, P., Zawiejska, J., Radecki-Pawlik, A., 2016. Impact of a large flood on mountain river habitats, channel morphology, and valley infrastructure. Geomorphology 272, 55–67.

Hallema, D.W., Sun, G., Caldwell, P., Robinne, F.N., Bladon, K.D., Norman, S., Liu, Y., Cohen, E.C., McNulty, S., 2019. Wildland Fire Impacts on Water Yield across the Contiguous United States. Gen. Tech. Rep. SRS-238. U.S. Department of Agriculture Forest Service, Southern Research Station, Asheville, NC (109p).

Harvey, A.M., 2001. Coupling between hillslopes and channels in upland fluvial systems: implications for landscape sensitivity, illustrated from the Howgill Fells, northwest England. Catena 42 (2–4), 225–250. https://doi.org/10.1016/S0341-8162(00)00139-9.

Harvey, A.M., 2002. Effective timescales of coupling within fluvial systems. Geomorphology, 44, 175–201. https://doi.org/10.1016/S0169-555X(01)00174-X.

Hayes, S.K., Montgomery, D.R., Newhall, C.G., 2002. Fluvial sediment transport and deposition following the 1991 eruption of Mount Pinatubo. Geomorphology 45, 211–224.

Heckmann, T., Schwanghart, W., 2013. Geomorphic coupling and sediment connectivity in an alpine catchment - Exploring sediment cascades using graph theory. Geomorphology 182, 89–103. https://doi.org/10.1016/j.geomorph.2012.10.033.

Heckmann, T., Cavalli, M., Cerdan, O., Foerster, S., Javaux, M., Lode, E., Smetanova, A., Vericat, D. Brardinoni, F., 2018. Indices of sediment connectivity: opportunities, challenges and limitations. Earth-Sci. Rev., 1–32 https://doi.org/10.1016/J.EARSCIREV.2018.08.004.

Holden, Z.A., Morgan, P., Hudak, A.T., 2010. Burn severity of areas reburned by wildfires in the Gila National Forest, New Mexico, USA. Fire Ecology 6 (3), 77–85.

Hooke, J., 2003. Coarse sediment connectivity in river channel systems: a conceptual framework and methodology. Geomorphology 56 (1–2), 79–94. https://doi.org/ 10.1016/S0169-555X(03)00047-3.

Hooke, J., Souza, J., 2021. Challenges of mapping, modelling and quantifying sediment connectivity. Earth-Science Reviews 223, 103847.

Hooke, J., Souza, J., Marchamalo, M., 2021. Evaluation of connectivity indices applied to a Mediterranean agricultural catchment. Catena 207, 105713.

Huang, C., Goward, S.N., Masek, J.G., Thomas, N., Zhu, Z., Vogelmann, J.E., 2010. An automated approach for reconstructing recent forest disturbance history using dense Landsat time series stacks. Remote Sens. Environ. 114 (1), 183–198.

Inbar, M., Reyes Enriquez, A., Graniel Graniel, J.H., 2001. Morphological changes and erosion processes following the 1982 eruption of El Chichón volcano, Chiapas, Mexico/ Modifications géomorphologiques et processus d'érosion consécutifs à l'éruption du volcan El Chichón, Chiapas, Mexico, en 1982. Géomorphologie: Relief, Processus, Environnement 7 (3), 175–183. https://doi.org/10.3406/morfo.2001.1100.

Iniguez, J.M., Swetnam, T.W., Yool, S.R., 2008. Topography affected landscape fire history patterns in southern Arizona, USA. For. Ecol. Manag. 256 (3), 295–303.

Iroumé, A., Mao, L., Andreoli, A., Ulloa, H., Ardiles, M.P., 2015. Large wood mobility processes in low-order Chilean river channels. Geomorphology 228, 681–693

James, L.A., 2010. Secular sediment waves, channel bed waves, and legacy sediment. Geogr. Compass 4, 576–598.

Jautzy, T., Maltais, M., Buffin-Bélanger, T., 2021. Interannual evolution of hydrosedimentary connectivity induced by forest cover change in a snow-dominated mountainous catchment. Land Degradation and Development, 32(7), 2318–2335. https://doi.org/10.1002/ldr.3902

Kalantari, Z., Cavalli, M., Cantone, C., Crema, S., Destouni, G., 2017. Flood probability quantification for road infrastructure: Data-driven spatial-statistical approach and case study applications. Sci. Total Environ. 581–582, 386–398. https://doi.org/10.1016/j. scitotenv.2016.12.147.

Kataoka, K.S., Manville, V., Nakajo, T., Urabe, A., 2009. Impacts of explosive volcanism on distal alluvial sedimentation: examples from the Pliocene-Holocene volcaniclastic successions of Japan. Sediment. Geol. 220 (3–4), 306–317. https://doi.org/10.1016/j. sedgeo.2009.04.016.

Keesstra, S., Nunes, J.P., Saco, P., Parsons, T., Poeppl, R., Masselink, R., Cerdà A., 2018. The way forward: can connectivity be useful to design better measuring and modelling schemes for water and sediment dynamics? Sci. Total Environ. 644, 1557-1572.

Key, C.H., Benson, N.C., 2006. Landscape assessment (LA). In: Lutes, D.C., Keane, R.E., Caratti, J.F., Key, C.H., Benson, N.C., Sutherland, S., Gangi, L.J. (Eds.), 2006. FIREMON: Fire Effects Monitoring and Inventory System. Gen. Tech. Rep. RMRS-GTR-164-CD. U.S. Department of Agriculture, Forest Service, Rocky Mountain Research Station, Fort Collins, CO, pp. LA–1-55.

Knighton, D., 1998. Fluvial Forms and Processes: a new perspective. Hodder Arnold, London.

Korup, O., 2005. Geomorphic imprint of landslides on alpine river systems, southwest New Zealand. Earth Sur. Proc. Land. 30 (7), 783–800.

Korup, O., Seidemann, J., Mohr, C.H., 2019. Increased landslide activity on forested hillslopes following two recent volcanic eruptions in Chile. Nat. Geosci. 12 (4), 284–289. https://doi.org/10.1038/s41561-019-0315-9.

Krapesch, G., Hauer, C., Habersack, H., 2011. Scale orientated analysis of river width changes due to extreme flood hazards. Nat. Hazards Earth Syst. Sci. 11, 2137–2147.

Lane, S.N., Westaway, R.M., Hicks, D.M., 2003. Estimation of erosion and deposition volumes in a large, gravel-bed, braided river using synoptic remote sensing. Earth Surf. Proc. Land. 28 (3), 249–271. https://doi.org/10.1002/esp.483.

Lara, L.E., 2009. The 2008 eruption of the Chaitén volcano, Chile: a preliminary report. Andean Geol. 36 (1), 125–129. https://doi.org/10.1007/s00445-010-0428-x.

Lara, L.E., Moreno, R., Amigo, Á., Hoblitt, R.P., Pierson, T.C., 2013. Late Holocene history of Chaitén Volcano: new evidence for a 17th century eruption. Andean Geol. 40 (2). https://doi.org/10.5027/andgeoV40n2-a04.

Larsen, I.J., MacDonald, L.H., Brown, E., Rough, D., Welsh, M.J., Pietraszek, J.H., Libohova, Z., Benavides-Solorio, J., Schaffrath, K., 2009. Causes of post-fire runoff and erosion: water repellency, Cover, or soil sealing? Soil Sci. Soc. Am. J. 73 (4), 1393–1407.

Lenzi, M.A., D'Agostino, V., Billi, P., 1999. Bedload transport in the instrumented catchment of the Rio Cordon: Part I: Analysis of bedload records, conditions and threshold of bedload entrainment. Catena 36 (3), 171–190.

Lenzi, M.A., Marchi, L., 2000. Suspended sediment load during floods in a small stream of the Dolomites (northeastern Italy). Catena 39 (4), 267–282. https://doi.org/ 10.1016/S0341-8162(00)00079-5.

Lenzi, M.A., 2001. Step-pool evolution in the Rio Cordon, Northeastern Italy. Earth Surf. Proc. Land. 26 (9), 991–1008. https://doi.org/10.1002/esp.239.

Lenzi, M.A., Mao, L., Comiti, F., 2006a. Effective discharge for sediment transport in a mountain river: computational approaches and geomorphic effectiveness. J. Hydrol. 326 (1–4), 257–276.

Lenzi, M.A., Mao, L., Comiti, F., 2006b. When does bedload transport begin in steep boulder-bed streams? Hydrol. Process. 20, 3517–3533.

Lexartza-Artza, I., Wainwright, J., 2009. Hydrological connectivity: linking concepts with practical implications. Catena 79 (2), 146-152.

Li, M., Zang, S., Zhang, B., Li, S., Wu, C., 2014. A review of remote sensing image classification techniques: the role of Spatio-contextual information. European Journal of Remote Sensing 47 (1), 389–411. https://doi.org/10.5721/EuJRS20144723.

Liébault, F., Piégay, H., 2002. Causes of the 20th century channel narrowing in mountain and piedmont rivers of southeastern France. Earth Surf. Proc. Land. 27, 425–444.

Liébault, F., Bellot, H., Chapuis, M., Klotz, S., Deschˆatres, M., 2012. Bedload tracing in a high-sediment-load mountain stream. Earth Surf. Proc. Land. 37, 385–399.

Liu, Y., Fu, B., 2016. Assessing sedimentological connectivity using WATEM/SEDEM model in a hilly and gully watershed of the Loess Plateau, China. Ecological Indicators, 66, 259–268. https://doi.org/10.1016/j.ecolind.2016.01.055.

Lizaga, I., Quijano, L., Palazón, L., Gaspar, L., Navas, A., 2017. Enhancing connectivity index to assess the effects of land use changes in a Mediterranean catchment. Land Degrad. Dev. 675 (June 2017), 663–675. https://doi.org/10.1002/ldr.2676.

Llena, M., Vericat, D., Cavalli, M., Crema, S., Smith, M.W., 2019. The effects of land use and topographic changes on sediment connectivity in mountain catchments. Sci. Total Environ. 660, 899–912. https://doi.org/10.1016/j.scitotenv.2018.12.479.

López-Escobar, L., Kilian, R., Kempton, P.D., Tagiri, M., 1993. Petrography and geochemistry of quaternary rocks from the southern volcanic zone of the Andes between 41°30′ and 46°00′S, Chile. Revista Geológica de Chile 20 (1), 33–55. https://doi.org/10.5027/ andgeoV20n1-a04.

López-Vicente, M., Poesen, J., Navas, A., Gaspar, L., 2013. Predicting runoff and sediment connectivity and soil erosion by water for different land use scenarios in the Spanish Pre-Pyrenees. Catena 102, 62-73.

López-Vicente, M., Álvarez, S., 2018. Influence of DEM resolution on modelling hydrological connectivity in a complex agricultural catchment with woody crops. Earth Surf. Process. Landf. 43 (7), 1403–1415. https://doi.org/10.1002/esp.4321.

López-Vicente, M., Ben-Salem, N., 2019. Computing structural and functional flow and sediment connectivity with a new aggregated index: a case study in a large Mediterranean catchment. Sci. Total Environ. 651, 179–191. https://doi.org/10.1016/J. SCITOTENV.2018.09.170.

López-Vicente, M., González-Romero, J., Lucas-Borja, M.E., 2020. Forest fire effects on sediment connectivity in headwater sub-catchments: Evaluation of indices performances. Science of the Total Environment 732, 139206.

Lu, D., Weng, Q., 2007. A survey of image classification methods and techniques for improving classification performance. Int. J. Remote Sens. 28 (5), 823–870. https://doi. org/10.1080/01431160600746456.

Lucía, A., Schwientek, M., Eberle, J., Zarfl, C., 2018. Planform changes and large wood dynamics in two torrents during a severe flash flood in Braunsbach, Germany 2016. Sci. Total Environ. 640–641, 315–326.

Magilligan, F.J., 1992. Thresholds and the spatial variability of flood power during extreme floods. Geomorphology 5, 373–390.

Magilligan, F.J., Buraas, E.M., Renshaw, C.E., 2015. The efficacy of stream power and flow duration on geomorphic responses to catastrophic flooding. Geomorphology 228, 175–188.

Major, J.J., 2003. Post-eruption hydrology and sediment transport in volcanic river systems. Water Resources IMPACT (January 2003), 10–15 Retrieved from. http://vulcan.wr.usgs. gov/Projects/JJMajor/Publications/WaterResImpact_2003/Major_IMPACT_2003.pdf.

Major, J.J., Pierson, T.C., Dinehart, R.L., Costa, J.E., 2000. Sediment yield following severe volcanic disturbance - a two-decade perspective from Mount St. Helens. Geology 28 (9), 819–822. https://doi.org/10.1130/0091-7613(2000)28b819:SYFSVDN2.0.CO;2.

Major, J.J., Yamakoshi, T., 2005. Decadal-scale change of infiltration characteristics of a tephra-mantled hillslope at Mount St Helens, Washington. Hydrol. Process. 19 (18), 3621–3630. https://doi.org/10.1002/hyp.5863.

Major, J.J., Lara, L.E., 2013. Overview of Chaitén Volcano, Chile, and its 2008-2009 eruption. Andean Geol. 40 (2). https://doi.org/10.5027/andgeoV40n2-a01.

Major, J:J., Pierson, T.C., Hoblitt, R.P., Moreno, H., 2013. Pyroclastic density currents associated with the 2008-2009 eruption of Chaitén Volcano (Chile): Forest disturbances, deposits, and dynamics. Andean Geol. 40 (2), 324–358. https://doi.org/ 10.5027/andgeoV40n2-a09.

Major, J.J., Bertin, D., Pierson, T.C., Amigo, Á., Iroumé, A., Ulloa, H., Castro, J., 2016. Extraordinary sediment delivery and rapid geomorphic response following the 2008–2009 eruption of Chaitén Volcano, Chile. Water Resour. Res. 52, 5075–5094. https://doi. org/10.1002/2015WR018250.

Mahoney, D.T., Fox, J.F., Al-Aamery, N., 2018. Watershed erosion modeling using the probability of sediment connectivity in gently rolling system. J. Hydrology 561, 862-883.

Manville, V., Németh, K., Kano, K., 2009. Source to sink: a review of three decades of progress in the understanding of volcaniclastic processes, deposits, and hazards. Sediment. Geol. 220 (3–4), 136–161. https://doi.org/10.1016/j.sedgeo.2009.04.022.

Mao, L., Lenzi, M.A., 2007. Sediment mobility and bedload transport conditions in an alpine stream. Hydrol. Process. 21, 1882–1891.

Marchi, L., Cavalli, M., Sangati, M., Borga, M., 2009a. Hydrometeorological controls and erosive response of an extreme alpine debris flow. Hydrol. Process. 23 (19), 2714–2727.

Marchi, L., Borga, M., Preciso, E., Sangati, M., Gaume, E., Bain, V., Delrieu, G., Bonnifait, L., Pogaćnik, N., 2009b. Comprehensive post-event survey of a flash flood in Western Slovenia: observation strategy and lessons learned. Hydrol. Process. 23, 3761–3770.

Marchi, L., Cavalli, M., Amponsah, W., Borga, M., Crema, S., 2016. Upper limits of flash flood stream power in Europe. Geomorphology 272 (1), 68–77.

Martini, L., Picco, L., Iroumé, A., Cavalli, M., 2019. Sediment connectivity changes in an Andean catchment affected by volcanic eruption. Sci. Total Environ. 692, 1209–1222.

Martini, L., Faes, L., Picco, L., Iroumé, A., Lingua, E., Garbarino, M. Cavalli, M., 2020. Assessing the effect of fire severity on sediment connectivity in central Chile. Science of the Total Environment 728, 139006. https://doi.org/10.1016/j.scitotenv.2020.139006.

Marzano, R., Lingua, E., Garbarino, M., 2012. Post-fire effects and short-term regeneration dynamics following high-severity crown fires in a Mediterranean forest. iForest - Bio-geosciences and Forestry 5, 93–100.

Marzano, R., Garbarino, M., Marcolin, E., Pividori, M., Lingua, E., 2013. Deadwood anisotropic facilitation on seedling establishment after a stand-replacing wildfire in Aosta Valley (NW Italy). Ecol. Eng. 51, 117–122.

Mazzorana, B., Picco, L., Rainato, R., Iroumé, A., Ruiz-Villanueva, V., Rojas, C., Valdebenito, G., Iribarren-Anacona, P., Melnick, D., 2019. Cascading processes in a changing environment:

disturbances on fluvial eco- systems in Chile and implications for hazard and risk management. Sci. Total Environ. 655 (November 2018), 1089–1103. https://doi.org/10.1016/j.scitotenv.2018.11.217.

McEwen, L.J., Werritty, A., 1988. The hydrology and long-term geomorphic significance of a flash flood in the Cairngorm mountains, Scotland. Catena 15, 361–377.

McFadden, D.P., 1973. Conditional logit analysis of qualitative choice behavior. In Frontier in Econometrics, ed. by Zarembka. New York: Academic Press.

Menard, S., 1995. An introduction to Logistic Regression Diagnostics. In Appliead Logistic Regression Analysis, 58-79. Thousand Oaks, CA: Sage Publications. Inc.

Messenzehl, K., Hoffmann, T., Dikau, R., 2014. Sediment connectivity in the high-alpine valley of Val Müschauns, Swiss National Park - linking geomorphic field mapping with geomorphometric modelling. Geomorphology 221, 215–229. https://doi.org/ 10.1016/j.geomorph.2014.05.033.

Meyer, D., Martinson, H., 1989. Rates and processes of channel development and recovery following the 1980 eruption of Mount St. Helens, Washington. Hydrological Sciences 34 (2), 115–127. https://doi.org/10.1080/02626668909491318.

Miller, A.J., 1990. Flood hydrology and geomorphic effectiveness in the central Appalachians. Earth Surf. Proc. Land. 15, 119–134

Miller, J.D., Thode, A.E., 2007. Quantifying burn severity in a heterogeneous landscape with a relative version of the Delta normalized burn ratio (DNBR). Remote Sens. Environ. 109 (1), 66–80.

Miller, J.D., Knapp, E.E., Key, C.H., Skinner, C.N., Isbell, C.J., Creasy, R.M., Sherlock, J.W., 2009. Calibration and validation of the relative differenced normalized burn ratio (RdNBR) to three measures of fire severity in the Sierra Nevada and Klamath Mountains, California, USA. Remote Sens. Environ. 113 (3), 645–656.

Mishra, K., Sinha, R., Jain, V., Nepal, S., Uddin, K., 2019. Towards the assessment of sediment connectivity in a large Himalayan River basin. Sci. Total Environ. 661, 251–265.

Molinas, C., Leverkus, A., Marañón-Jiménez, S., Castro, J., 2017. Fall rate of burnt pines across an elevational gradient in a Mediterranean mountain. Eur. J. For. Res. 136 (3). https://doi.org/10.1007/s10342-017-1040-9.

Montgomery, D.R., Buffington, J.M., 1997. Channel-reach morphology in mountain drainage basins. Geol. Soc. Am. Bull. 109 (5), 596–611.

Morresi, D., Vitali, A., Urbinati, C., Garbarino, M., 2019. Forest spectral recovery and regeneration dynamics in stand-replacing wildfires of central Apennines derived from Landsat time series. Remote Sens. 11 (3), 308.

Najafi, S., Dragovich, D., Heckmann, T., Sadeghi, S. H., 2021. Sediment connectivity concepts and approaches. Catena, 196(March 2020), 104880. https://doi.org/10.1016/j.catena.2020.104880

Nannoni, A., Vigna, B., Fiorucci, A., Antonellini, M., De Waele, J., 2020. Effects of an extreme flood event on an alpine karst system. J. Hydrol. 590, 125493.

Neary, Daniel G., Ryan, Kevin C., DeBano, Leonard F., 2005. Wildland fire in ecosystems: effects of fire on soils and water. Gen. Tech. Rep. RMRS-GTR-42. vol.4. U.S. Department of Agriculture, Forest Service, Rocky Mountain Research Station, Ogden, UT 250 p.

Nicoll, T., Brierley, G., 2017. Within-catchment variability in landscape connectivity measures in the Garang catchment, upper yellow river. Geomorphology https://doi.org/ 10.1016/j.geomorph.2016.03.014.

Oliveras, I., Gracia, M., Moré, G., Retana, J., 2009. Factors influencing the pattern of fire severities in a large wildfire under extreme meteorological conditions in the Mediterranean Basin. Int. J. Wildland Fire 18 (7), 755–764.

Ortíz-Rodríguez, A.J., Borselli, L., Sarocchi, D., 2017. Flow connectivity in active volcanic areas: use of index of connectivity in the assessment of lateral flow contribution to main streams. Catena 157 (May), 90–111. https://doi.org/10.1016/j.catena.2017.05.009.

Ortíz-Rodríguez, A.J., Muñoz-robles, C., Borselli, L., 2019. Changes in connectivity and hydrological efficiency following wildland fires in Sierra Madre Oriental, Mexico. Sci. Total Environ. 655, 112–128 (https://doi.org/S0048969718345923).

Oss Cazzador, D., Rainato, R., Cavalli, M., Lenzi, M.A., Picco, L., 2020. Integrated analysis of sediment source areas in an Alpine basin. Catena 188, 104416. https:// doi.org/10.1016/j.catena.2019.104416.

Oss Cazzador, D., Rainato, R., Mao, L., Martini, L., Picco, L., 2021. Coarse sediment transfer and geomorphic changes in an alpine headwater stream. Geomorphology 376, 107569. https://doi.org/10.1016/j.geomorph.2020.107569.

Pagano, S.G., Rainato, R., Garcia-Rama, A., Gentile, F., Lenzi, M.A., 2019. Analysis of suspended sediment dynamics at event scale: comparison between a Mediterranean and an Alpine basin. Hydrol. Sci. J. 64 (8), 948–961.

Pallister, J.S., Diefenbach, A.K., Burton, W.C., Muñoz, J., Griswold, J.P., Lara, L.E., Valenzuela, C.E., 2013. The Chaitén rhyolite lava dome: eruption sequence, lava dome volumes, rapid effusion

rates and source of the rhyolite magma. Andean Geol. 40 (2). https:// doi.org/10.5027/andgeoV40n2-a06.

Panagos, P., Borrelli, P., Meusburger, K., Alewell, C., Lugato, E. Montanarella, L., 2015. Estimating the soil erosion cover-management factor at the European scale. Land Use Policy, 48, 38–50. https://doi.org/10.1016/j.landusepol.2015.05.021.

Parks, S.A., Dillon, G.K., Miller, C., 2014a. A new metric for quantifying burn severity: the relativized burn ratio. Remote Sens. 6 (3), 1827–1844.

Parks, S.A., Miller, C., Nelson, C.R., Holden, Z.A., 2014b. Previous fires moderate burn severity of subsequent Wildland fires in two large Western US wilderness areas. Ecosystems 17 (1), 29–42.

Pastorello, R., D'Agostino, V., Hürlimann, M., 2020. Debris flow triggering characterization through a comparative analysis among different mountain.

Peleg, N., Skinner, C., Fatichi, S., Molnar, P., 2020. Temperature effects on the spatial structure of heavy rainfall modify catchment hydro-morphological response. Earth Surf. Dyn. 8, 17–36.

Pellegrini, G., Martini, L., Cavalli, M., Rainato, R., Cazorzi, A., Picco, L., 2021. The morphological response of the Tegnas alpine catchment (Northeast Italy) to a Large Infrequent Disturbance. Sci. Total Environ. 770, 145209 https://doi.org/10.1016/j. scitotenv.2021.145209.

Pereira, P., Brevik, E., Trevisani, S., 2018. Mapping the environment. Science of The Total Environment, 611, 17–23. https://doi.org/10.1016/j.scitotenv.2017.08.001.

Persichillo, M.G., Bordoni, M., Cavalli, M., Crema, S., Meisina, C., 2018. The role of human activities on sediment connectivity of shallow landslides. Catena 160 (August 2016), 261–274. https://doi.org/10.1016/j.catena.2017.09.025.

Pickell, P.D., Hermosilla, T., Frazier, R.J., Coops, N.C., Wulder, M.A., 2016. Forest recovery trends derived from Landsat time series for North American boreal forests. Int. J. Remote Sens. 37 (1), 138–149.

Picco, L., Rainato, R., Pellegrini, G., Martini, L., Lenzi, M.A., Mao, L., 2020. An extraordinary event changed the (morphological) appearance of a famous Alpine stream. ISBN 0367627736. In: Proceedings of the 10th Conference on Fluvial Hydraulics (Delft, Netherlands, 7-10 July 2020). Taylor and Francis, pp. 1653–1658.

Pierson, T.C., Major, J.J., Amigo, Á., Moreno, H., 2013. Acute sedimentation response to rainfall following the explosive phase of the 2008-2009 eruption of Chaitén volcano, Chile. Bull. Volcanol. 75 (5), 1–17. https://doi.org/10.1007/s00445-013-0723-4.

Pierson, T.C., Major, J.J., 2014. Hydrogeomorphic effects of explosive volcanic eruptions on drainage basins. Annu. Rev. Earth Planet. Sci. 42 (1), 469–507. https://doi.org/ 10.1146/annurev-earth-060313-054913.

Piton, G., Recking, A., 2017. The concept of travelling bedload and its consequences for bedload computation in mountain streams. Earth Surf. Proc. Land. 42, 1505–1519.

Pomeroy, J.W., Xing, F., Marks, D., 2016. The Cold Rain-on-Snow Event of June 2013 in the Canadian Rockies - Characteristics and Diagnosis. Hydrol. Process. 30 (17), 2899–2914.

Poeppl, R., Keesstra, S., Maroulis, J., 2017. A conceptual framework for understanding geomorphic change in human-impacted fluvial systems. Geomorphology 277, 237-250.

Poeppl, R., Parson, A.J., 2018. The geomorphic cell: a basis for studying connectivity. Earth Surface Processes and Landforms 43(5), 1155-1159.

Poeppl, R., Fryris, K.A., Tunnicliffe, J., Brierely, G.J., 2020. Managing sediment (dis)connectivity in fluvial systems. Science of The Total Environment 736, 13927.

Pringle, C.M., 2001. Hydrological connectivity and the management of biological reserves: a global perspective. Ecological Applications, 11, 981-998.

Rainato, R., Mao, L., García-Rama, A., Picco, L., Cesca, M., Vianello, A., Preciso, E., Scussel, G.R., Lenzi, M.A., 2017. Three decades of monitoring in the Rio Cordon instrumented basin: Sediment budget and temporal trend of sediment yield. Geomorphology 291, 45–56.

Rainato, R., Mao, L., Picco, L., 2018. Near-bankfull floods in an Alpine stream: effects on the sediment mobility and bedload magnitude. Int. J. Sedim. Res. 33 (1), 27–34.

Rainato, R., Picco, L., Cavalli, M., Mao, L., Neverman, A.J., Tarolli, P., 2018. Coupling climate conditions, sediment sources and sediment transport in an alpine basin. Land Degrad. Dev. 29 (4), 1154–1166. https://doi.org/10.1002/ldr.2813.

Rainato, R., Mao, L., Picco, L., 2020. The effects of low-magnitude flow conditions on bedload mobility in a steep mountain stream. Geomorphology 367, 107345.

Rainato, R., Martini, L., Pellegrini, G., Picco, L., 2021. Hydrological, geomorphic and sedimentological responses of an alpine basin to a severe weather event (Vaia storm). Catena, 207, 105600. https://doi.org/10.1016/j.catena.105600.

Recking, A., 2012. Influence of sediment supply on mountain streams bedload transport. Geomorphology 175–176, 139–150.

Reid, D.E., Hickin, E.J., 2008. Flow resistance in steep mountain streams. Earth Surf. Proc. Land. 33, 2211–2240.

Renard, K. G., Foster, G. R., Weesies, G. A., McCool, D. K., Yoder, D. C., 1997. Predicting soil erosion by water: a guide to conservation planning with the revised universal soil loss equation (RUSLE). Agriculture Handbook 703. US Department of Agriculture.

Rickenmann, D., 1997. Sediment transport in Swiss torrents. Earth Surf. Proc. Land. 22 (10), 937–951.

Rickenmann, D., 2020. Effect of sediment supply on cyclic fluctuations of the disequilibrium ratio and threshold transport discharge, inferred from bedload transport measurements over 27 years at the Swiss Erlenbach stream. Water Resour. Res. 56 (11) e2020WR027741.

Rico, M., Benito, G., Barnolas, A., 2001. Combined palaeoflood and rainfall–runoff assessment of mountain floods (Spanish Pyrenees). J. Hydrol. 245, 59–72.

Rinaldi, M., Surian, N., Comiti, F., Bussettini, M., 2013. A method for the assessment and analysis of the hydromorphological condition of Italian streams: the Morphological Quality Index (MQI). Geomorphology 180–181, 96–108.

RStudio Team, 2016. RStudio: Integrated Development for R. RStudio, Inc., Boston, MA URL. http://www.rstudio.com/.

Ruiz-Villanueva, V., Badoux, A., Rickenmann, D., B¨ockli, M., Schlaefli, S., Steeb, N., Stoffel, M., Rickli, C., 2018. Impacts of a large flood along a mountain river basin: the importance of channel widening and estimating the large wood budget in the upper Emme River (Switzerland). Earth Surf. Dyn. 6, 1115–1137.

Schoklitsch, A., 1962. Handbuch des Wasserbaues, third ed. Springer, Wien.

Schopper, N., Mergili, M., Frigerio, S., Cavalli, M., Poeppl, R., 2019. Science of the Total Environment Analysis of lateral sediment connectivity and its connection to debris flow intensity patterns at different return periods in the Fella River system in northeastern Italy. Sci. Total Environ. 658, 1586–1600.

Schroeder, T.A., Wulder, M.A., Healey, S.P., Moisen, G.G., 2011. Mapping wildfire and clearcut harvest disturbances in boreal forests with Landsat time series data. Remote Sens. Environ. 115 (6), 1421–1433.

Schumm, S.A., 1977. The Fluvial System. John Wiley and Sons, New York.

Scorpio, V., Crema, S., Marra, F., Righini, M., Ciccarese, G., Borga, M., Cavalli, M., Corsini, A., Marchi, L., Surian, N., Comiti, F., 2018. Basin-scale analysis of the geomorphic effectiveness of flash floods: A study in the northern Apennines (Italy). Sci. Total Environ. 640–641, 337–351. https://doi.org/10.1016/j. scitotenv.2018.05.252.

SedAlp, 2017. SedAlp - Sediment Management in Alpine Basins. Available at. http://www.sedalp.eu/download/.

Settle, J.J., Briggs, S.A., 1987. Fast maximum likelihood classification of remotely-sensed imagery. Int. J. Remote Sens. 8 (5), 723–734. https://doi.org/10.1080/ 01431168708948683.

Shakesby, R.A., Doerr, S.H., 2006. Wildfire as a hydrological and geomorphological agent. Earth Sci. Rev. 74, 269–307.

Shakesby, R.A., 2011. Post-wildfire soil erosion in the Mediterranean: review and future research directions. Earth Sci. Rev. 105 (3–4), 71–100.

Shakti, P.C., Nakatani, T., Misumi, R., 2017. Hydrological simulation of small river basins in northern Kyushu, Japan, during the extreme rainfall event of July 5–6. J. Disaster Res. 13 (2), 396–409.

Sholtes, J.S., Yochum, S.E., Scott, J.A., Bledsoe, B.P., 2018. Longitudinal variability of geomorphic response to floods. Earth Surf. Proc. Land. 43, 3099–3113.

Singh, M., Sinha, R., 2019. Evaluating dynamic hydrological connectivity of a floodplain wetland in North Bihar, India using geostatistical methods. Sci. Total Environ. 651, 2473–2488.

Stevens-Rumann, C.S., Prichard, S.J., Strand, E.K., Morgan, P., 2016. Prior wildfires influence burn severity of subsequent large fires. Can. J. For. Res. 46 (11), 1375–1385.

Stoffel, M., Bollschweiler, M., 2008. Tree-ring analysis in natural hazards research – an overview. Nat. Hazards Earth Syst. Sci. 8, 187–202.

Swanson, F.J., 1981. Fire and geomorphic processes. In: Mooney, H.A., Bonnicksen, T.M., Christiansen, N.L., Lotan, J.E., Reiners, W.A. (Eds.), Fire Regime and Ecosystem Properties, United States Department of Agriculture, Forest Service, General Technical Report WO. vol. 26. United States Government Planning Office, Washington, DC, pp. 401–421.

Swanson, F.J., Jones, J.A., Crisafulli, C.M., Lara, A., 2013. Effects of volcanic and hydrologic processes on forest vegetation: Chaitén Volcano, Chile. Andean Geol. 40 (2). https://doi.org/10.5027/andgeoV40n2-a10.

Tarboton, D.G., 1997. A new method for the determination of flow directions and upslope areas in grid digital elevation models. Water Resour. Res. 33, 309–319.

Tarolli, P., Cavalli, M., Masin, R., 2019. High-resolution morphologic characterization of conservation agriculture. Catena 172 (August 2018), 846–856. https://doi.org/10.1016/j.catena.2018.08.026.

Taylor, J., 1997. An Introduction to Error Analysis: the Study of Uncertainties in Physical Measurements, second ed. University Science Books, Sausalito, CA.

Theler, D., Reynard, E., Lambiel, C., Bardou, E., 2010. The contribution of geomorphological mapping to sediment transfer evaluation in small alpine catchments. Geomorphology 124, 113–123.

Thomas, M. F., 2001. Landscape sensitivity in time and space – an introduction. Catena, 83-98.

Tiranti, D., Cavalli, M., Crema, S., Zerbato, M., Graziadei, M., Barbero, S., Cremonini, R., Silvestro, C., Bodrato, G., Tresso, F., 2016. Semi-quantitative method for the assessment of debris supply from slopes to river in ungauged catchments. Sci. Total Environ. 554–555,337–348. https://doi.org/10.1016/j.scitotenv.2016.02.150.

Tonon, A., Iroumé, A., Picco, L., Oss-Cazzador, D., Lenzi, M.A., 2017. Temporal variations of large wood abundance and mobility in the Blanco River affected by the Chaitén volcanic eruption, southern Chile. Catena 156 (February), 149–160. https://doi.org/ 10.1016/j.catena.2017.03.025.

Trevisani, S., Cavalli, M., 2016. Topography-based flow-directional roughness: potential and challenges. Earth Surface Dynamics 4 (2), 343–358.

Turnbull, L., Wainwright, J., Brazier, R.E., 2008. A conceptual framework for understanding semi-arid land degradation: ecohydrological interactions across multiple-space and time scales. Ecohydrology 1, 23-34.

Turnbull, L., Hütt, M. T., Ioannides, A. A., Kininmonth, S., Poeppl, R., Tockner, K., Bracken, L. J., Keestra, S., Liu, L., Masselink, R. Parsons, A. J., 2018. Connectivity and complex systems: learning from a multi-disciplinary perspective. Applied Network Science, 3(1). https://doi.org/10.1007/s41109-018-0067-2.

Turner, M.G., Dale, V.H., 1998. Comparing large, infrequent disturbances: what have we learned? Ecosystems 1, 493–496. https://doi.org/10.1007/s100219900045.

Turowski, J.M., Yager, E.M., Badoux, A., Rickenmann, D., Molnar, P., 2009. The impact of exceptional events on erosion, bedload transport and channel stability in a step pool channel. Earth Surf. Proc. Land. 34, 1661–1673.

Úbeda, X., Sarricolea, P., 2016. Wildfires in Chile: a review. Glob. Planet. Chang. 146, 152–161.

Uchida, T., Sakurai, W., Iuchi, T., Izumiyama, H., Borgatti, L., Marcato, G., Pasuto, A., 2018. Effects of episodic sediment supply on bedload transport rate in mountain rivers. Detecting debris flow activity using continuous monitoring. Geomorphology 306, 198–209.

Ulloa, H., Iroumé, A., Mao, L., Andreoli, A., Diez, S., Lara, L.E., 2015. Use of remote imagery to analyse changes in morphology and longitudinal large wood distribution in the Blanco River after the 2008 Chaitén volcanic eruption, southern Chile. Geografiska Annaler, Series A: Physical Geography 97 (3), 523–541. https://doi.org/10.1111/ geoa.12091.

Ulloa, H., Iroumé, A., Picco, L., Mohr, C.H., Mazzorana, B., Lenzi, M.A., Mao, L., 2016. Spatial analysis of the impacts of the Chaitén volcano eruption (Chile) in three fluvial systems. J. S. Am. Earth Sci. 69, 213–225. https://doi.org/10.1016/j.jsames.2016.04.008.

Veblen, T.T., Donoso, C., Schlegel, F.M., Escobar, B., 1981. Forest dynamics in south-Central Chile. J. Biogeogr. 8 (3), 211–247.

Veblen, T.T., 1982. Regeneration patterns in Araucaria araucana forests in Chile. J. Biogeogr. 9 (1), 11–28.

Vericat, D., Smith, M.W., Brasington, J., 2014. Patterns of topographic change in sub- humid badlands determined by high resolution multi-temporal topographic surveys. Catena 120, 164–176. https://doi.org/10.1016/j.catena.2014.04.012.

Vericat, D., Wheaton, J.M., Brasington, J., 2017. Revisiting the morphological approach: opportunities and challenges with repeat high-resolution topography. In: Tsutsumi, D., Laronne, J.B. (Eds.), Gravel-bed Rivers: Processes and Disasters, first ed. John Wiley & Sons Ltd, pp. 121–158.

Victoriano, A., Díez-Herrero, A., Génova, M., Guinau, M., Furdada, G., Khazaradze, G., Calvet, J., 2018. Four-topic correlation between flood dendrogeomorphological evidence and hydraulic parameters (the Portain´e stream, Iberian Peninsula). Catena 162, 216–229.

Vieira, D.C.S., Fernandez, C., Vega, J.A., Keizer, J.J., 2015. Does soil burn severity affect the post-fire runoff and interrill erosion response? A review based on meta-analysis of field rainfall simulation data. J. Hydrol. 523, 452–464.

Wainwright, J., Turnbull, L., Ibrahim, T. G., Lexartza-Artza, I., Thornton, S. F. Brazier, R. E. 2011. Linking environmental régimes, space and time: Interpretations of structural and functional connectivity. Geomorphology, 126(3–4), 387–404. https://doi.org/10.1016/j.geomorph.2010.07.027.

Weltz, M.A., Arslan, A.B., Lane, L.J., 1992. Hydraulic roughness coefficients for native rangelands. J. Irrig. Drain. Eng. 118 (5), 776–790. https://doi.org/10.1061/(ASCE) 0733-9437(1992)118:5(776).

Wester, T., Wasklewicz, T. and Staley, D., 2014. Functional and structural connectivity within a recently burned drainage basin. Geomorphology, 206, 362–373. https://doi.org/10.1016/j.geomorph.2013.10.011.

Wheaton, J.M., Brasington, J., Darby, S.E., Sear, D.A., 2010. Accounting for uncertainty in DEMs from repeat topographic surveys: Improved sediment budgets. Earth Surf. Proc. Land. 35 (2), 136–156. https://doi.org/10.1002/esp.1886.

Wheaton, J.M., Brasington, J., Darby, S.E., Kasprak, A., Sear, D., Vericat, D., 2013. Morphodynamic signatures of braiding mechanisms as expressed through change in sediment storage in a gravel-bed river. J. Geophys. Res. Earth Surf. 118 (2), 759–779. https://doi.org/10.1002/jgrf.20060.

White, P.S., Pickett, S.T.A., 1985. Natural disturbance and patch dynamics: an introduction. The Ecology of Natural Disturbance and Patch Dynamics. Academic Press Inc. https://doi.org/10.1016/B978-0-08-050495-7.50006-5.

Wicherski, W., Dethier, D.P., Ouimet, W.B., 2017. Erosion and channel changes due to extreme flooding in the Fourmile Creek catchment, Colorado. Geomorphology 294, 87–98.

Williams, C.J., Pierson, F.B., Robichaud, P.R., Al-Hamdan, O.Z., Boll, J., Strand, E.K., 2016. Structural and functional connectivity as a driver of hillslope erosion following disturbance. Int. J. Wildland Fire 25 (3), 306–321.

Wischmeier, W.H., Smith, D.D., 1978. Predicting Rainfall Erosion Losses - A Guide to Conservation Planning. Predicting Rainfall Erosion Losses - A Guide to Conservation Planning. USDA, Science and Education Administration.

Wohl, E., 2015. Legacy effects on sediments in river corridors. Earth Sci. Rev. 147, 30–53.

Wohl, E., Scott, D.N., 2017. Transience of channel head locations following disturbance. Earth Surf. Process. Landf. 42 (7), 1132–1139.

Wohl, E., Brierley, G., Cadol, D., Coulthard, T.J., Covino, T., Fryirs, K.A., Grant, G., Hilton, R.G., Lane, S.N., Magilligan, F.J., Meitzen, K.M., Passalacqua, P., Poeppl, R., Rathburn, S.L., Sklar, L.S., 2018. Connectivity as an emergent property of geomorphic systems. Earth Surf. Process. Landf. 44, 4–26. https://doi.org/10.1002/esp.4434.

Wohl, E., 2020. Rivers in the Landscape. John Wiley and Sons, Inc. Hoboken, NJ, USA.

Woods, S.W., Balfour, V.N., 2008. The effect of ash on runoff and erosion after a severe forest wildfire, Montana, USA. Int. J. Wildland Fire 17, 535–548.

Wu, B.S., Zheng, S., Thorne, C.R., 2012. A general framework for using the rate law to simulate morphological response to disturbance in the fluvial system. Prog. Phys. Geogr. 36(5), 575-597.

Wyzga, B., Radecki-Pawlik, A., Galia, T., Plesiński, K., Škarpich, V., Dušek, R., 2020. Use of high-water marks and effective discharge calculation to optimize the height of bank revetments in an incised river channel. Geomorphology 356, 107098.

Yochum, S.E., Sholtes, J.S., Scott, J.A., Bledsoe, B.P., 2017. Stream power and geomorphic change during the 2013 Colorado front range flood. Geomorphology 292, 178–192.

Young, N.E., Anderson, R.S., Chignell, S.M., Vorster, A.G., Lawrence, R., Evangelista, P.H., 2017. A survival guide to Landsat preprocessing. Ecology 98 (4), 920–932.

Youssef, A. M., Pourghasemi, H. R., Pourtaghi, Z. S., Al-Katheeri, M. M., 2016. Landslide susceptibility mapping using random forest, boosted regression tree, classification and regression tree, and general linear models and comparison of their performance at Wadi Tayyah Basin, Asir Region, Saudi Arabia. Landslides, 13(5), 839–856. https://doi.org/10.1007/s10346-015-0614-1.

Zanandrea, F., Michel, G.P., Kobiyama, M., 2020. Impedance influence on the index of sediment connectivity in a forested mountainous catchment. Geomorphology 351, 106962.

Zingaro, M., Re, A., Giachetta, E., Addabbo, A. D., Lovergine, F., Pasquale, V. De, Pepe, G., Brandolini, P., Cevasco, A., Capolongo, D., 2019. Sediment mobility and connectivity in a catchment: A new mapping approach. Science of the Total Environment, 672, 763–775. https://doi.org/10.1016/j.scitotenv.2019.03.461.

Zink, J.M., Jennings, G.D., 2014. Channel roughness in North Carolina Mountain Streams. J. Am. Water Resour. Assoc. (JAWRA) 50 (5), 1354–1358.